January 1996 • NREL/TP-442-7818

Effects of Grit Roughness and Pitch Oscillations on the S801 Airfoil

Airfoil Performance Report, Revised (12/99)

R. Reuss Ramsay
M. J. Hoffmann
G.M. Gregorek
The Ohio State University
Columbus, Ohio

National Renewable Energy Laboratory
1617 Cole Boulevard
Golden, Colorado 80401-3393
A national laboratory of the U.S. Department of Energy
Managed by Midwest Research Institute
for the U.S. Department of Energy
under contract No. DE-AC36-83CH10093

Foreword

Airfoils for wind turbines have been selected by comparing data from different wind tunnels, tested under different conditions, making it difficult to make accurate comparisons. Most wind tunnel data sets do not contain airfoil performance in stall commonly experienced by turbines operating in the field. Wind turbines commonly experience extreme roughness for which there is very little data. Finally, recent tests have shown that dynamic stall is a common occurrence for most wind turbines operating in yawed, stall or turbulent conditions. Very little dynamic stall data exists for the airfoils of interest to a wind turbine designer. In summary, very little airfoil performance data exists which is appropriate for wind turbine design.

Recognizing the need for a wind turbine airfoil performance data base, the National Renewable Energy Laboratory (NREL), funded by the U.S. Department of Energy, awarded a contract to Ohio State University (OSU) to conduct a wind tunnel test program. Under this program, OSU tested a series of popular wind turbine airfoils. A standard test matrix was developed to assure that each airfoil was tested under the same conditions. The test matrix was developed in partnership with industry and is intended to include all of the operating conditions experienced by wind turbines. These conditions include airfoil performance at high angles of attack, rough leading edge (bug simulation), steady and unsteady angles of attack.

Special care has been taken to report as much of the test conditions and raw data as practical so that designers can make their own comparisons and focus on details of the data relevant to their design goals. Some of the airfoil, coordinates are proprietary to NREL or an industry partner. To protect the information which defines the exact shape of the airfoil the coordinates have not been included in the report. Instructions on how to obtain these coordinates may be obtained by contacting C.P. (Sandy) Butterfield at NREL.

C. P. (Sandy) Butterfield
Wind Technology Division
National Renewable Energy Laboratory
1617 Cole Blvd.
Golden, Colorado, 80401 USA
Internet Address: Sandy_Butterfield@NREL.GOV
Phone 303-384-6902
FAX 303-384-6901

Preface

The Ohio State University Aeronautical and Astronautical Research Laboratory is conducting a series of steady state and unsteady wind tunnel tests on a set of airfoils that have been or will be used for horizontal-axis wind turbines. The purpose of these tests is to investigate the effect of pitch oscillations and leading edge grit roughness (LEGR) on airfoil performance. The study of pitch oscillation effects can help to understand the behavior of horizontal axis wind turbines in yaw. The results of these tests will aid in the development of new airfoil performance codes that account for unsteady behavior and also aid in the design of new airfoils for wind turbines. The application of LEGR simulates surface irregularities on wind turbines blades. These irregularities on the blades are caused by the accumulation of insect debris, ice, and/or the aging process and can significantly reduce the power output of the horizontal axis wind turbines. The experimental results from the application of LEGR will promote the development of airfoils that are less sensitive to roughness.

The present work was made possible by the efforts and financial support of the National Renewable Energy Laboratory which provided major funding and technical monitoring, the U.S. Department of Energy is credited for its funding of this document through the National Renewable Energy Laboratory under contract number DE-AC36-83CH10093 and KENETECH, U.S. Windpower Incorporated which provided technical assistance. The staff of The Ohio State University Aeronautical and Astronautical Research Laboratory appreciate the contributions made by personnel from both organizations. In addition the authors would like to recognize the efforts of the following student research assistants, Fernando Falasca, Jolanta M. Janiszewska, and Monica Angelats i Coll.

Summary

A S801 airfoil model was tested in The Ohio State University Aeronautical and Astronautical Research Laboratory 3x5 subsonic wind tunnel under steady state and unsteady conditions. The test defined baseline conditions for steady state angles of attack from -20° to +40° and examined unsteady behavior by oscillating the model about its pitch axis for three mean angles, three frequencies, and two amplitudes. For all oscillating cases, Reynolds numbers of 0.75, 1, 1.25, and 1.4 million were used. In addition, the above conditions were repeated after the application of leading edge grit roughness (LEGR) to determine contamination effects on airfoil performance.

Steady state results of the S801 testing showed a baseline maximum lift coefficient of 1.46 at 16.2° angle of attack for Reynolds number of 1 million. The application of LEGR reduced the maximum lift coefficient by 12% and increased the 0.0058 minimum drag coefficient value by more than 88%. The zero lift pitching moment of -0.1238 showed a 7% reduction in magnitude to -0.1146 with LEGR applied.

Data were also obtained for two pitch oscillation amplitudes: ±5.5° and ±10°. The larger amplitude consistently gave a higher maximum lift coefficient than the smaller amplitude, and both sets of unsteady maximum lift coefficients were greater than the steady state values. Stall is delayed on the airfoil while the angle of attack is increasing, thereby causing an increase in maximum lift coefficient. A hysteresis behavior was exhibited for all the unsteady test cases. The hysteresis loops were larger for the higher reduced frequencies and for the larger amplitude oscillations. As in the steady case, the effect of LEGR in the unsteady case was to reduce the lift coefficient at high angles of attack. In addition, with LEGR, the hysteresis behavior persisted into lower angles of attack than for the clean case.

In general, the unsteady maximum lift coefficient was 7% to 53% higher than the steady state maximum lift coefficient, and variation in the quarter chord pitching moment coefficient magnitude was 13% to 137% larger than the steady state values at high angles of attack. These findings indicate the importance of considering the unsteady flow behavior occurring in wind turbine operation in order to obtain accurate load estimates.

Table of Contents Page

List of Figures   Page

List of Tables Page

List of Symbols

AOA	Angle of attack
A/C, a.c.	Alternating current
c	Model chord length
C_d	Drag coefficient
C_{dmin}	Minimum drag coefficient
C_{dp}	Pressure drag coefficient
C_{dw}	Wake drag coefficient
C_{du}	Uncorrected drag coefficient
C_l	Lift coefficient
C_{lmax}	Maximum lift coefficient
$C_{l\ dec}$	Lift coefficient at angle of maximum lift, but with angle of attack decreasing
C_{lu}	Uncorrected lift coefficient
C_m, $C_{m1/4}$	Pitching moment coefficient about the quarter chord
$C_{m\ dec}$	Pitching moment coefficient at angle of maximum lift, but with angle of attack decreasing
$C_{m\ inc}$	Pitching moment coefficient at angle of maximum lift, but with angle of attack increasing
C_{mo}	Pitching moment coefficient about the quarter chord, at zero lift
$C_{m1/4u}$	Uncorrected pitching moment coefficient about the quarter chord
C_p	Pressure coefficient, $(p- p_\infty)/q_\infty$
C_{pmin}	Minimum pressure coefficient
f	Frequency
h	Wind tunnel test section height
hp, Hp, HP	Horsepower
Hz	Hertz
k	Grit particle size
k/c	Grit particle size divided by airfoil model chord length
p	Pressure
q	Dynamic pressure
q_u	Uncorrected dynamic pressure
q_w	Dynamic pressure through the model wake
q_∞	Free stream dynamic pressure
Re	Reynolds number
Re_u	Uncorrected Reynolds number
t	Time
U_∞	Corrected free stream velocity
V	Velocity
V_u	Uncorrected velocity
x	Axis parallel to model reference line
y	Axis perpendicular to model reference line

α	Angle of attack
α_{dec}	Decreasing angle of attack
α_{inc}	Increasing angle of attack
α_m	Median angle of attack
α_{mean}	Mean angle of attack
α_u	Uncorrected angle of attack
ϵ	Tunnel solid wall correction scalar
ϵ_{sb}	Solid blockage correction scalar
ϵ_{wb}	Wake blockage correction scalar
Λ	Body-shape factor
π	3.1416
σ	Tunnel solid wall correction parameter
ω_{red}, $\omega_{reduced}$	Reduced frequency, $\pi fc/U_\infty$

Introduction

Horizontal axis wind turbine rotors experience unsteady aerodynamics due to wind shear when the rotor is yawed, when rotor blades pass through the support tower wake, and when the wind is gusting. An understanding of this unsteady behavior is necessary to assist in the calculation of rotor performance and loads. The rotors also experience performance degradation due to surface roughness. These surface irregularities are due to the accumulation of insect debris, ice, and the aging process. Wind tunnel studies that examine both the steady and unsteady behavior of airfoils can help define pertinent flow phenomena, and the resultant data can be used to validate analytical computer codes.

A S801 airfoil model was tested in The Ohio State University Aeronautical and Astronautical Research Laboratory (OSU/AARL) 3x5 subsonic wind tunnel (3x5) under steady flow and stationary model conditions, as well as with the model undergoing pitch oscillations. To study the possible extent of performance loss due to surface roughness, a standard grit pattern (LEGR) was used to simulate leading edge contamination. After baseline cases were completed, the LEGR was applied for both steady state and model pitch oscillation cases. The Reynolds numbers used for steady state conditions were 0.75, 1, 1.25, and 1.5 million, while the angle of attack ranged from -20° to +40°. With the model undergoing pitch oscillations, data were acquired at Reynolds numbers of 0.75, 1, 1.25, and 1.4 million, at frequencies of 0.6, 1.2, and 1.8 Hz. Two sine wave forcing functions were used, ±5.5° and ±10°, at mean angles of attack of 8°, 14°, and 20°. For purposes herein, any reference to unsteady conditions means that the airfoil model was in pitch oscillation about the quarter chord.

Experimental Facility

Wind Tunnel

The OSU/AARL 3×5 was used to conduct tests on the S801 airfoil section. Schematics of the top and side views of the tunnel are shown in figures 1 and 2, respectively. This open circuit tunnel has a velocity range of 0 - 55 m/s (180 ft/sec) produced by a 2.4-m (8-ft) diameter, six-bladed fan. The fan is belt driven by a

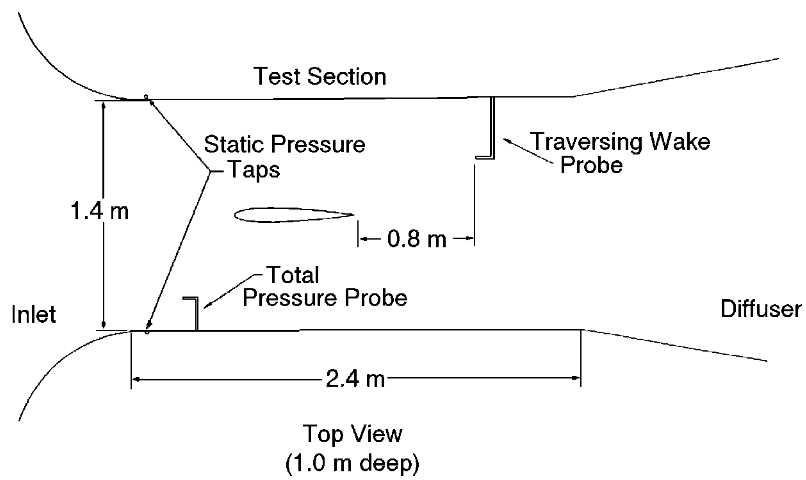

Figure 1. 3x5 Subsonic wind tunnel, top view.

93.2-kw (125-hp) three phase a.c. motor connected to a variable frequency motor controller. Nominal test section dimensions are 1.0-m (39-inches) high by 1.4-m (55-inches) wide by 2.4-m (96-inches) long. The 457-mm (18-inch) chord airfoil model was mounted vertically in the test section. A steel tube through the

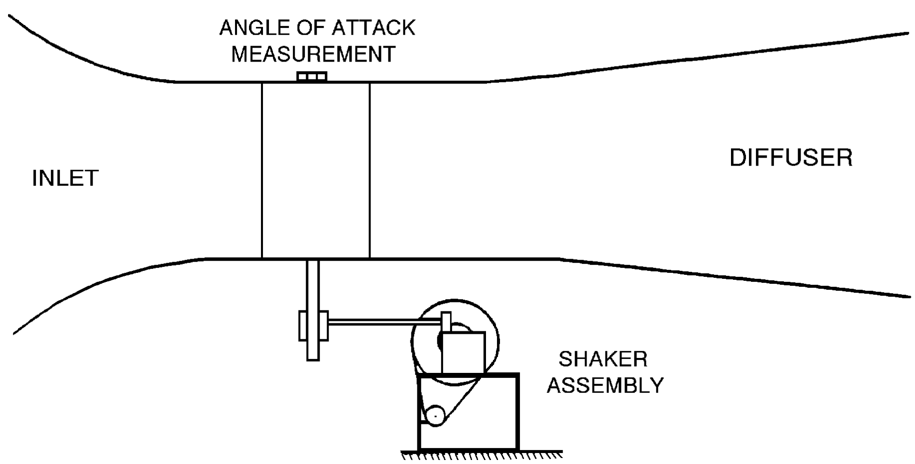

Figure 2. 3x5 Subsonic wind tunnel, side view.

quarter chord of the model attached the model to the tunnel during testing. An angle of attack potentiometer was fastened to the model at the top of the tunnel, as shown in figure 2. The steady state angle of attack was adjusted with a worm gear drive attached to the model strut below the tunnel floor.

Oscillation System

Portions of the airfoil model testing required the use of a reliable pitch oscillation system. The OSU/AARL "shaker" system incorporated a face cam and follower arm attached to the model support tube below the wind tunnel floor, as shown in figure 3. The choice of cam governed the type and amplitude of the wave form produced. Sine wave forms with amplitudes of ±5.5° and ±10° were used for these tests. The wave form is defined by the equation

$$\alpha = \alpha_m + A\sin(2\pi ft)$$

where A is the respective amplitude. The shaker system was powered by a 5-hp a.c. motor with variable line frequency controller. The useable oscillating frequency range was 0.1 - 2.0 Hz, with three frequencies used for this test: 0.6, 1.2, and 1.8 Hz.

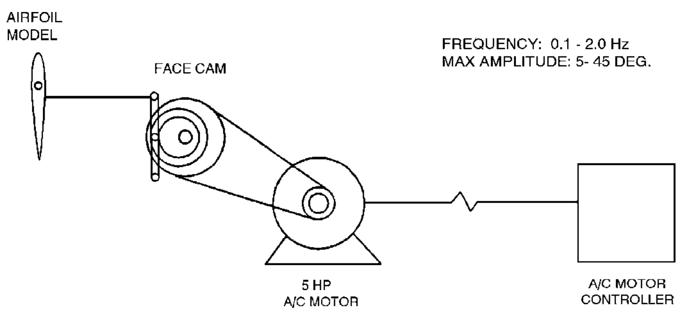

Figure 3. 3x5 Wind tunnel oscillation system.

Model Details

A 457-mm (18-inch) constant chord S801 airfoil model was provided by KENETECH, Windpower Inc. Figure 4 shows the airfoil section. Due to their proprietary nature, model coordinates are not presented in tabular form. The model was made of a sandwiched composite skin over ribs. The main load bearing

Figure 4. S801 airfoil section.

member was a 38-mm (1.5-inch) diameter steel tube which passed through the model quarter chord station. Ribs and end plates were used to transfer loads from the composite skin to the steel tube. The final surface was hand worked using templates to attain given coordinates within a requested tolerance of ±0.25-mm (±0.01-inch). The completed model was measured at three spanwise locations using a Sheffield-Cordax coordinate measurement machine. Measurements were made in English units and later converted to metric. Figure 5 shows the results of comparing measured-to-desired coordinates by calculating differences normal to the profiled surface at three stations on the model. The model was thickened near the trailing edge for fabrication reasons. This shows as a discrepancy between the measured and the desired coordinates near the

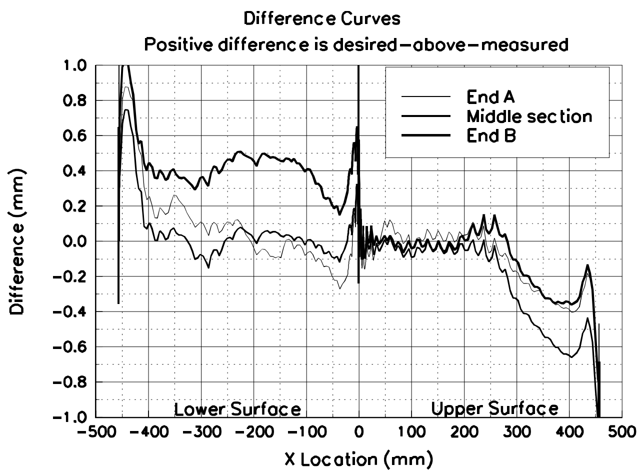

Figure 5. Comparison of desired to measured coordinates.

trailing edge of the airfoil model. The measured coordinates were compared to the only set of coordinates available, which had a sharp trailing edge. The "spikes" apparent near the trailing edge are due to the numerical methods used and are not real.

To minimize pressure response times, which is important for the unsteady testing, the surface pressure tap lead-out lines had to be as short as possible. Consequently, a compartment was built into the model so pressure scanning modules could be installed inside the model. This compartment was accessed through a panel door fitted flush with the model contour on the lower (pressure) surface.

For test cases involving roughness, a standard, repeatable pattern with grit as roughness elements was desired. The roughness pattern used was jointly developed by OSU/AARL and KENETECH, Windpower personnel from a molded insect pattern taken from a wind turbine in the field by personnel at the University of Texas Permian Basin. The particle density was 5 particles per cm^2 (32 particles per square inch) in the middle of the pattern, thinning to 1.25 particles per cm^2 (8 particles per square inch) at the edge of the pattern. Figure 6 shows the pattern. To make a usable template, the pattern was repeatedly cut into a steel sheet 102-mm (4-inch) wide and 91-cm (3-ft) long with holes just large enough for one piece of grit. Based on average particle size from the field specimen, standard #40 lapidary grit was chosen for the roughness elements, giving k/c=0.0019 for a 457-mm (18-inch) chord model.

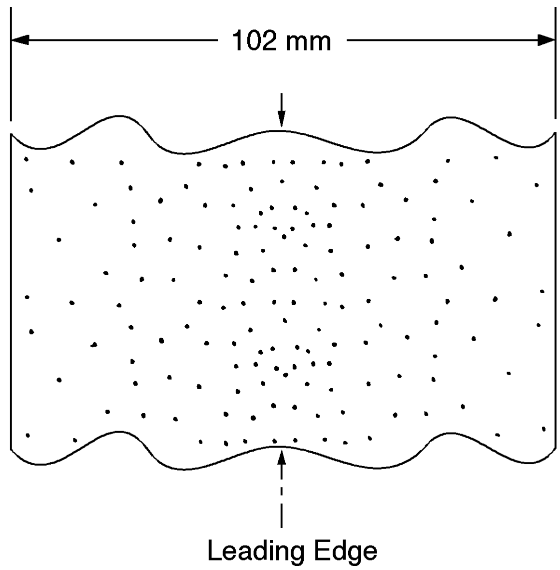

Figure 6. Roughness pattern.

To use the template, 102-mm (4-inch) wide double-tack tape was applied to one side of the template and grit was poured and brushed from the opposite side. The tape was then removed from the template and transferred to the model. This method allowed the same roughness pattern to be replicated for any test.

Test Equipment and Procedures

Data Acquisition

Data were acquired and processed from 60 surface pressure taps, four individual tunnel pressure transducers, an angle of attack potentiometer, a wake probe position potentiometer, and a tunnel thermocouple. The data acquisition system included an IBM PC compatible 80486-based computer connected to a Pressure Systems Incorporated (PSI) data scanning system. The PSI system included a 780B Data Acquisition and Control Unit (DACU), 780B Pressure Calibration Unit (PCU), 81-IFC scanning module interface, two 2.5-psid pressure scanning modules (ESPs), one 20-inch water column range pressure scanning module, and a 30-channel Remotely Addressed Millivolt Module (RAMM-30). Figure 7 shows the data acquisition system schematic.

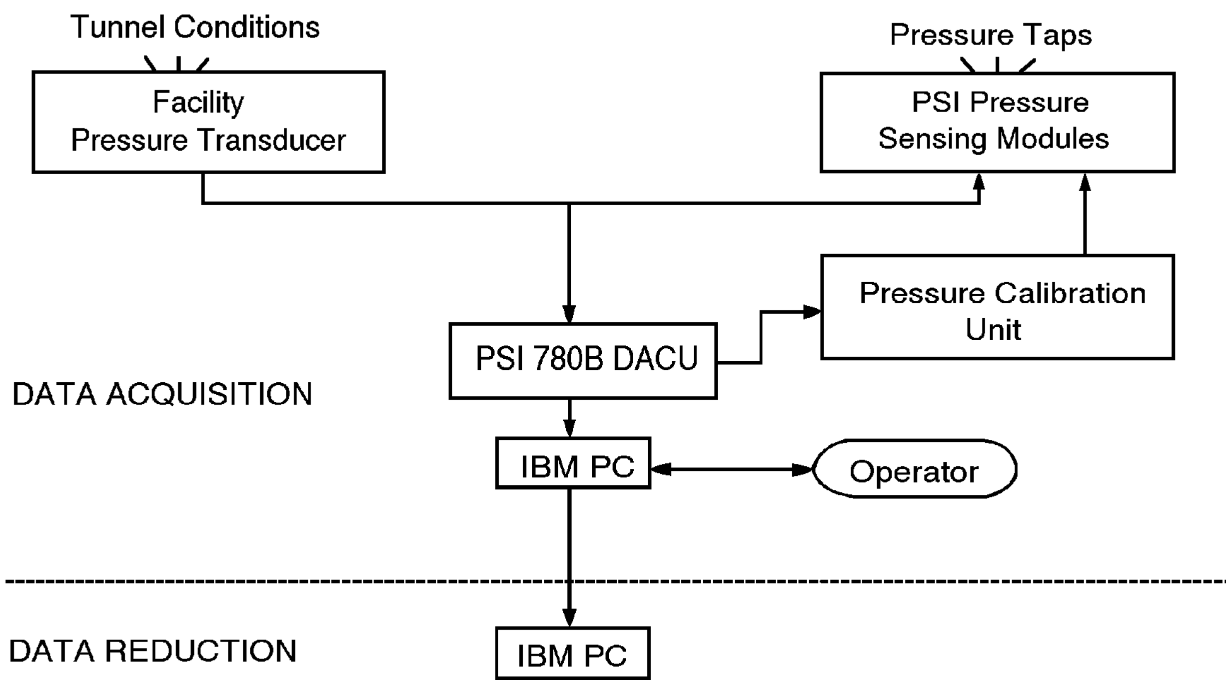

Figure 7. Data acquisition schematic.

Four individual pressure transducers read tunnel total pressure, tunnel north static pressure, tunnel south static pressure, and wake dynamic pressure. Before the test began, these transducers were bench calibrated using a water manometer to determine their sensitivities and offsets. Related values were entered into the data acquisition and reduction program so the transducers could be shunt resistor calibrated before each series of wind tunnel runs.

The rotary angle of attack potentiometer of 0.5% linearity was regularly calibrated during the tunnel pressure transducers shunt calibration. The angle of attack calibration was accomplished by taking voltage readings at known values of set angle of attack. This calibration method gave angle of attack readings within ±0.25° over the entire angle range. The wake probe position potentiometer was a linear potentiometer, and it was also regularly calibrated during the shunt calibration of the tunnel pressure transducers.

Calibration of the three ESPs was done simultaneously using the DACU and PCU. At operator request, the DACU commanded the PCU to apply known regulated pressures to the ESPs and read the output voltages from each integrated pressure sensor. From these values, the DACU calculated the calibration coefficients and stored them internally until the coefficients were requested by the controlling computer. This calibration was done several times during a run set because the ESPs were installed inside the model and their outputs tended to drift with temperature changes during a test sequence. Frequent on-line calibrations minimized the effect.

For steady state cases, the model was set to angle of attack and the tunnel conditions were adjusted. At operator request, pressure measurements from the airfoil surface taps and all other channels of information were acquired and stored by the DACU and subsequently passed to the controlling computer for final processing. The angles of attack were always set in the same progression from negative to positive values.

For model oscillating cases, the tunnel conditions were set while the model was stationary at the desired mean angle of attack. The "shaker" was started, and after approximately 10 seconds model surface pressure and tunnel condition data were acquired. Generally, 120 data scans were acquired over three model oscillation cycles. Since surface pressures were scanned sequentially, the data rate was set so the model rotated through less than 0.50° during any data burst. Finally, due to the unsteady and complex nature of the pitch oscillation cases, model wake surveys (for drag) were not conducted.

Data Reduction

The data reduction routine was included as a section of the data acquisition program. This combination of data acquisition and reduction routines allowed data to be reduced on-line during a test. By quickly reducing selected runs, integrity checks could be made to ensure the equipment was working properly and to allow timely decisions about the test matrix.

The ambient pressure was manually input into the computer and was updated regularly. This value, along with measurements from the tunnel pressure transducers and the tunnel thermocouple, were used to calculate tunnel airspeed. As a continuous check of readings, the tunnel total and static pressures were read by both the tunnel individual pressure transducers and the 20-inch water column ESP.

A typical steady state datum point was derived by acquiring 10 data scans of all channels over a 10 second window at each angle of attack and tunnel condition. The reduction portion of the program processed each data scan to coefficients (C_p, C_l, $C_{m¼}$, and C_{dp}) using the measured surface pressure voltages, calibration coefficients, tap locations and wind tunnel conditions. All scan sets for a given condition were then ensemble averaged to provide one data set and that data set was corrected for the effects of solid tunnel walls. All data were saved in electronic form.

Corrections due to solid tunnel sidewalls were applied to the wind tunnel data. As described by Pope and Harper (1966), tunnel conditions are represented by the following equations:

$$q = q_u(1 + 2\epsilon)$$

$$V = V_u(1 + \epsilon)$$

$$R_e = R_{e_u}(1 + \epsilon)$$

Airfoil aerodynamic characteristics are corrected by:

$$\alpha = \alpha_u + \frac{57.3\sigma}{2\pi}(C_{l_u} + 4C_{m\frac{1}{4}_u})$$

$$C_l = C_{l_u}(1 - \sigma - 2\epsilon)$$

$$C_{m_{\frac{1}{4}}} = C_{m_{\frac{1}{4}u}}(1-2\epsilon) + \frac{\sigma\ C_l}{4}$$

$$C_d = C_{d_u}(1-3\epsilon_{sb}-2\epsilon_{wb})$$

where

$$\sigma = \frac{\pi^2}{48}(\frac{c}{h})^2$$

$$\epsilon = \epsilon_{sb} + \epsilon_{wb}$$

$$\epsilon_{sb} = \Lambda\sigma$$

$$\epsilon_{wb} = \frac{c}{h4}C_{d_u}$$

Model wake data were taken for steady state cases when the wake could be completely traversed. Pressures were acquired from a pitot-static probe which was connected to measure incompressible dynamic pressure through the wake. These pressure measurements were used to calculate drag coefficient using a form of the Jones equation derived from Schlichting (1979).

$$C_{dw} = \frac{2}{c}\int \sqrt{\frac{q_w}{q_\infty}}\left(1-\sqrt{\frac{q_w}{q_\infty}}\right)\ dy$$

This equation assumes that static pressure at the measurement site is the free-stream value. The integration was done automatically except the computer operator chose the end points of the integration from a plot of the wake survey displayed on the computer screen.

For pitch oscillation cases, model surface pressures were reduced to pressure coefficient form with subsequent integrations and angle of attack considerations giving lift, moment and pressure drag coefficients. The wind tunnel was not calibrated for unsteady model pitch conditions; therefore, the unsteady pressure data were not corrected for any possible effects due to time dependent pitching or solid tunnel walls. Also, for these cases, the wind tunnel contraction pressures (used for steady state cases) could not be used to calculate instantaneous freestream conditions due to slow response. The tunnel conditions were obtained from a total pressure probe and the average of opposing static taps in the test section entrance; thereby giving near instantaneous flow pressure conditions for the pitching frequencies used.

Test Matrix

The test was designed to study steady state and unsteady pitch oscillation data. Steady state data were acquired at Reynolds numbers of 0.75, 1, 1.25, and 1.5 million, with and without LEGR. Refer to the tabular data in Appendix B for the actual Reynolds number for each angle of attack for the steady state data. The angle of attack increment was two degrees when $-20° < \alpha < +10°$ or $+20° < \alpha < +40°$ and one degree when $+10° < \alpha < +20°$. Wake surveys were conducted to find total airfoil drag over an approximate angle of attack range of -10° to +10°. Unsteady data were taken for Reynolds numbers of 0.75, 1, 1.25, and 1.4 million. Sine wave cams with amplitudes ±5.5° and ±10° were used for pitch oscillations, and the mean angles for both these amplitudes were 8°, 14°, and 20°. For all these conditions, the frequencies were varied to 0.6 Hz, 1.2 Hz, and 1.8 Hz. All data points for the unsteady cases were acquired for both clean and LEGR cases.

Results and Discussion

The S801 airfoil model was tested under steady state and pitch oscillation conditions. A brief discussion of the results follows, beginning with a comparison of experimental data and computational predictions.

Comparison With Theory

The wind tunnel steady state data were compared with computed predictions made using the North Carolina State Airfoil Analysis Code. This analysis code has proven to be accurate for moderate angles of attack. The analysis was made with specifications set to allow free transition from laminar to turbulent flow, and the pressure distribution comparisons were matched to the same angle of attack as the wind tunnel cases. Figure 8 shows the lift coefficient versus angle of attack for the 1 million Reynolds number case. For

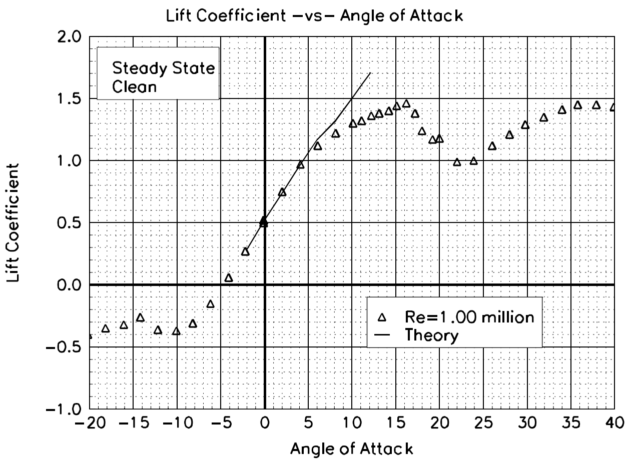

Figure 8. Comparison with theory, C_l vs α.

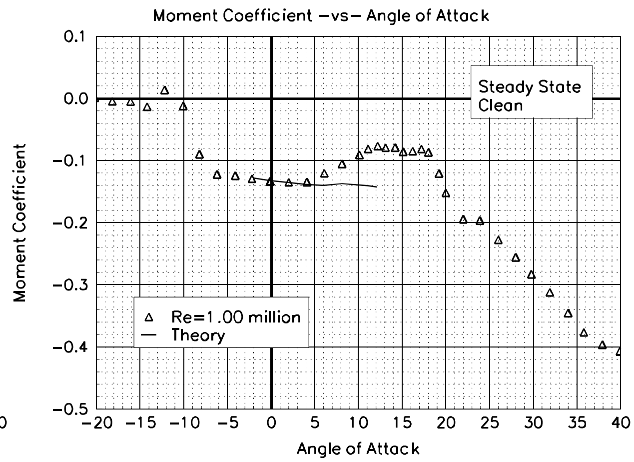

Figure 9. Comparison with theory, C_m vs α.

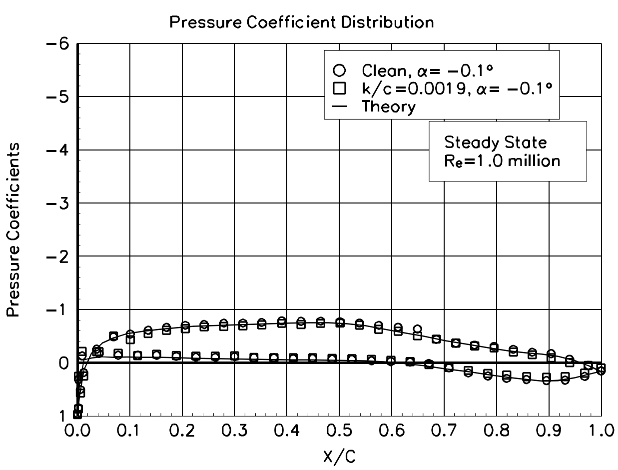

Figure 10. Comparison with theory, C_p vs x/c, α=-0.1°.

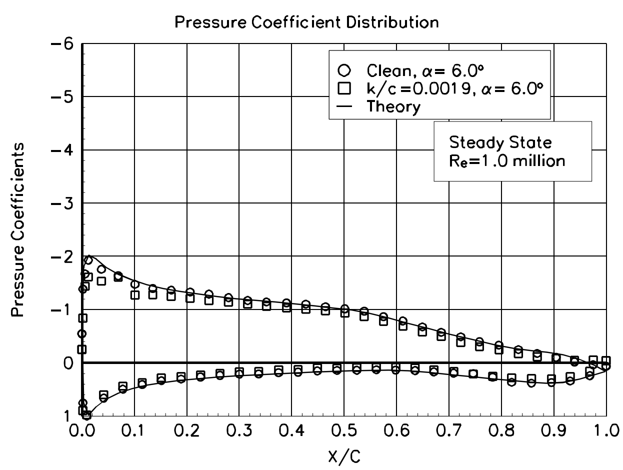

Figure 11. Comparison with theory, C_p vs x/c, α=6.0°.

moderate angles of attack, where the analysis code is valid, the comparison shows good agreement. The pitching moment about the quarter chord, figure 9, also shows good agreement for angles of attack from -5° to +5°. The pressure distributions shown in figures 10 and 11 are for angles of attack of -0.1° and 6.0°, respectively, and include clean and LEGR wind tunnel data as compared to computed free transition pressure distributions. For both angles of attack, there is excellent correlation between the experimental and predicted values.

Steady State Data

The S801 airfoil model was tested at four Reynolds numbers at nominal angles of attack from -20° to +40°. Figures 12 and 13 show lift coefficients for all the test Reynolds numbers for clean model and with LEGR applied, respectively. The maximum positive lift coefficient for the clean cases is about 1.46 and about 1.28 for the LEGR cases, a 12% reduction. The stall characteristic is similar for both clean and LEGR cases, with stall occurring earlier for the LEGR cases. Finally, the average lift curve slope for clean data is about 0.111; it is slightly lower for the LEGR case at 0.101. The associated average lift coefficients at zero angle of attack are 0.52 for the clean case and 0.43 for the LEGR case.

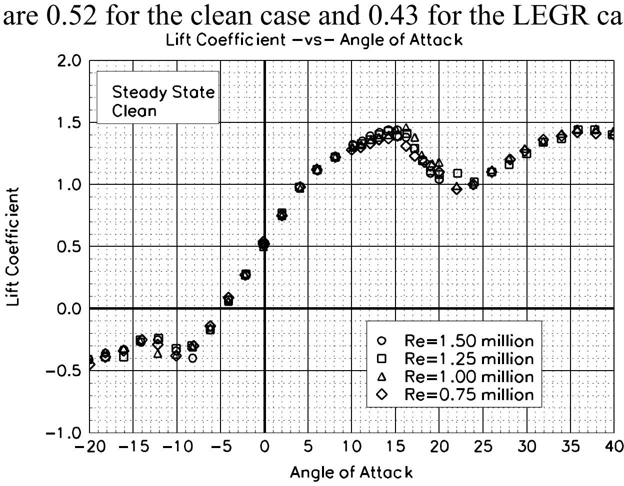

Figure 12. C_l vs α, clean.

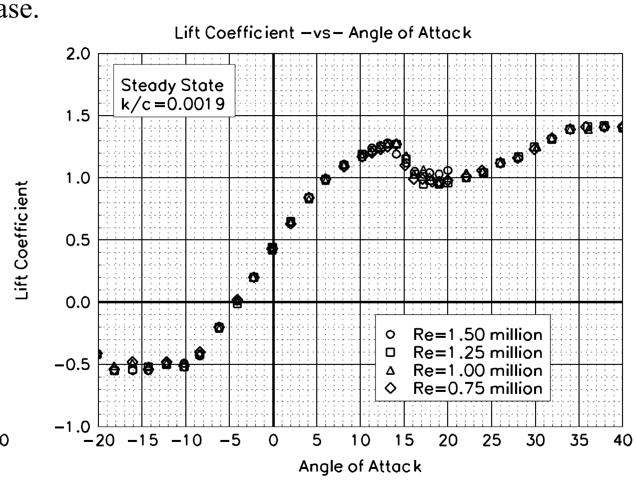

Figure 13. C_l vs α, LEGR, k/c=0.0019.

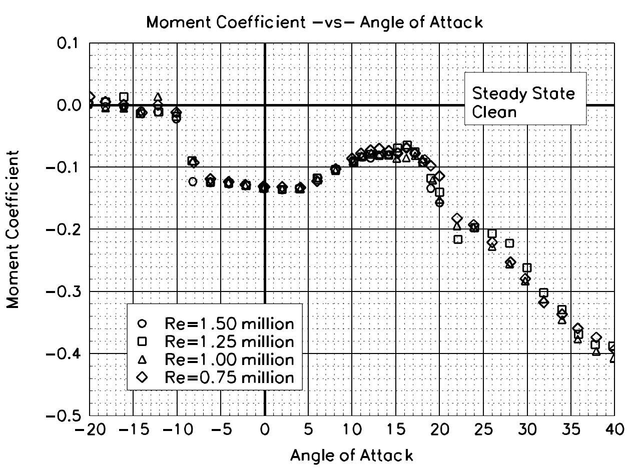

Figure 14. C_m vs α, clean.

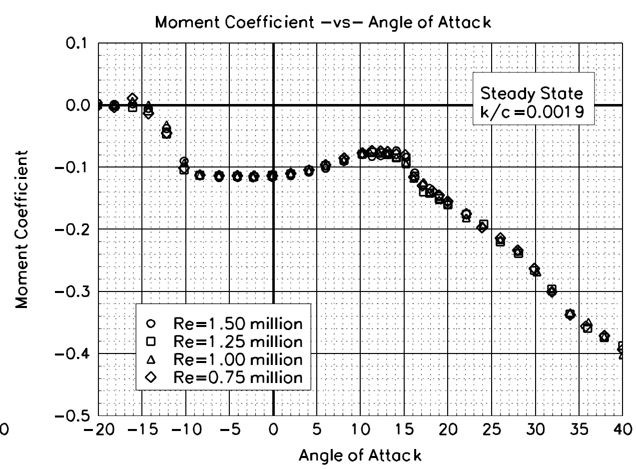

Figure 15. C_m vs α, LEGR, k/c=0.0019.

Figure 14 shows the pitching moment about the quarter chord for the clean cases, and figure 15 shows the same for the LEGR cases. The LEGR data have slightly more positive pitching moment at low angles of attack. The pitching moment coefficient about the quarter chord for the 1 million Reynolds number, is -0.1238 for the clean case and -0.1146 for the LEGR case.

Total wake drag data were obtained for both the clean and LEGR cases over an angle of attack range of -10° to +10°. A pitot-static probe was used to describe the wake profile. This method is reliable when there is relatively low turbulence in the wake flow; therefore, only moderate angles of attack have reliable total drag coefficient data. At angles of attack other than -10° to +10°, surface pressure data were integrated to give C_{dp} and are shown in the drag polars as small symbols. The model clean drag data are shown in figure 16, and the LEGR case is shown in figure 17. At 1 million Reynolds number, minimum drag coefficient for the clean cases was measured as 0.0058, and 0.0109 for LEGR, an 88% increase. The general effect of LEGR is to increase drag consistently through most angles of attack.

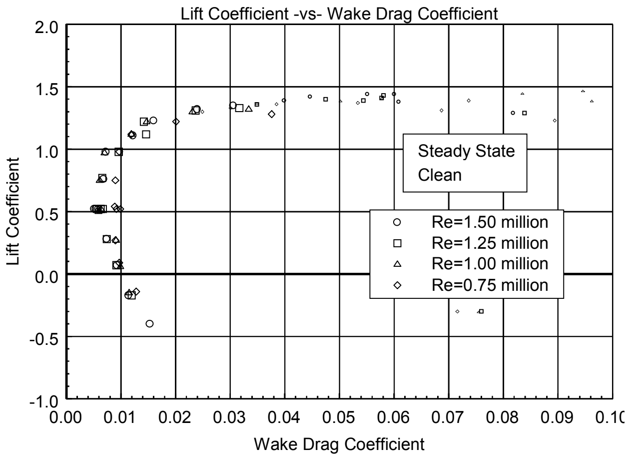

Figure 16. Clean, drag polar.

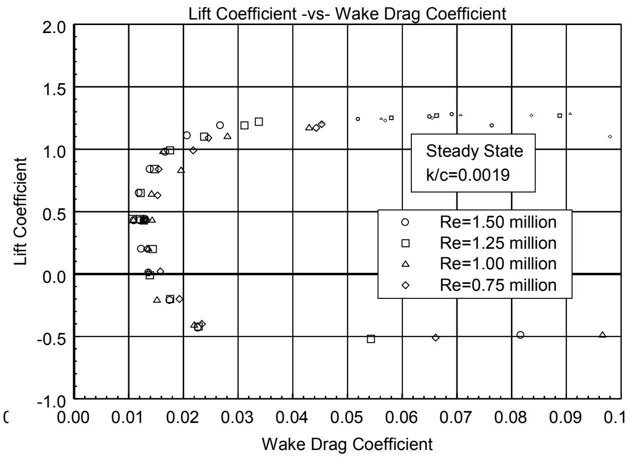

Figure 17. LEGR, drag polar.

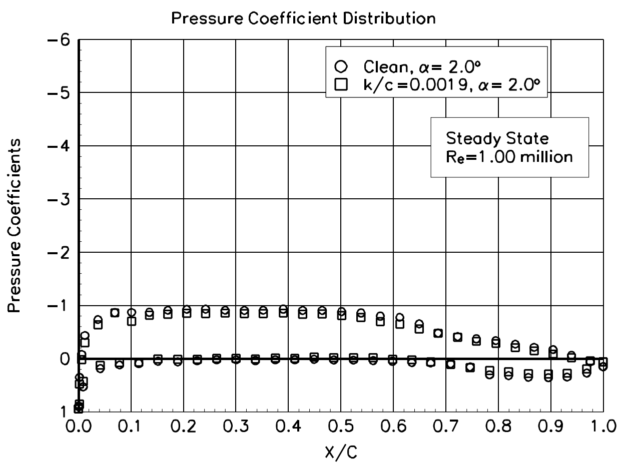

Figure 18. Pressure distribution, α=2.0°.

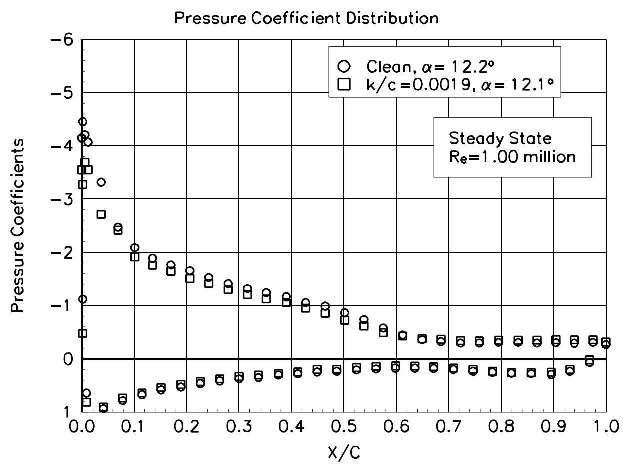

Figure 19. Pressure distribution, α=12.2°.

Two examples of the surface pressure distributions are shown in figures 18 and 19 for 2.0° and 12.2°, respectively, for 1 million Reynolds number. At angles of attack close to zero degrees, the effect of LEGR does not appear to significantly affect the pressure distribution in comparison with the clean case distribution. However, there is an effect apparent in the lift coefficient with values of 0.64 for the LEGR case and 0.75 for the clean case. For the higher angle of attack, figure 19, the effect of LEGR is to reduce the magnitude of the pressure peak from -4.4 to -3.7 and increase the pressures on the upper (suction) surface over the forward 60% of the chord. The net effect is a reduction in lift coefficient from 1.36 to 1.24, a 9% decrease.

Unsteady Data

Unsteady experimental data were obtained for the S801 airfoil model undergoing sinusoidal pitch oscillations. As mentioned earlier, no attempt was made to calibrate the wind tunnel for the unsteady oscillating model conditions; the steady state tunnel calibration was used to set the flow conditions while the model was stationary at its mean angle of attack. The use of the unsteady data should be limited to comparisons with other models tested in this same facility and can be used to detect possible trends. A comprehensive set of test conditions was used to describe unsteady behavior of an airfoil, including two angle of attack amplitudes, ±5.5° and ±10°; four Reynolds numbers, 0.75, 1, 1.25, and 1.4 million; three pitch oscillation frequencies, 0.6, 1.2, and 1.8; and three mean angles of attack, 8°, 14°, and 20°.

Figure 20 shows the lift coefficient versus angle of attack for the ±5.5° amplitude, model clean case, at reduced frequency of 0.027 and 1 million Reynolds number. Note that all three mean angles of attack are plotted on the same figure. The maximum pre-stall lift coefficient for this case is near 1.61 and occurs when the airfoil is traveling with the angle of attack increasing. In contrast, when the model is traveling through decreasing angles of attack, the stall recovery is delayed and a hysteresis behavior is exhibited in the lift coefficient that can be seen throughout all of the unsteady data. To obtain some measure of this hysteresis behavior, the lift coefficient on the "return" portion of the curve, at the angle of attack where maximum lift coefficient occurs, can be used. For the case discussed here, the hysteresis lift coefficient is 1.12, a 30% decrease from the 1.61 unsteady maximum value. In comparison, the steady state maximum lift coefficient is 1.46. At higher reduced frequency of 0.083, the hysteresis behavior is more pronounced, as seen in figure 21. In addition to greater hysteresis, the maximum lift coefficient is increased to about 1.73, an 18% increase over the steady state value. The corresponding hysteresis lift coefficient is 0.93. This difference between steady state behavior and unsteady hysteresis behavior is a main reason that unsteady testing should be required for airfoils used in wind turbine applications.

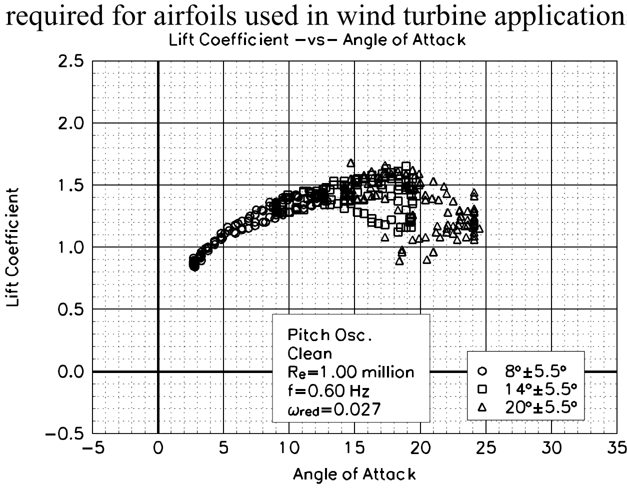

Figure 20. Clean, C_l vs α, ω_{red}=0.027, ±5.5°.

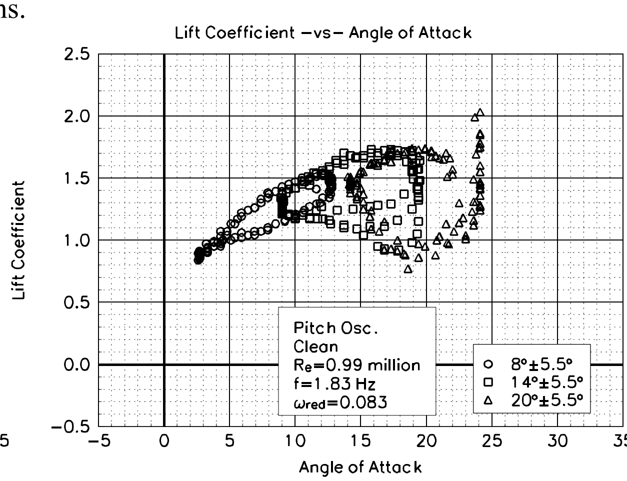

Figure 21. Clean, C_l vs α, ω_{red}=0.083, ±5.5°.

The pitching moment shown in figures 22 and 23 corresponds to the same conditions as the two lift coefficient plots previously discussed. Hysteresis behavior is evident but it is not as apparent as in the lift coefficient plots. However, the higher reduced frequency case does show more hysteresis than the lower reduced frequency case. For reference, the steady state maximum lift occurs near 16° angle of attack, and the steady state pitching moment at this maximum lift point is -0.0849. By comparison, when the airfoil is undergoing pitch oscillation for the lower frequency, pitching moment varies from -0.1108 to -0.0990 (at the angle of attack where maximum lift occurs), a 31% to 17% increase in magnitude from the steady state value.

Note the angle of attack where the maximum lift coefficient occurs does not necessarily show the "greatest" hysteresis behavior but does give a relative indication of the effect.

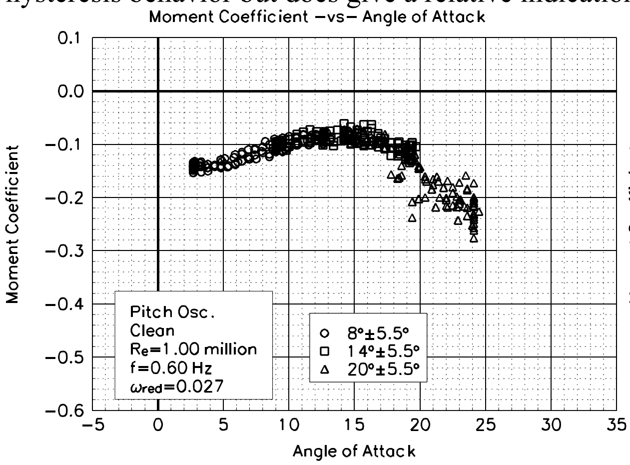

Figure 22. Clean, C_m vs α, ω_{red}=0.027, ±5.5°.

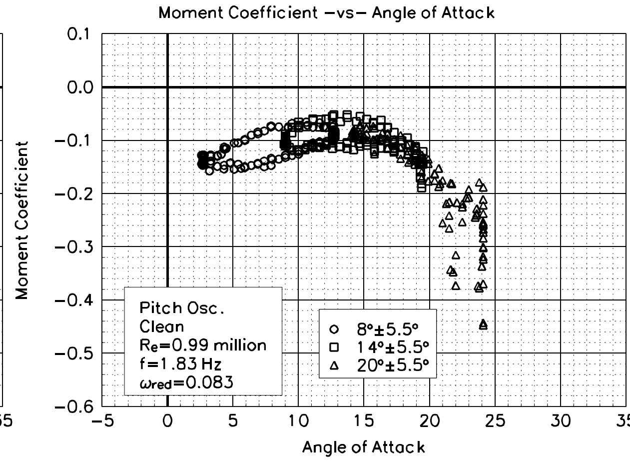

Figure 23. Clean, C_m vs α, ω_{red}=0.083, ±5.5°.

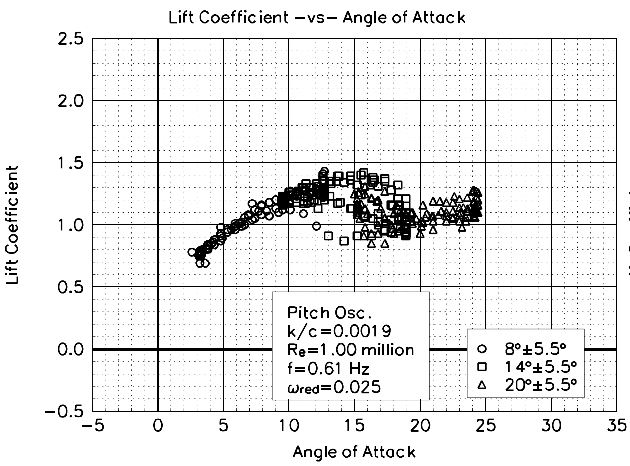

Figure 24. LEGR, C_l vs α, ω_{red}=0.025, ±5.5°.

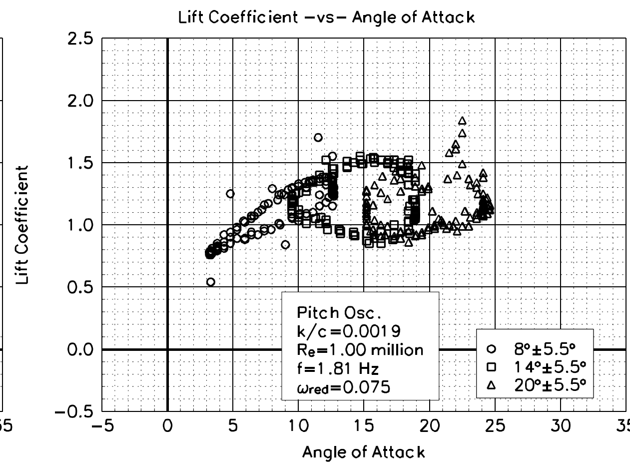

Figure 25. LEGR, C_l vs α, ω_{red}=0.075, ±5.5°.

Compared to the clean data, the application of LEGR reduces the maximum lift coefficient in the pitch oscillation cases. Lift coefficient versus angle of attack with LEGR applied is shown in figure 24 for the 0.025 reduced frequency case. The 0.075 reduced frequency case is shown in figure 25. Both correspond to the same run conditions described earlier for the clean cases. For the lower reduced frequency, the maximum unsteady lift coefficient is reduced to 1.40 from the corresponding clean case of 1.61, a 13% decrease. Hysteresis behavior is apparent at this frequency and is of similar order as the clean case; the corresponding hysteresis lift coefficient is 0.91 when LEGR is applied. In contrast, the higher frequency LEGR case has a maximum lift coefficient of 1.55 while the model is increasing in angle of attack, and the corresponding decreasing angle of attack lift coefficient is 0.92. In this case, the application of LEGR reduces the hysteresis loop behavior for larger angles of attack compared to the clean case at the same run conditions.

The pitching moment coefficient shown in figure 26 is for 0.025 reduced frequency with LEGR applied. At the angle of unsteady maximum lift, the pitching moment ranges from -0.1084 to -0.1328, while the steady state LEGR pitching moment is -0.0840 at the steady state stall angle of attack (14.1°). The higher reduced frequency of 0.075 with LEGR applied is shown in figure 27. As was seen with the lift coefficient, pitching moment hysteresis is more apparent at the higher reduced frequency than in the corresponding low reduced frequency case. Unsteady maximum lift angle of attack for this reduced frequency occurs at 14.7°, and the pitching moment ranges from -0.1211 to -0.0577 at that angle. Throughout the higher angle of attack range, the magnitude of the unsteady pitching moment can be very different than the steady state clean case (steady state pitching moment at maximum lift is -0.0840). It seems these differences can have an impact on the fatigue life predictions of a wind turbine system.

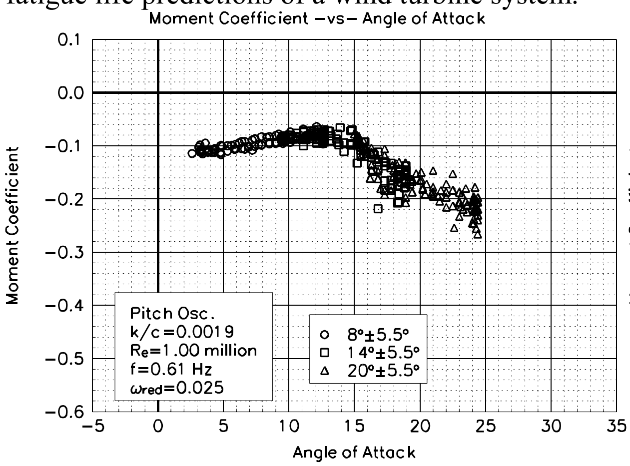

Figure 26. LEGR, C_m vs α, ω_{red}=0.025, ±5.5°.

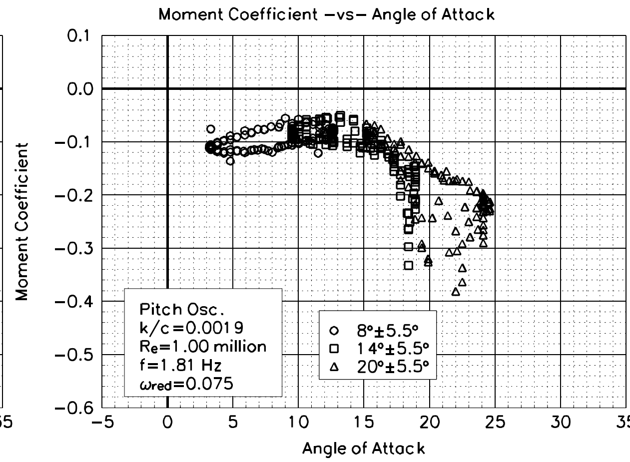

Figure 27. LEGR, C_m vs α, ω_{red}=0.075, ±5.5°.

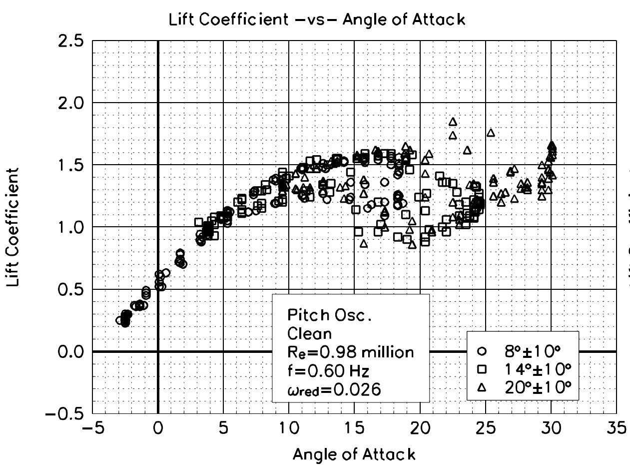

Figure 28. Clean, C_l vs α, ω_{red}=0.026, ±10°.

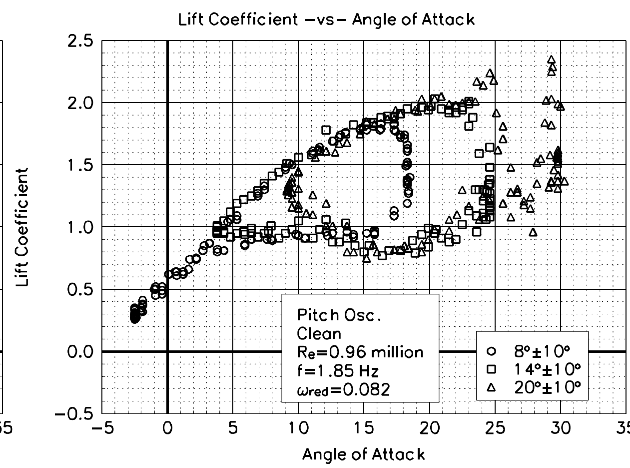

Figure 29. Clean, C_l vs α, ω_{red}=0.082, ±10°.

In addition to the ±5.5° unsteady experimental data, ±10° unsteady data were obtained with and without LEGR. The data were taken at 1 million Reynolds number using the same mean angles and frequencies as the 5.5° amplitude cases. Figures 28 and 29 show the ±10°, unsteady, clean, lift coefficient for the reduced frequencies of 0.026 and 0.082, respectively. The maximum lift coefficient for the lower frequency is 1.59 and occurs, as expected, when the airfoil is traveling through increasing angle of attack. The hysteresis lift coefficient (at 17.3°) is 1.02. At the higher reduced frequency, the maximum lift coefficient occurs at a higher angle of attack, 18.9°, and is 1.97. The corresponding hysteresis lift coefficient is 0.79. The difference between the maximum lift coefficient and the hysteresis lift coefficient indicates a much greater hysteresis response than experienced for the lower reduced frequency. The steady state, clean, maximum lift coefficient is 1.46; therefore, the unsteady behavior created lift coefficients up to 35% higher than the steady state conditions.

The quarter chord pitching moments with the same reduced frequencies as the lift coefficient cases are shown in figures 30 and 31. The hysteresis behavior observed in the lift coefficient plots is also reflected in this pitching moment data. Near the maximum lift angle, 17.3° for the lower frequency, the pitching moment coefficient ranges from -0.1028 to -0.1797; the 0.082 reduced frequency case has maximum lift near 18.9° and pitching moment ranges from -0.1492 to -0.1413. In comparison, the steady state pitching moment is -0.0849 near the steady state maximum lift coefficient angle of attack of 16°. The higher reduced frequency again shows large hysteresis loops for all three mean angles of attack. The data also show that the increasing angle of attack and the decreasing angle of attack pitching moment curves cross over each other near the maximum lift angle of attack.

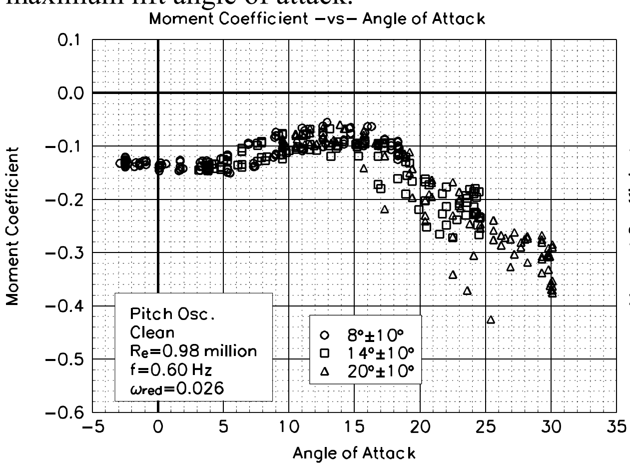

Figure 30. Clean, C_m vs α, ω_{red}=0.026, ±10°.

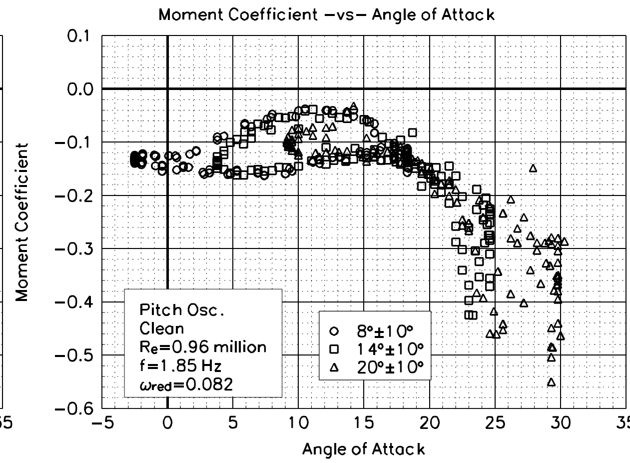

Figure 31. Clean, C_m vs α, ω_{red}=0.082, ±10°.

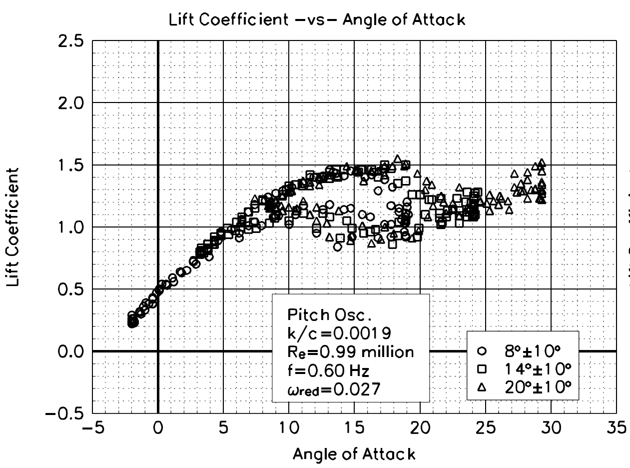

Figure 32. LEGR, C_l vs α, ω_{red}=0.027, ±10°.

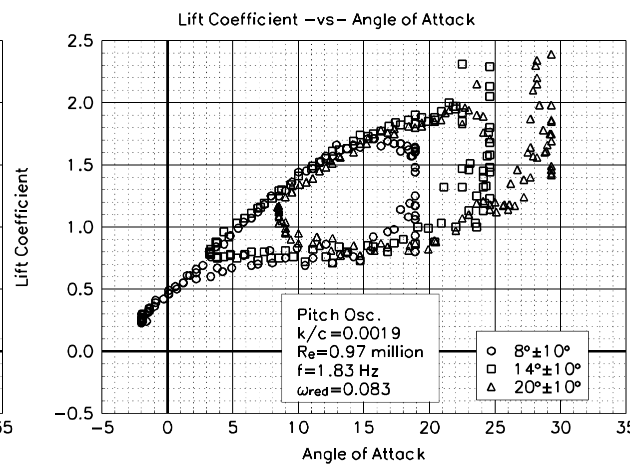

Figure 33. LEGR, C_l vs α, ω_{red}=0.083, ±10°.

The application of LEGR degrades the lift performance of the airfoil, as would be expected from the results discussed previously. The LEGR lift coefficient data for reduced frequencies of 0.027 and 0.083 are shown in figures 32 and 33, respectively. The maximum lift coefficient is reduced to 1.50 from 1.59 for the low frequency clean case. Although there is a reduction, this value is still significantly higher than the LEGR steady state case, which has a maximum lift coefficient of 1.28 at 14.1° angle of attack. The higher reduced frequency has a maximum lift coefficient of 1.90, which occurs near 19° angle of attack. The corresponding lift coefficient at 19° for the airfoil traveling with decreasing angle of attack is 0.86, a 55% reduction from the maximum.

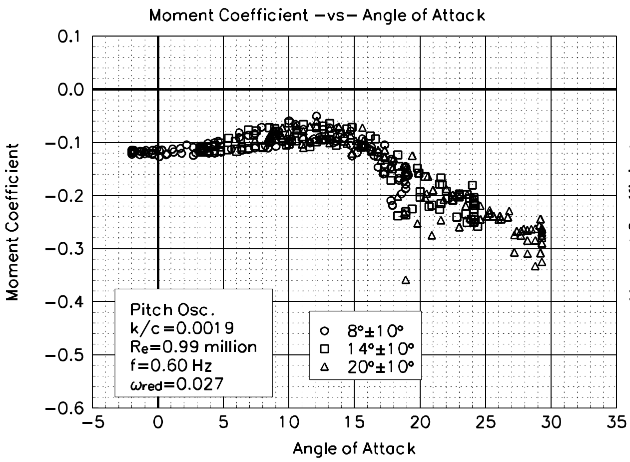

Figure 34. LEGR, C_m vs α, ω_{red}=0.027, ±10°.

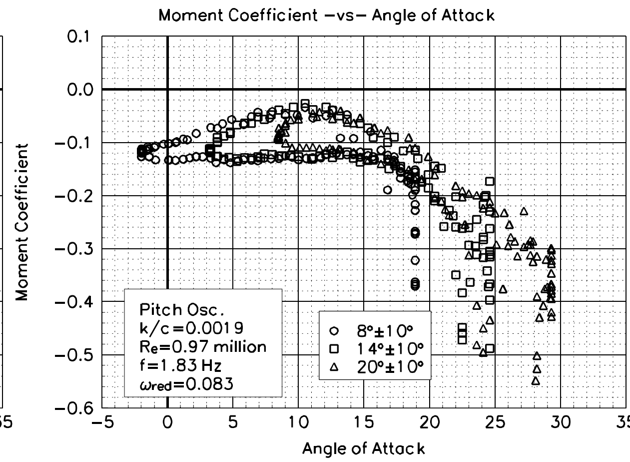

Figure 35. LEGR, C_m vs α, ω_{red}=0.083, ±10°.

Figures 34 and 35 show the corresponding pitching moment coefficients for the reduced frequencies of 0.027 and 0.083. For the 0.027 reduced frequency case, the pitching moment varies from -0.1551 to -0.1353 at 17.3° (where the maximum lift occurs). The hysteresis behavior is more pronounced for the higher reduced frequency case, where the range of pitching moments at the maximum lift angle of 18.9° is from -0.1834 to -0.1145. These values can then be compared to the steady state LEGR value of -0.0840.

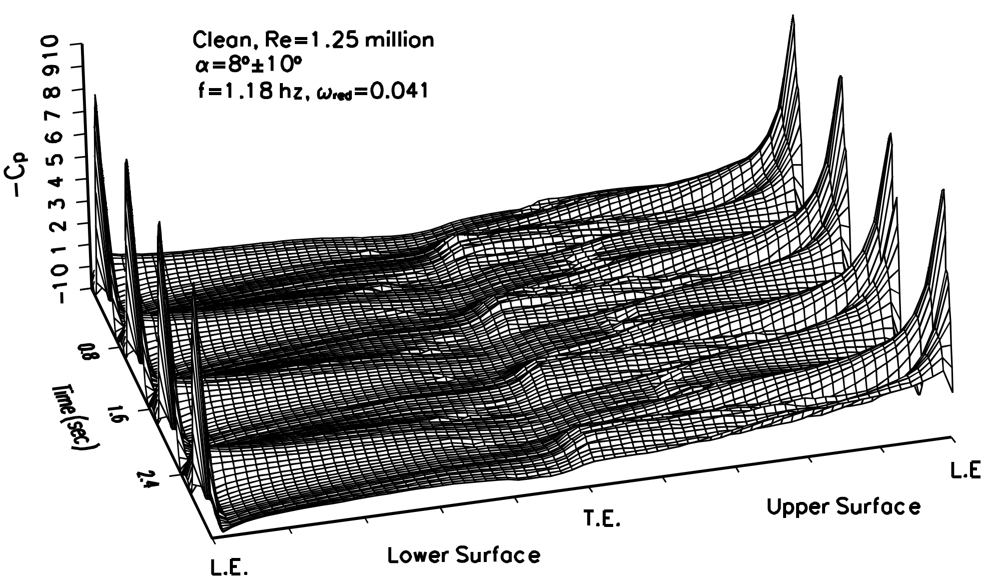

Figure 36. Unsteady pressure distribution, clean, ω_{red}=0.041, 8±10°.

Although all the unsteady data have not been discussed here, the previous discussion included typical examples of the wind tunnel data. The remaining cases of the ±5.5° and ±10° oscillation data for all the Reynolds numbers are included in Appendix C.

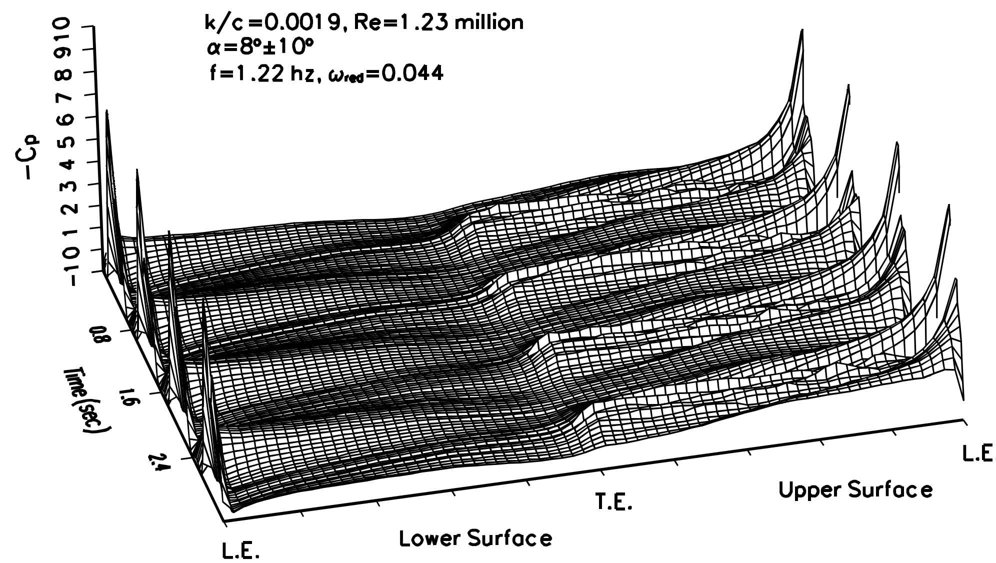

Figure 37. Unsteady pressure distribution, LEGR, ω_{red}=0.044, 8±10°.

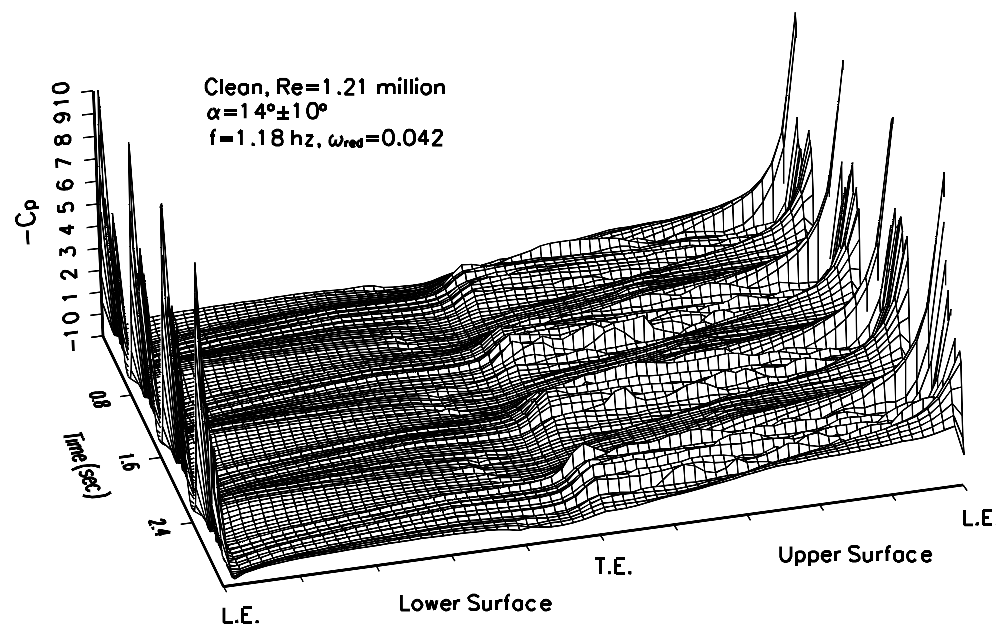

Figure 38. Unsteady pressure distribution, clean, ω_{red}=0.042, 14±10°.

The following four unsteady pressure distributions show examples of the data used to calculate the lift, pressure drag, and pitching moment coefficients. Figure 36 shows the distribution for a clean model, with a reduced frequency of 0.041, 8° mean angle of attack, and ±10° pitch oscillation. For plotting clarity, the model pressures were "unwrapped" about the trailing edge. The upper surface pressures are depicted on the right side of the surface plot; lower surface values are on the left. The trailing edge is at the midpoint of the x-axis, with the leading edge at each extreme. For clarification of the irregularities in the pressure distribution, an equally spaced grid was used. The pressure coefficients were linearly interpolated to the specified number of evenly spaced x positions. The time scale corresponds to angle of attack. For this case, the separated flow area is defined by the irregular, "rough" areas of the upper surface trailing edge portion of the plot. The lower surface stays attached through all the airfoil oscillations. Figure 37 shows the LEGR case for the same test conditions as the previous figure. In this case, the pressure peaks were not as high as for the clean case, and the stall behavior is more pronounced.

Figure 38 shows the same clean run conditions at a higher mean angle of attack. This case is characterized by significant portions of the upper surface in stall and high pressure peaks. The pressure coefficient peaks are beyond -10 for this case and near -8 for the previous 8° mean angle of attack case.

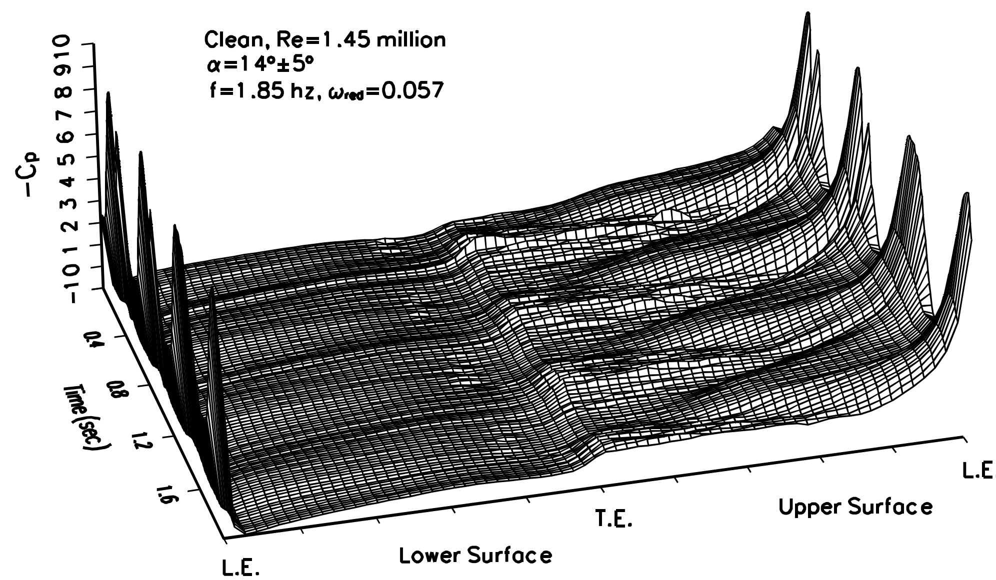

Figure 39. Unsteady pressure distribution, clean, ω_{red}=0.057, 14±5.5°.

Figure 39 shows the clean run conditions for a ±5.5° pitch oscillation at a higher Reynolds number and reduced frequency. The structure is different from the previous figure because less of the upper surface flow was separated, a consequence of lower angles of attack.

Summary of Results

A S801 airfoil model was tested under steady state and pitch oscillation conditions. Baseline tests were made while the model was clean, and then corresponding tests were conducted with LEGR applied.

Table 1. S801 Steady State Parameters Summary

Grit Pattern	Re x 10^{-6}	C_{lmax}	C_{dmin}	C_{mo}
Clean	0.75	1.39 @ 15.2°	0.0089	-0.1219
k/c=0.0019	0.75	1.27 @ 14.1°	0.0127	-0.1136
Clean	1.00	1.46 @ 16.2°	0.0058	-0.1238
k/c=0.0019	1.00	1.28 @ 14.1°	0.0109	-0.1146
Clean	1.25	1.43 @ 14.2°	0.0056	-0.1255
k/c=0.0019	1.25	1.27 @ 14.1°	0.0107	-0.1149
Clean	1.50	1.44 @ 15.2°	0.0051	-0.1262
k/c=0.0019	1.50	1.28 @ 13.1°	0.0110	-0.1170

A summary of the steady state aerodynamic parameters is shown in Table 1. As observed, the application of LEGR reduced the maximum lift of the airfoil up to 12% and the minimum drag coefficient increased more than 43%. LEGR also affects the zero lift pitching moment, which reduces the magnitude an average of 7%.

Table 2. S801, Unsteady, Clean, ±5.5°

ω_{red}	Re x 10^{-6}	f	C_{lmax}	α_{max}	$C_{l\ dec}$	$C_{m\ inc}$	$C_{m\ dec}$
0.036	0.76	0.61	1.63	16.3	1.27	-0.1056	-0.0717
0.072	0.76	1.21	1.65	17.3	1.09	-0.1006	-0.0845
0.109	0.76	1.83	1.79	16.8	1.06	-0.1343	-0.1082
0.027	1.00	0.60	1.61	18.3	1.12	-0.1108	-0.0990
0.055	0.99	1.21	1.65	18.4	1.22	-0.1111	-0.1035
0.083	0.99	1.83	1.73	17.3	0.93	-0.1220	-0.0755
0.022	1.25	0.61	1.61	17.3	1.23	-0.1031	-0.1002
0.043	1.25	1.19	1.60	15.3	1.22	-0.0911	-0.0583
0.067	1.24	1.85	1.69	17.3	1.12	-0.1092	-0.0745
0.018	1.45	0.60	1.55	16.3	1.33	-0.0858	-0.0683
0.038	1.45	1.22	1.67	17.3	1.23	-0.1192	-0.1013
0.057	1.45	1.85	1.68	16.3	1.30	-0.0884	-0.0770

The pitch oscillation data can be divided into two groups, the ±5.5° amplitude and ±10° amplitude oscillations, which show similar trends. For both ±5.5° and ±10°, the unsteady test conditions and some parameters are listed in Tables 2, 3, 4, and 5. As the reduced frequency, which takes oscillation and tunnel speed into account, is increased, the maximum lift coefficient also increases. In addition, the hysteresis behavior becomes increasingly apparent with increased reduced frequency.

Table 3. S801, Unsteady, LEGR, ±5.5°

ω_{red}	Re x 10^{-6}	f	C_{lmax}	α_{max}	$C_{l\ dec}$	$C_{m\ inc}$	$C_{m\ dec}$
0.033	0.75	0.61	1.46	16.3	0.95	-0.1237	-0.1048
0.065	0.75	1.18	1.49	16.4	0.96	-0.1211	-0.0797
0.101	0.75	1.83	1.59	16.3	0.92	-0.1191	-0.1190
0.025	1.00	0.61	1.40	15.5	0.91	-0.1084	-0.1328
0.050	0.99	1.19	1.48	14.7	0.89	-0.1094	-0.0721
0.075	1.00	1.81	1.55	14.7	0.92	-0.1211	-0.0577
0.020	1.25	0.61	1.40	14.2	1.07	-0.1019	-0.0744
0.040	1.25	1.19	1.49	15.8	1.04	-0.1084	-0.0815
0.061	1.24	1.83	1.49	15.2	0.85	-0.1075	-0.0919
0.018	1.37	0.60	1.37	14.2	1.13	-0.0922	-0.0818
0.035	1.36	1.18	1.42	15.2	0.99	-0.1160	-0.0816
0.055	1.36	1.83	1.49	16.3	0.93	-0.1138	-0.0993

Table 4. S801, Unsteady, Clean, ±10°

ω_{red}	Re x 10^{-6}	f	C_{lmax}	α_{max}	$C_{l\ dec}$	$C_{m\ inc}$	$C_{m\ dec}$
0.034	0.74	0.59	1.67	16.3	0.75	-0.1180	-0.0620
0.070	0.73	1.19	1.88	18.3	0.81	-0.1271	-0.1260
0.107	0.74	1.83	2.12	20.4	0.97	-0.1845	-0.1763
0.026	0.98	0.60	1.59	17.3	1.02	-0.1028	-0.1797
0.053	0.98	1.19	1.80	17.3	0.80	-0.1266	-0.1223
0.082	0.96	1.85	1.97	18.9	0.79	-0.1492	-0.1413
0.022	1.22	0.61	1.62	17.8	1.37	-0.1060	-0.1625
0.042	1.21	1.18	1.77	18.9	1.26	-0.1353	-0.2037
0.064	1.21	1.81	1.93	19.4	0.89	-0.1728	-0.1400
0.018	1.44	0.61	1.61	16.3	1.13	-0.0924	-0.0946
0.036	1.43	1.19	1.70	17.3	1.31	-0.1064	-0.0766
0.053	1.42	1.79	1.84	17.3	1.50	-0.1316	-0.1281

As expected, the application of LEGR reduces the aerodynamic performance of the airfoil. The maximum lift coefficient is reduced by 7% - 15% for the ±5.5° case and 4% - 11% for the ±10° case. In addition to following the same trends as the clean, unsteady data discussed previously, the LEGR causes the hysteresis behavior to persist into lower angles of attack than for the clean cases. Overall, the unsteady wind tunnel data show hysteresis behavior that becomes more apparent with increased reduced frequency. The maximum unsteady lift coefficient can be up to 29% higher for the ±5.5° amplitude and up to 53% higher for the ±10° amplitude than the steady state maximum lift coefficient. Variation in the quarter chord pitching moment coefficient can be more than twice that indicated by steady state results. These findings indicate that it is important to consider the unsteady loading that will occur in wind turbine operation because steady state results can greatly underestimate the forces.

Table 5. S801, Unsteady, LEGR, ±10°

ω_{red}	Re x 10^{-6}	ω	C_{lmax}	α_{max}	$C_{l\,dec}$	$C_{m\,inc}$	$C_{m\,dec}$
0.036	0.75	0.60	1.55	15.7	0.99	-0.1123	-0.0835
0.073	0.74	1.21	1.81	19.2	0.93	-0.2015	-0.1505
0.111	0.73	1.81	1.94	16.8	0.95	-0.1474	-0.1211
0.027	0.99	0.60	1.50	17.3	0.86	-0.1551	-0.1353
0.054	0.98	1.18	1.69	18.8	0.95	-0.1727	-0.1385
0.083	0.97	1.83	1.90	18.9	0.86	-0.1834	-0.1145
0.021	1.24	0.61	1.44	15.1	0.93	-0.1030	-0.1115
0.044	1.22	1.22	1.59	17.3	0.94	-0.1357	-0.1083
0.066	1.23	1.83	1.76	18.2	0.92	-0.1506	-0.1031
0.019	1.44	0.61	1.43	15.2	0.89	-0.0985	-0.1073
0.037	1.43	1.21	1.56	16.3	0.94	-0.1171	-0.0926
0.056	1.43	1.83	1.69	17.4	0.94	-0.1540	-0.1227

References

Pope, A.; Harper, J.J. 1966. *Low Speed Wind Tunnel Testing*. New York, NY: John Wiley & Sons, Inc.

Schlichting, H. 1979. *Boundary Layer Theory*. New York, NY: McGraw-Hill Inc.

Smetana, F., Summey, D. et-al. 1975. *Light Aircraft Lift, Drag, and Moment Prediction - a Review and Analysis.* North Carolina State University. NASA CR-2523.

Appendix A: Surface Pressure Tap Coordinates

List of Tables

Table A1. S801 Surface Pressure Taps, Non-Dimensional Coordinates		
Tap Number	Chord Station	Ordinate
1	0.9991	--
2	0.9684	--
3	0.9312	--
4	0.8952	--
5	0.8571	--
6	0.8190	--
7	0.7830	--
8	0.7458	--
9	0.7090	--
10	0.6714	--
11	0.6354	--
12	0.5979	--
13	0.5611	--
14	0.5235	--
15	0.4865	--
16	0.4488	--
17	0.4124	--
18	0.3751	--
19	0.3372	--
20	0.3003	--
21	0.2634	--
22	0.2258	--
23	0.1890	--
24	0.1514	--
25	0.1150	--
26	0.0779	--
27	0.0414	--
28	0.0091	--
29	0.0019	--
30	-0.0002	--
31	0.0018	--
32	0.0059	--
33	0.0124	--
34	0.0373	--
35	0.0692	--
36	0.1007	--

Table A1. S801 Surface Pressure Taps, Non-Dimensional Coordinates		
Tap Number	Chord Station	Ordinate
37	0.1353	--
38	0.1701	--
39	0.2063	--
40	0.2418	--
41	0.2791	--
42	0.3458	--
43	0.3525	--
44	0.3900	--
45	0.4271	--
46	0.4645	--
47	0.5012	--
48	0.5384	--
49	0.5752	--
50	0.6123	--
51	0.6486	--
52	0.6853	--
53	0.7220	--
54	0.7583	--
55	0.7948	--
56	0.8316	--
57	0.8675	--
58	0.9038	--
59	0.9395	--
60	0.9754	--
End of Table A2		

Appendix B: Steady State Data
Integrated Coefficients and Pressure Distributions

List of Figures

List of Tables

Table B1. S801, Clean, Re = 0.75 x 10^6						
RUN	AOA	C_l	C_{dp}	$C_{m¼}$	Re x10^{-6}	C_{dw}
11	-20.0	-0.45	0.2892	0.0132	0.75	--
10	-18.2	-0.39	0.2467	0.0050	0.75	--
9	-16.1	-0.34	0.2094	0.0005	0.74	--
8	-14.0	-0.25	0.1670	-0.0124	0.75	--
7	-12.2	-0.29	0.1561	-0.0002	0.74	--
6	-10.1	-0.38	0.1385	-0.0118	0.75	--
5	-8.1	-0.30	0.0716	-0.0929	0.76	--
4	-6.2	-0.14	0.0087	-0.1191	0.74	0.0128
3	-4.1	0.09	0.0040	-0.1237	0.74	0.0097
2	-2.2	0.27	0.0028	-0.1286	0.75	0.0090
12	-0.1	0.52	0.0041	-0.1308	0.75	0.0099
38	-0.1	0.54	0.0023	-0.1315	0.73	0.0089
1	0.0	0.52	0.0045	-0.1316	0.75	0.0092
13	2.0	0.75	0.0068	-0.1317	0.75	0.0090
14	4.1	0.98	0.0105	-0.1331	0.76	0.0097
15	6.0	1.12	0.0133	-0.1227	0.75	0.0119
16	8.1	1.22	0.0188	-0.1030	0.74	0.0201
17	10.0	1.28	0.0217	-0.0859	0.75	0.0376
18	11.0	1.30	0.0249	-0.0777	0.75	--
19	12.1	1.33	0.0301	-0.0727	0.73	--
20	13.1	1.36	0.0385	-0.0700	0.74	--
21	14.2	1.37	0.0534	-0.0739	0.74	--
22	15.2	1.39	0.0737	-0.0778	0.75	--
23	16.2	1.31	0.0687	-0.0690	0.73	--
24	17.2	1.23	0.0894	-0.0775	0.74	--
25	18.3	1.18	0.1173	-0.0883	0.74	--
26	19.0	1.15	0.1405	-0.0976	0.74	--
27	20.0	1.10	0.1800	-0.1146	0.75	--

Table B1. S801, Clean, Re = 0.75 x 10^6						
RUN	AOA	C_l	C_{dp}	$C_{m¼}$	Re x10^{-6}	C_{dw}
28	22.0	0.96	0.4063	-0.1825	0.75	--
29	23.9	1.00	0.4610	-0.1929	0.77	--
30	26.0	1.10	0.5520	-0.2212	0.74	--
31	28.1	1.20	0.6562	-0.2528	0.76	--
32	29.8	1.27	0.7448	-0.2794	0.75	--
33	31.9	1.36	0.8662	-0.3176	0.72	--
34	34.0	1.39	0.9536	-0.3367	0.75	--
35	35.8	1.42	1.0430	-0.3594	0.74	--
36	37.9	1.41	1.1203	-0.3742	0.73	--
37	40.0	1.40	1.2014	-0.3937	0.74	--
End of Table B1						

Table B2. S801, Clean, Re = 1.0 x 10^6

RUN	AOA	C_l	C_{dp}	$C_{m1/4}$	Re x10^{-6}	C_{dw}
206	-20.2	-0.40	0.2717	0.0011	1.00	--
205	-18.2	-0.35	0.2329	-0.0047	0.98	--
204	-16.1	-0.32	0.2059	-0.0054	1.00	--
203	-14.2	-0.26	0.1712	-0.0135	1.00	--
202	-12.2	-0.36	0.1736	0.0136	1.01	--
201	-10.1	-0.37	0.1401	-0.0122	1.00	--
200	-8.2	-0.31	0.0755	-0.0898	0.98	--
199	-6.2	-0.15	0.0053	-0.1224	0.99	0.0115
198	-4.1	0.06	0.0028	-0.1244	1.00	0.0099
197	-2.2	0.27	0.0024	-0.1293	0.99	0.0091
196	-0.1	0.50	0.0053	-0.1335	1.01	0.0059
207	-0.1	0.52	0.0055	-0.1338	1.00	0.0064
233	-0.1	0.52	0.0052	-0.1337	1.01	0.0058
208	2.0	0.75	0.0094	-0.1350	0.99	0.0061
209	4.1	0.97	0.0127	-0.1348	0.98	0.0070
210	6.1	1.12	0.0155	-0.1206	0.99	0.0119
211	8.1	1.22	0.0220	-0.1053	0.99	0.0147
212	10.1	1.30	0.0298	-0.0907	0.98	0.0231
213	11.1	1.32	0.0303	-0.0813	1.00	0.0334
214	12.2	1.36	0.0349	-0.0769	1.00	--
215	13.1	1.38	0.0502	-0.0794	0.99	--
216	14.2	1.40	0.0578	-0.0791	1.00	--
217	15.1	1.44	0.0835	-0.0857	0.99	--
218	16.2	1.46	0.0946	-0.0849	1.00	--
219	17.2	1.38	0.0962	-0.0812	1.00	--
220	18.0	1.24	0.1105	-0.0867	0.99	--
221	19.2	1.17	0.1805	-0.1209	1.01	--
222	20.0	1.18	0.2456	-0.1521	1.01	--
223	22.0	0.99	0.4204	-0.1944	1.01	--

Table B2. S801, Clean, Re = 1.0 x 10^6						
RUN	AOA	C_l	C_{dp}	$C_{m¼}$	Re $x10^{-6}$	C_{dw}
224	23.9	1.00	0.4659	-0.1967	1.00	--
225	26.0	1.12	0.5649	-0.2277	0.99	--
226	28.0	1.21	0.6616	-0.2557	1.00	--
227	29.8	1.29	0.7551	-0.2831	1.00	--
228	31.9	1.35	0.8572	-0.3121	1.00	--
229	34.0	1.41	0.9705	-0.3455	1.00	--
230	35.8	1.45	1.0744	-0.3765	0.98	--
231	37.9	1.45	1.1621	-0.3962	0.99	--
232	39.9	1.43	1.2331	-0.4073	0.98	--
End of Table B2						

Table B3. S801, Clean, Re = 1.25 x 10^6						
RUN	AOA	C_l	C_{dp}	$C_{m¼}$	Re x10^{-6}	C_{dw}
91	-20.2	-0.41	0.2747	0.0022	1.24	--
90	-18.2	-0.39	0.2480	0.0049	1.26	--
89	-16.1	-0.39	0.2285	0.0131	1.24	--
88	-14.2	-0.25	0.1699	-0.0140	1.26	--
87	-12.1	-0.24	0.1476	-0.0113	1.25	--
86	-10.1	-0.32	0.1336	-0.0184	1.27	--
85	-8.3	-0.30	0.0760	-0.0901	1.26	--
84	-6.2	-0.17	0.0031	-0.1243	1.25	0.0120
83	-4.1	0.07	0.0025	-0.1260	1.23	0.0092
82	-2.1	0.28	0.0028	-0.1295	1.25	0.0074
81	-0.1	0.52	0.0048	-0.1339	1.26	0.0067
92	-0.1	0.52	0.0045	-0.1336	1.26	0.0056
118	-0.1	0.52	0.0043	-0.1336	1.24	0.0063
93	2.0	0.77	0.0072	-0.1360	1.27	0.0066
94	4.0	0.98	0.0109	-0.1351	1.25	0.0096
95	6.0	1.12	0.0090	-0.1175	1.26	0.0146
96	8.1	1.22	0.0189	-0.1033	1.25	0.0142
97	10.2	1.31	0.0328	-0.0923	1.24	0.0237
98	11.1	1.33	0.0311	-0.0833	1.24	0.0317
99	12.1	1.36	0.0349	-0.0795	1.26	--
100	13.1	1.40	0.0475	-0.0814	1.25	--
101	14.2	1.43	0.0581	-0.0807	1.25	--
102	15.2	1.39	0.0544	-0.0695	1.25	--
103	16.3	1.41	0.0577	-0.0645	1.24	--
104	17.2	1.29	0.0839	-0.0754	1.25	--
105	18.1	1.19	0.1165	-0.0923	1.25	--
106	19.0	1.11	0.1648	-0.1180	1.25	--
107	20.0	1.08	0.2169	-0.1403	1.25	--
108	22.1	1.09	0.4559	-0.2164	1.28	--

Table B3. S801, Clean, Re = 1.25 x 10^6						
RUN	AOA	C_l	C_{dp}	$C_{m1/4}$	Re x10^{-6}	C_{dw}
109	24.0	1.02	0.4704	-0.1974	1.26	--
110	26.0	1.10	0.5215	-0.2069	1.24	--
111	28.0	1.16	0.5887	-0.2225	1.25	--
112	30.0	1.25	0.7187	-0.2620	1.24	--
113	31.9	1.34	0.8412	-0.3022	1.24	--
114	34.0	1.37	0.9421	-0.3296	1.26	--
115	35.9	1.44	1.0634	-0.3690	1.23	--
116	37.8	1.44	1.1417	-0.3858	1.23	--
117	39.8	1.40	1.1958	-0.3880	1.24	--
End of Table B3						

Table B4. S801, Clean, Re = 1.5 x 10^6						
RUN	AOA	C_l	C_{dp}	$C_{m¼}$	Re x10^{-6}	C_{dw}
244	-20.1	-0.41	0.2739	0.0031	1.51	--
243	-18.2	-0.36	0.2382	-0.0028	1.51	--
242	-16.1	-0.33	0.2098	-0.0035	1.51	--
241	-14.1	-0.27	0.1747	-0.0100	1.51	--
240	-12.2	-0.25	0.1523	-0.0110	1.50	--
239	-10.1	-0.34	0.1340	-0.0225	1.52	--
238	-8.2	-0.40	0.0046	-0.1234	1.48	0.0153
237	-6.2	-0.17	0.0030	-0.1248	1.50	0.0114
236	-4.1	0.07	0.0025	-0.1268	1.50	0.0093
235	-2.1	0.28	0.0027	-0.1294	1.51	0.0074
234	-0.1	0.52	0.0048	-0.1348	1.51	0.0054
245	-0.1	0.52	0.0042	-0.1341	1.50	0.0051
261	-0.1	0.52	0.0045	-0.1339	1.49	0.0059
246	2.0	0.76	0.0082	-0.1364	1.50	0.0068
247	4.0	0.98	0.0080	-0.1331	1.48	0.0072
248	6.1	1.11	0.0132	-0.1173	1.49	0.0122
249	8.1	1.23	0.0199	-0.1049	1.50	0.0160
250	10.1	1.32	0.0243	-0.0896	1.51	0.0240
251	11.2	1.35	0.0306	-0.0839	1.49	0.0306
252	12.1	1.39	0.0399	-0.0851	1.50	--
253	13.2	1.42	0.0446	-0.0813	1.50	--
254	14.2	1.44	0.0551	-0.0805	1.49	--
255	15.2	1.44	0.0600	-0.0756	1.50	--
256	16.2	1.38	0.0608	-0.0685	1.48	--
257	17.1	1.29	0.0818	-0.0774	1.48	--
258	18.1	1.20	0.1191	-0.0924	1.50	--
259	19.0	1.09	0.1937	-0.1343	1.50	--
260	20.0	1.04	0.2481	-0.1576	1.51	--
End of Table B4						

Table B5. S801, LEGR, Re = 0.75 x 10^6						
RUN	AOA	C_l	C_{dp}	$C_{m¼}$	Re x10^{-6}	C_{dw}
424	-20.2	-0.41	0.2726	0.0033	0.75	--
423	-18.2	-0.54	0.2696	-0.0040	0.76	--
422	-16.1	-0.48	0.2341	0.0107	0.76	--
421	-14.3	-0.54	0.1967	-0.0137	0.76	--
420	-12.2	-0.48	0.1423	-0.0454	0.75	--
419	-10.2	-0.51	0.0540	-0.1016	0.76	0.0661
418	-8.4	-0.40	0.0121	-0.1127	0.75	0.0234
417	-6.2	-0.20	0.0049	-0.1140	0.75	0.0193
416	-4.1	0.02	0.0025	-0.1136	0.75	0.0158
415	-2.2	0.20	0.0032	-0.1145	0.75	0.0134
414	-0.1	0.43	0.0043	-0.1139	0.76	0.0130
425	-0.1	0.43	0.0057	-0.1141	0.75	0.0127
451	-0.1	0.43	0.0055	-0.1140	0.75	0.0133
426	2.0	0.63	0.0082	-0.1103	0.76	0.0153
427	4.1	0.84	0.0106	-0.1048	0.76	0.0155
428	6.0	0.99	0.0107	-0.0964	0.75	0.0218
429	8.1	1.09	0.0223	-0.0854	0.75	0.0246
430	10.2	1.17	0.0366	-0.0774	0.75	0.0443
431	11.3	1.20	0.0450	-0.0739	0.75	0.0453
432	12.3	1.23	0.0569	-0.0745	0.75	--
433	13.1	1.25	0.0655	-0.0753	0.75	--
434	14.1	1.27	0.0836	-0.0787	0.76	--
435	15.1	1.10	0.0980	-0.0806	0.75	--
436	16.1	0.99	0.1648	-0.1161	0.75	--
437	17.1	0.99	0.2031	-0.1299	0.75	--
438	18.2	0.97	0.2375	-0.1383	0.77	--
439	19.0	0.97	0.2603	-0.1454	0.76	--
440	20.0	0.98	0.2954	-0.1552	0.76	--
441	22.1	1.01	0.3674	-0.1752	0.76	--

Table B5. S801, LEGR, Re = 0.75 x 10^6						
RUN	AOA	C_l	C_{dp}	$C_{m¼}$	Re x10^{-6}	C_{dw}
442	23.9	1.06	0.4430	-0.1972	0.75	--
443	26.0	1.12	0.5201	-0.2142	0.75	--
444	28.0	1.16	0.6107	-0.2338	0.74	--
445	29.9	1.23	0.7118	-0.2633	0.74	--
446	31.9	1.32	0.8351	-0.3008	0.75	--
447	34.0	1.39	0.9557	-0.3377	0.75	--
448	35.8	1.41	1.0384	-0.3562	0.75	--
449	37.9	1.41	1.1204	-0.3715	0.74	--
450	40.0	1.41	1.2124	-0.3937	0.73	--
End of Table B5						

Table B6. S801, LEGR, Re = 1.0 x 10^6						
RUN	AOA	C_l	C_{dp}	$C_{m1/4}$	Re x10^{-6}	C_{dw}
386	-20.1	-0.41	0.2708	0.0007	1.01	--
385	-18.2	-0.51	0.2672	-0.0003	0.98	--
384	-16.1	-0.49	0.2316	0.0065	1.02	--
383	-14.3	-0.51	0.2009	0.0002	1.00	--
382	-12.2	-0.49	0.1540	-0.0315	1.00	--
381	-10.2	-0.49	0.0697	-0.0930	1.01	0.0966
380	-8.4	-0.41	0.0107	-0.1131	1.00	0.0220
379	-6.2	-0.21	0.0047	-0.1137	1.00	0.0152
378	-4.1	0.01	0.0027	-0.1146	1.00	0.0136
377	-2.3	0.20	0.0037	-0.1157	1.00	0.0136
376	-0.1	0.43	0.0057	-0.1142	1.00	0.0109
387	-0.1	0.43	0.0052	-0.1138	0.98	0.0143
413	-0.1	0.42	0.0060	-0.1142	1.01	0.0127
388	2.0	0.64	0.0087	-0.1108	1.00	0.0142
389	4.1	0.83	0.0116	-0.1055	1.00	0.0196
390	6.0	0.98	0.0158	-0.0977	1.00	0.0163
391	8.1	1.10	0.0271	-0.0890	0.99	0.0281
392	10.2	1.17	0.0394	-0.0792	1.01	0.0430
393	11.1	1.21	0.0453	-0.0767	0.98	--
394	12.1	1.24	0.0562	-0.0776	1.01	--
395	13.1	1.27	0.0707	-0.0796	1.00	--
396	14.1	1.28	0.0907	-0.0840	1.00	--
397	15.2	1.18	0.1173	-0.0945	1.00	--
398	16.1	1.03	0.1667	-0.1176	1.00	--
399	17.2	1.07	0.1939	-0.1242	1.00	--
400	17.9	1.01	0.2329	-0.1402	1.02	--
401	19.0	0.96	0.2722	-0.1526	1.02	--
402	20.0	1.00	0.2941	-0.1546	1.01	--
403	22.1	1.04	0.3785	-0.1814	1.00	--

Table B6. S801, LEGR, Re = 1.0 x 10^6

RUN	AOA	C_l	C_{dp}	$C_{m¼}$	Re x10^{-6}	C_{dw}
404	24.0	1.05	0.4381	-0.1943	1.01	--
405	26.0	1.12	0.5204	-0.2166	0.99	--
406	28.0	1.16	0.6032	-0.2350	1.02	--
407	30.2	1.25	0.7257	-0.2685	1.00	--
408	31.9	1.32	0.8285	-0.2990	1.00	--
409	34.0	1.39	0.9488	-0.3340	0.98	--
410	36.1	1.39	1.0270	-0.3494	0.99	--
411	37.9	1.41	1.1167	-0.3725	1.00	--
412	40.0	1.43	1.2242	-0.4025	1.00	--

End of Table B6

Table B7. S801, LEGR, Re = 1.25 x 10^6						
RUN	AOA	C_l	C_{dp}	$C_{m1/4}$	Re x10^{-6}	C_{dw}
462	-20.2	-0.42	0.2757	0.0022	1.27	--
461	-18.2	-0.55	0.2692	-0.0020	1.27	--
460	-16.1	-0.54	0.2333	-0.0040	1.28	--
459	-14.3	-0.52	0.2001	-0.0094	1.27	--
458	-12.2	-0.50	0.1428	-0.0468	1.27	--
457	-10.2	-0.52	0.0395	-0.1046	1.25	0.0543
456	-8.4	-0.42	0.0113	-0.1129	1.25	0.0228
455	-6.2	-0.20	0.0059	-0.1140	1.25	0.0176
454	-4.1	-0.01	0.0036	-0.1149	1.25	0.0139
453	-2.2	0.20	0.0038	-0.1153	1.25	0.0144
452	-0.1	0.43	0.0051	-0.1142	1.26	0.0128
463	-0.1	0.44	0.0045	-0.1137	1.25	0.0107
489	-0.1	0.44	0.0051	-0.1132	1.26	0.0121
464	2.0	0.65	0.0070	-0.1109	1.24	0.0122
465	4.1	0.84	0.0110	-0.1054	1.25	0.0147
466	6.0	0.99	0.0144	-0.0977	1.24	0.0176
467	8.1	1.10	0.0243	-0.0881	1.25	0.0238
468	10.2	1.19	0.0371	-0.0789	1.25	0.0312
469	11.3	1.22	0.0459	-0.0760	1.25	0.0338
470	12.3	1.25	0.0580	-0.0767	1.26	--
471	13.1	1.27	0.0663	-0.0783	1.25	--
472	14.1	1.27	0.0888	-0.0849	1.25	--
473	15.2	1.15	0.1131	-0.0923	1.25	--
474	16.2	1.03	0.1643	-0.1144	1.26	--
475	17.2	0.95	0.2215	-0.1399	1.27	--
476	17.9	0.98	0.2382	-0.1420	1.26	--
477	19.0	0.95	0.2715	-0.1507	1.26	--
478	20.0	0.96	0.3057	-0.1608	1.25	--
479	22.1	1.00	0.3712	-0.1761	1.25	--

Table B7. S801, LEGR, Re = 1.25 x 10^6

RUN	AOA	C_l	C_{dp}	$C_{m1/4}$	Re x10^{-6}	C_{dw}
480	24.1	1.04	0.4364	-0.1917	1.26	--
481	26.0	1.12	0.5280	-0.2203	1.24	--
482	28.1	1.17	0.6127	-0.2390	1.25	--
483	29.9	1.25	0.7112	-0.2663	1.25	--
484	31.9	1.31	0.8225	-0.2960	1.24	--
485	34.0	1.39	0.9472	-0.3363	1.24	--
486	36.0	1.41	1.0383	-0.3591	1.24	--
487	37.9	1.42	1.1222	-0.3742	1.23	--
488	40.0	1.40	1.1955	-0.3876	1.21	--

End of Table B7

Table B8. S801, LEGR, Re = 1.5 x 10^6						
RUN	AOA	C_l	C_{dp}	$C_{m¼}$	Re x10^{-6}	C_{dw}
288	-20.2	-0.41	0.2721	-0.0029	1.49	--
287	-18.2	-0.55	0.2444	0.0010	1.50	--
286	-16.1	-0.55	0.2248	0.0019	1.50	--
285	-14.3	-0.55	0.1950	-0.0057	1.50	--
284	-12.2	-0.49	0.1500	-0.0378	1.51	--
283	-10.2	-0.49	0.0685	-0.0904	1.51	0.0817
282	-8.4	-0.43	0.0140	-0.1138	1.50	0.0227
281	-6.2	-0.21	0.0055	-0.1168	1.50	0.0175
280	-4.1	0.01	0.0030	-0.1170	1.50	0.0137
279	-2.3	0.20	0.0033	-0.1174	1.50	0.0123
278	-0.1	0.44	0.0052	-0.1161	1.50	0.0130
289	-0.1	0.43	0.0057	-0.1165	1.50	0.0110
305	-0.1	0.43	0.0054	-0.1158	1.51	0.0121
290	2.0	0.65	0.0090	-0.1138	1.50	0.0119
291	4.1	0.84	0.0139	-0.1081	1.51	0.0139
292	6.0	0.98	0.0215	-0.1020	1.51	0.0167
293	8.1	1.11	0.0282	-0.0907	1.50	0.0207
294	10.2	1.19	0.0392	-0.0799	1.51	0.0268
295	11.3	1.24	0.0519	-0.0828	1.49	--
296	12.3	1.26	0.0650	-0.0821	1.50	--
297	13.1	1.28	0.0691	-0.0797	1.50	--
298	14.1	1.19	0.0764	-0.0740	1.50	--
299	15.2	1.12	0.1040	-0.0843	1.50	--
300	16.2	1.05	0.1531	-0.1093	1.50	--
301	17.2	1.03	0.1986	-0.1281	1.51	--
302	17.9	1.04	0.2225	-0.1344	1.51	--
303	19.0	1.03	0.2605	-0.1473	1.51	--
304	20.0	1.06	0.2988	-0.1605	1.49	--
End of Table B8						

S801

Pressure Distributions, Steady State, Re = 0.75 million

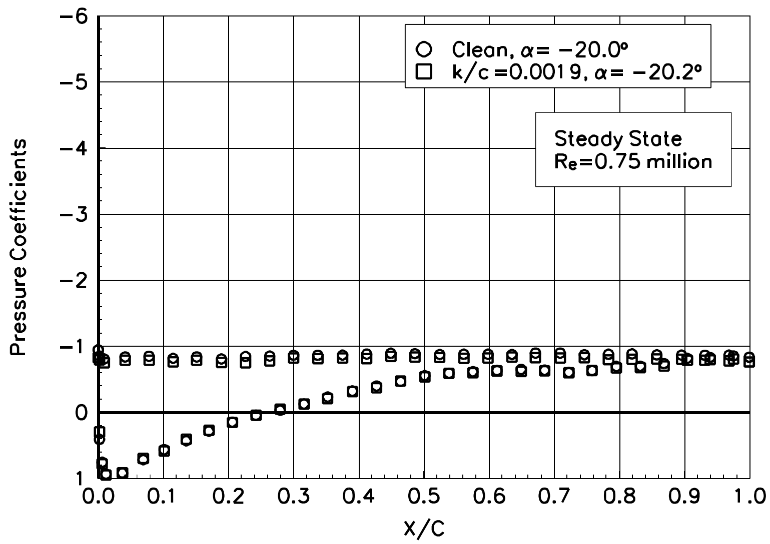

Figure 1. α **= -20.0°**

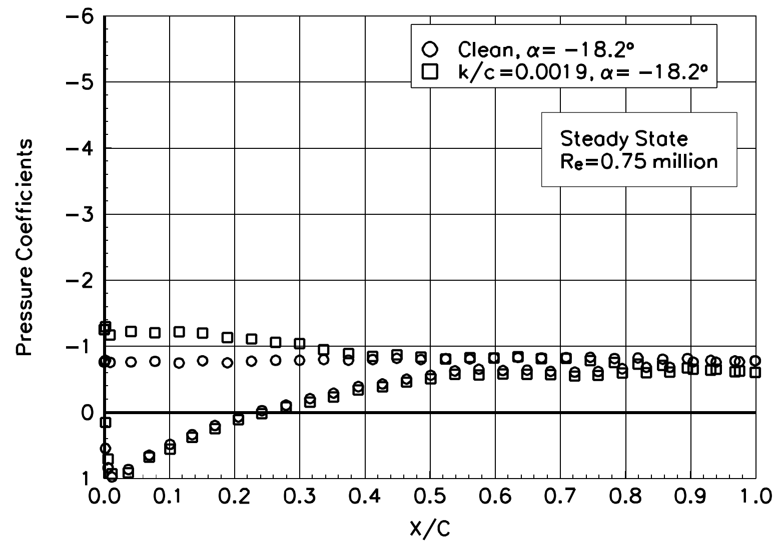

Figure 2. α **= -18.2°**

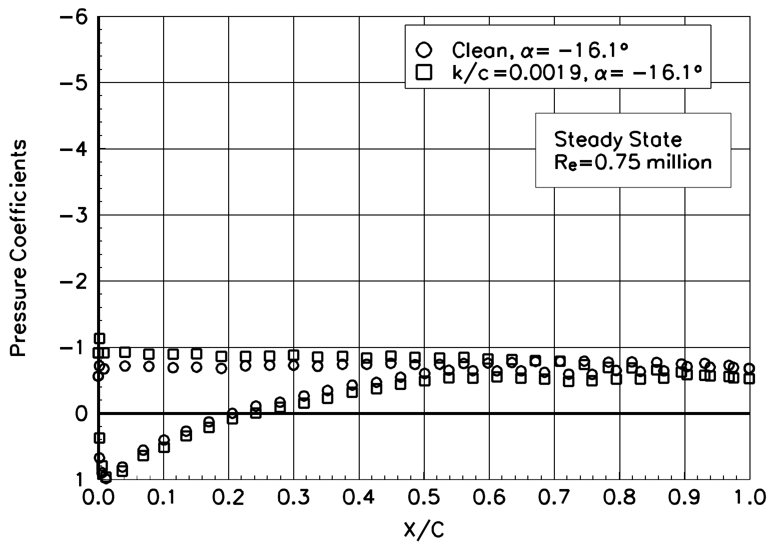

Figure 3. α **= -16.1°**

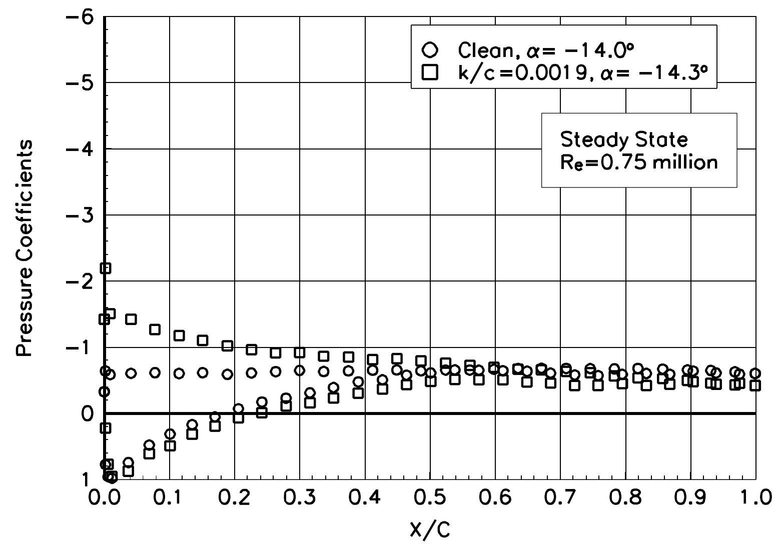

Figure 4. α **= -14.0°**

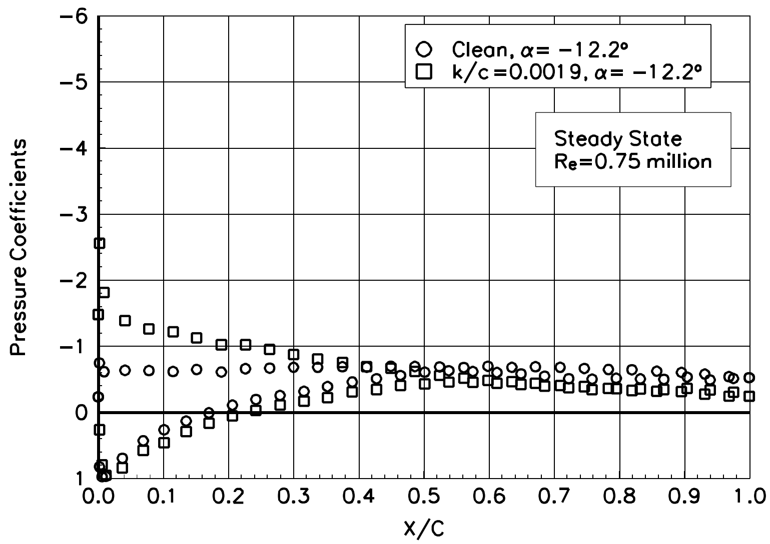

Figure 5. α **= -12.2°**

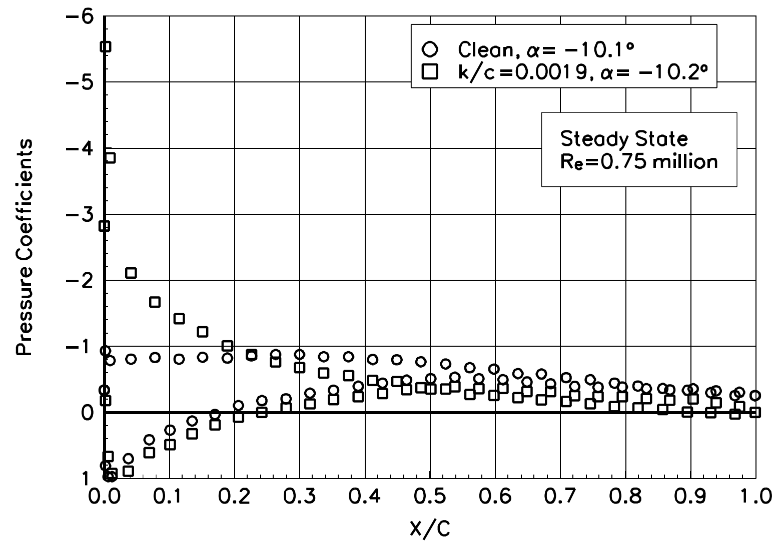

Figure 6. α **= -10.1°**

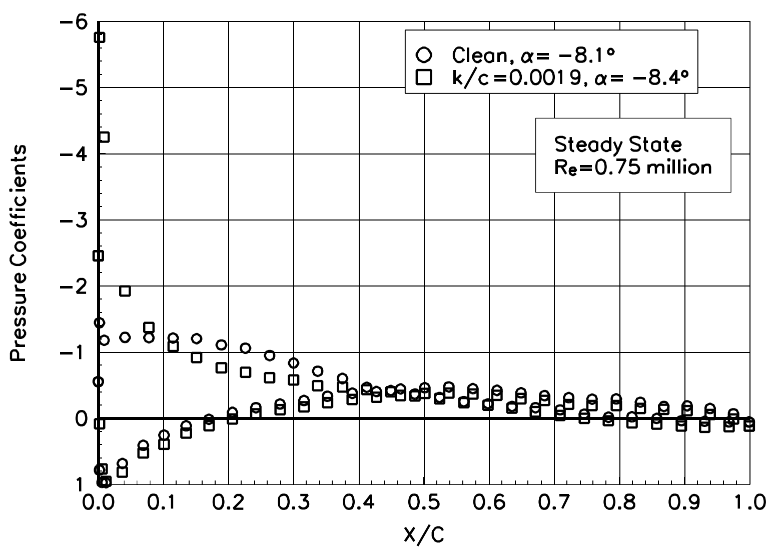

Figure 7. α **= -8.1°**

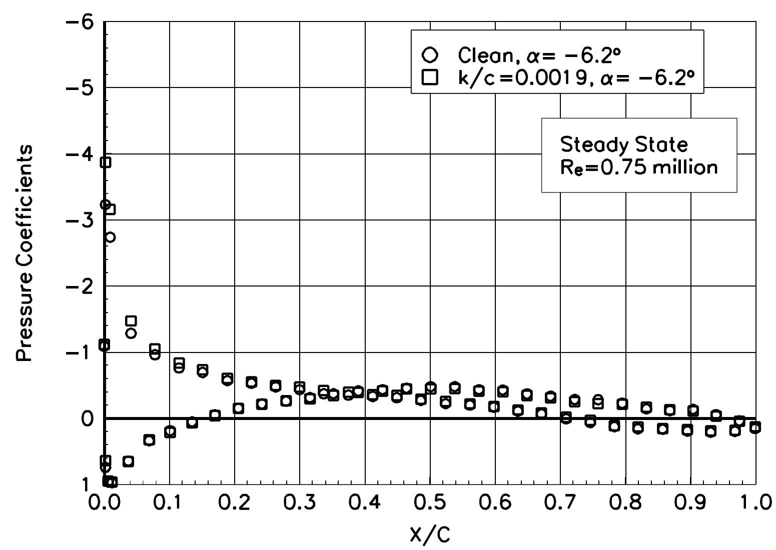

Figure 8. α **= -6.2°**

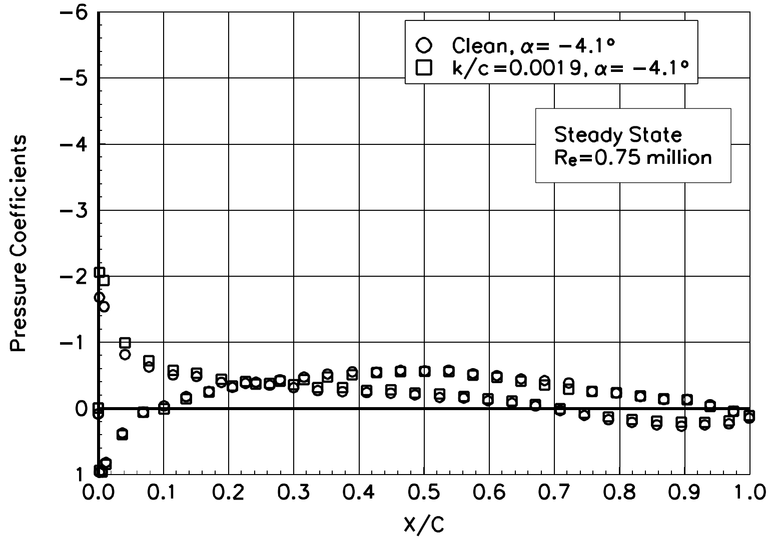

Figure 9. α **= -4.1°**

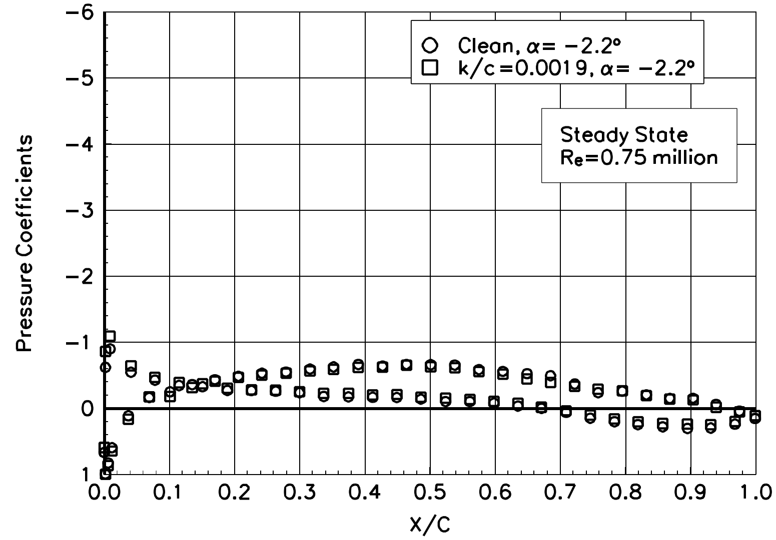

Figure 10. α **= -2.2°**

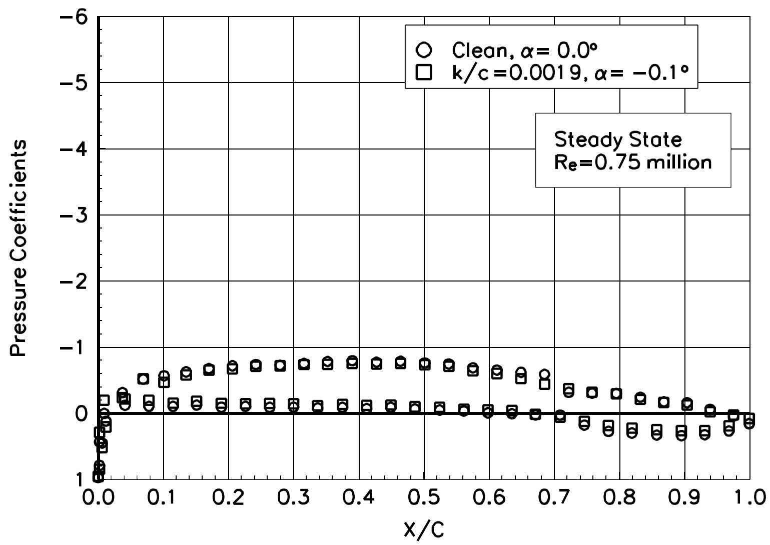

Figure 11. α **= 0.0°**

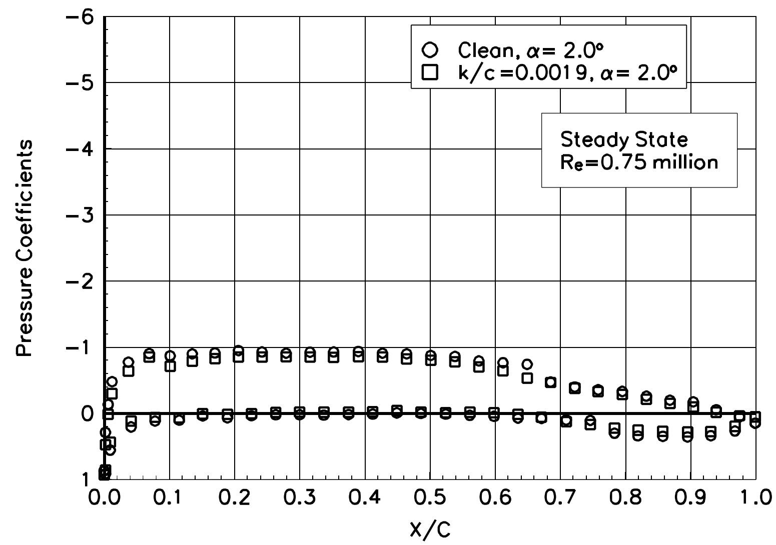

Figure 12. α **= 2.0°**

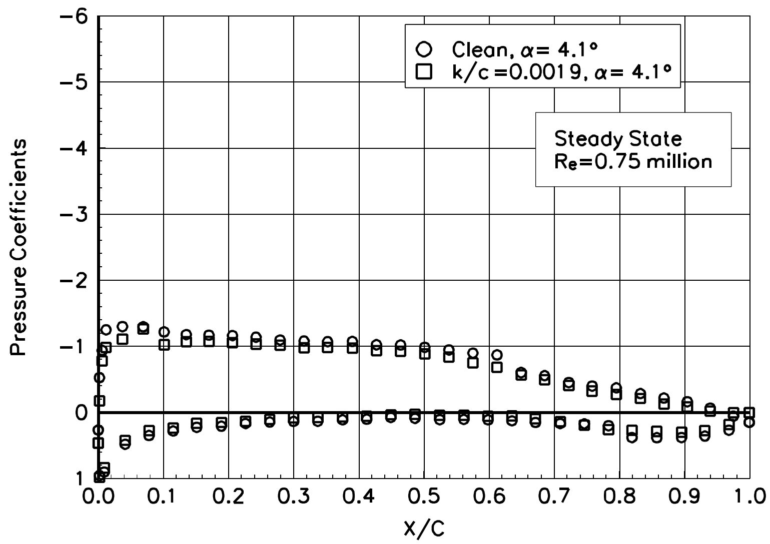

Figure 13. α = 4.1°

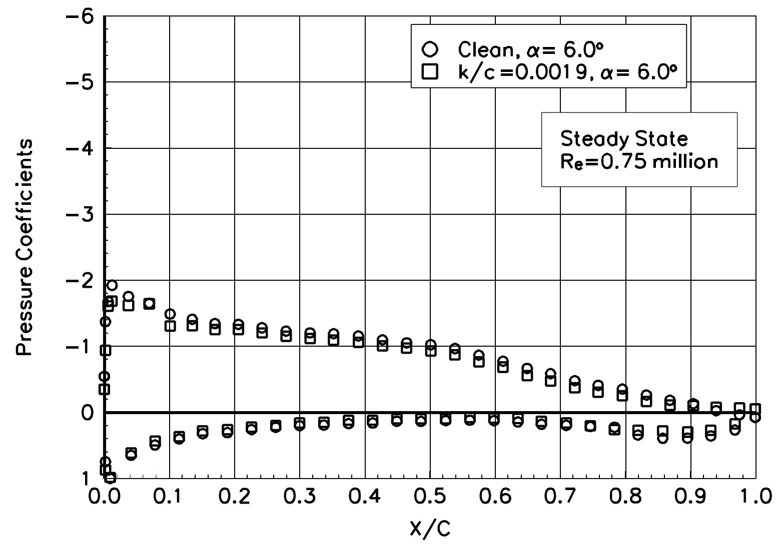

Figure 14. α = 6.0°

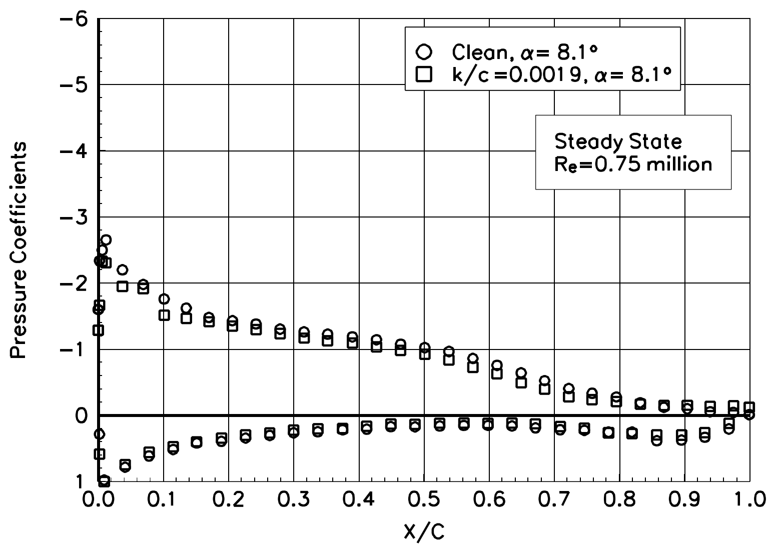

Figure 15. α = 8.1°

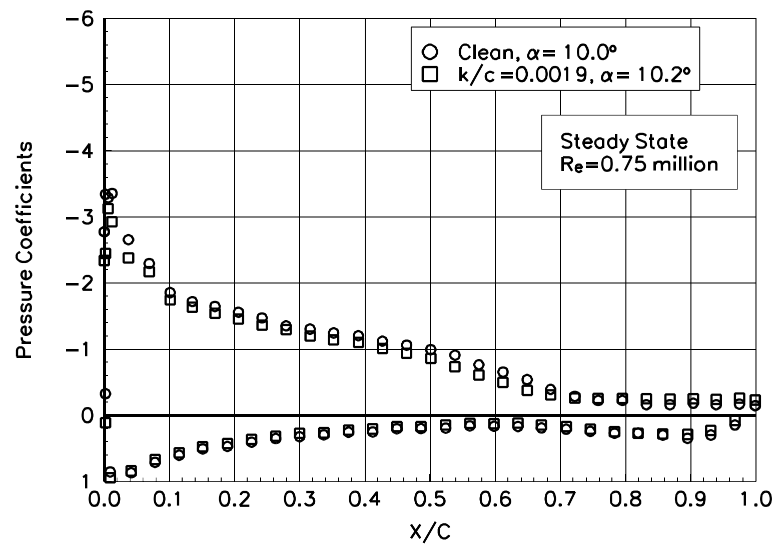

Figure 16. α = 10.0°

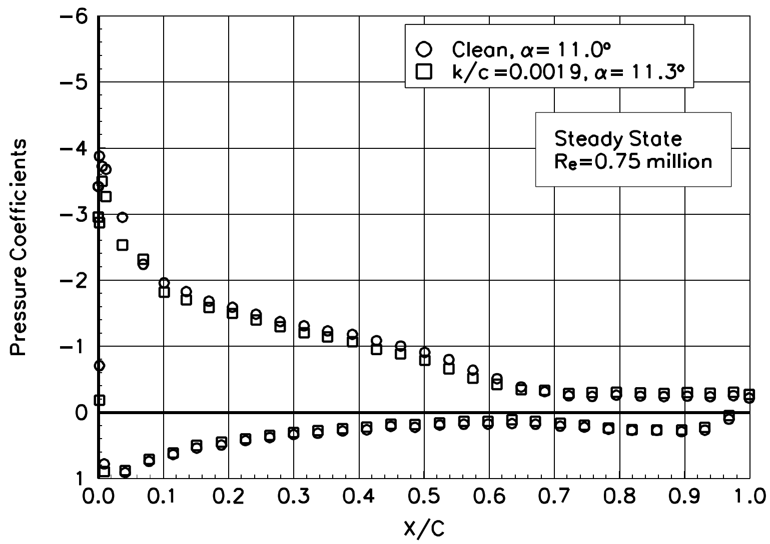

Figure 17. α **= 11.0°**

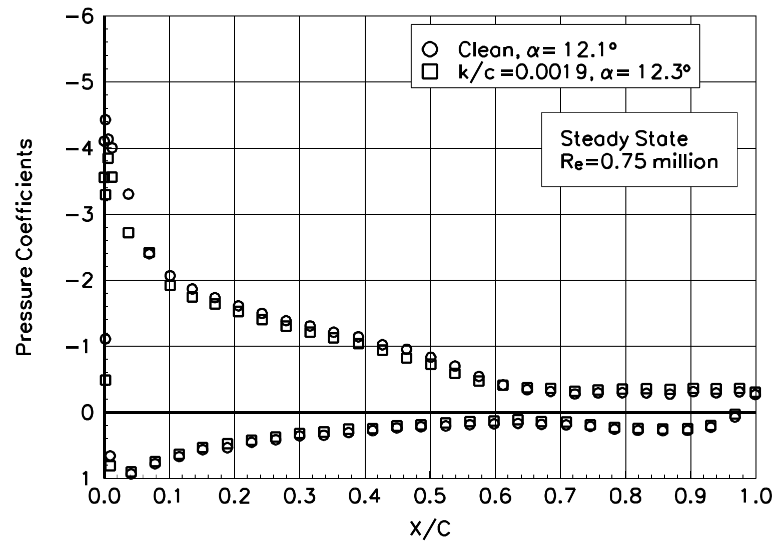

Figure 18. α **= 12.1°**

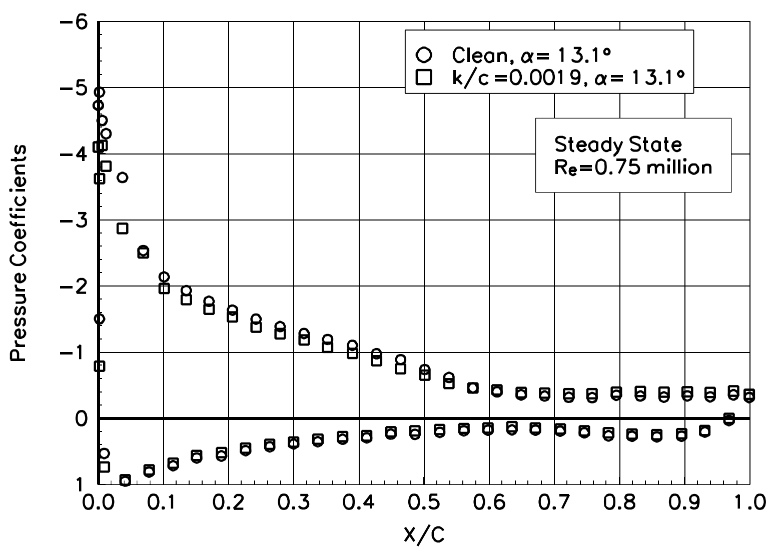

Figure 19. α **= 13.1°**

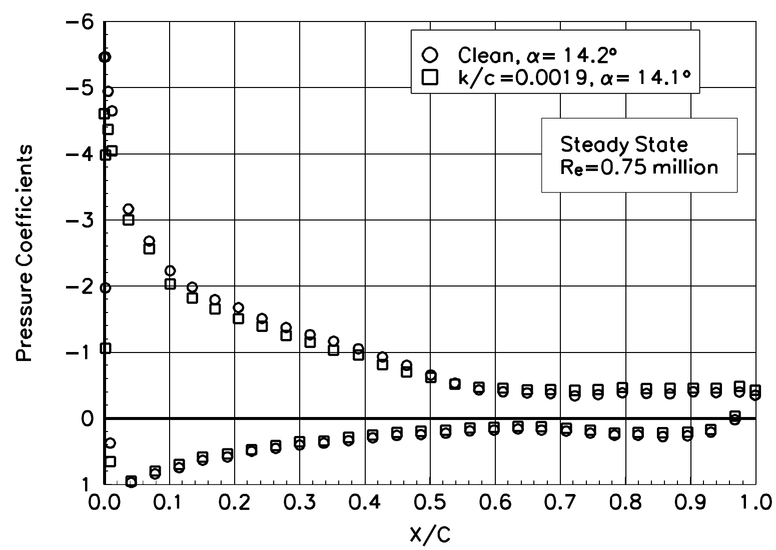

Figure 20. α **= 14.2°**

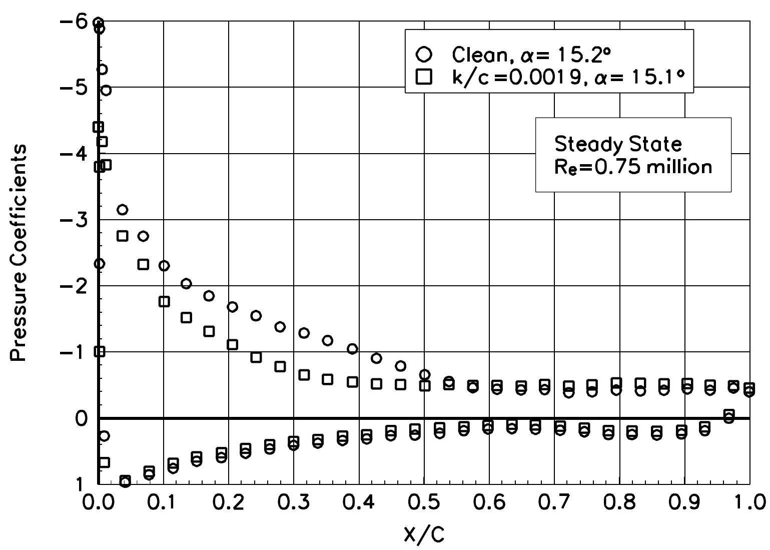

Figure 21. $\alpha = 15.2^{\cdot}$

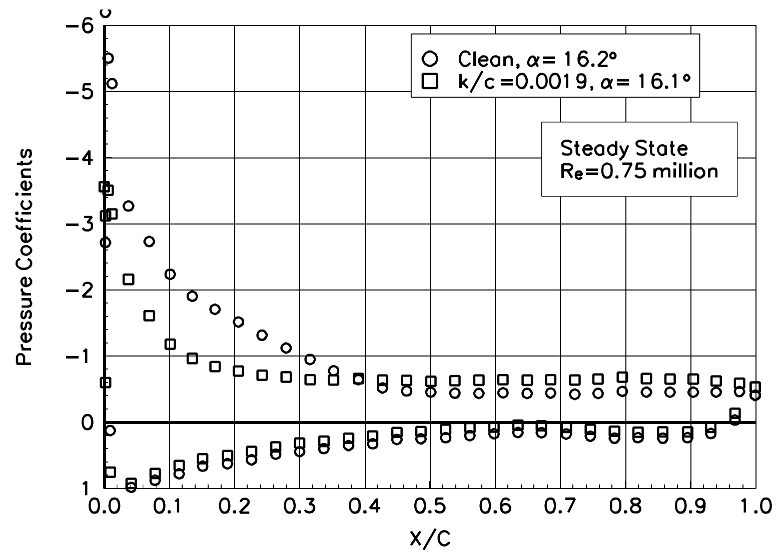

Figure 22. $\alpha = 16.2°$

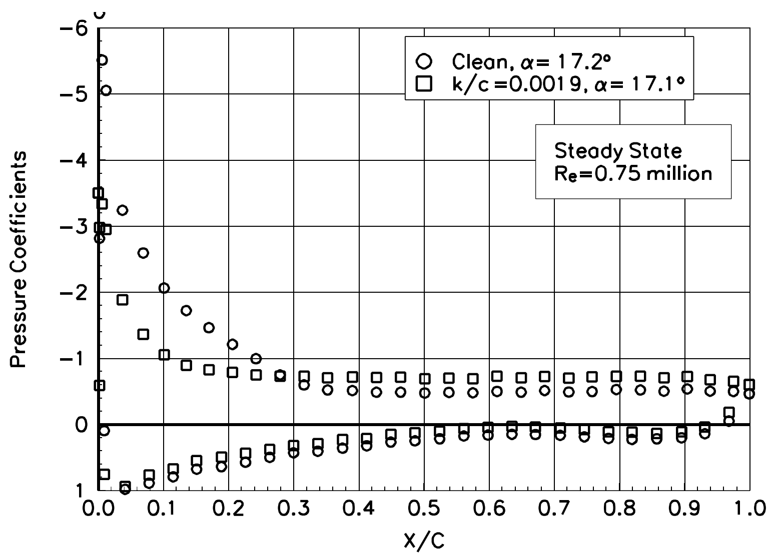

Figure 23. $\alpha = 17.2°$

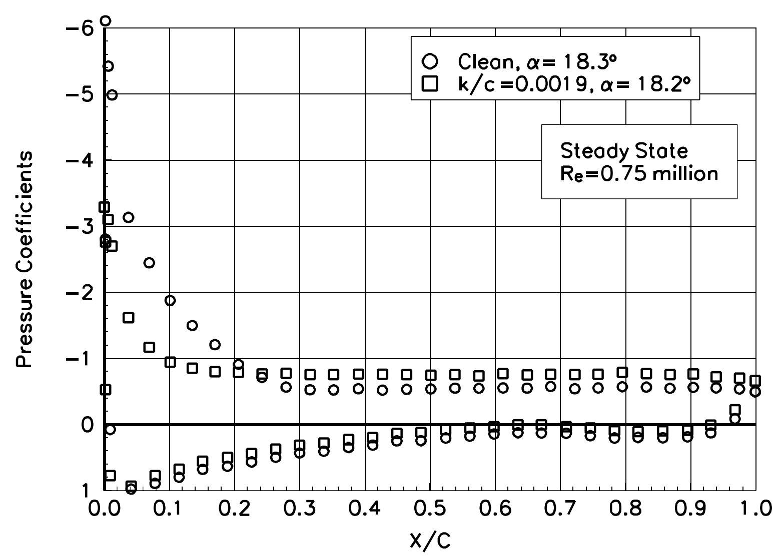

Figure 24. $\alpha = 18.3°$

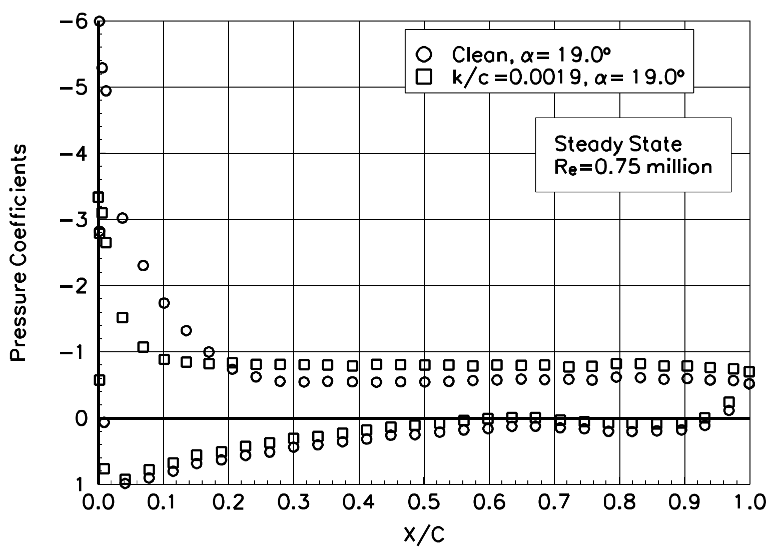

Figure 25. α **= 19.0°**

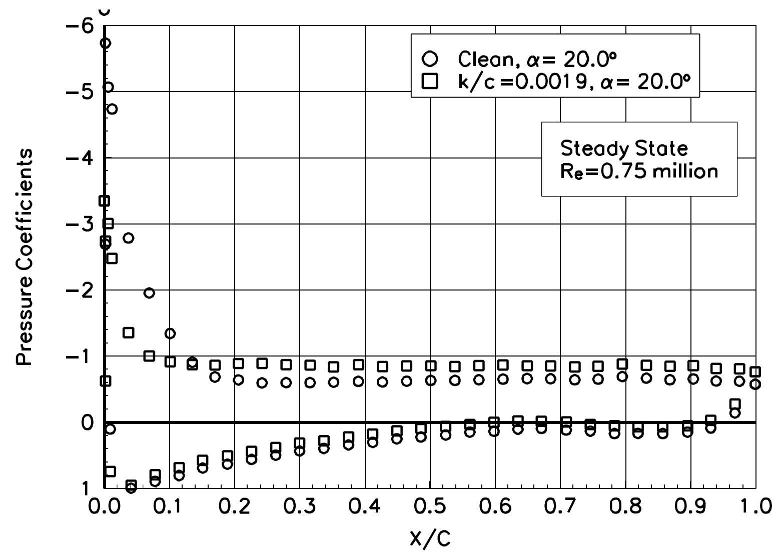

Figure 26. α **= 20.0°**

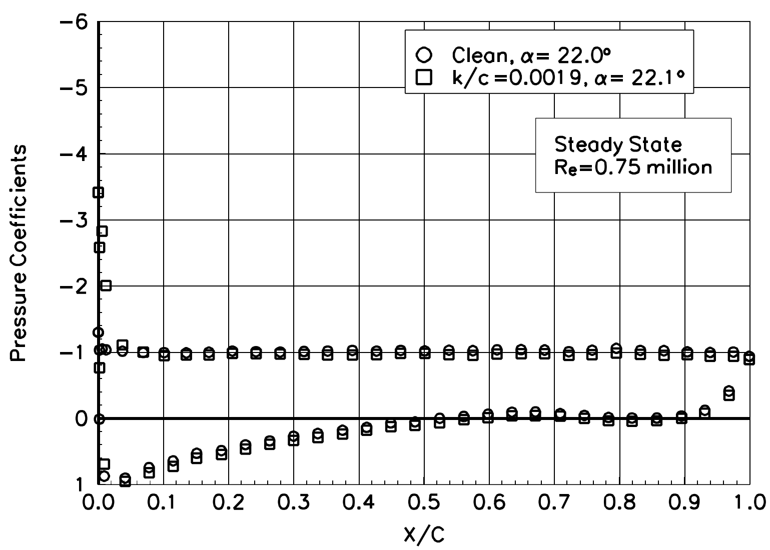

Figure 27. α **= 22.0°**

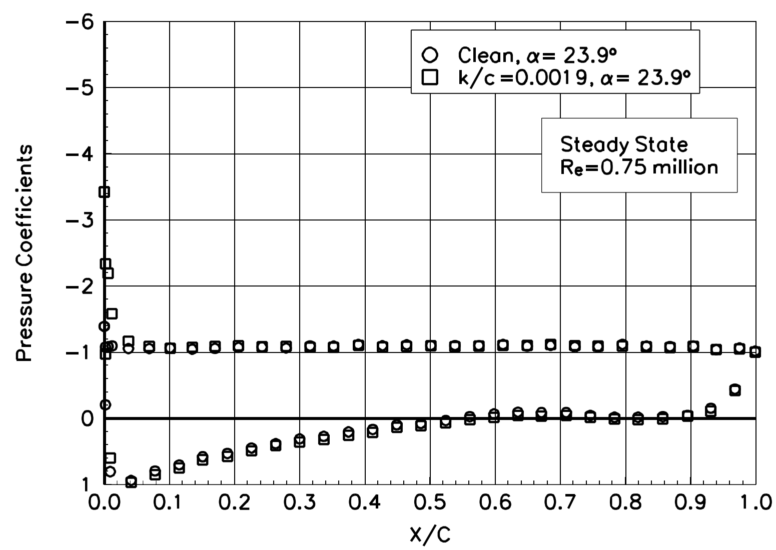

Figure 28. α **= 23.9°**

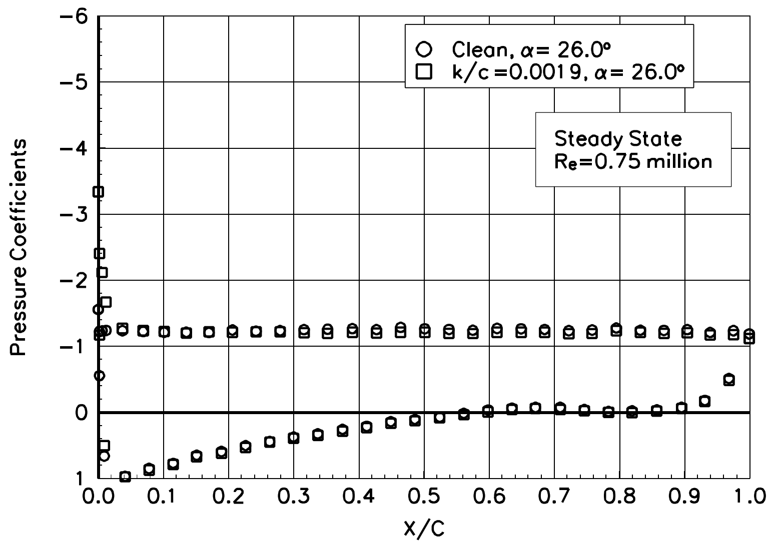

Figure 29. α **= 26.0°**

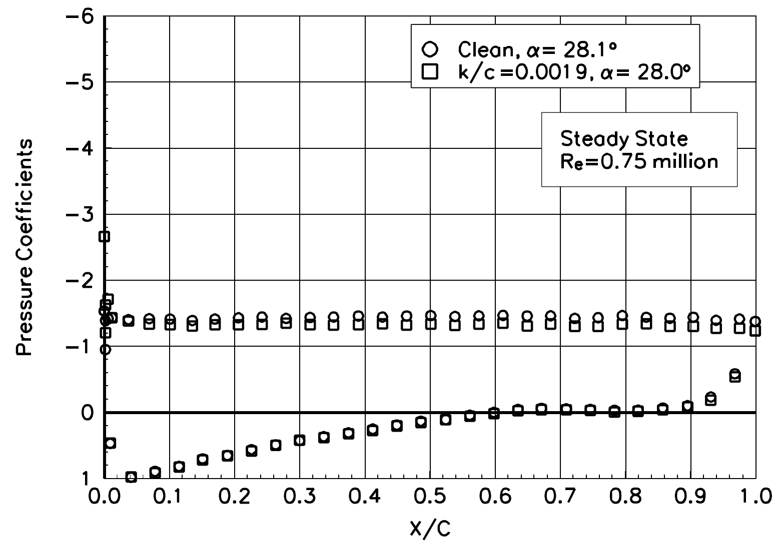

Figure 30. α **= 28.1°**

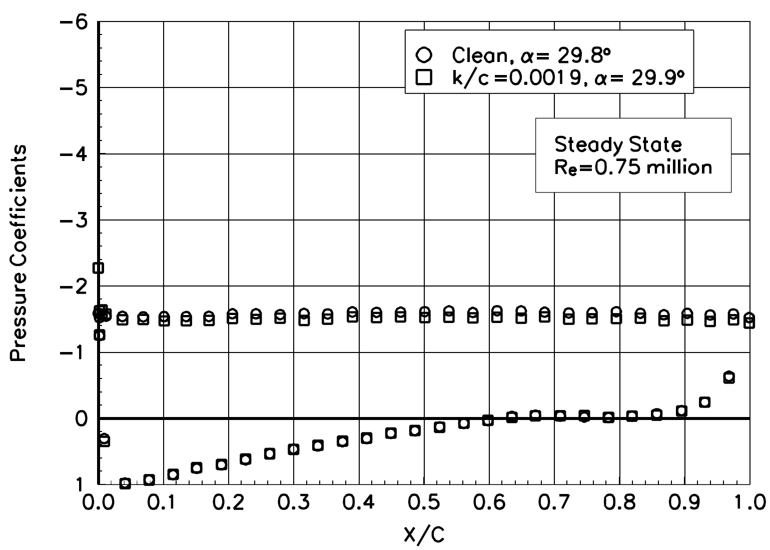

Figure 31. α **= 29.8°**

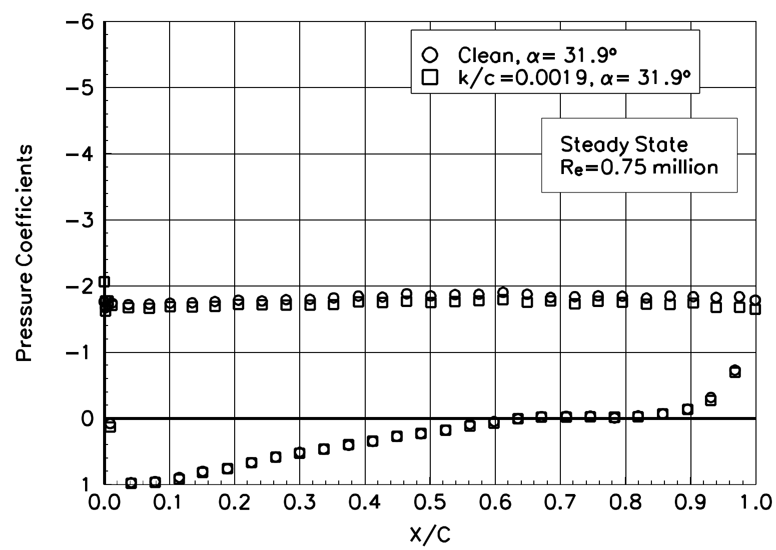

Figure 32. α **= 31.9°**

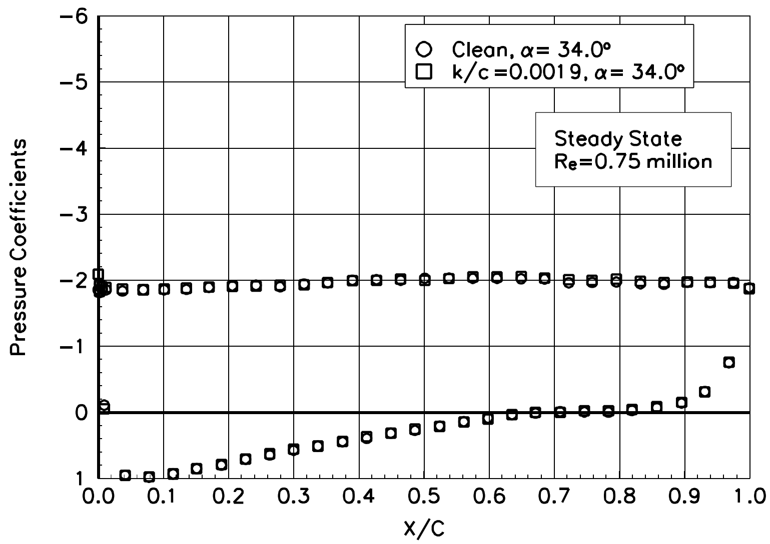

Figure 33. $\alpha = 34.0°$

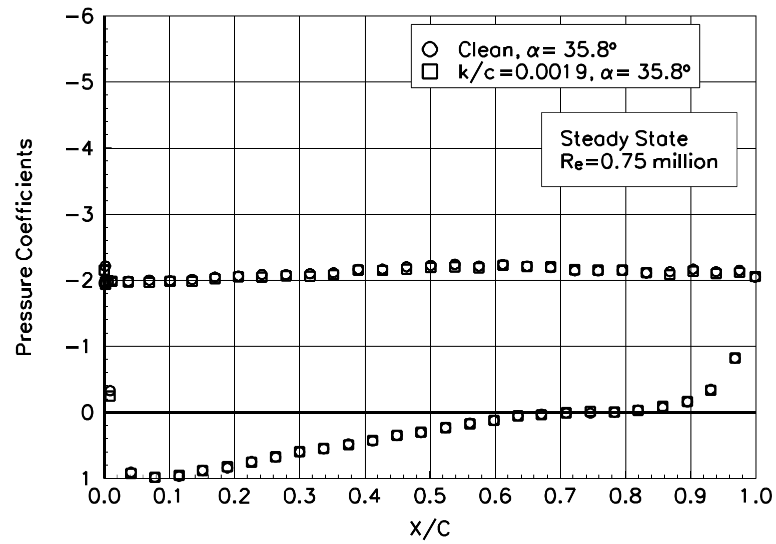

Figure 34. $\alpha = 35.8°$

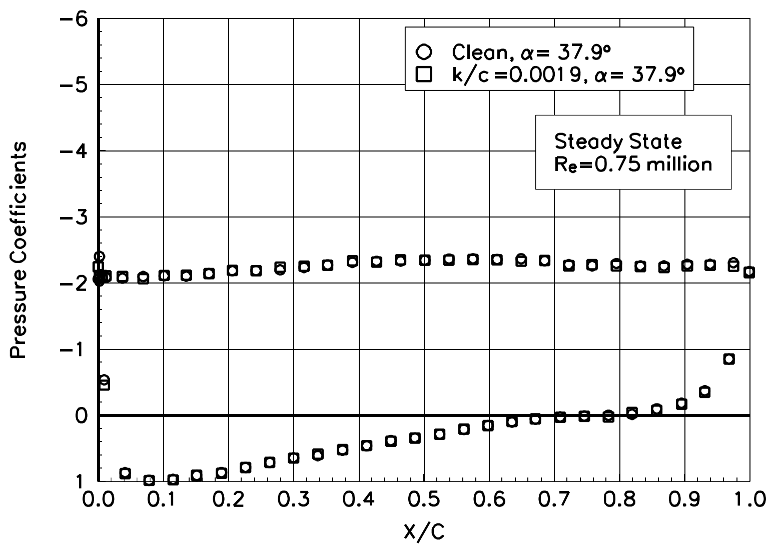

Figure 35. $\alpha = 37.9°$

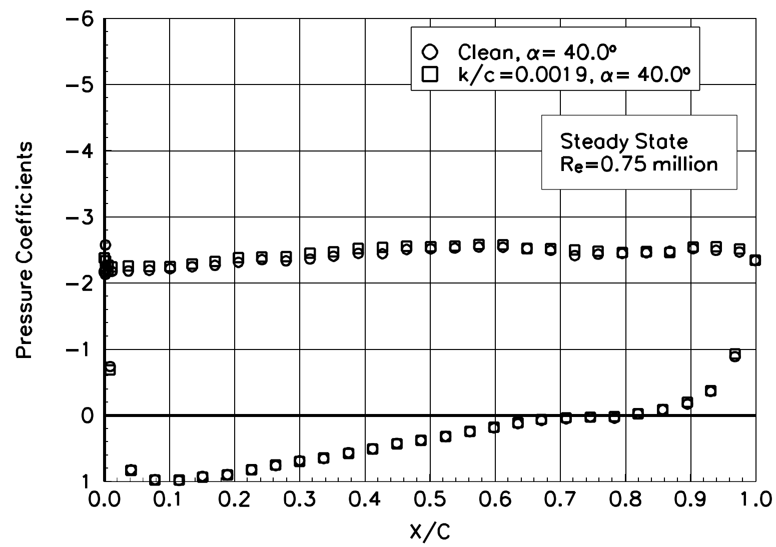

Figure 36. $\alpha = 40.0°$

S801

Pressure Distributions, Steady State, Re = 1 million

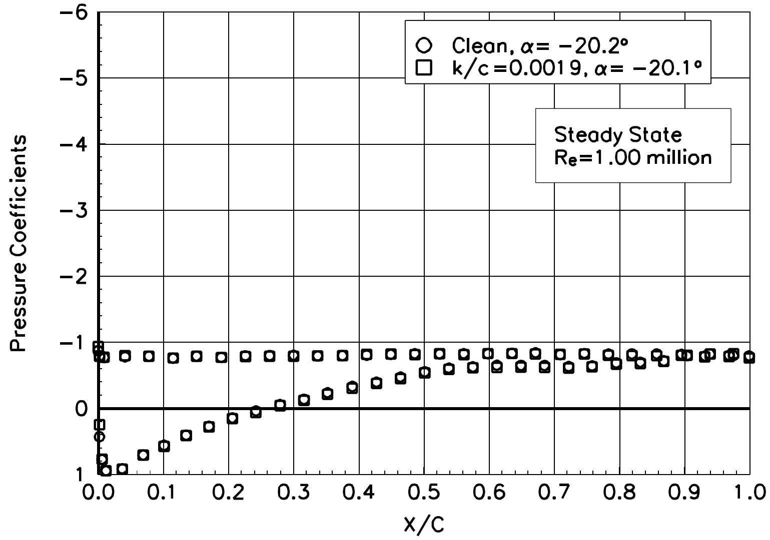

Figure 37. α **= -20.2°**

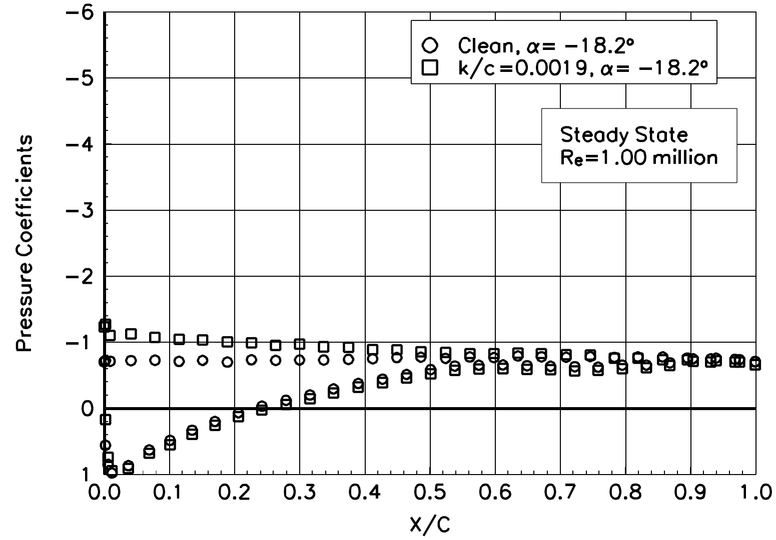

Figure 38. α **= -18.2°**

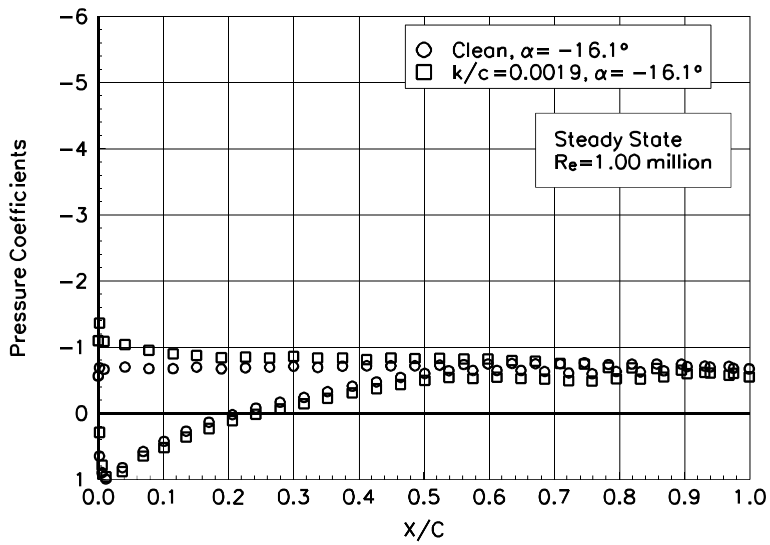

Figure 39. α **= -16.1°**

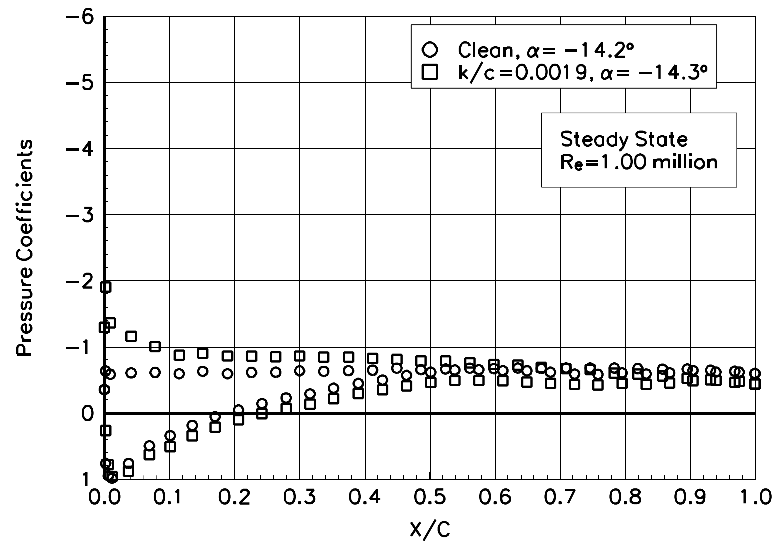

Figure 40. α **= -14.2°**

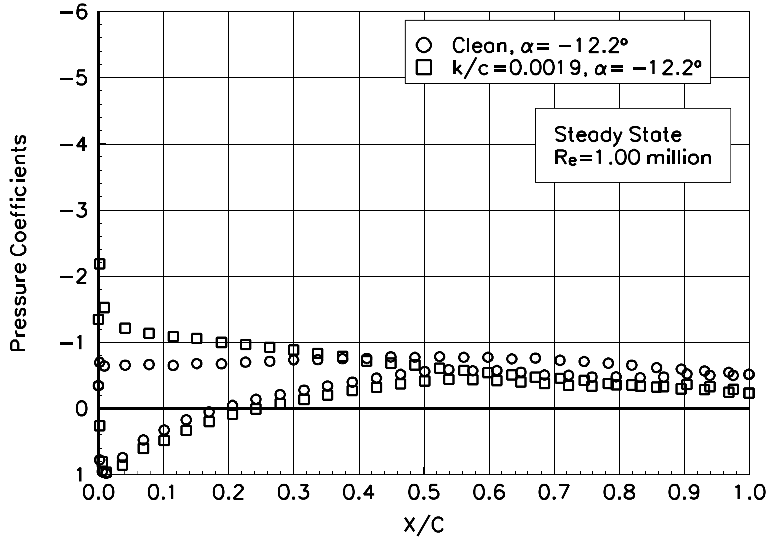

Figure 41. α **= -12.2°**

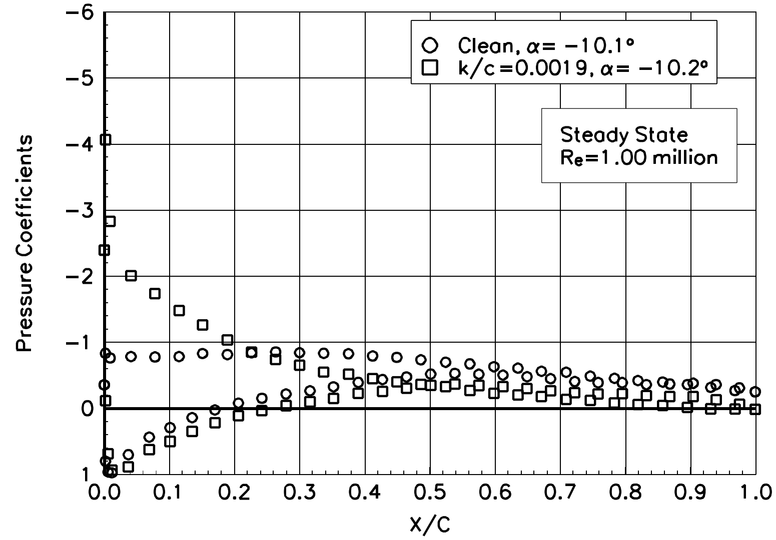

Figure 42. α **= -10.1°**

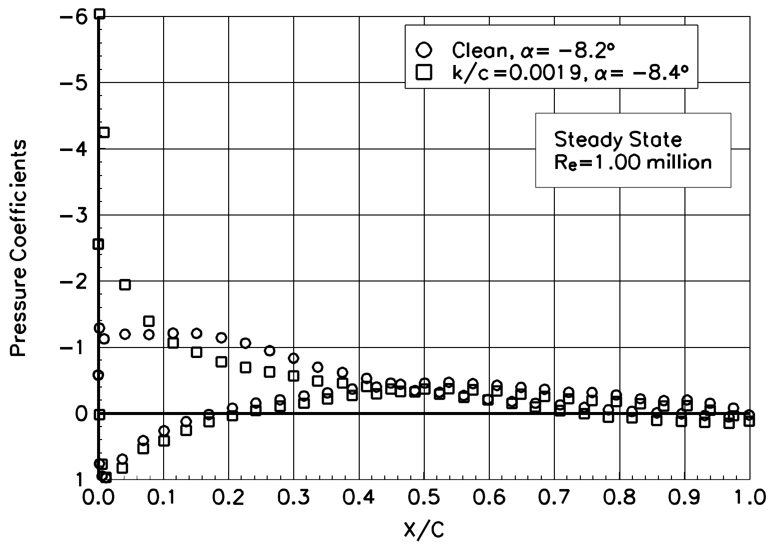

Figure 43. α **= -8.2°**

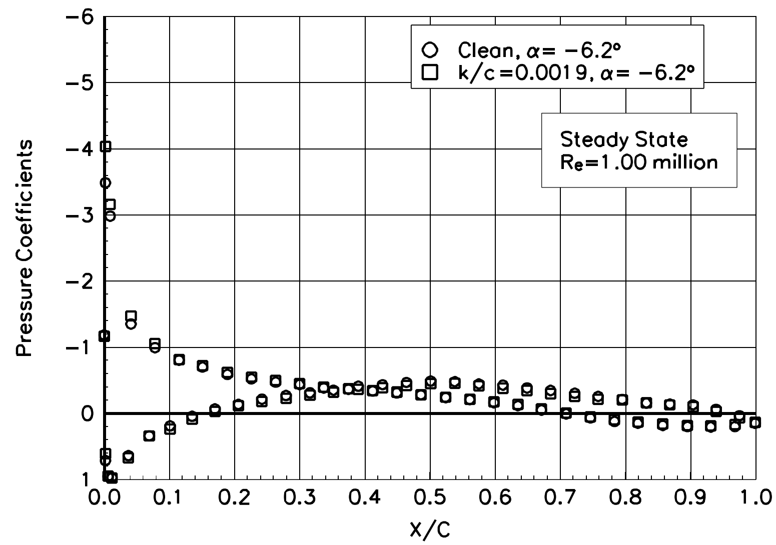

Figure 44. α **= -6.2°**

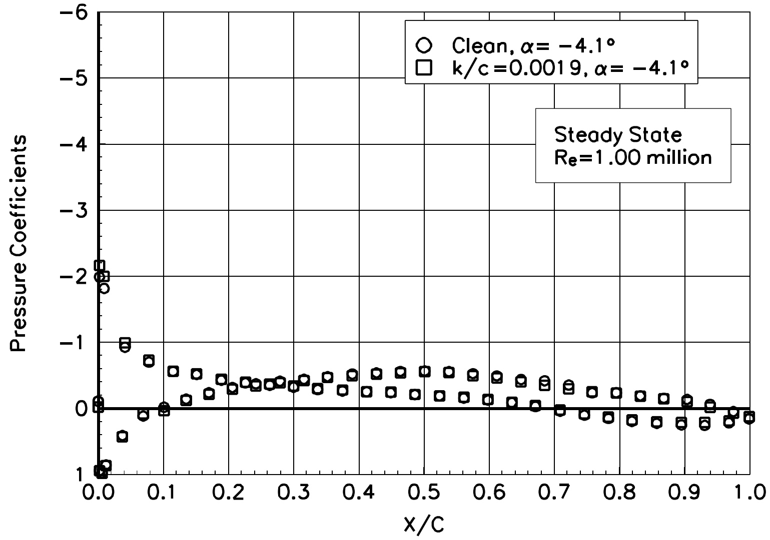

Figure 45. α **= -4.1°**

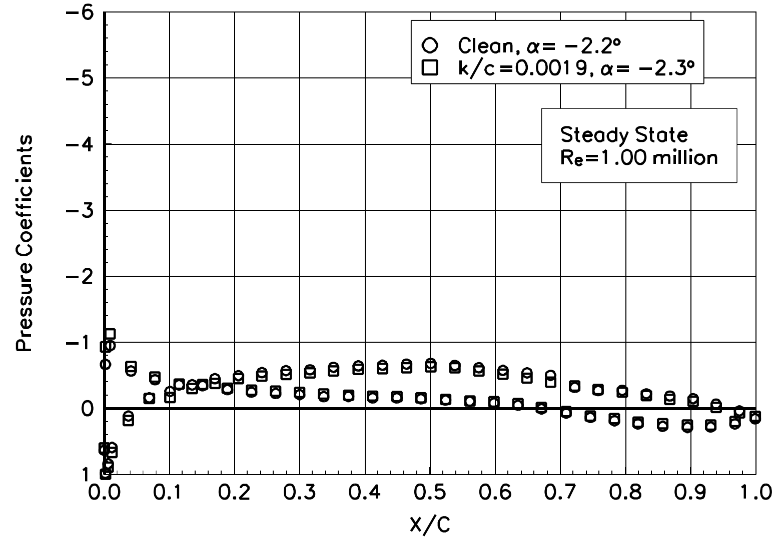

Figure 46. α **= -2.2°**

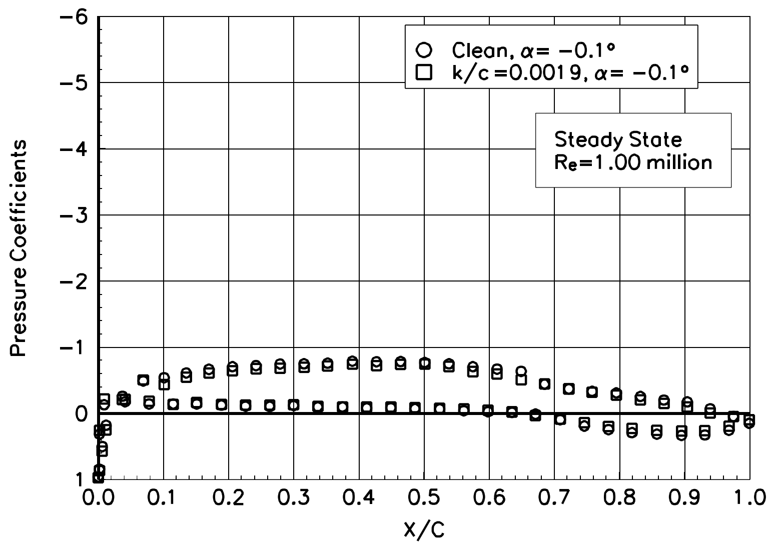

Figure 47. α **= -0.1°**

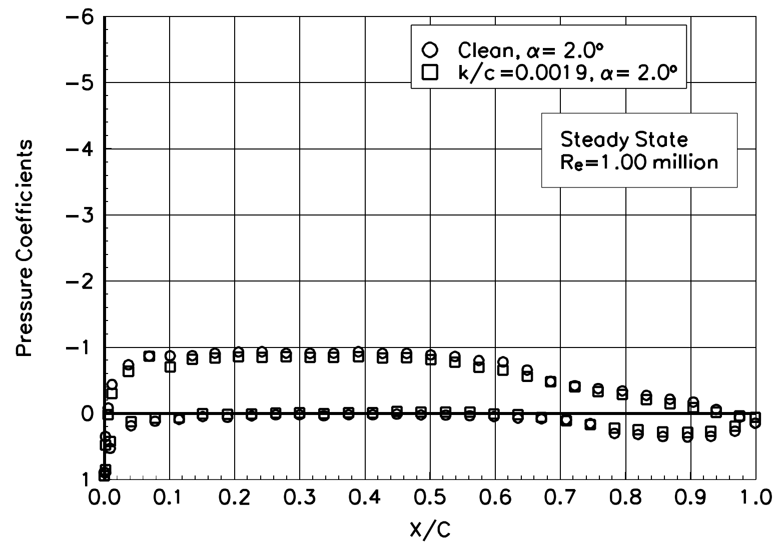

Figure 48. α **= 2.0°**

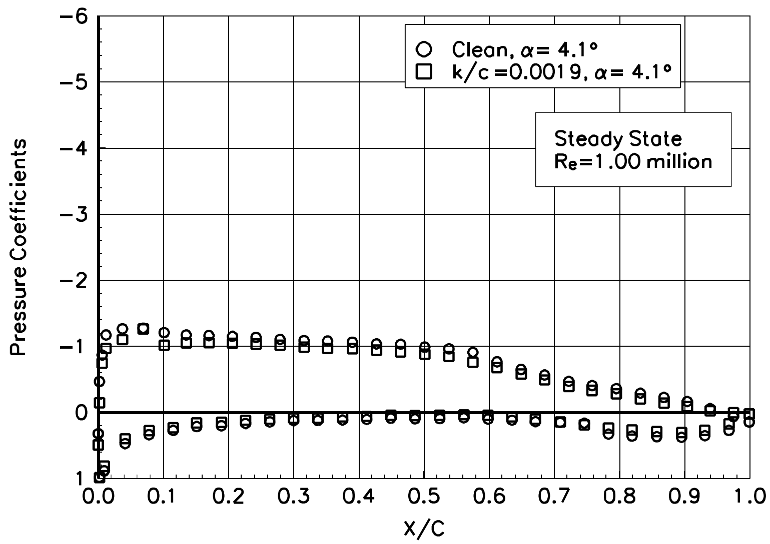

Figure 49. $\alpha = 4.1°$

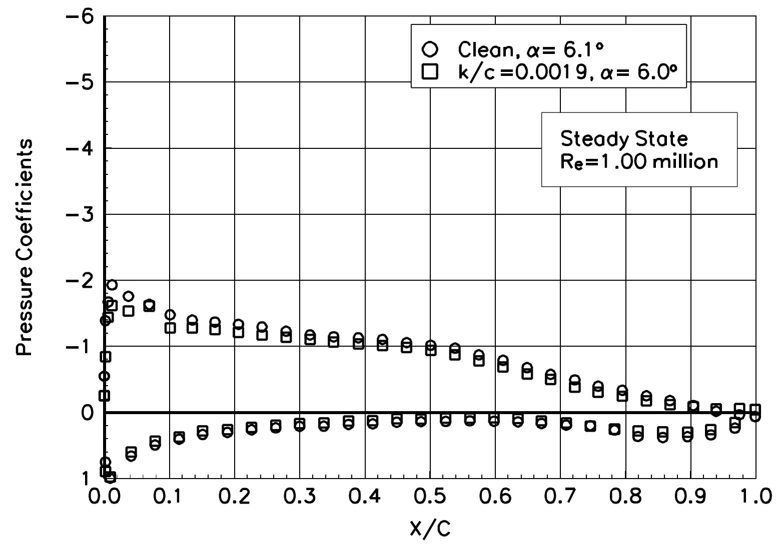

Figure 50. $\alpha = 6.1°$

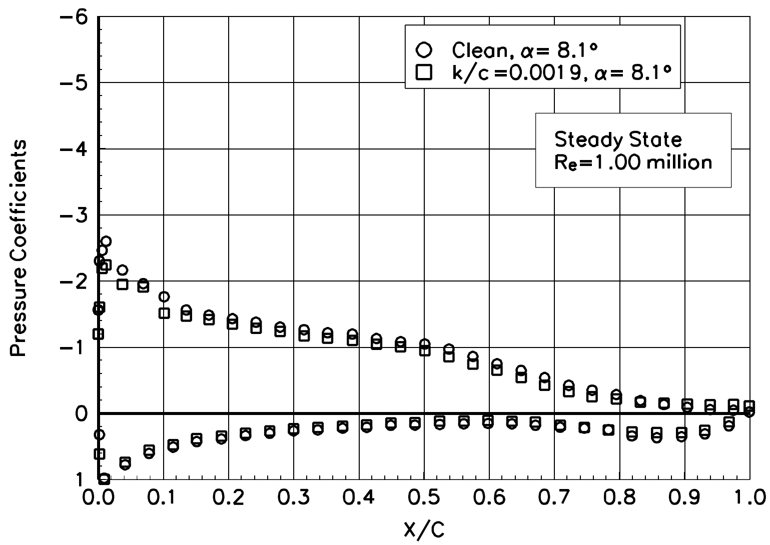

Figure 51. $\alpha = 8.1°$

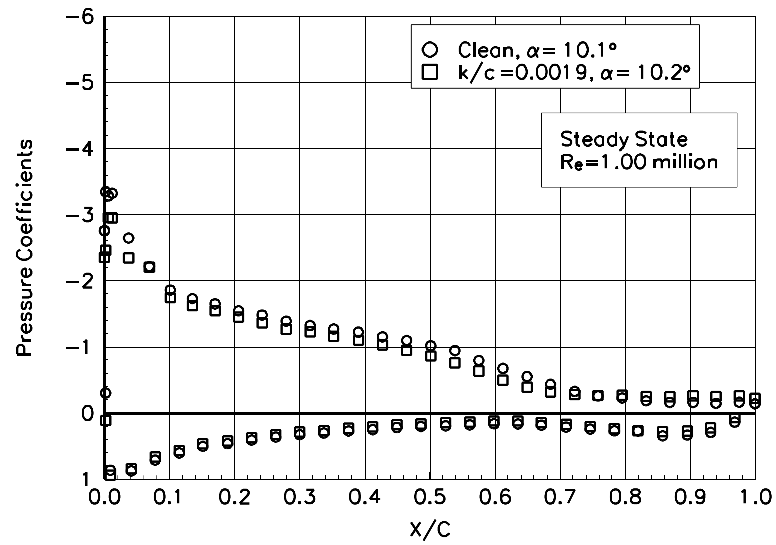

Figure 52. $\alpha = 10.1°$

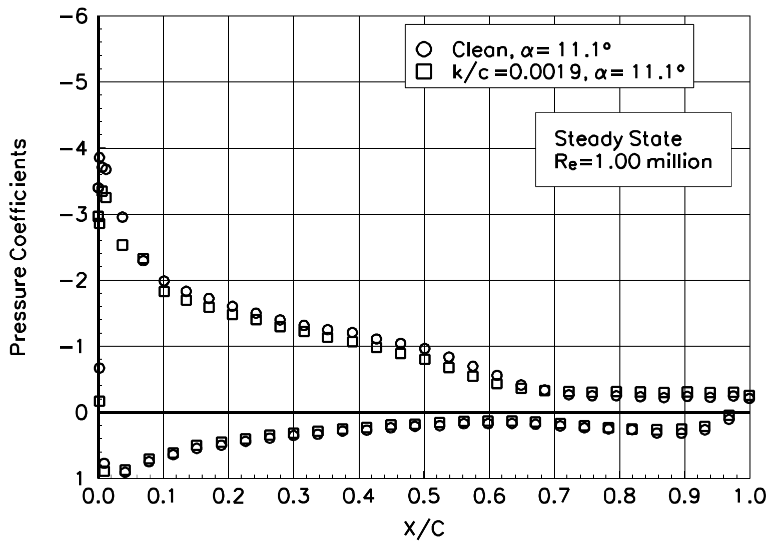

Figure 53. $\alpha = 11.1°$

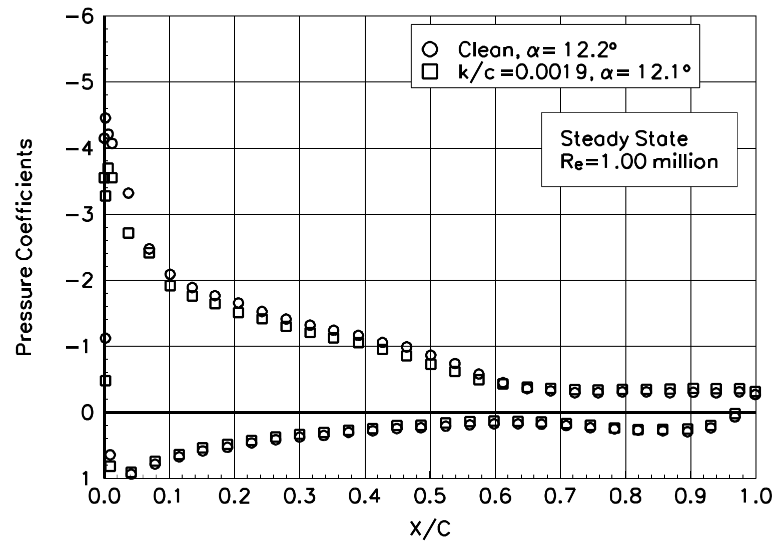

Figure 54. $\alpha = 12.2°$

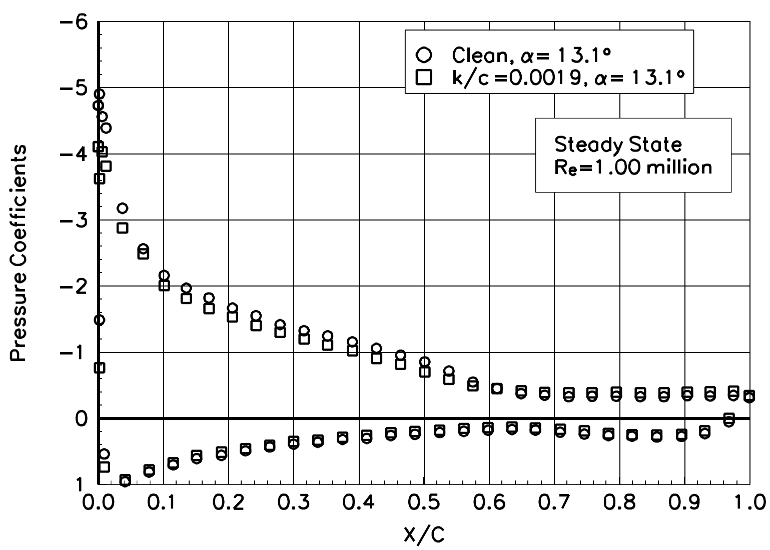

Figure 55. $\alpha = 13.1°$

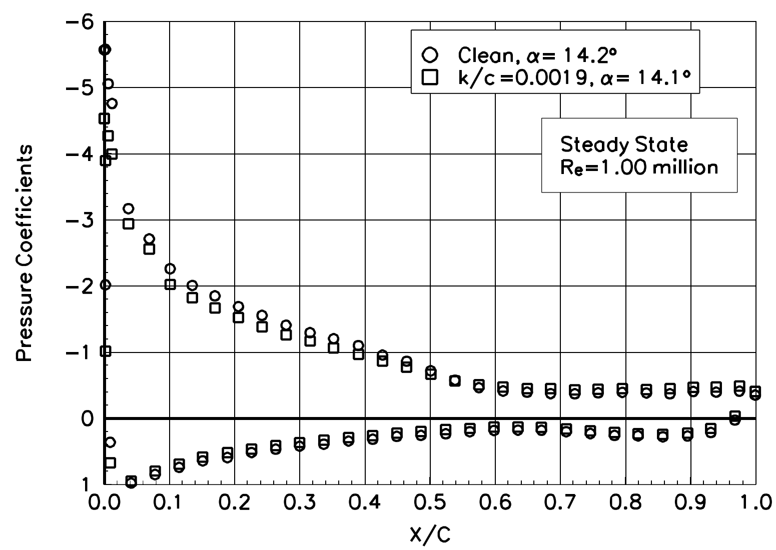

Figure 56. $\alpha = 14.2°$

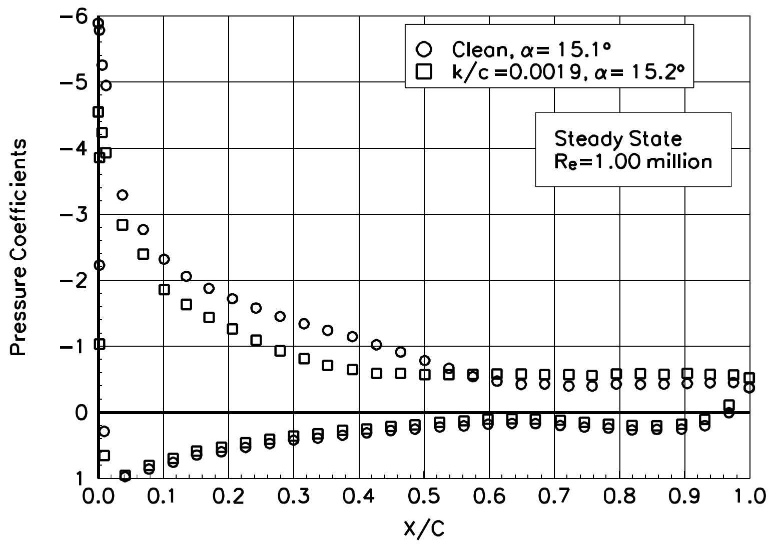

Figure 57. α **= 15.1°**

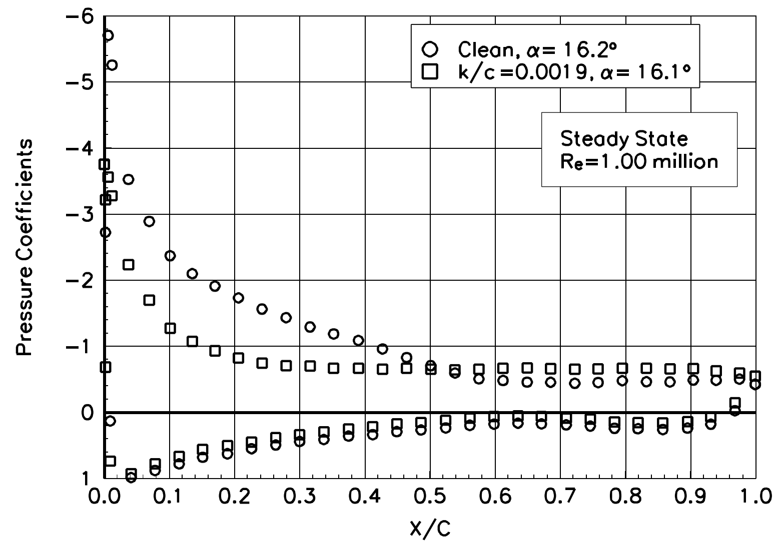

Figure 58. α **= 16.2°**

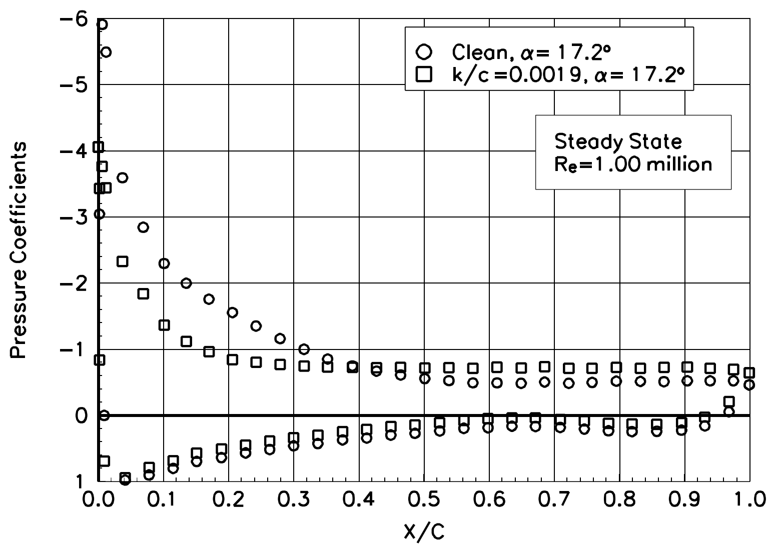

Figure 59. α **= 17.2°**

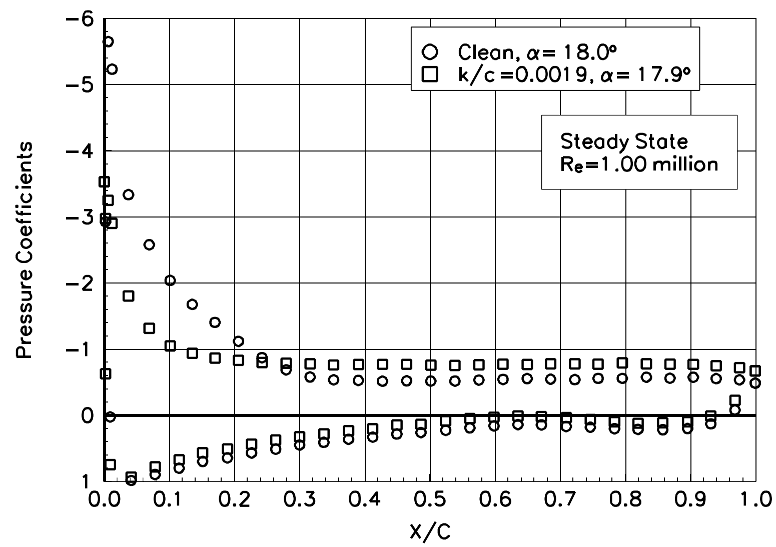

Figure 60. α **= 18.0°**

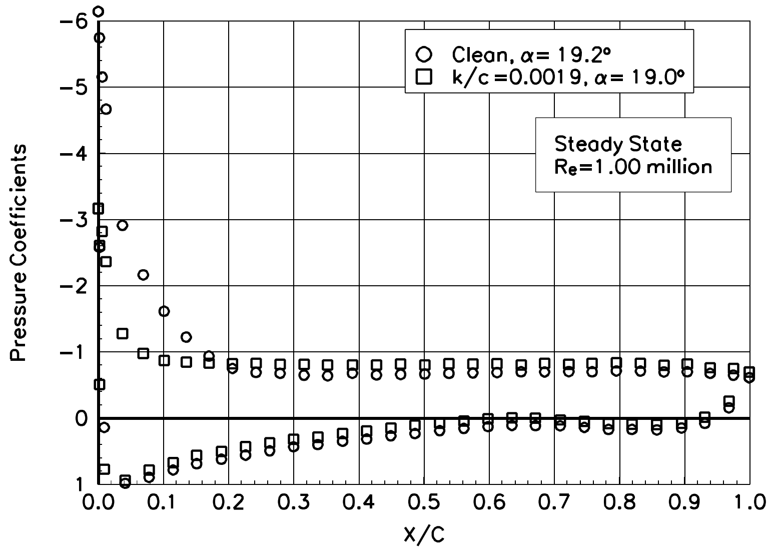

Figure 61. α **= 19.2°**

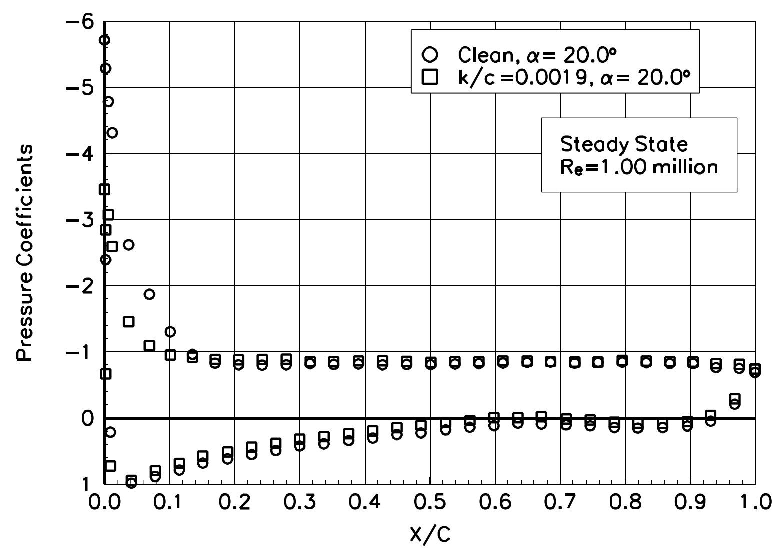

Figure 62. α **= 20.0°**

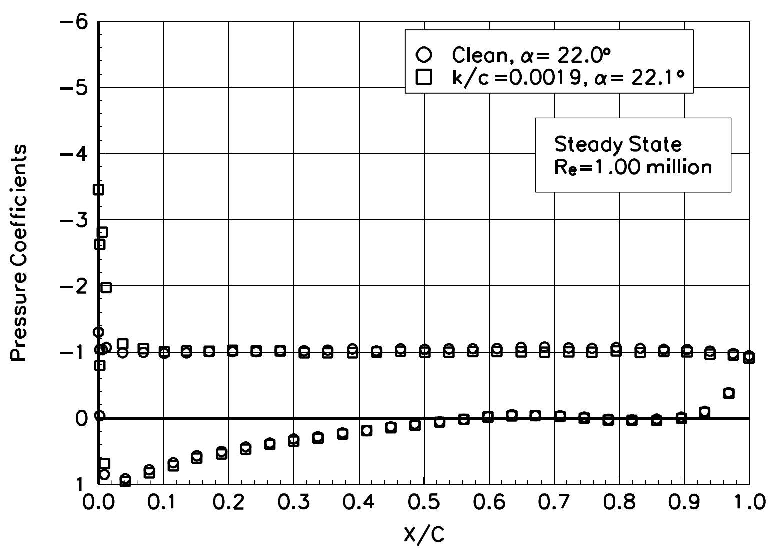

Figure 63. α **= 22.0°**

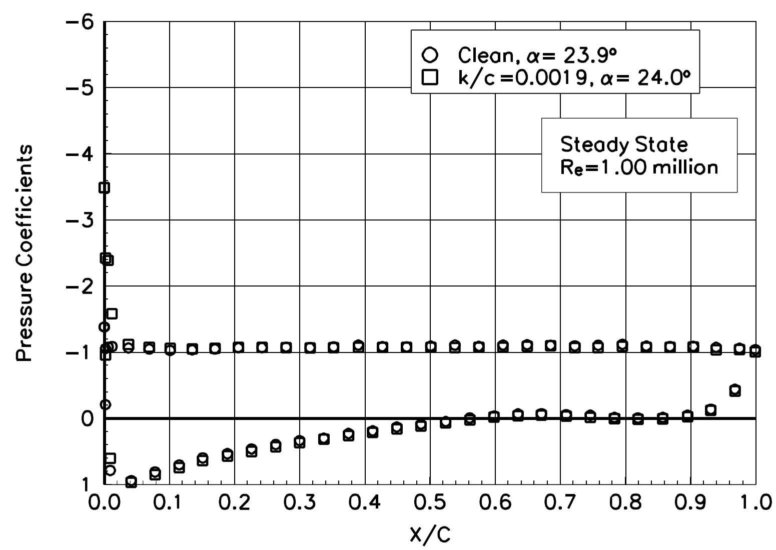

Figure 64. α **= 23.9°**

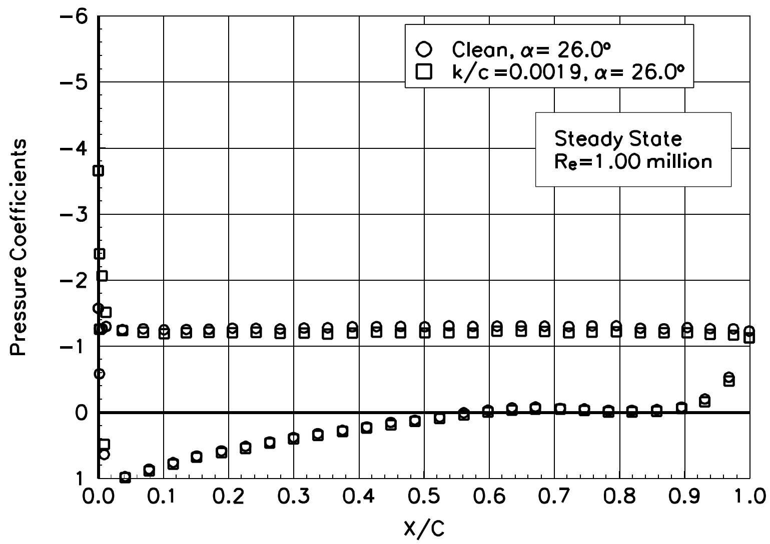

Figure 65. α = 26.0°

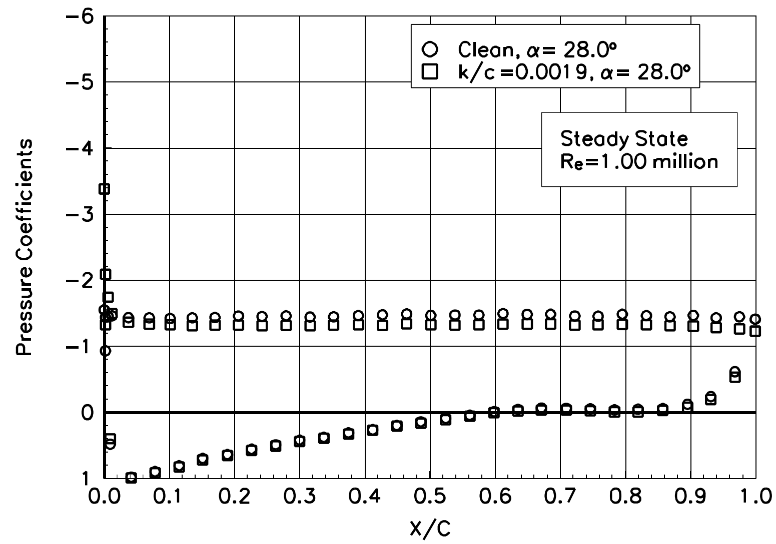

Figure 66. α = 28.0°

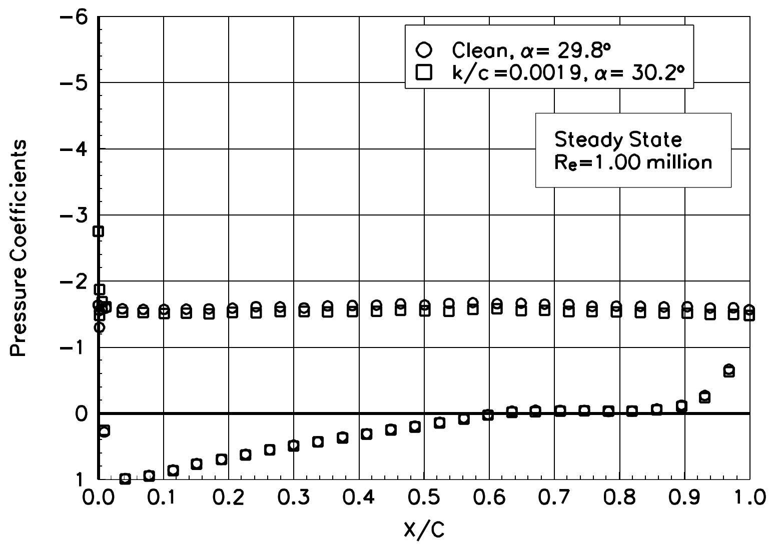

Figure 67. α = 29.8°

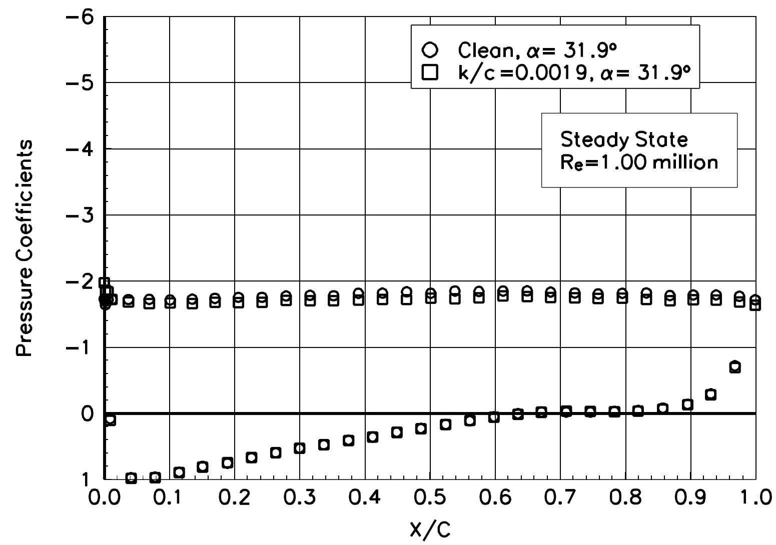

Figure 68. α = 31.9°

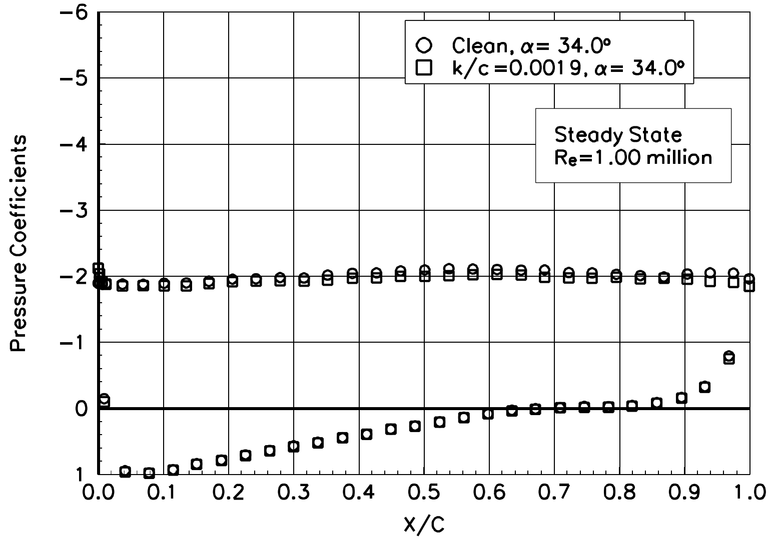

Figure 69. α = 34.0°

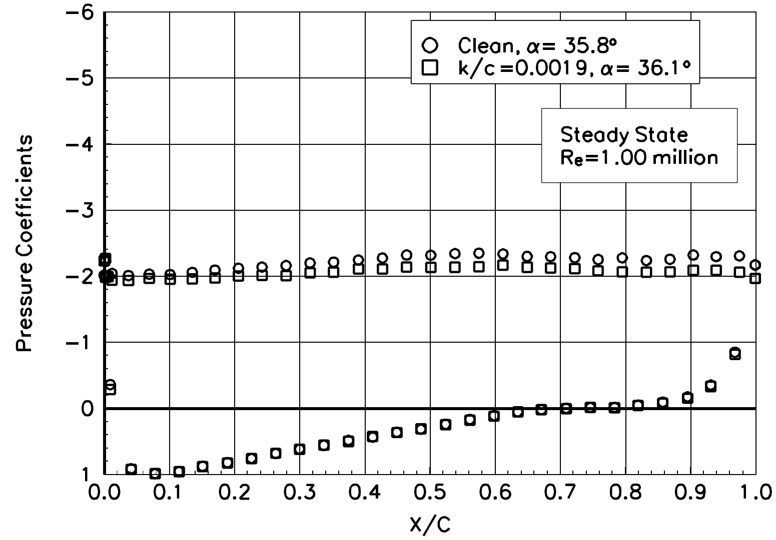

Figure 70. α = 35.8°

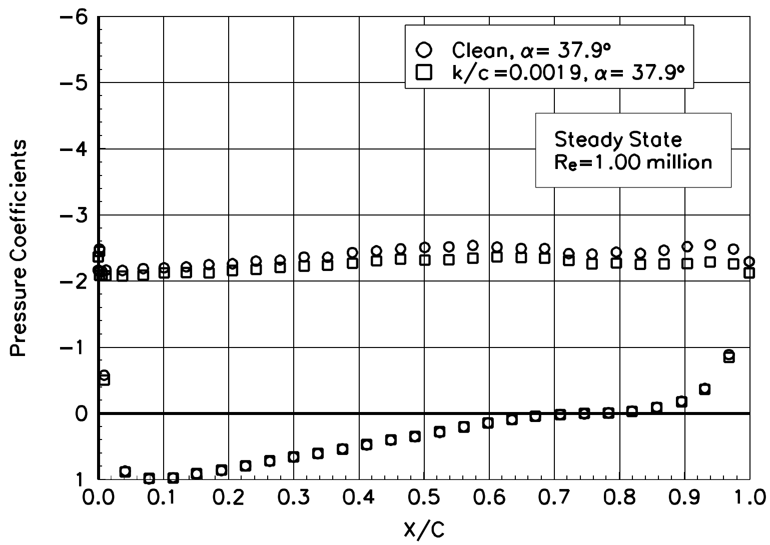

Figure 71. α = 37.9°

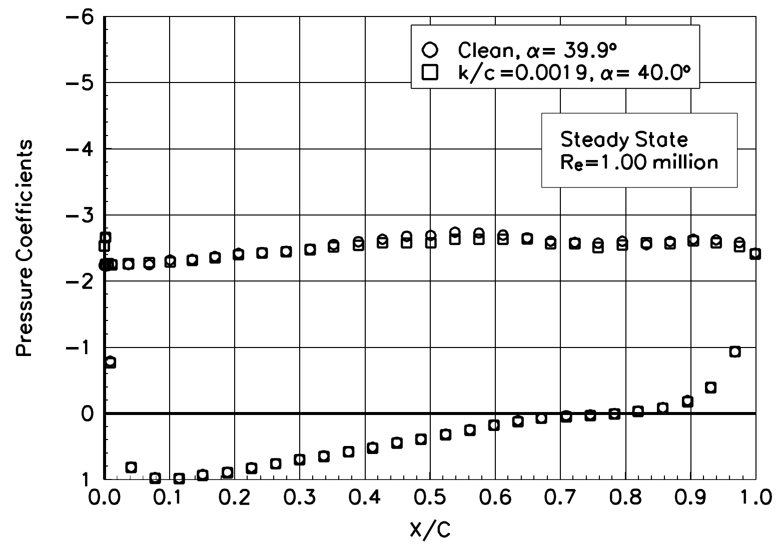

Figure 72. α = 39.9°

S801

Pressure Distributions, Steady State, Re = 1.25 million

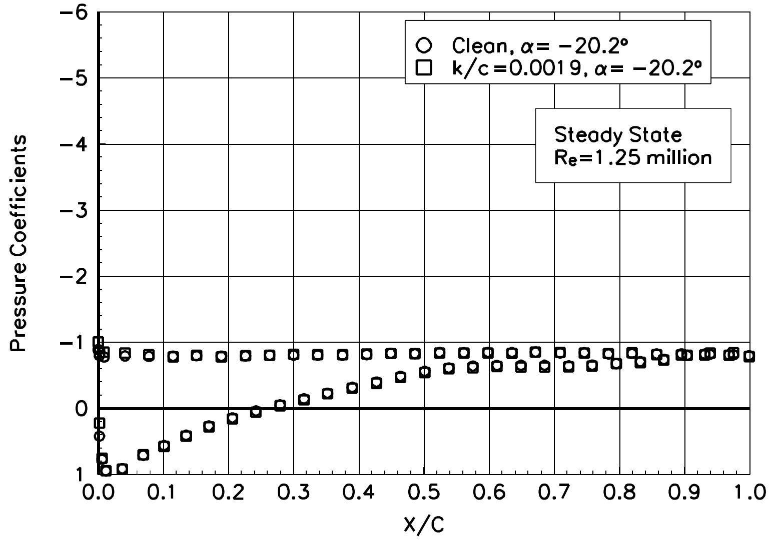

Figure 73. α **= -20.2°**

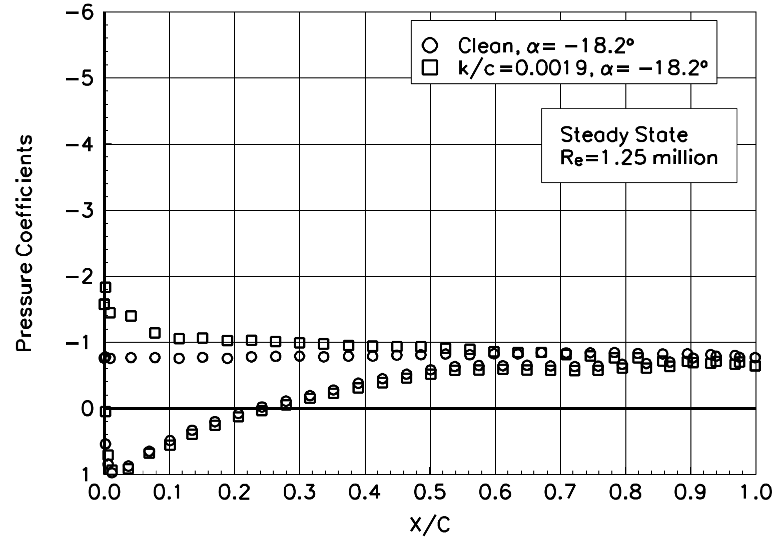

Figure 74. α **= -18.2°**

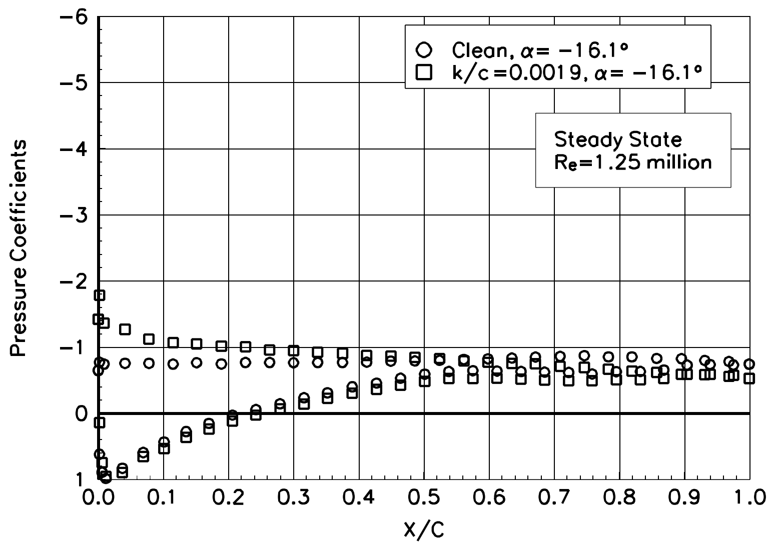

Figure 75. α **= -16.1°**

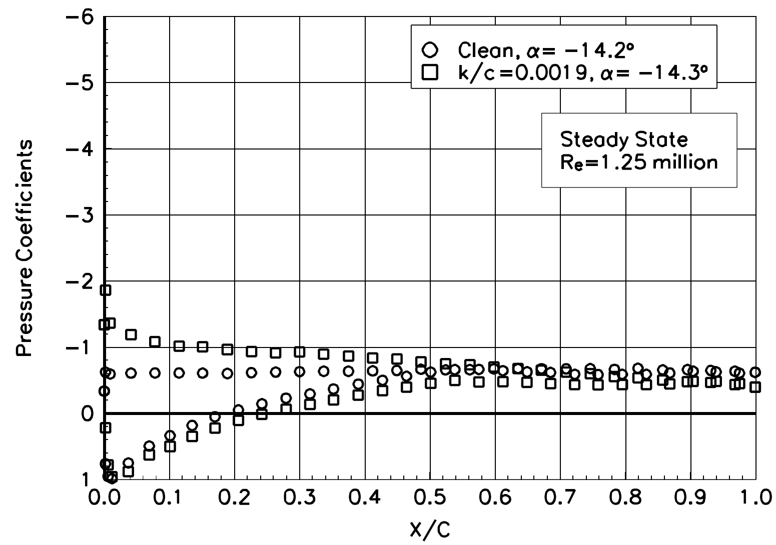

Figure 76. α **= -14.2°**

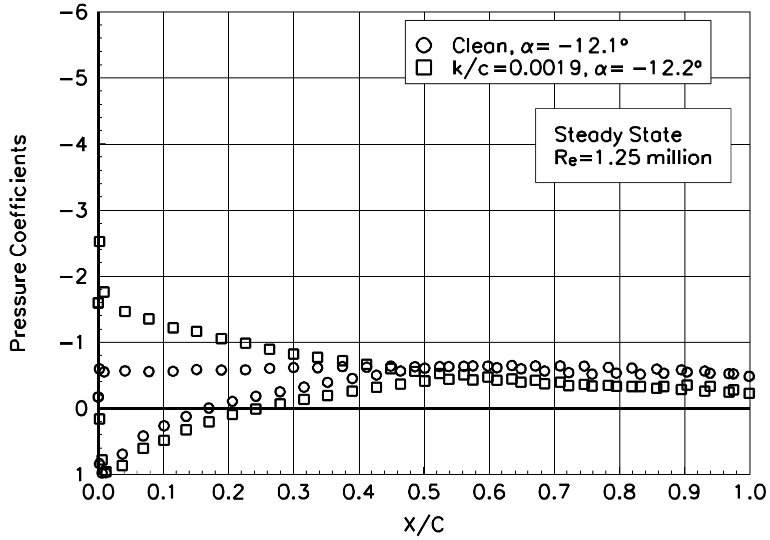

Figure 77. α = -12.1°

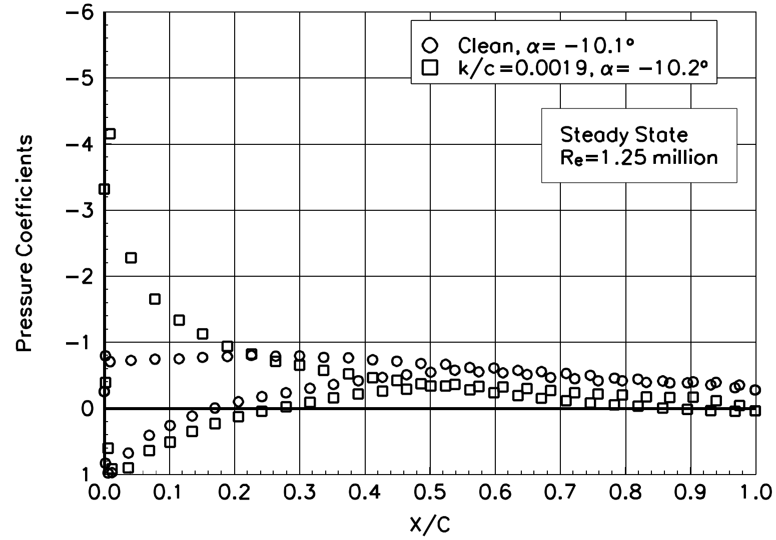

Figure 78. α = -10.1°

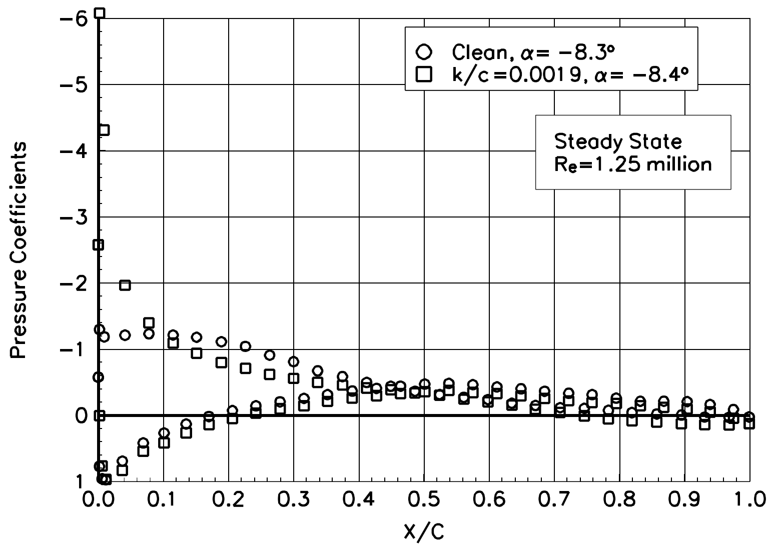

Figure 79. α = -8.3°

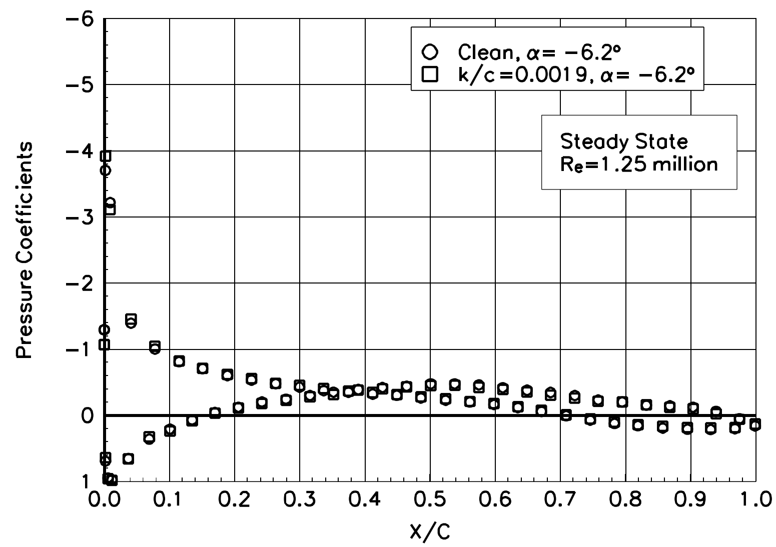

Figure 80. α = -6.2°

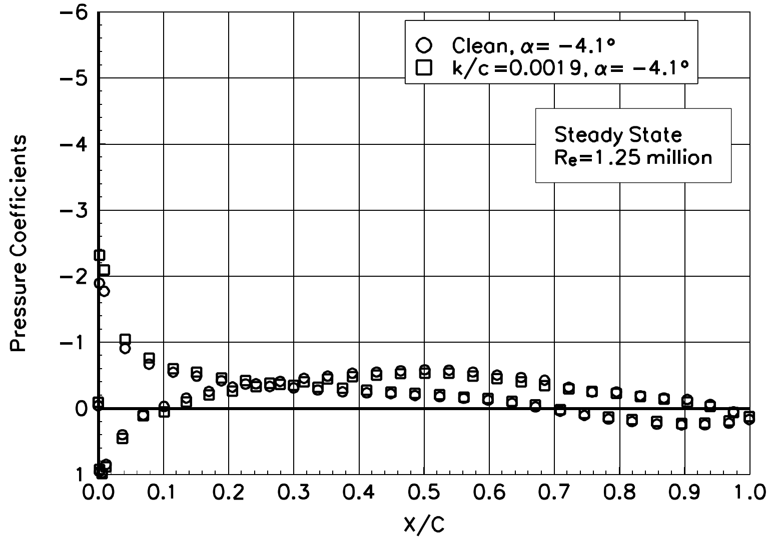

Figure 81. α = -4.1°

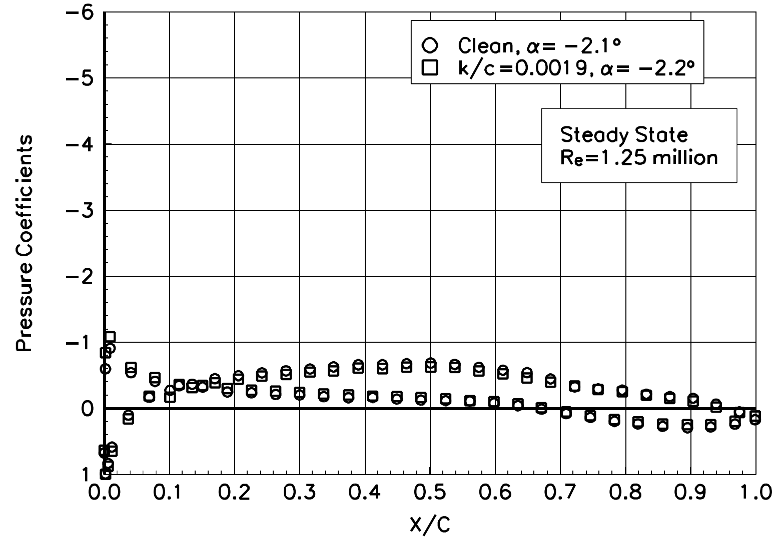

Figure 82. α = -2.1°

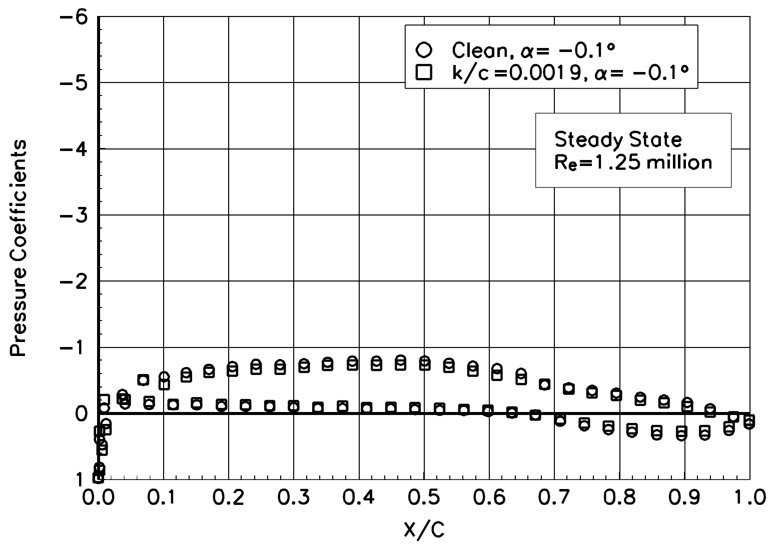

Figure 83. α = -0.1°

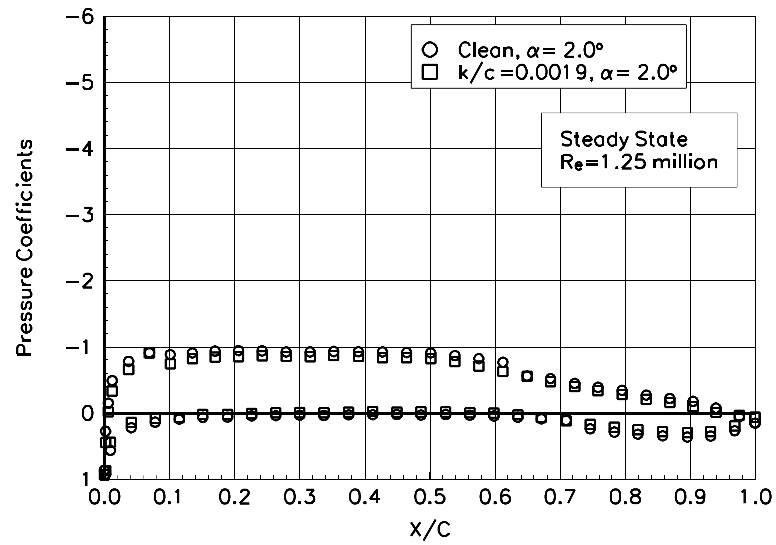

Figure 84. α = 2.0°

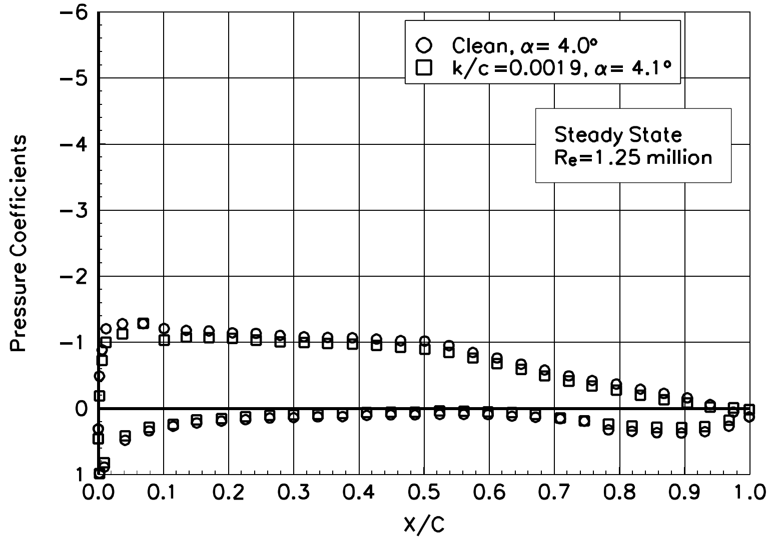

Figure 85. α = 4.0°

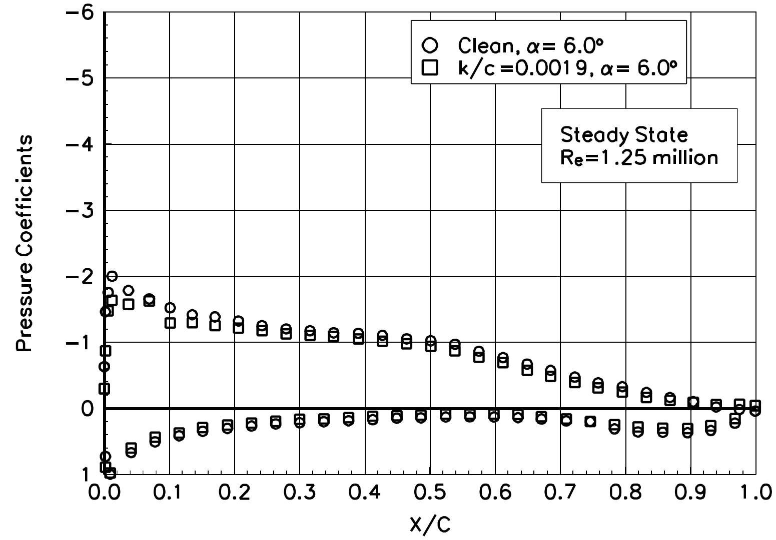

Figure 86. α = 6.0°

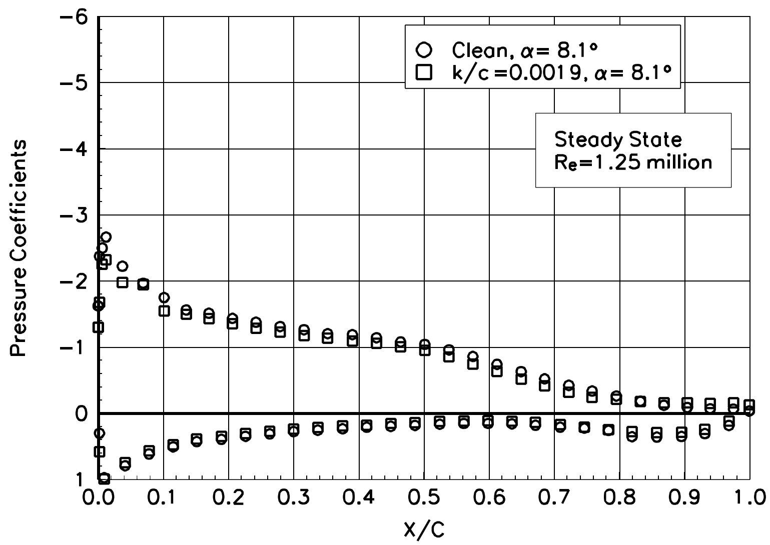

Figure 87. α = 8.1°

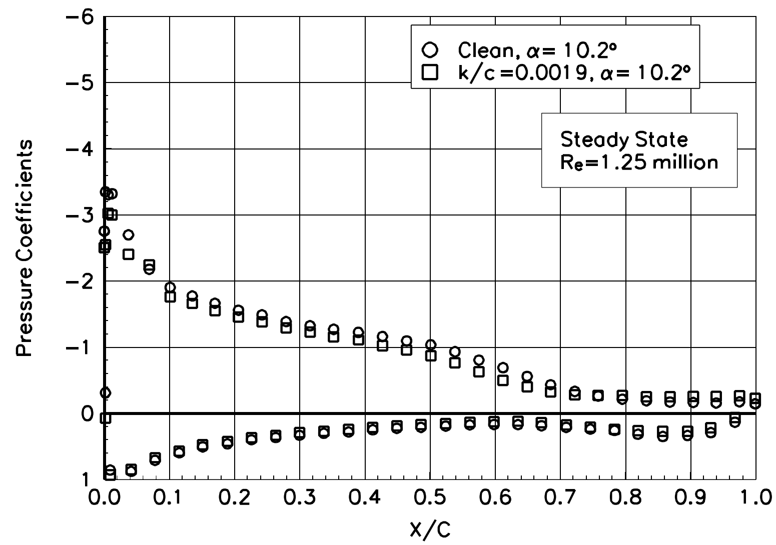

Figure 88. α = 10.2°

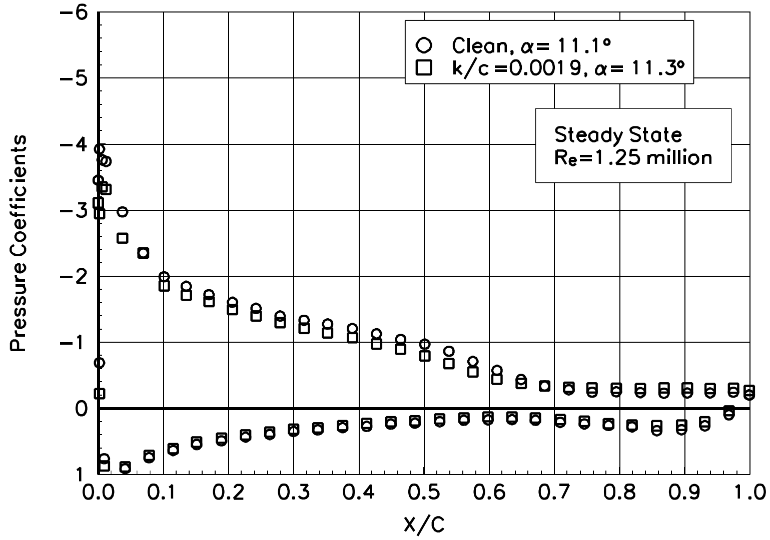

Figure 89. α = 11.1°

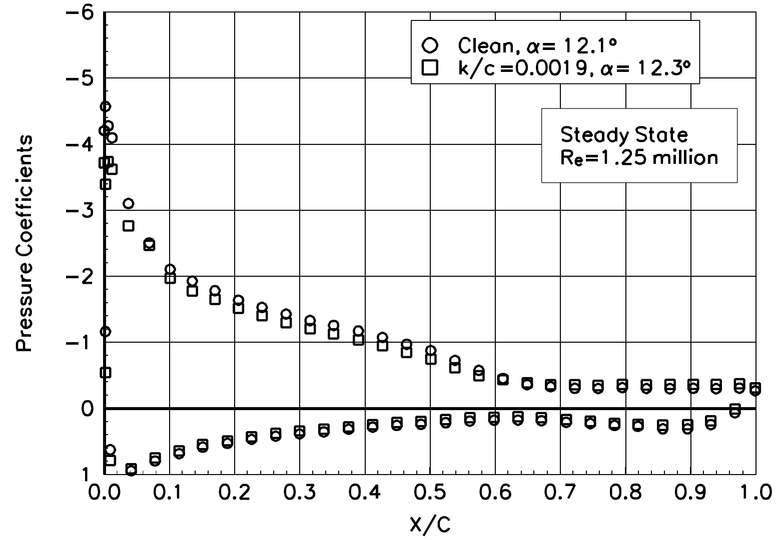

Figure 90. α = 12.1°

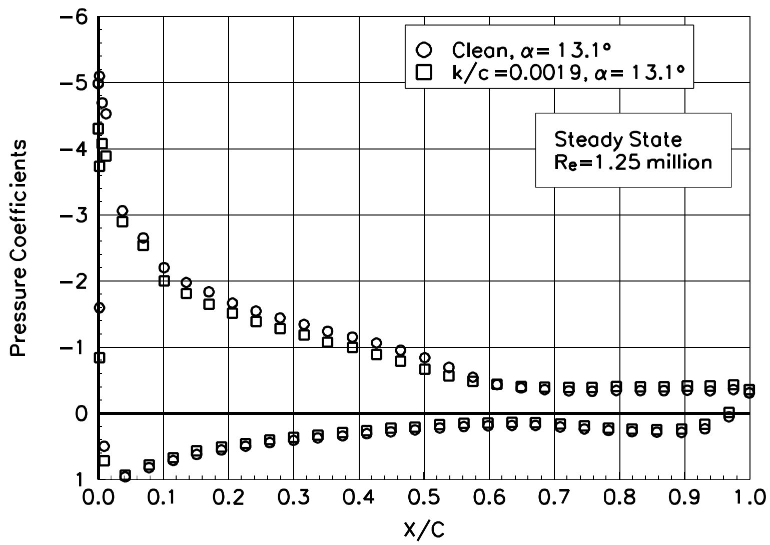

Figure 91. α = 13.1°

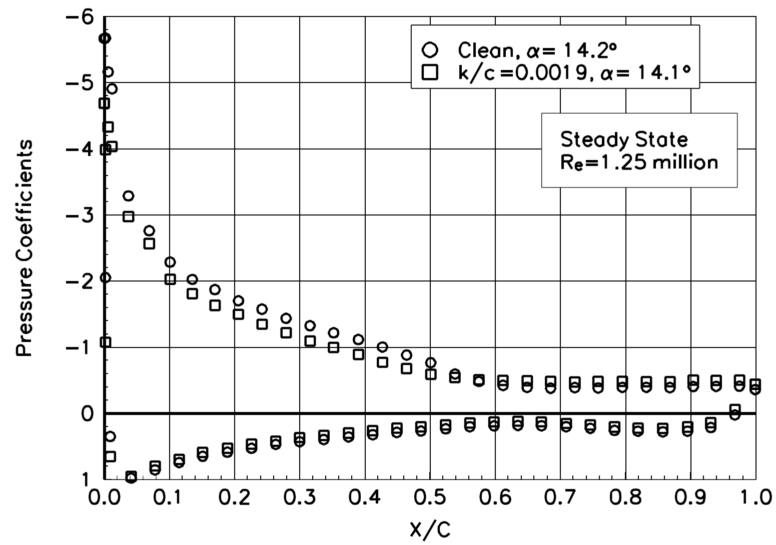

Figure 92. α = 14.2°

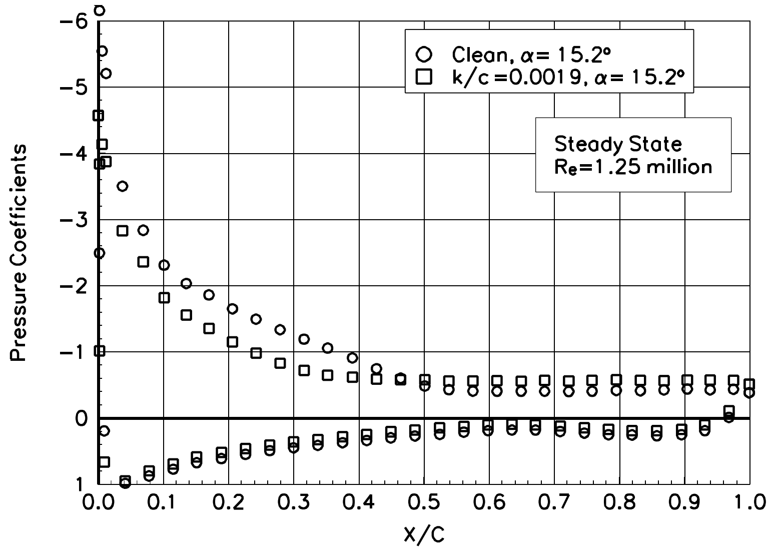

Figure 93. α = 15.2°

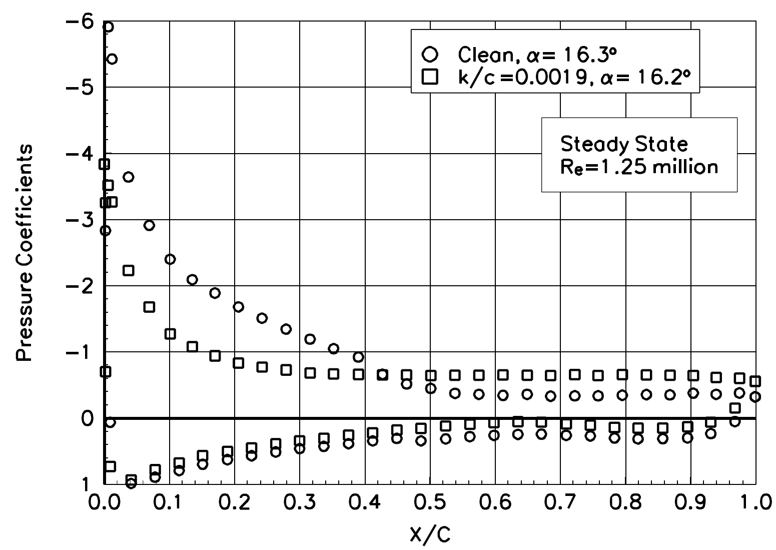

Figure 94. α = 16.3°

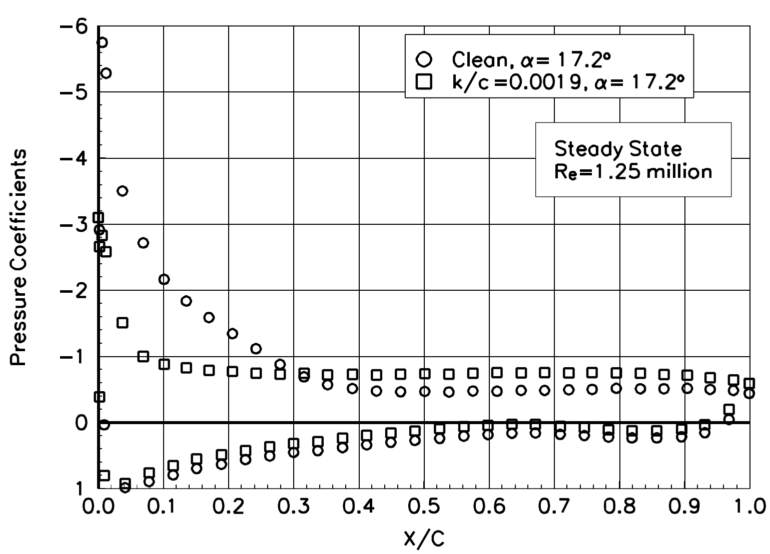

Figure 95. α = 17.2°

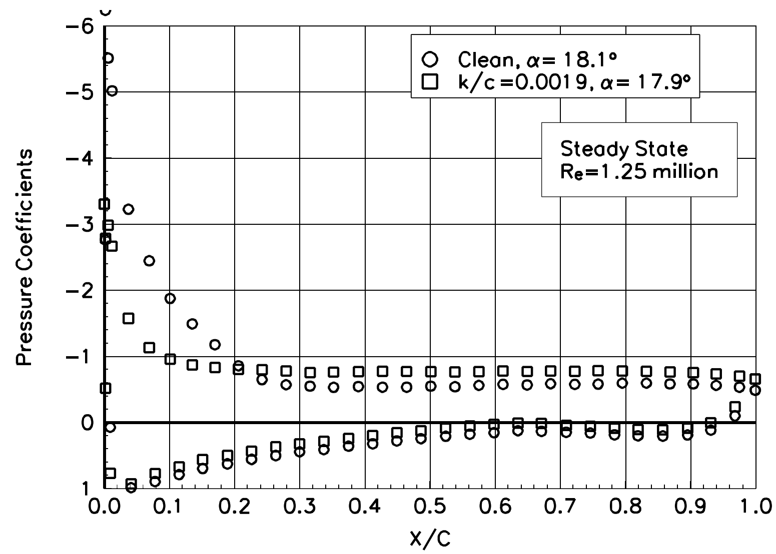

Figure 96. α = 18.1°

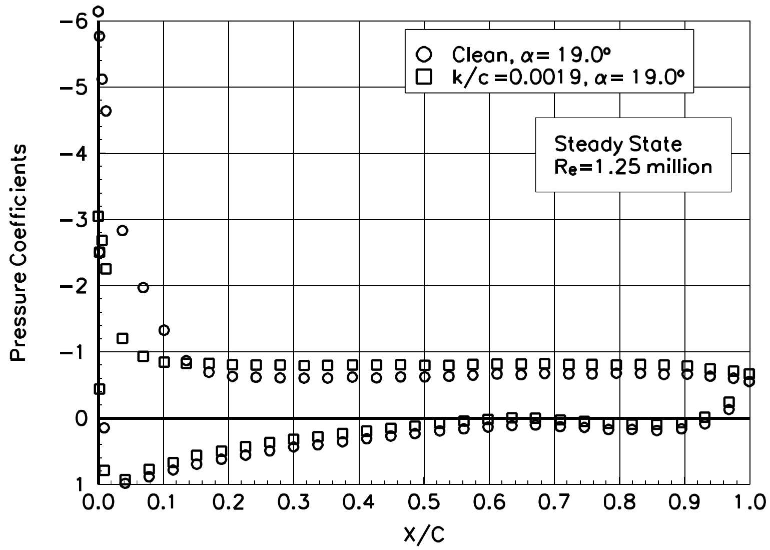

Figure 97. α = 19.0°

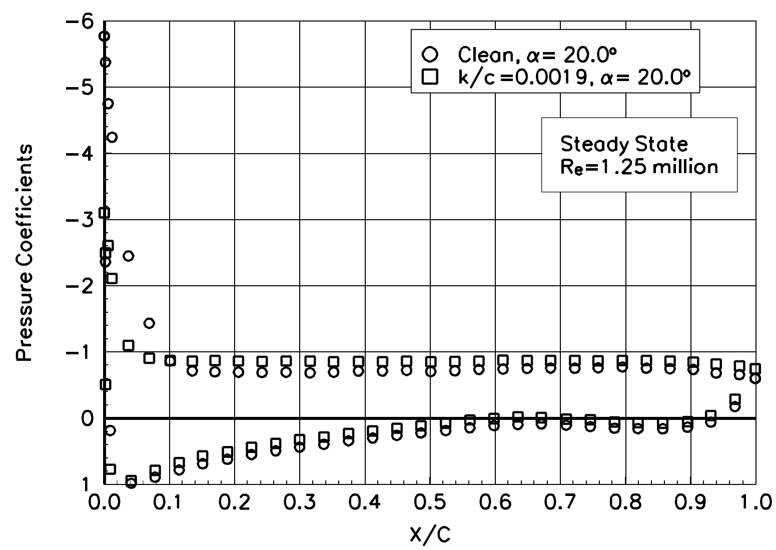

Figure 98. α = 20.0°

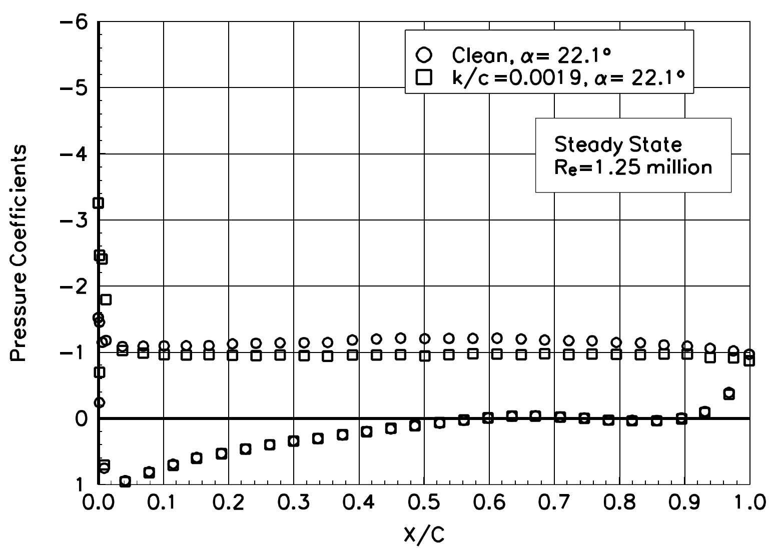

Figure 99. α = 22.1°

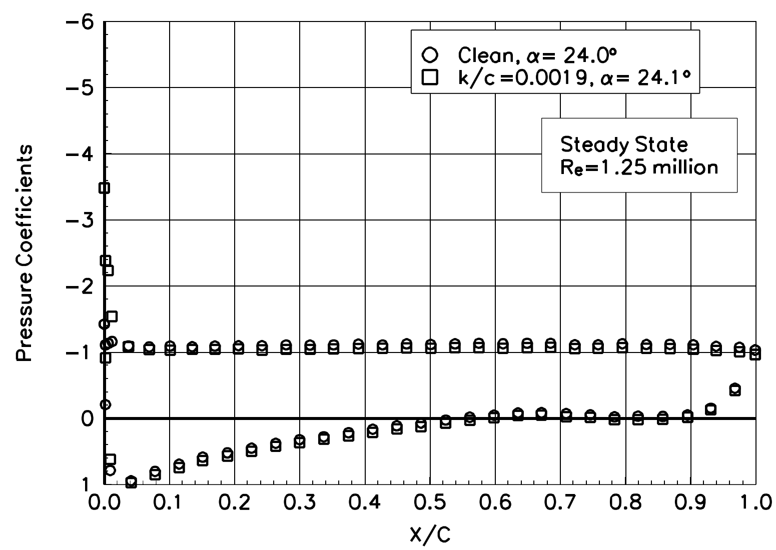

Figure 100. α = 24.0°

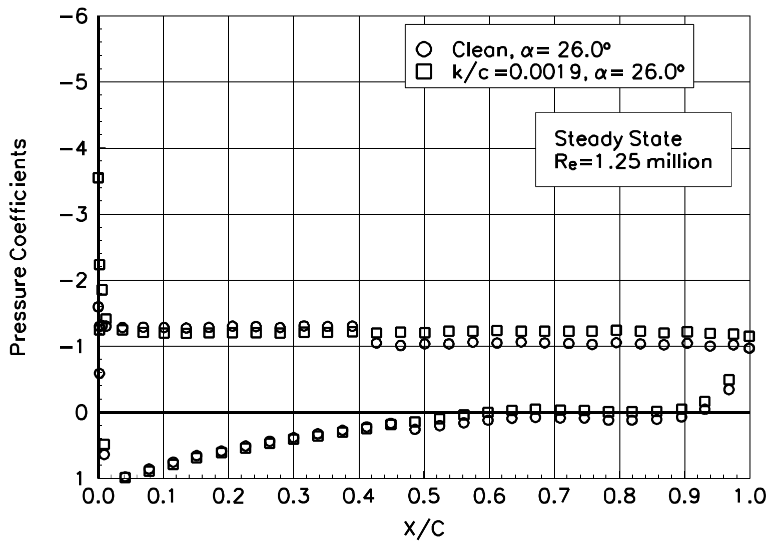

Figure 101. α **= 26.0°**

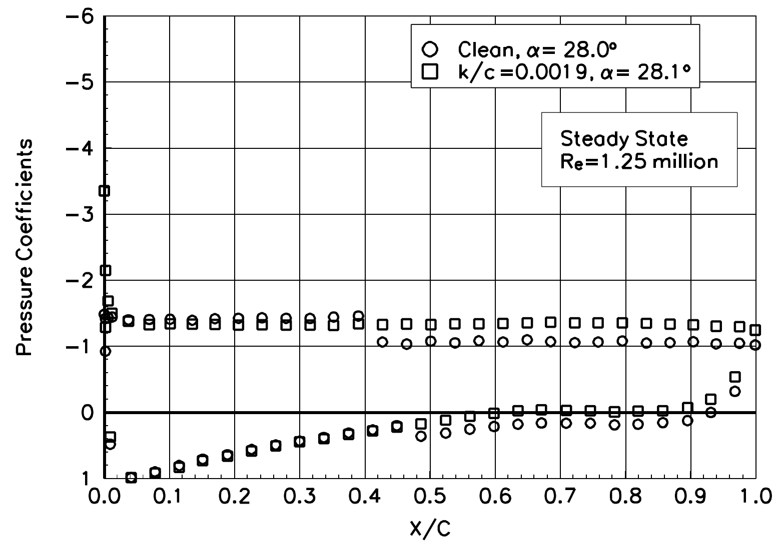

Figure 102. α **= 28.0°**

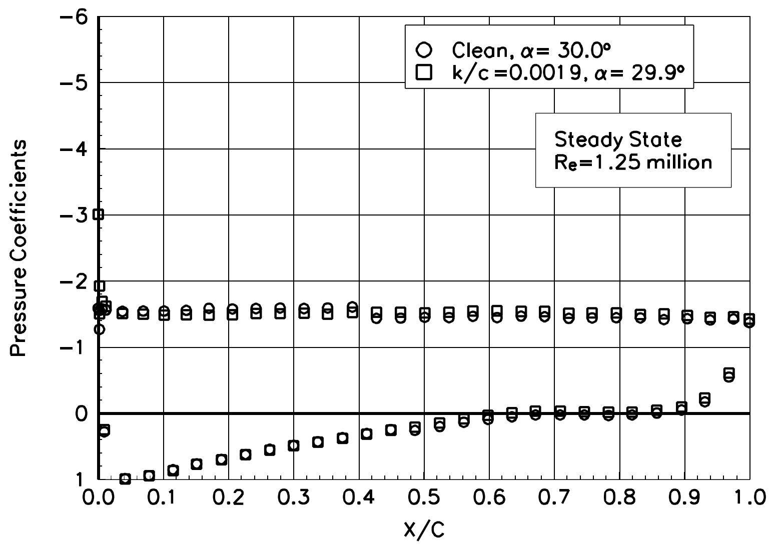

Figure 103. α **= 30.0°**

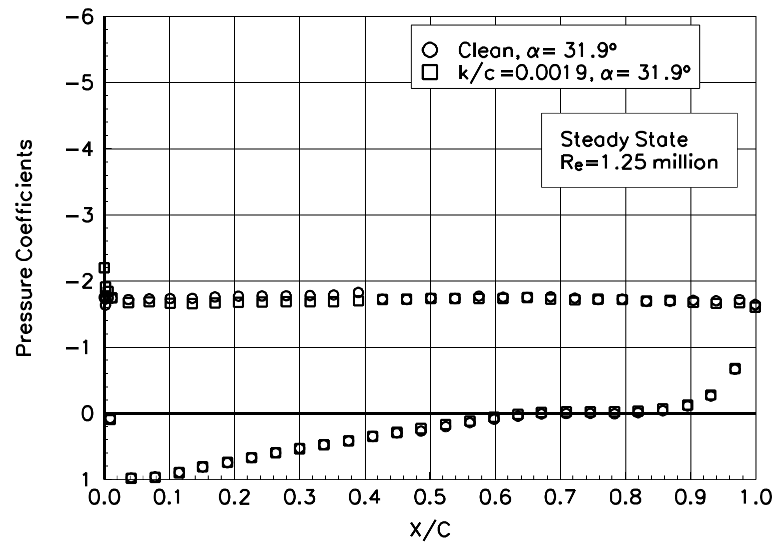

Figure 104. α **= 31.9°**

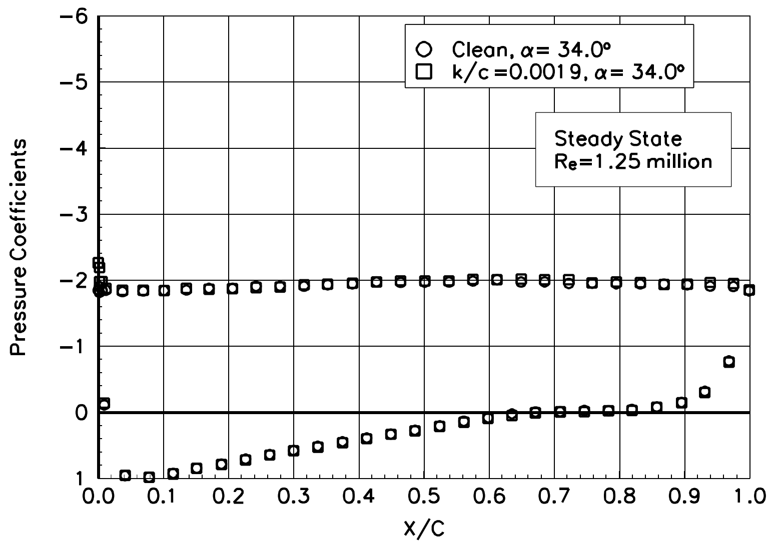

Figure 105. α = 34.0°

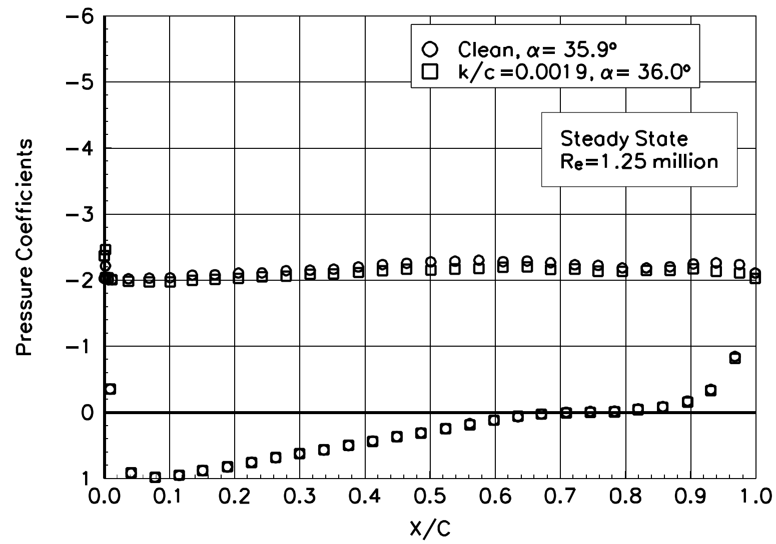

Figure 106. α = 35.9°

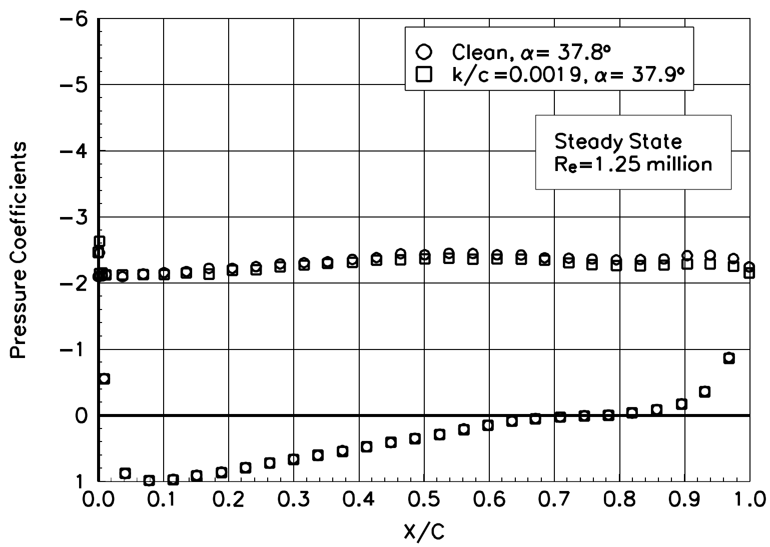

Figure 107. α = 37.8°

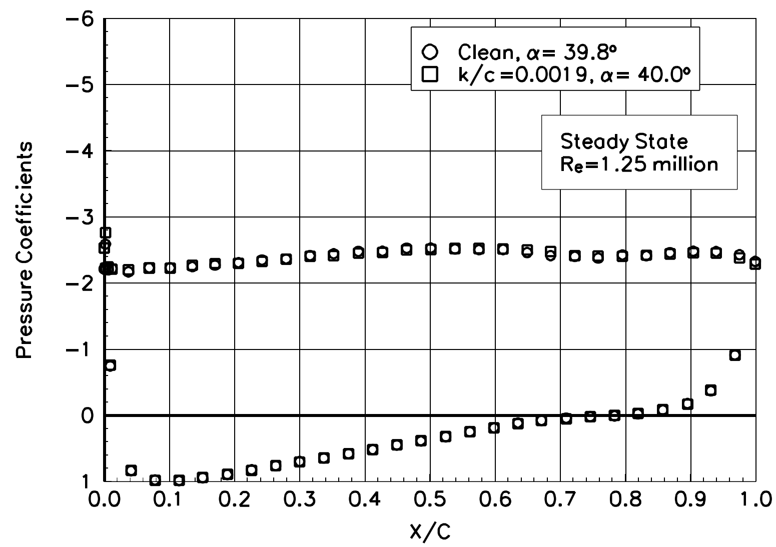

Figure 108. α = 39.8°

S801

Pressure Distributions, Steady State, Re = 1.5 million

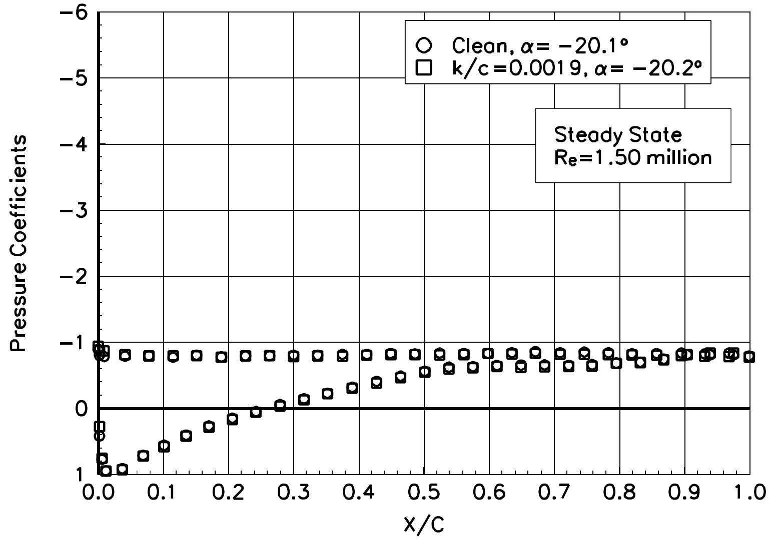

Figure 109. α **= -20.1°**

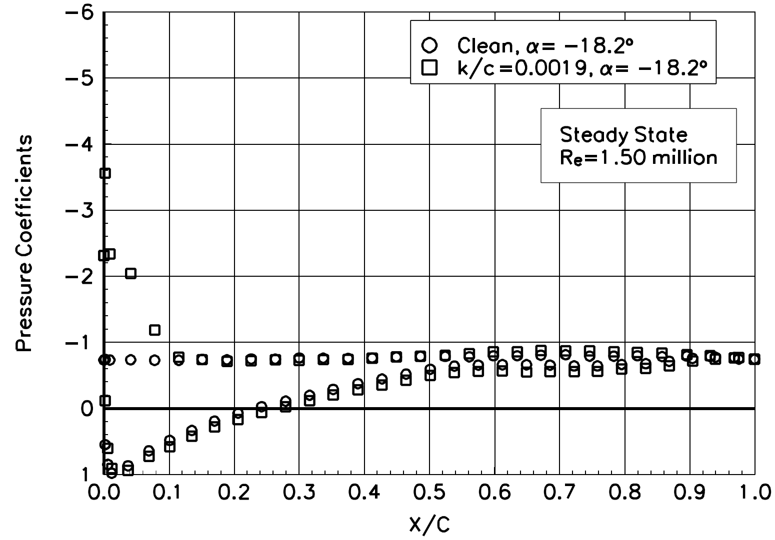

Figure 110. α **= -18.2°**

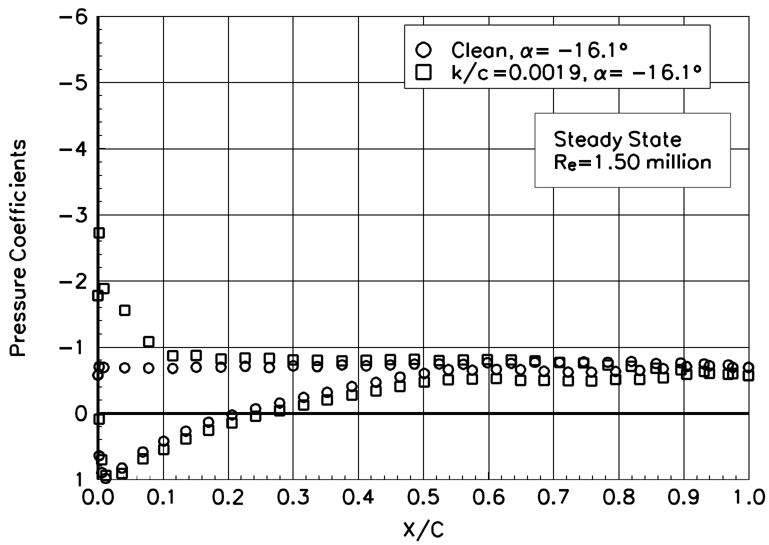

Figure 111. α **= -16.1°**

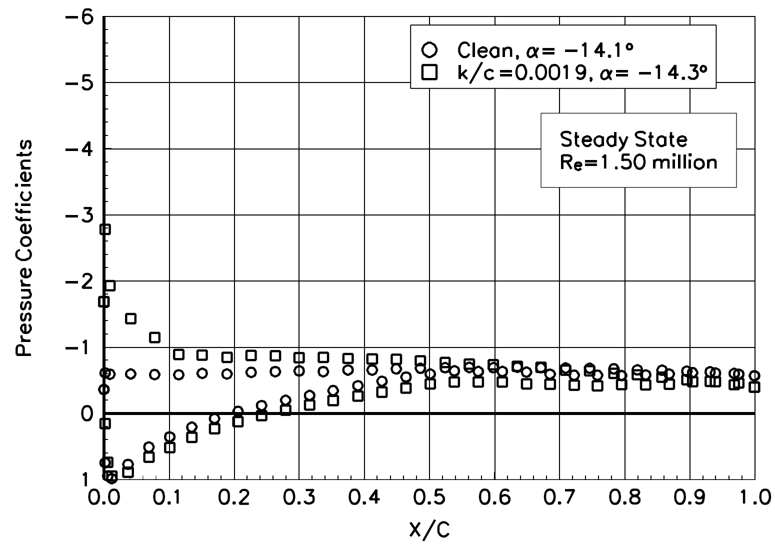

Figure 112. α **= -14.1°**

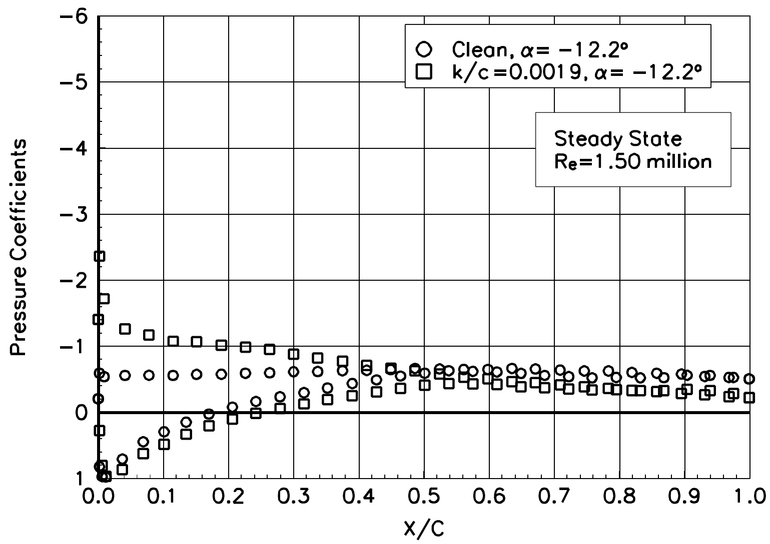

Figure 113. α **= -12.2°**

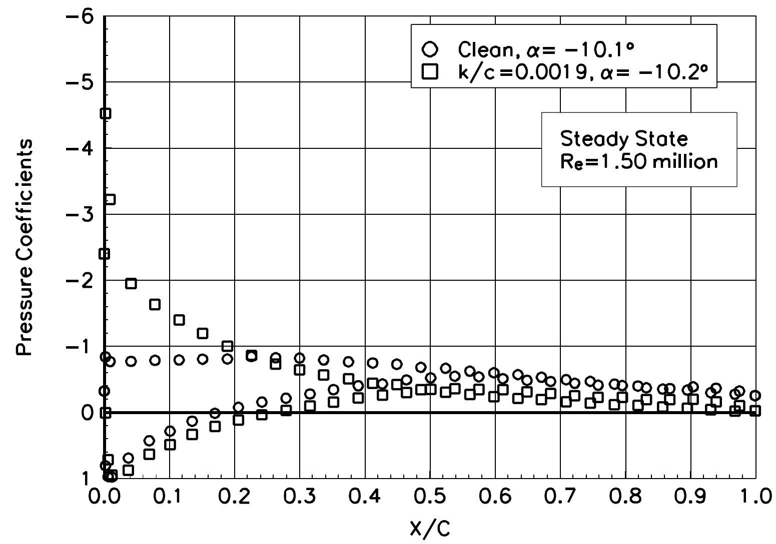

Figure 114. α **= -10.1°**

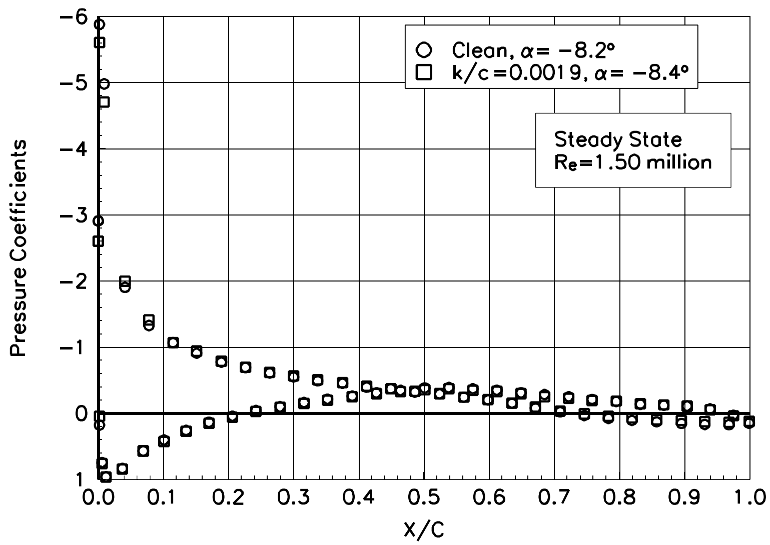

Figure 115. α **= -8.2°**

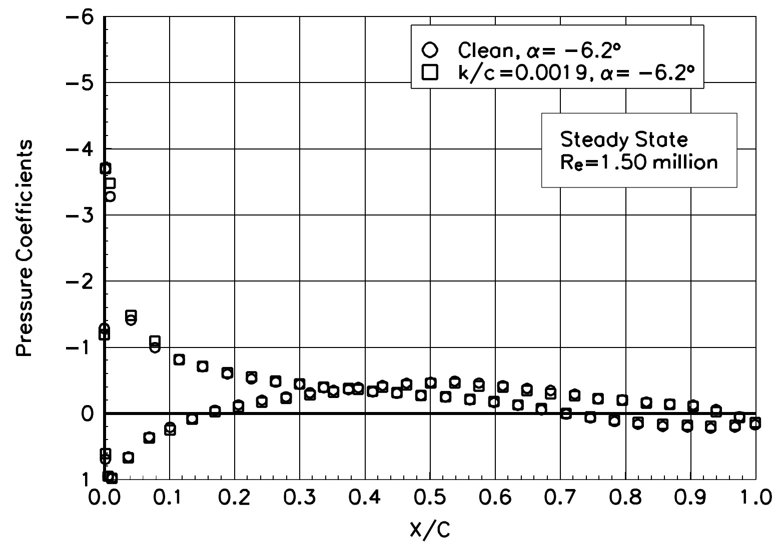

Figure 116. α **= -6.2°**

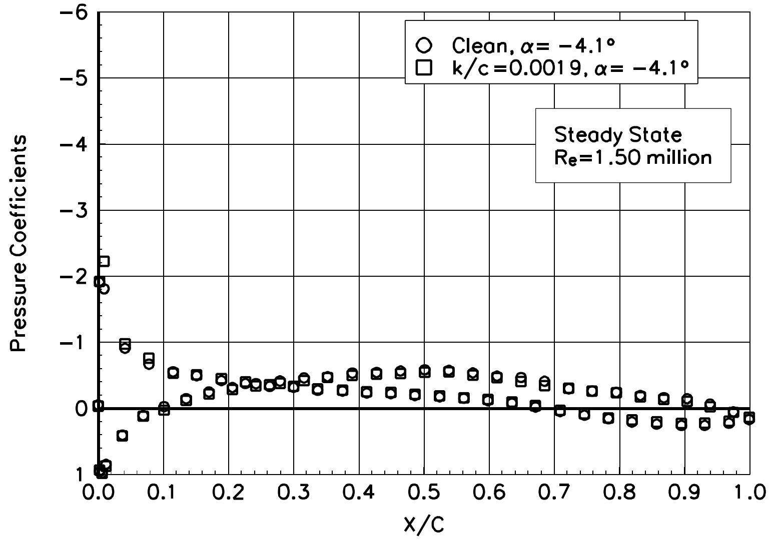

Figure 117. α **= -4.1°**

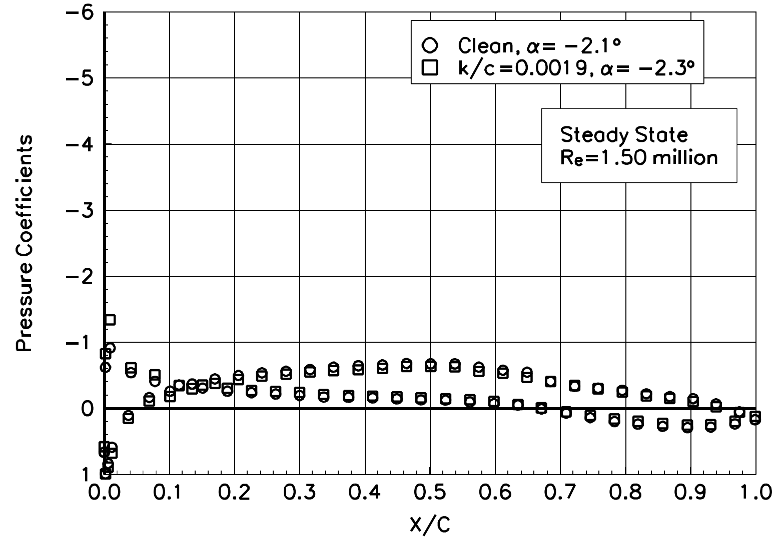

Figure 118. α **= -2.1°**

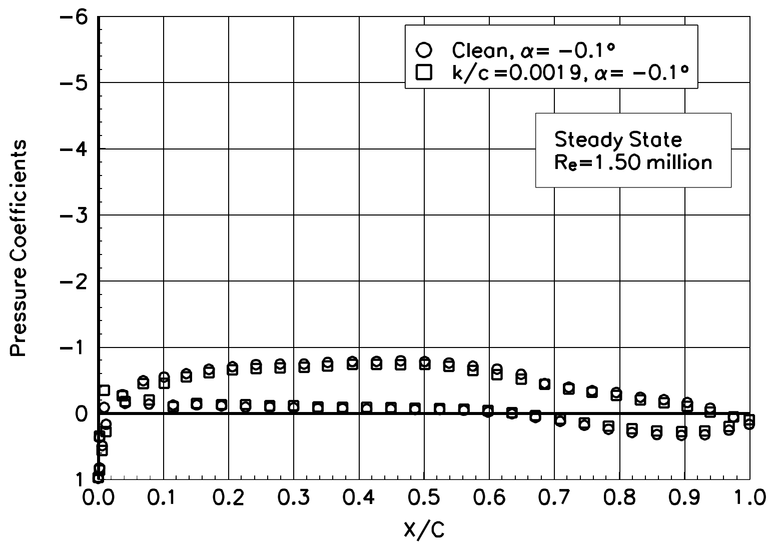

Figure 119. α **= -0.1°**

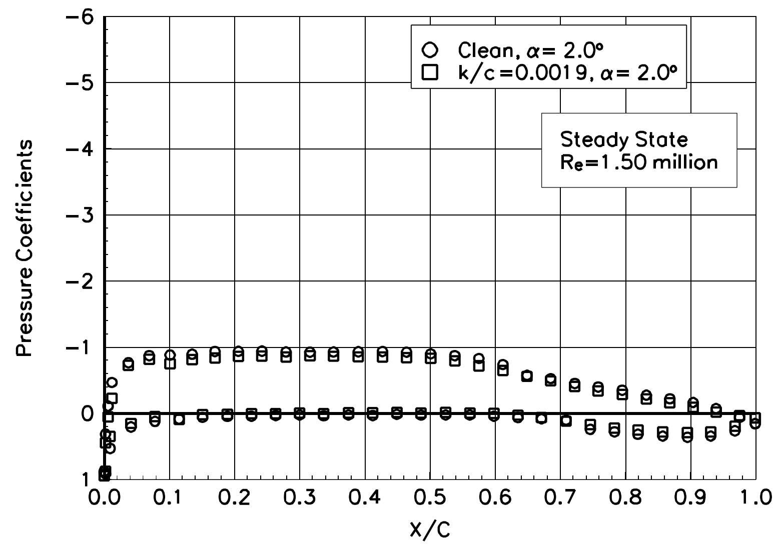

Figure 120. α **= 2.0°**

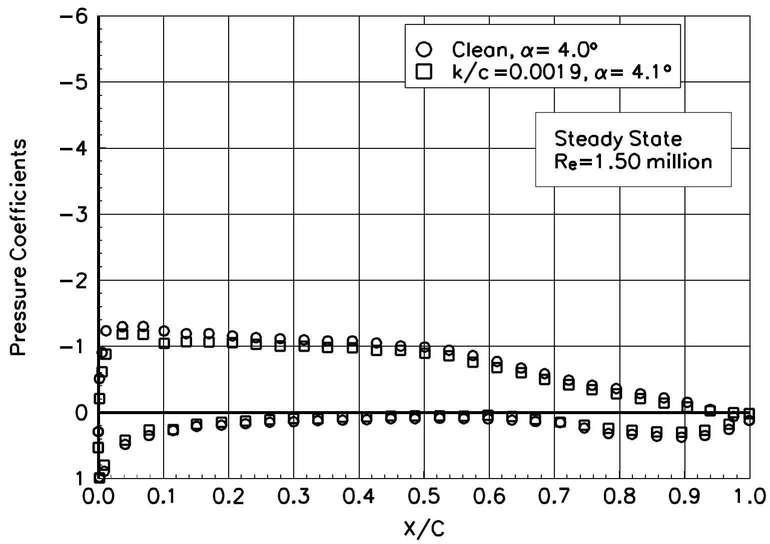

Figure 121. α = 4.0°

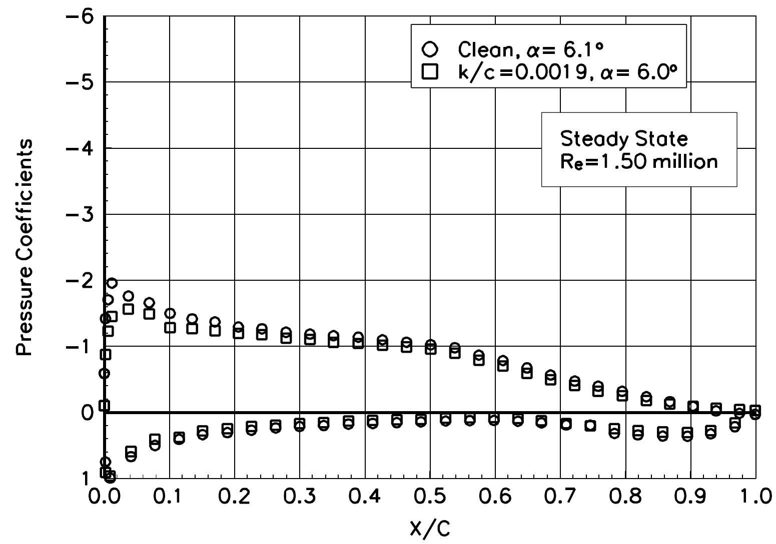

Figure 122. α = 6.1°

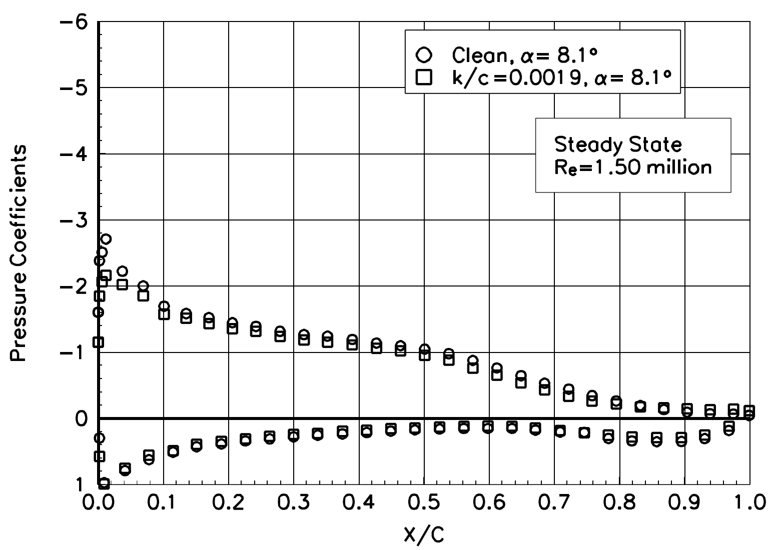

Figure 123. α = 8.1°

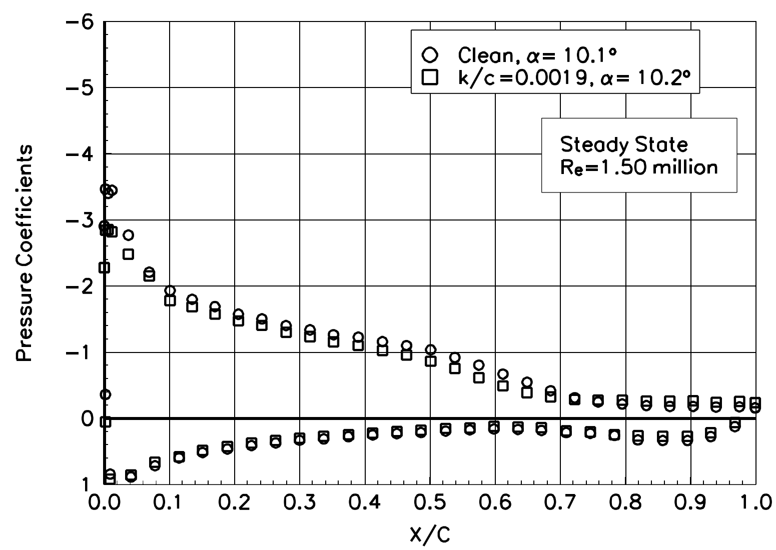

Figure 124. α = 10.1°

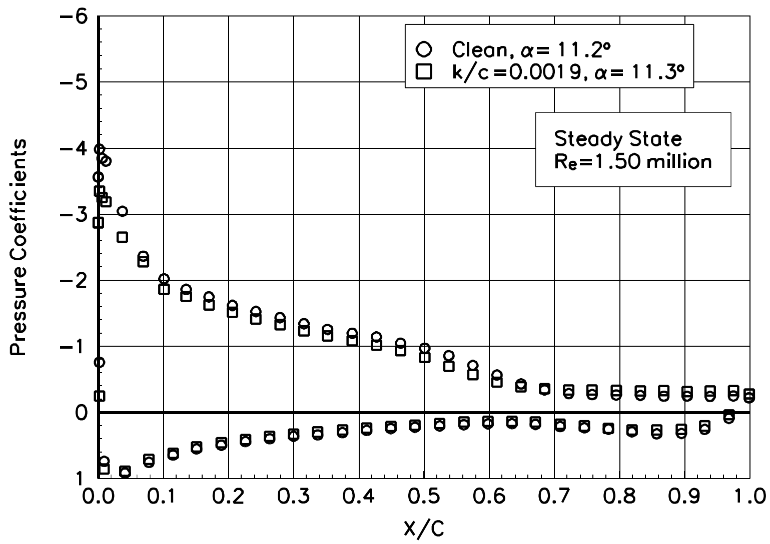

Figure 125. α **= 11.2°**

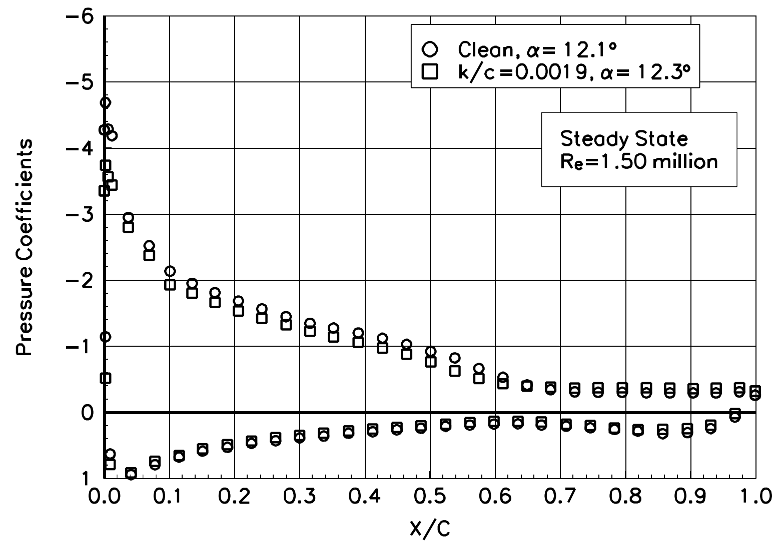

Figure 126. α **= 12.1°**

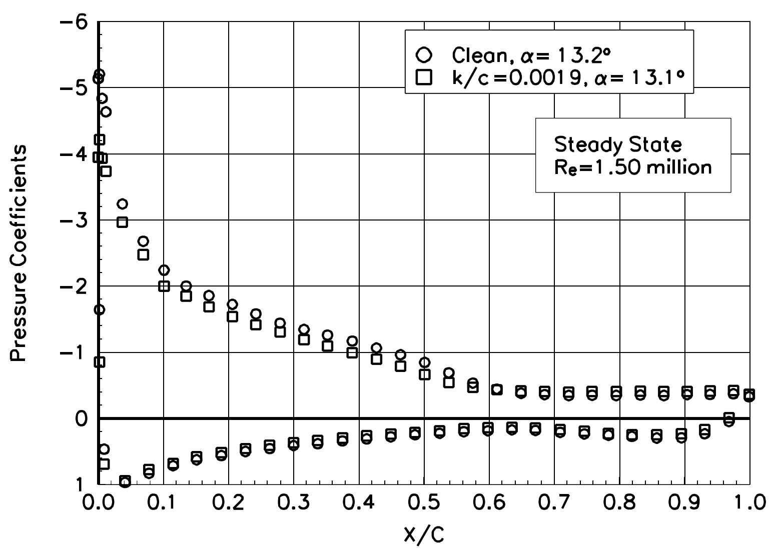

Figure 127. α **= 13.2°**

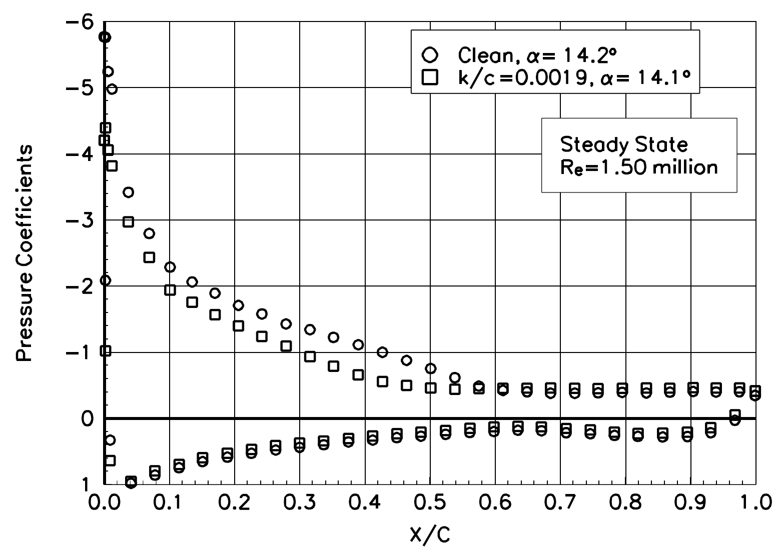

Figure 128. α **= 14.2°**

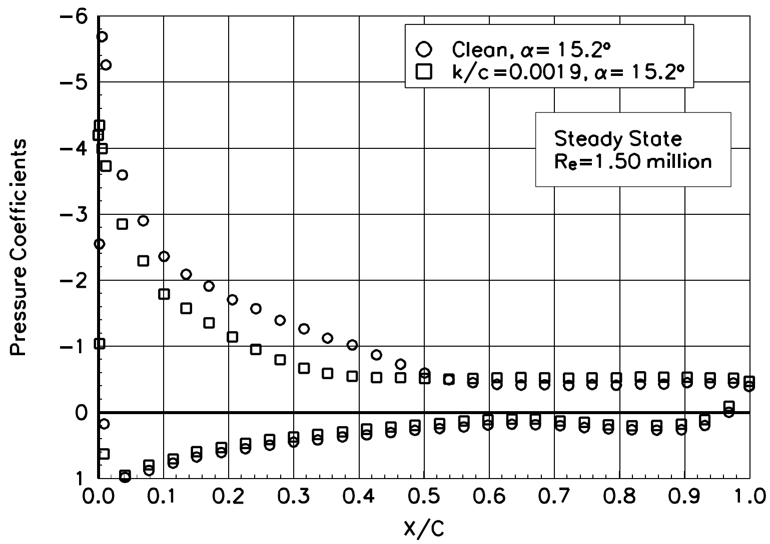

Figure 129. $\alpha = 15.2°$

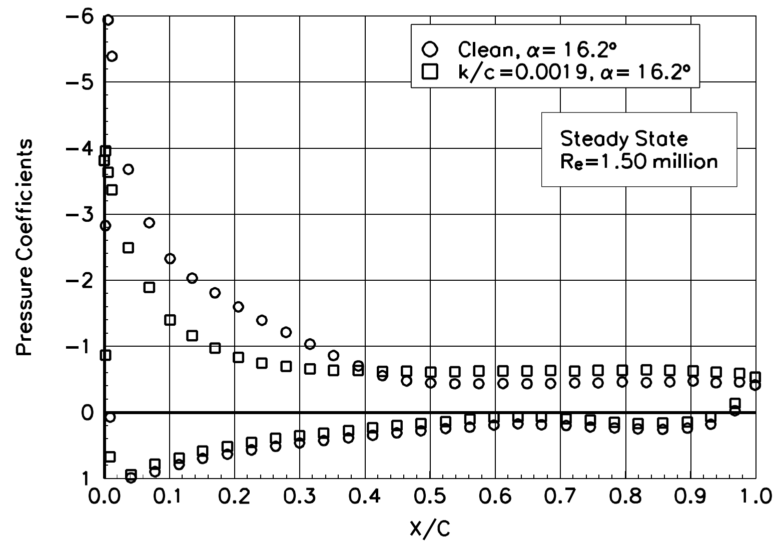

Figure 130. $\alpha = 16.2°$

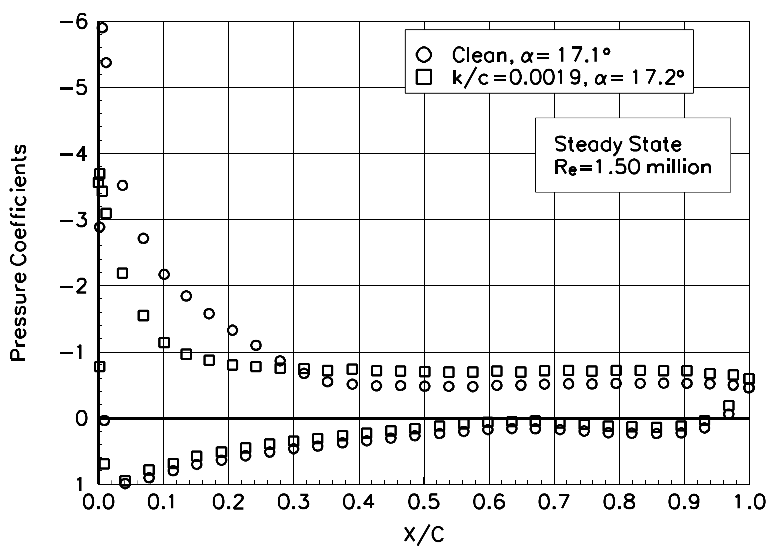

Figure 131. $\alpha = 17.1°$

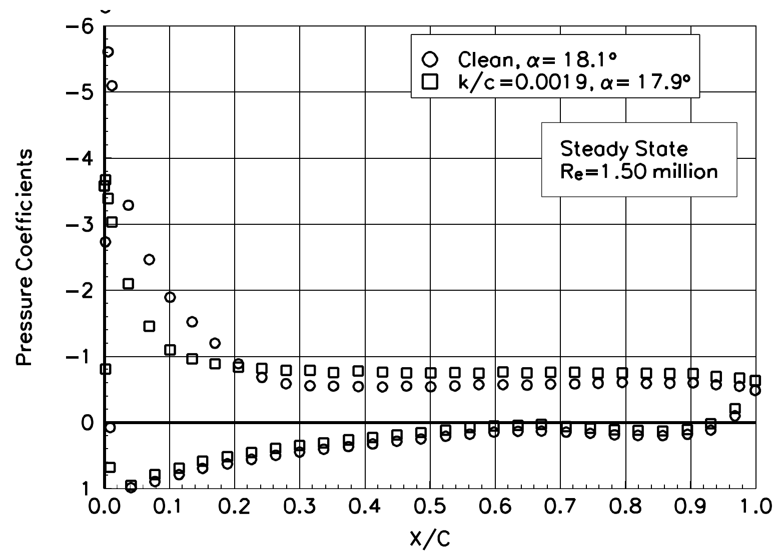

Figure 132. $\alpha = 18.1°$

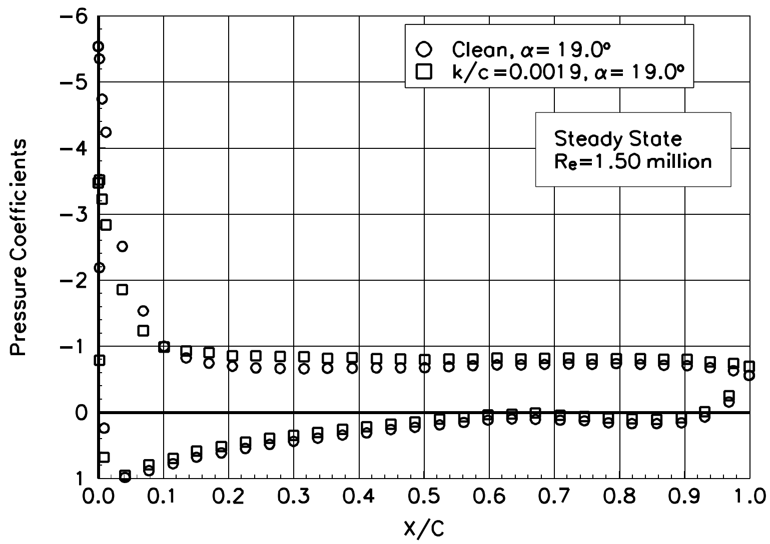

Figure 133. $\alpha = 19.0°$

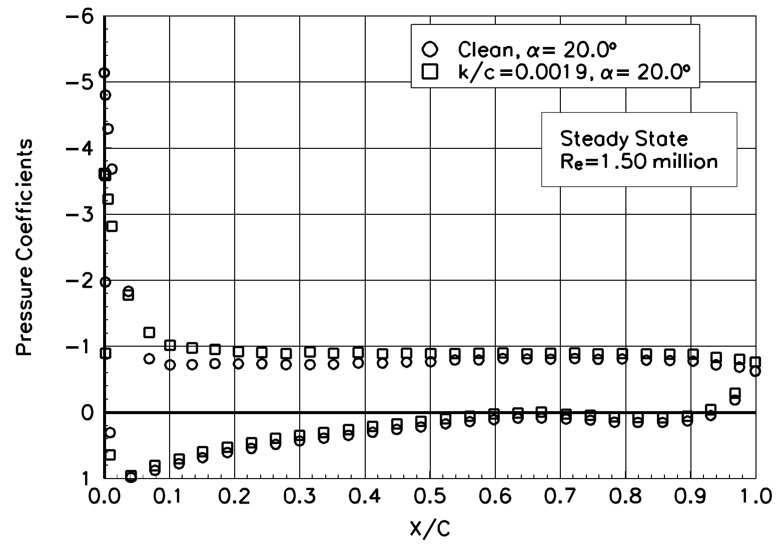

Figure 134. $\alpha = 20.0°$

Appendix C: Unsteady Integrated Coefficients

List of Figures

Unsteady Airfoil Characteristics

±5.5° Sine, Re = 0.75 million

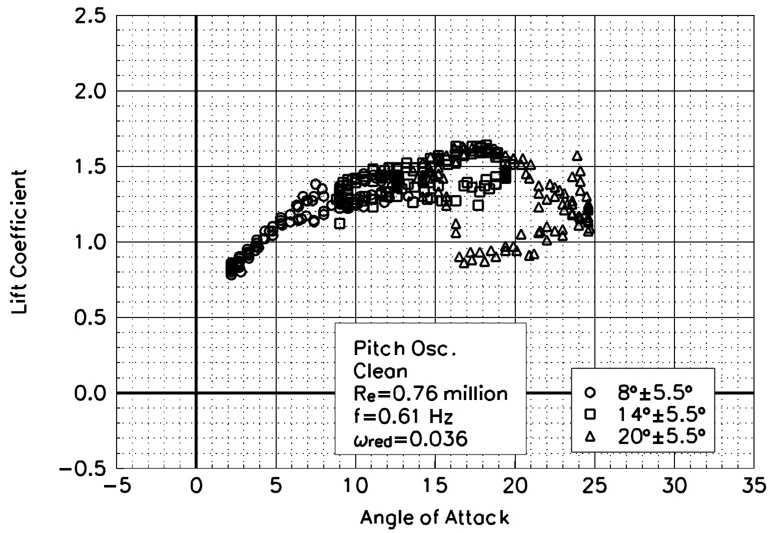

Figure C1. Lift coefficient vs α.

S801
Clean
Re=0.76 million
$\omega_{reduced}$=0.036

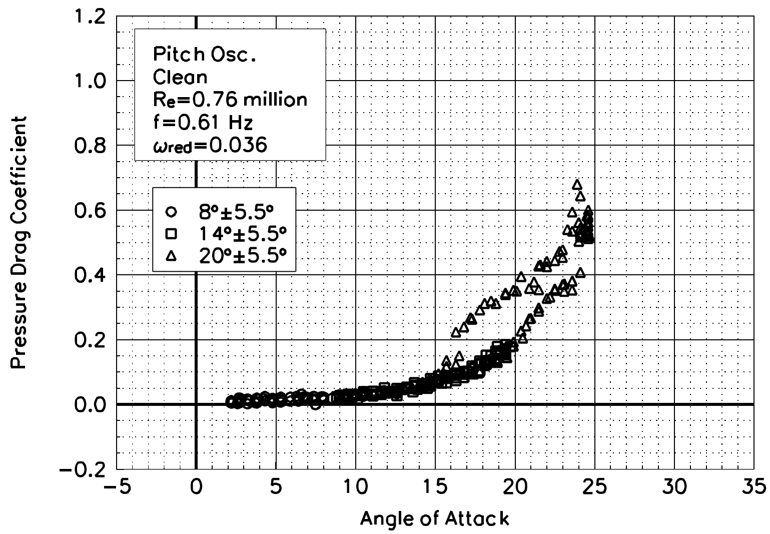

Figure C2. Pressure drag coefficient vs α.

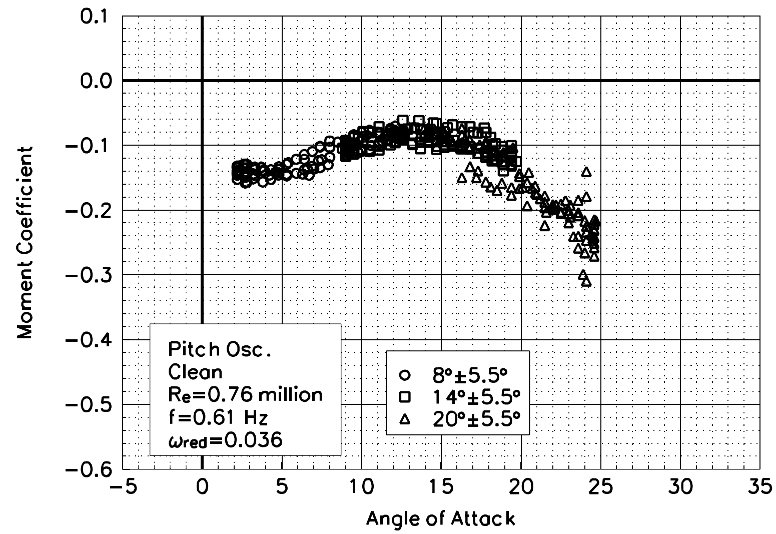

Figure C3. Moment coefficient vs α.

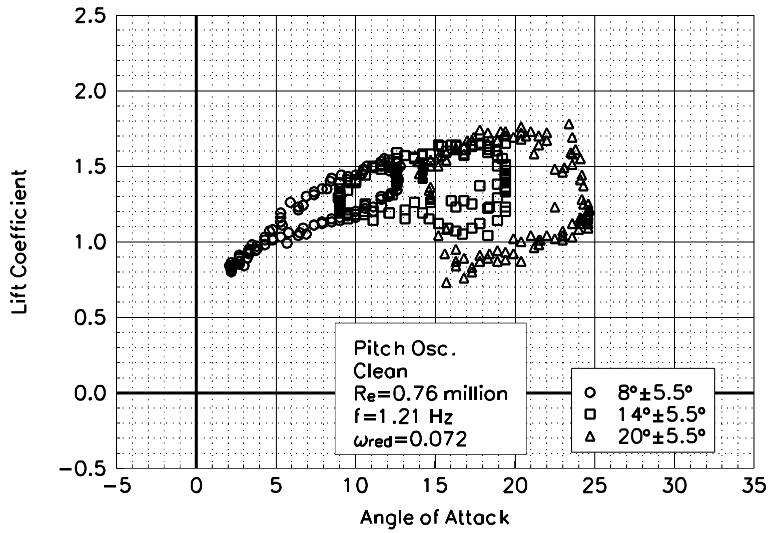

Figure C4. Lift coefficient vs α.

S801
Clean
Re=0.76 million
$\omega_{reduced}$=0.072

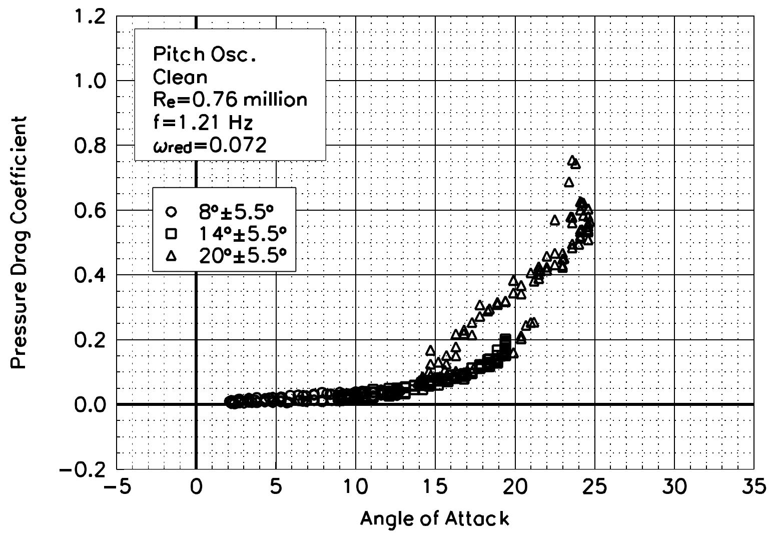

Figure C5. Pressure drag coefficient vs α.

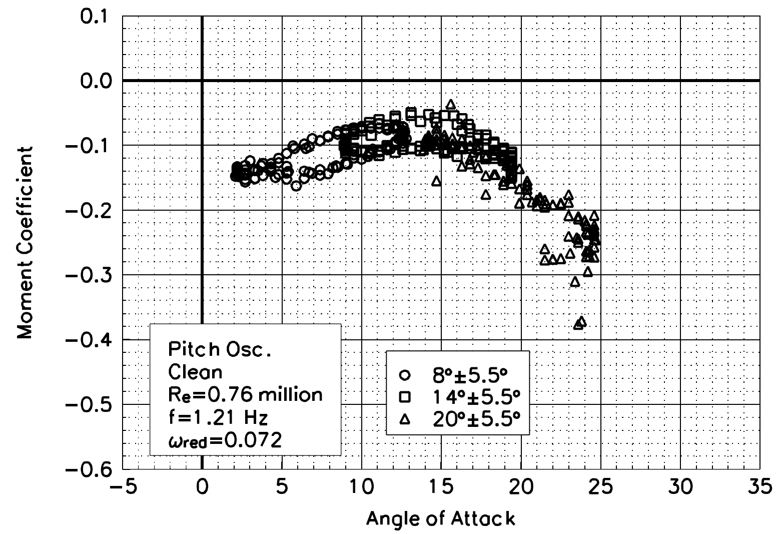

Figure C6. Moment coefficient vs α.

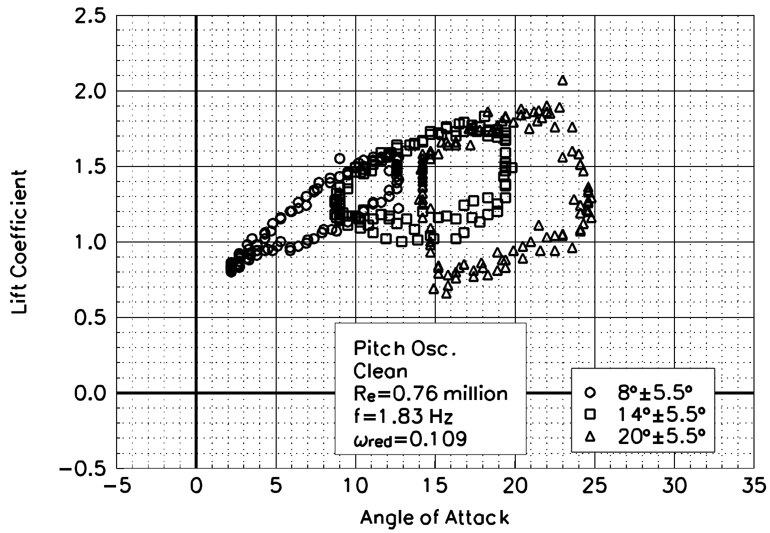

Figure C7. Lift coefficient vs α.

S801
Clean
Re=0.76 million
$\omega_{reduced}$=0.109

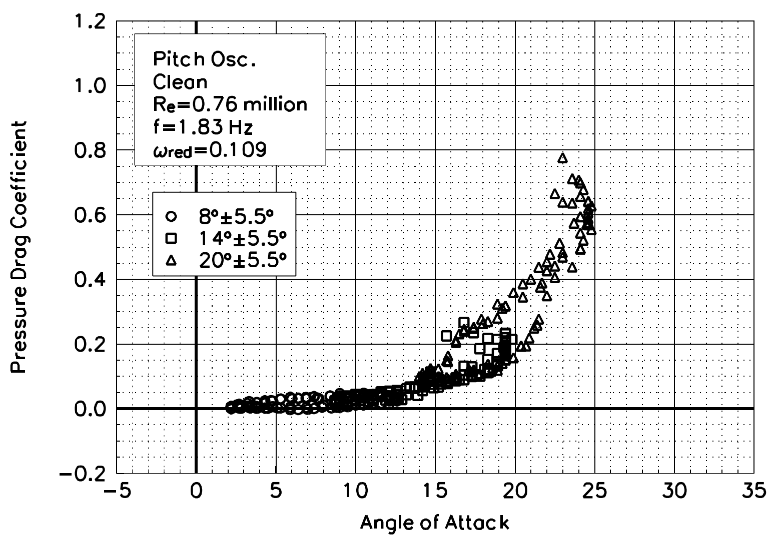

Figure C8. Pressure drag coefficient vs α.

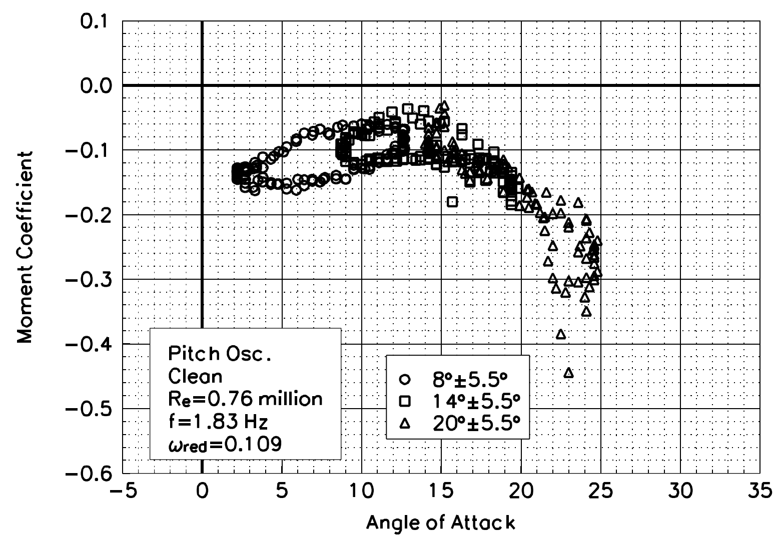

Figure C9. Moment coefficient vs α.

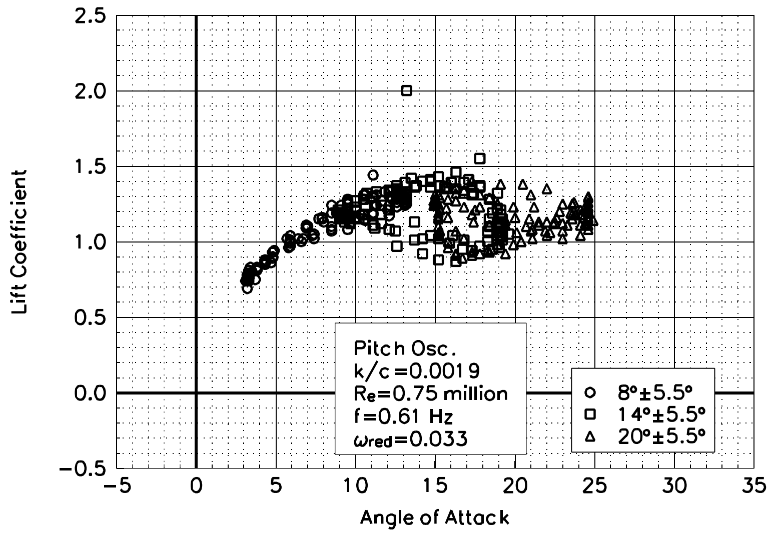

Figure C10. Lift coefficient vs α.

S801
LEGR
Re=0.75 million
$\omega_{reduced}$=0.033

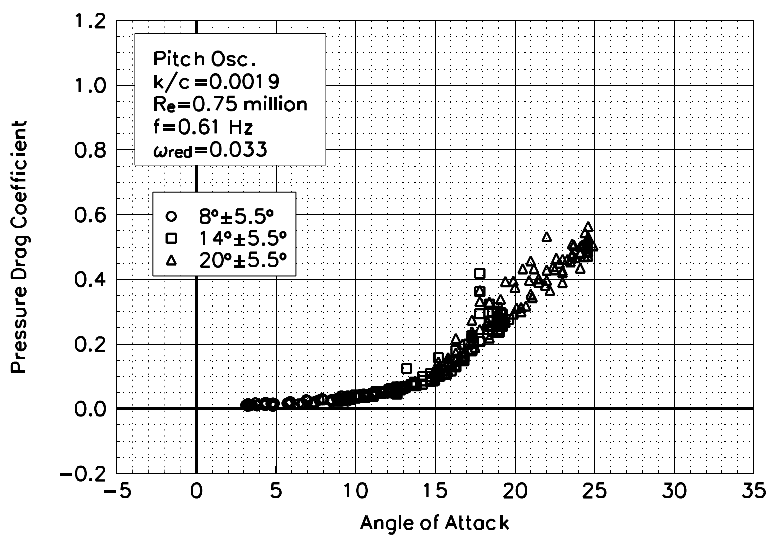

Figure C11. Pressure drag coefficient vs α.

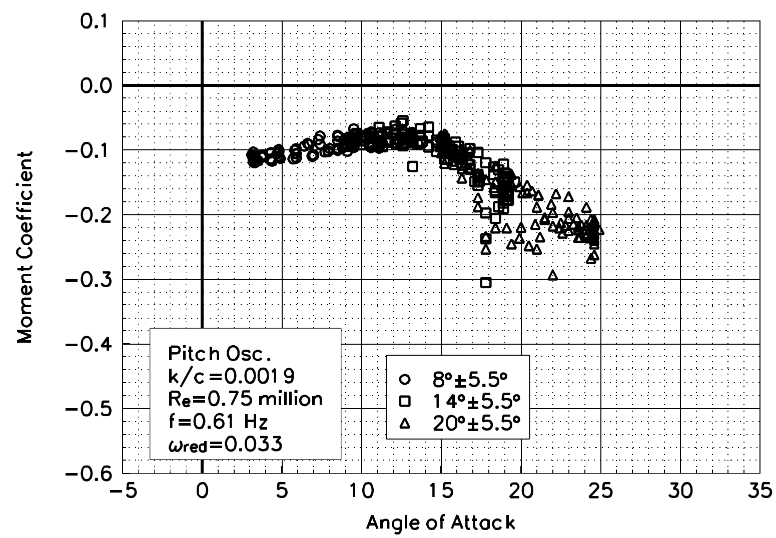

Figure C12. Moment coefficient vs α.

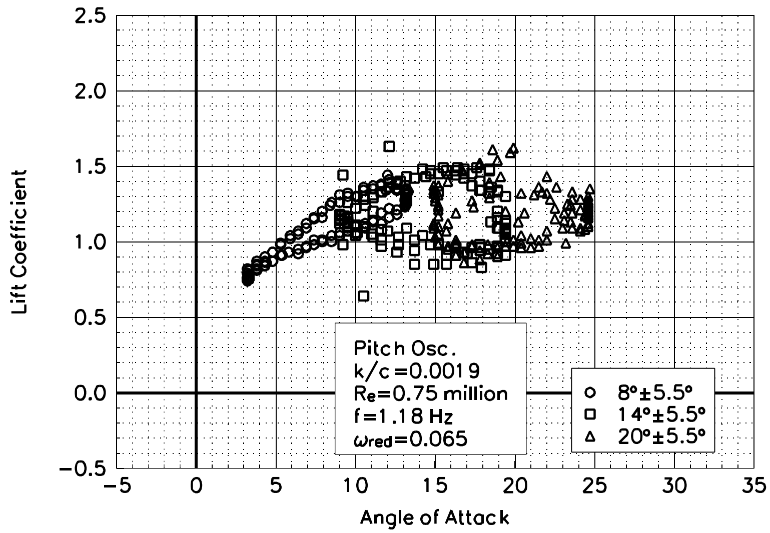

Figure C13. Lift coefficient vs α.

S801
LEGR
Re=0.75 million
$\omega_{reduced}$=0.065

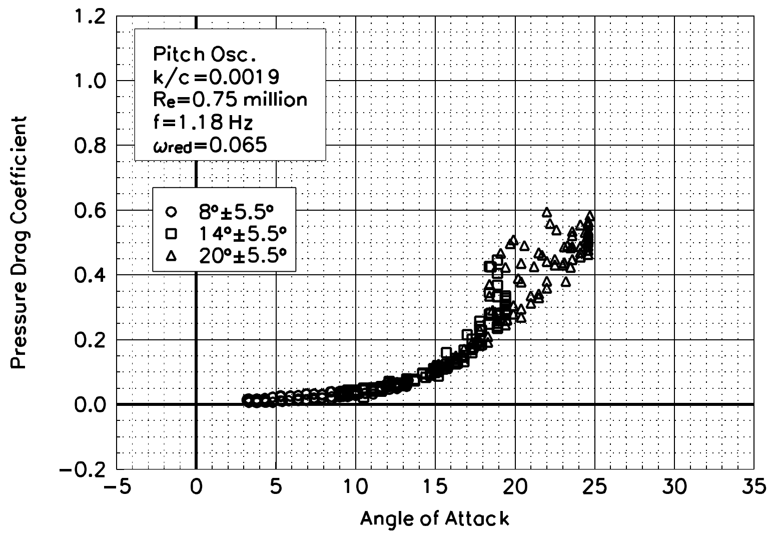

Figure C14. Pressure drag coefficient vs α.

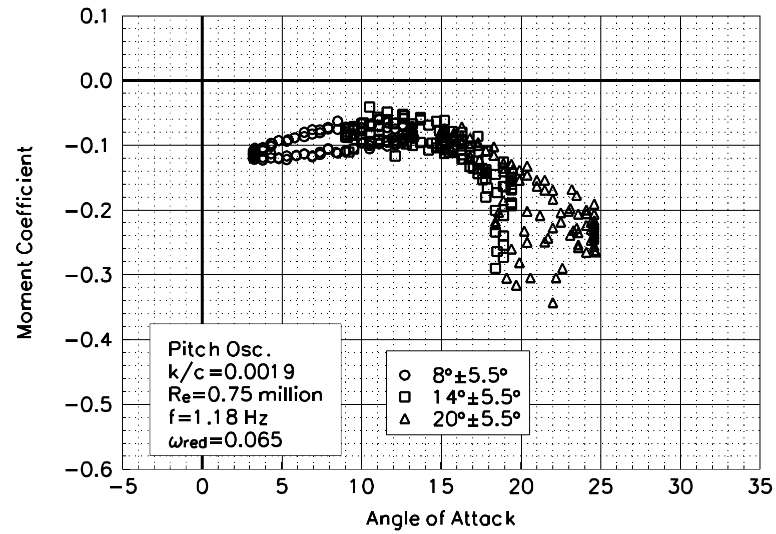

Figure C15. Moment coefficient vs α.

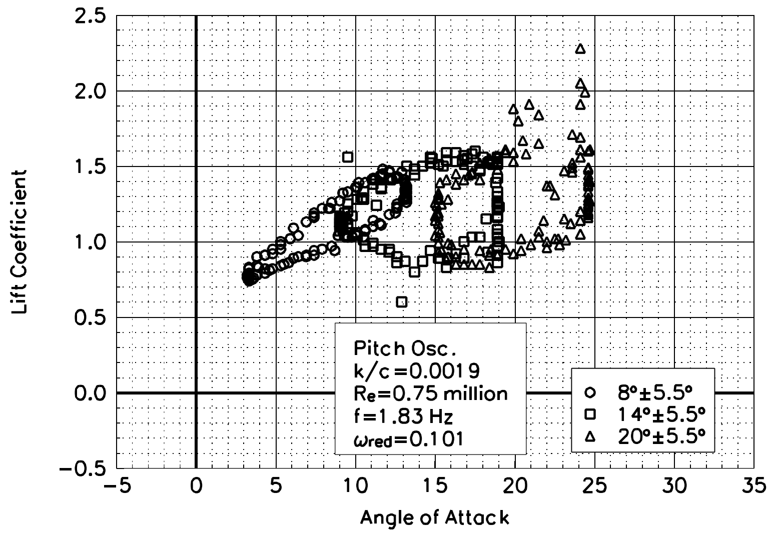

Figure C16. Lift coefficient vs α.

S801
LEGR
Re=0.75 million
$\omega_{reduced}$=0.101

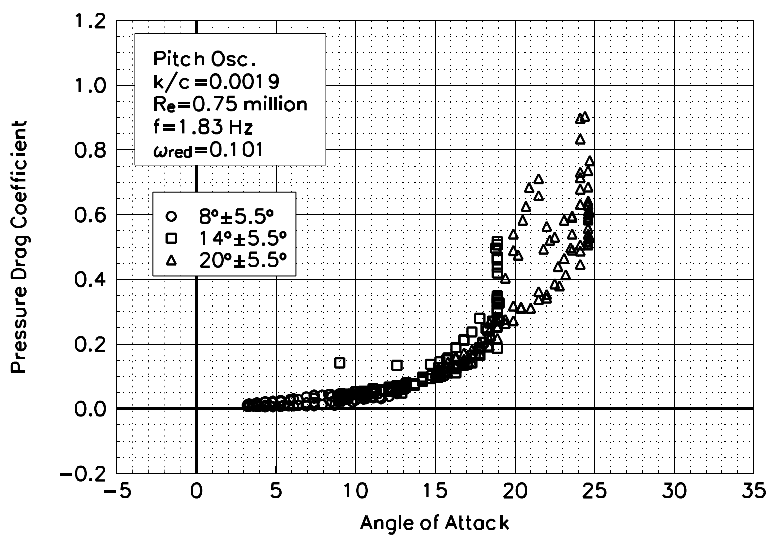

Figure C17. Pressure drag coefficient vs α.

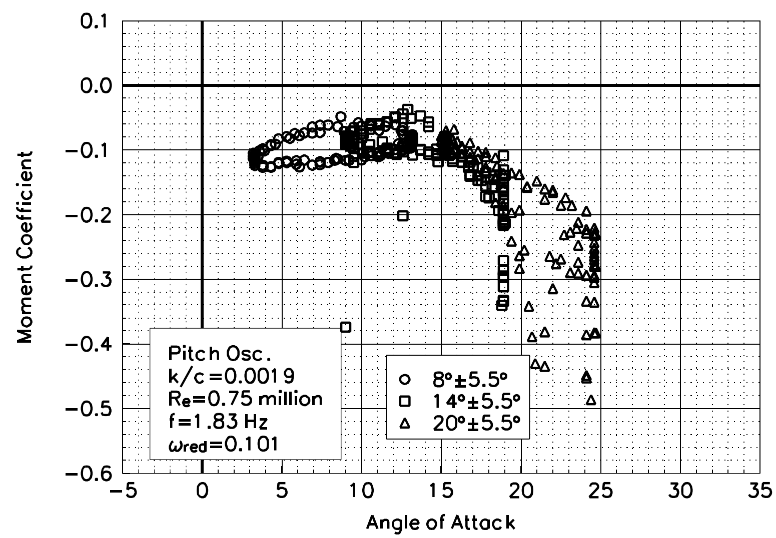

Figure C18. Moment coefficient vs α.

Unsteady Airfoil Characteristics

±5.5° Sine, Re = 1 million

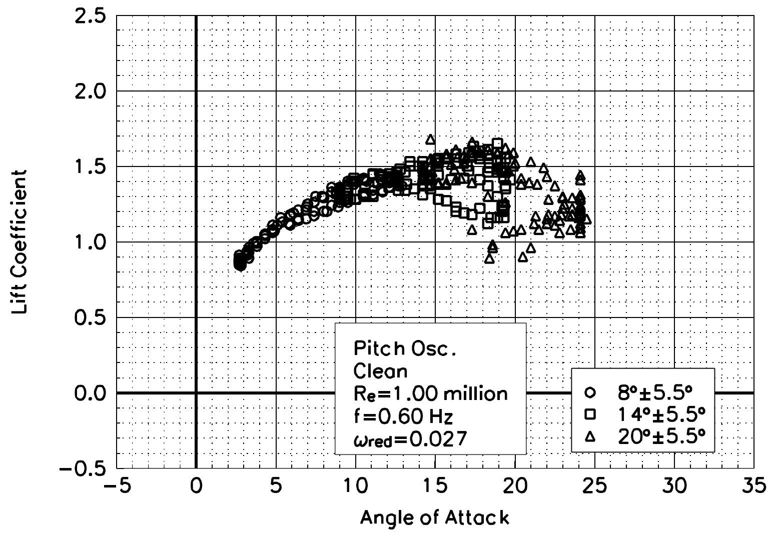

Figure C19. Lift coefficient vs α.

S801
Clean
Re=1.00 million
$\omega_{reduced}$=0.027

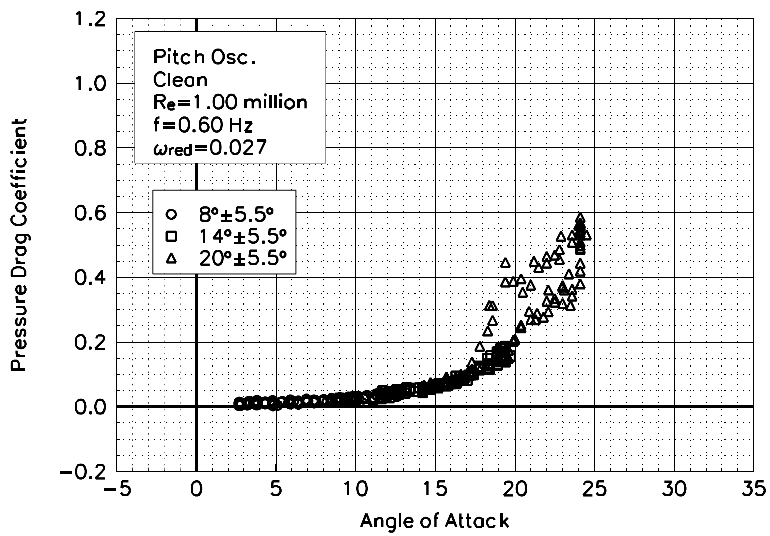

Figure C20. Pressure drag coefficient vs α.

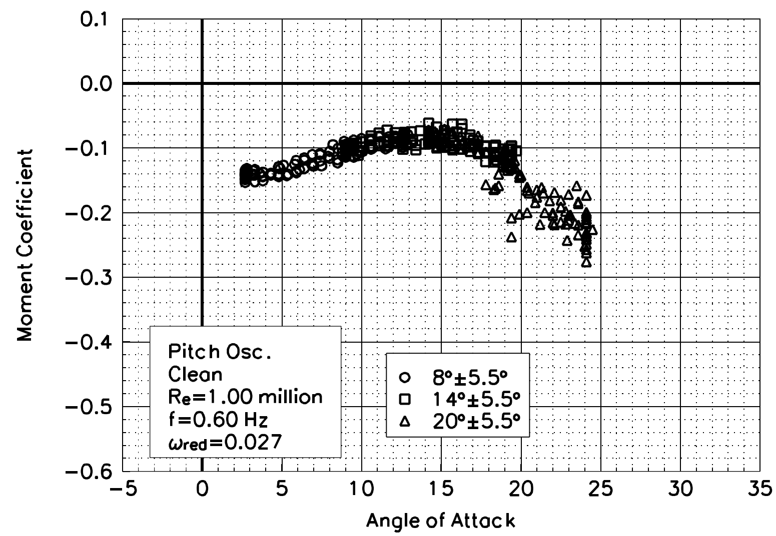

Figure C21. Moment coefficient vs α.

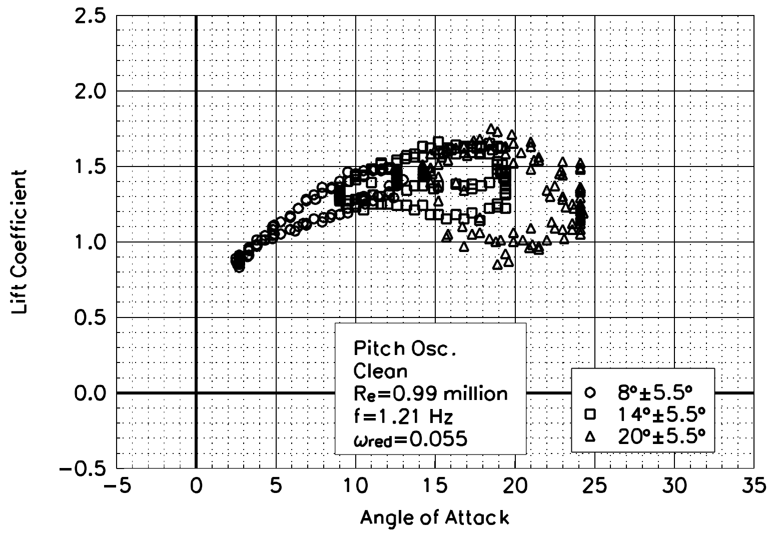

Figure C22. Lift coefficient vs α.

S801
Clean
Re=0.99 million
$\omega_{reduced}$=0.055

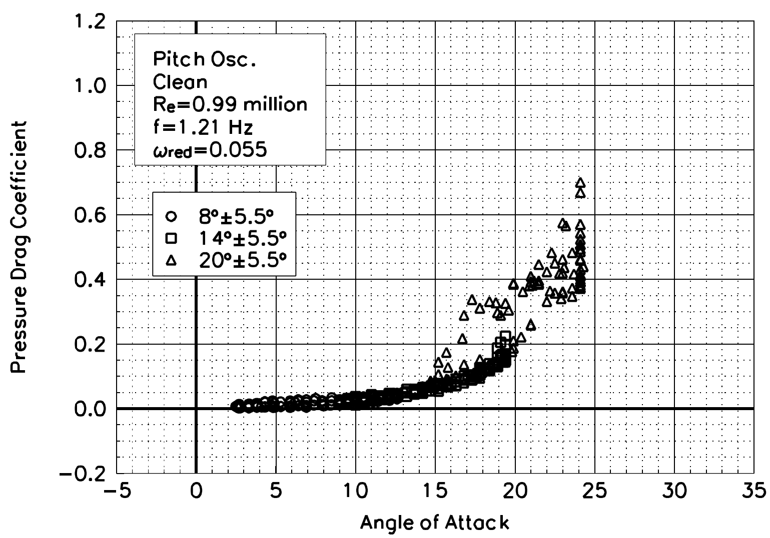

Figure C23. Pressure drag coefficient vs α.

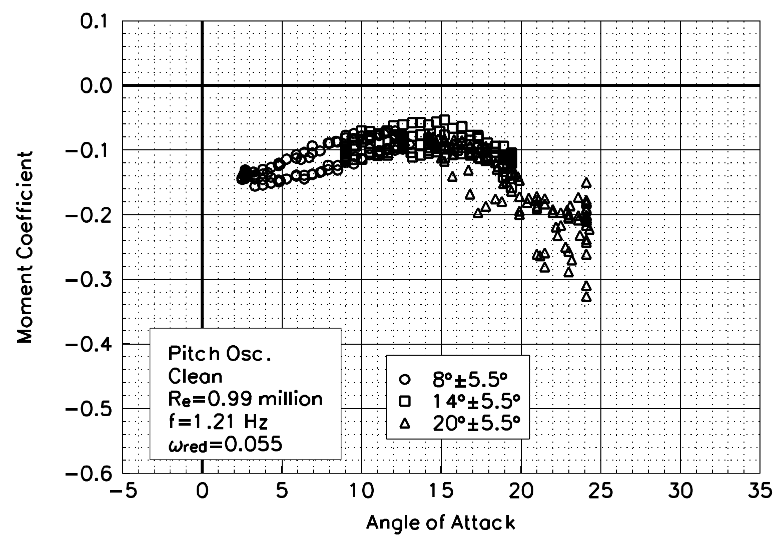

Figure C24. Moment coefficient vs α.

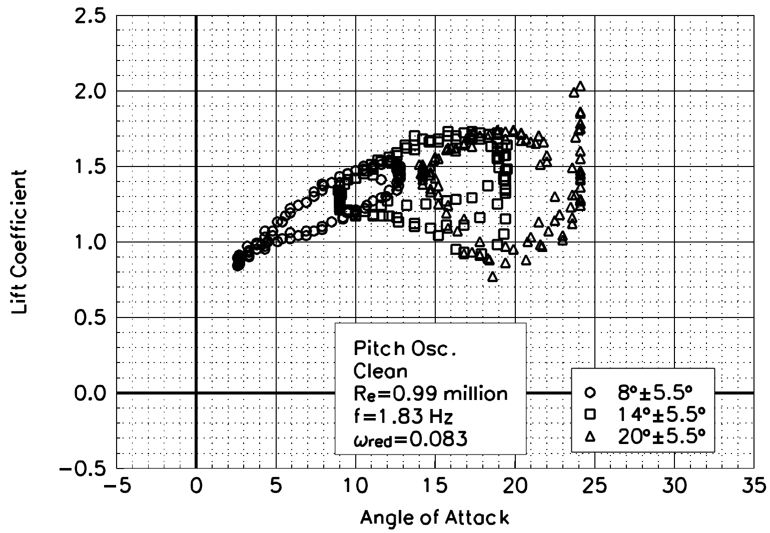

Figure C25. Lift coefficient vs α.

S801
Clean
Re=0.99 million
$\omega_{reduced}$=0.083

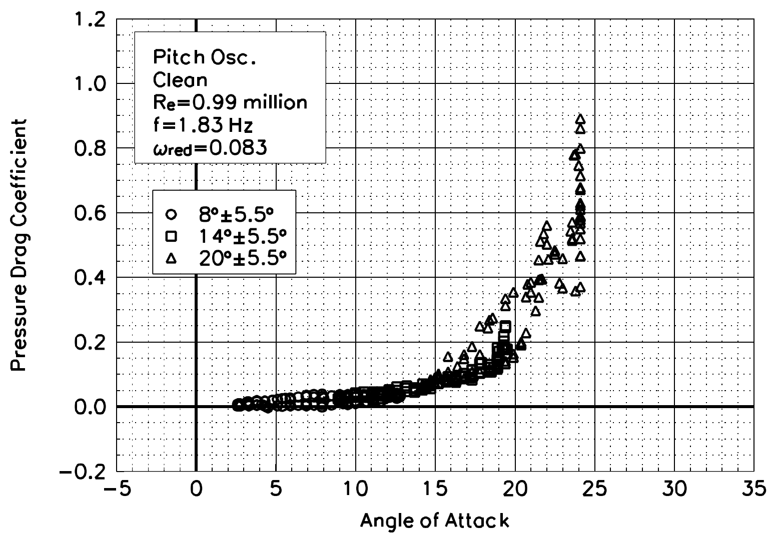

Figure C26. Pressure drag coefficient vs α.

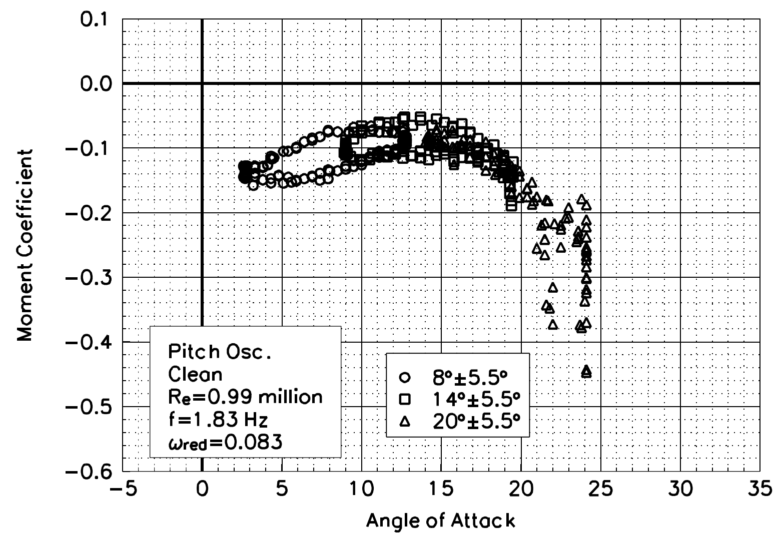

Figure C27. Moment coefficient vs α.

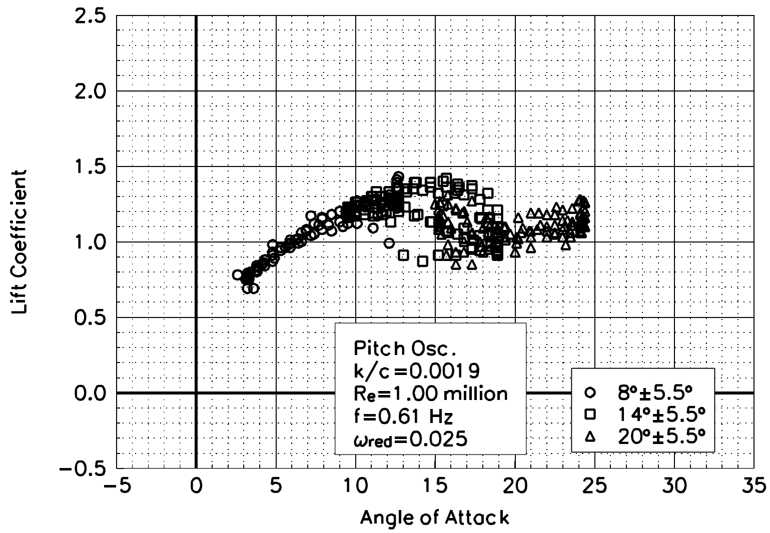

Figure C28. Lift coefficient vs α.

S801
LEGR
Re=1.00 million
$\omega_{reduced}$=0.025

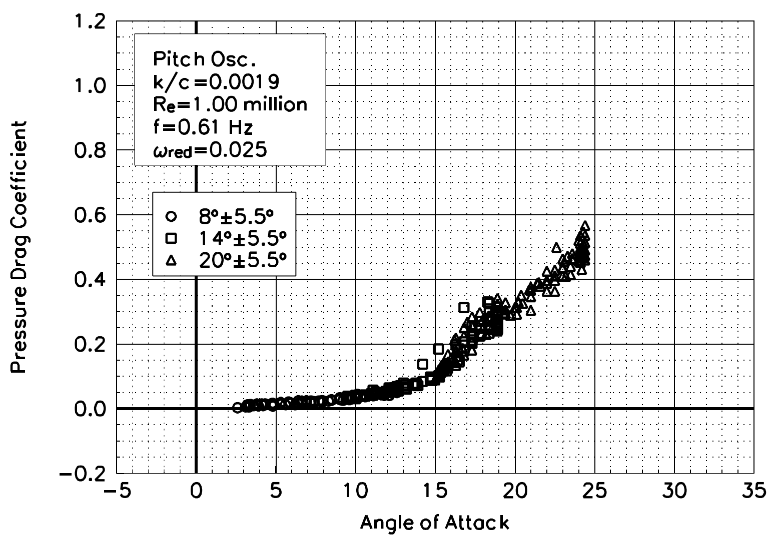

Figure C29. Pressure drag coefficient vs α.

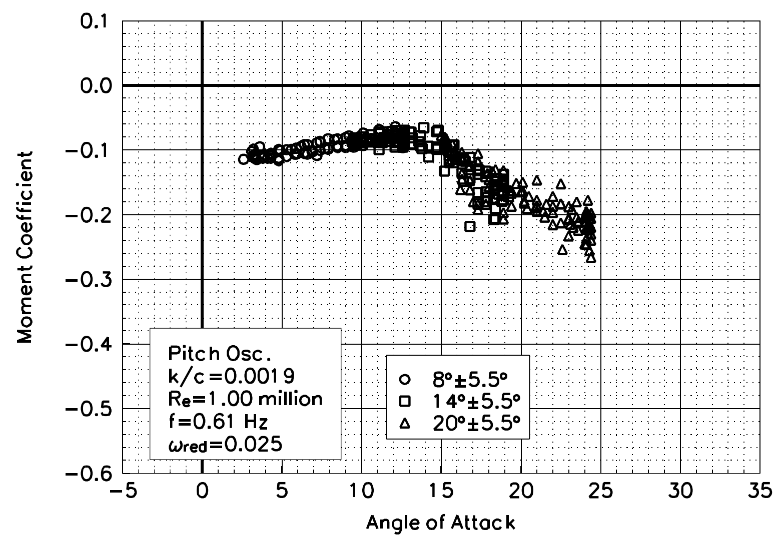

Figure C30. Moment coefficient vs α.

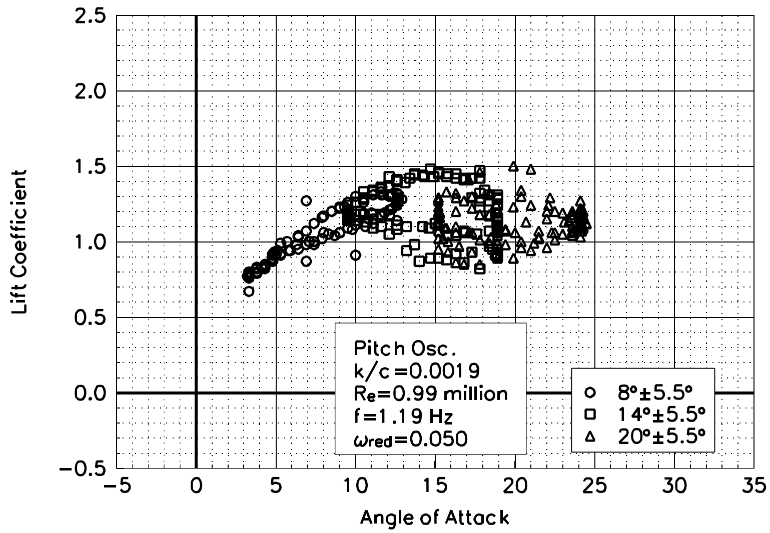

Figure C31. Lift coefficient vs α.

S801
LEGR
Re=0.99 million
$\omega_{reduced}$=0.050

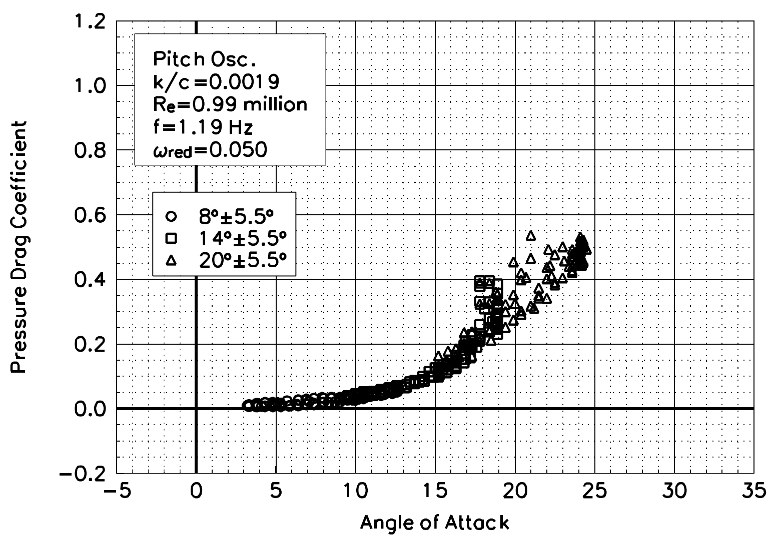

Figure C32. Pressure drag coefficient vs α.

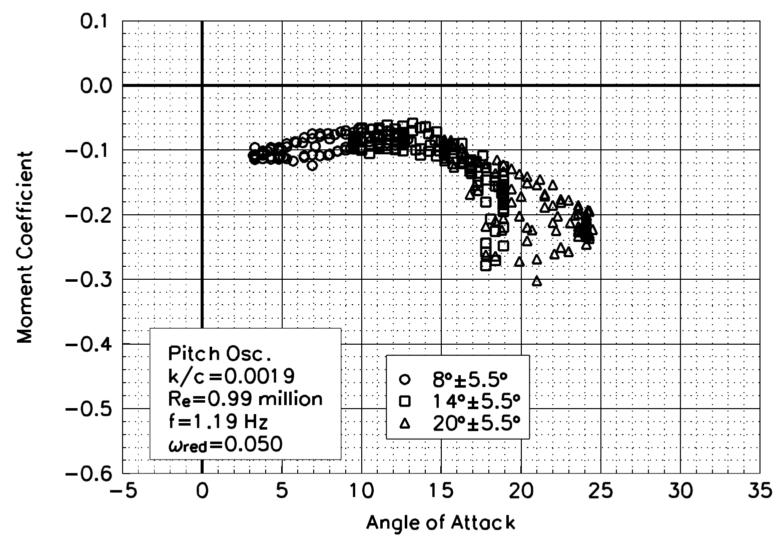

Figure C33. Moment coefficient vs α.

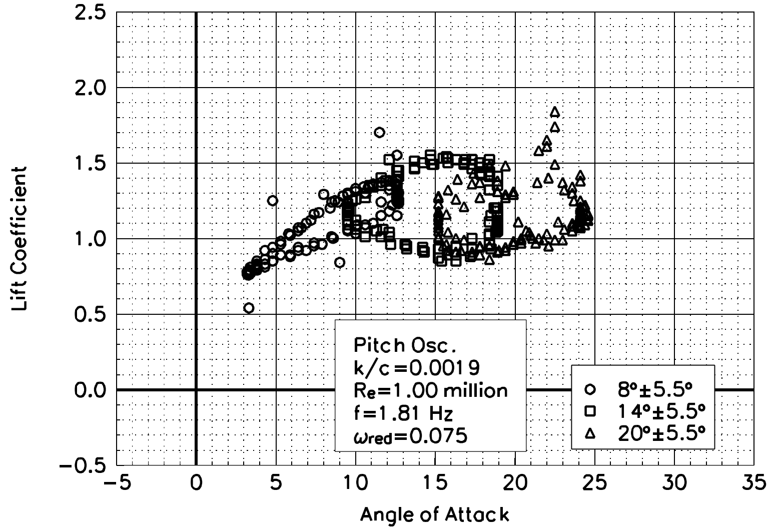

Figure C34. Lift coefficient vs α.

S801
LEGR
Re=1.00 million
$\omega_{reduced}$=0.075

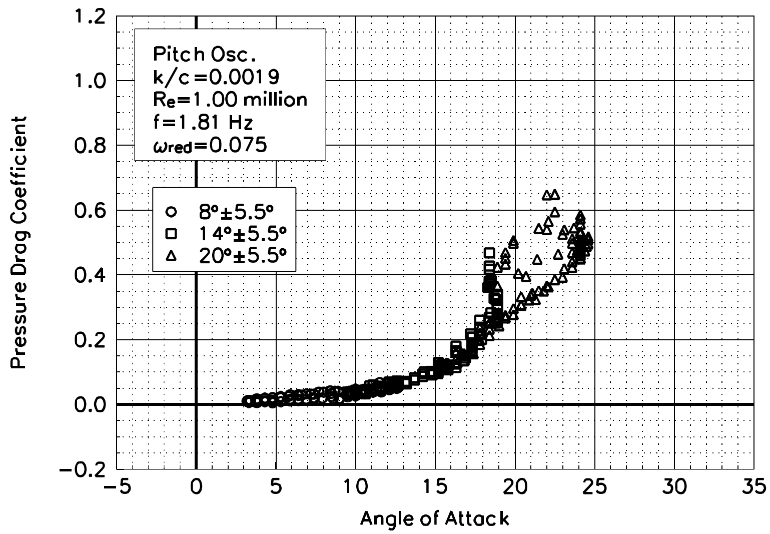

Figure C35. Pressure drag coefficient vs α.

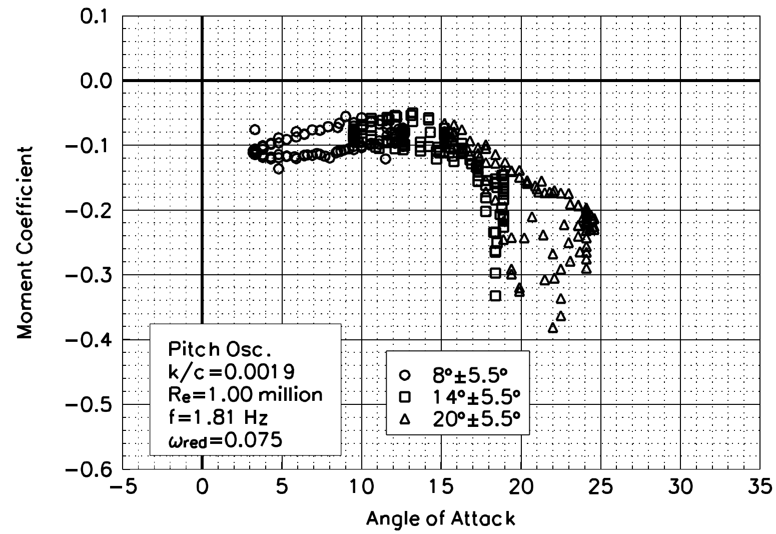

Figure C36. Moment coefficient vs α.

Unsteady Airfoil Characteristics

±5.5° Sine, Re= 1.25 million

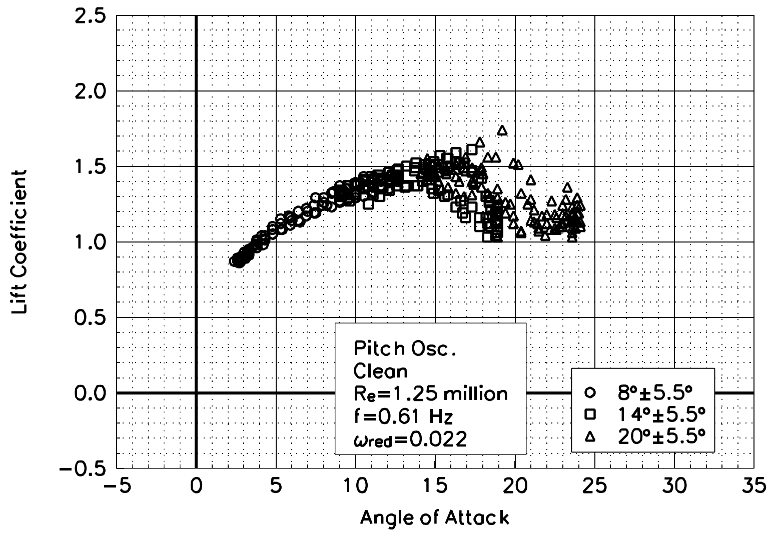

Figure C37. Lift coefficient vs α.

S801
Clean
Re=1.25 million
$\omega_{reduced}$=0.022

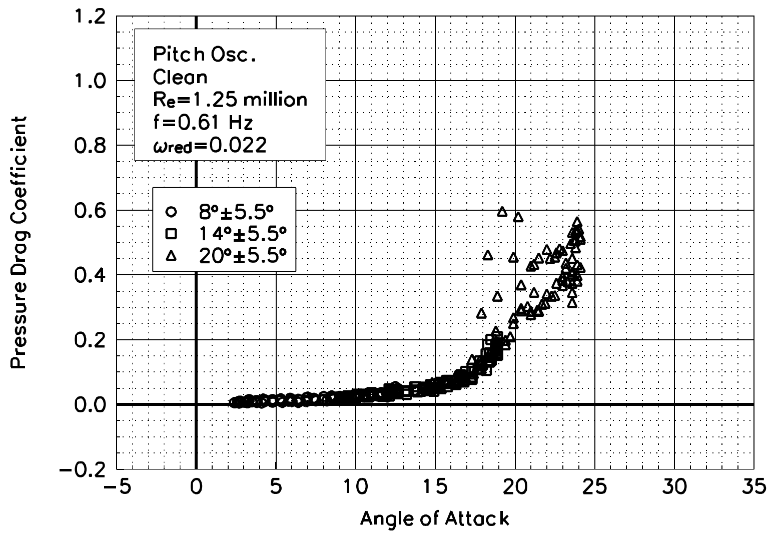

Figure C38. Pressure drag coefficient vs α.

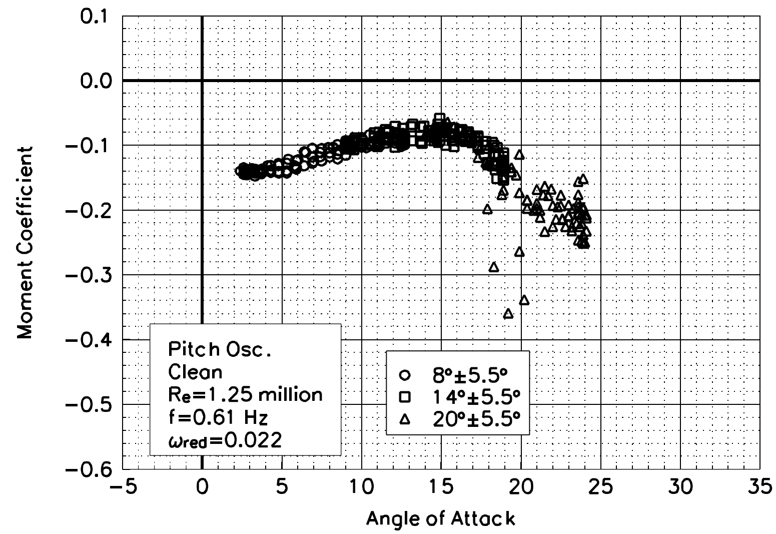

Figure C39. Moment coefficient vs α.

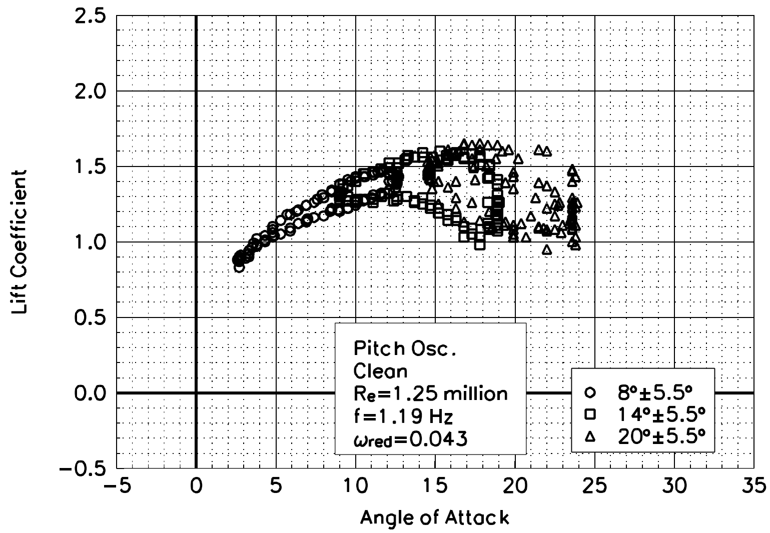

Figure C40. Lift coefficient vs α.

S801
Clean
Re=1.25 million
$\omega_{reduced}$=0.043

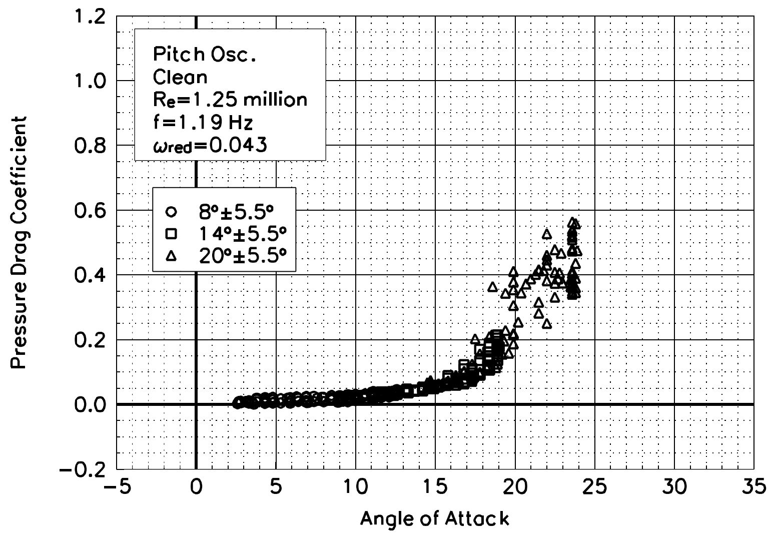

Figure C41. Pressure drag coefficient vs α.

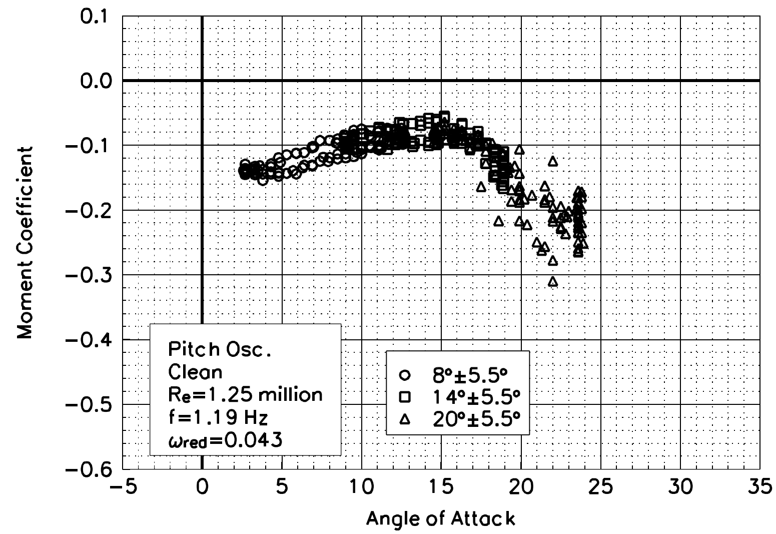

Figure C42. Moment coefficient vs α.

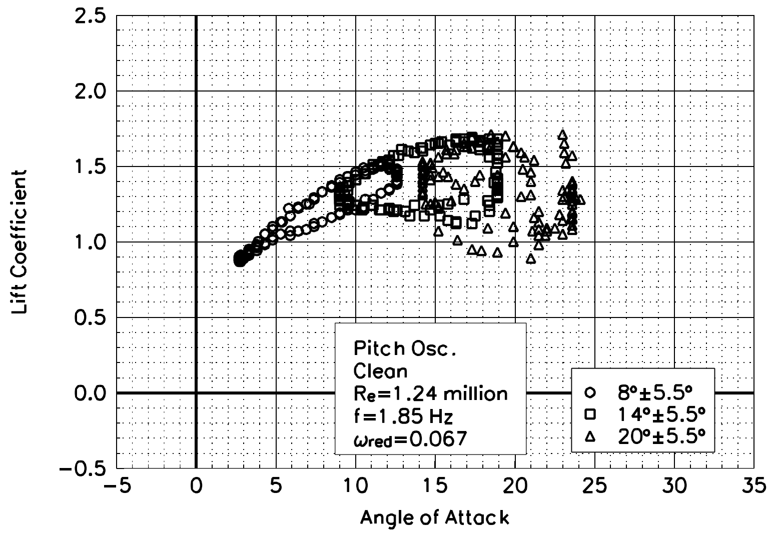

Figure C43. Lift coefficient vs α.

S801
Clean
Re=1.24 million
$\omega_{reduced}$=0.067

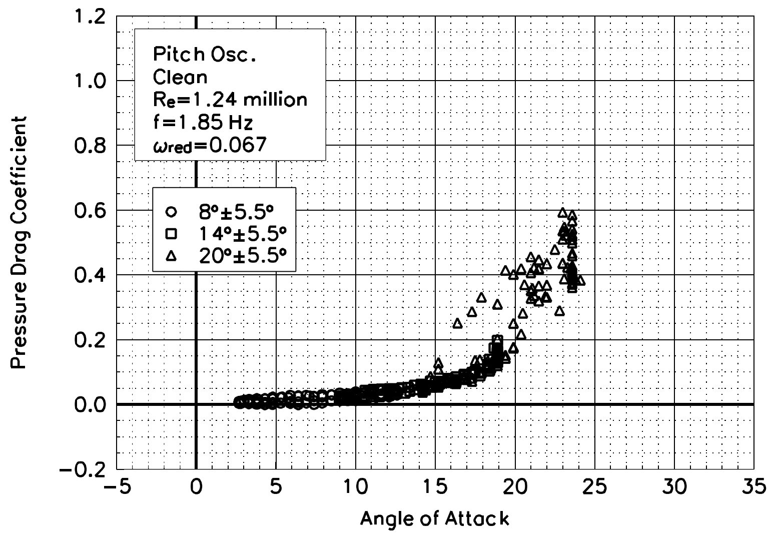

Figure C44. Pressure drag coefficient vs α.

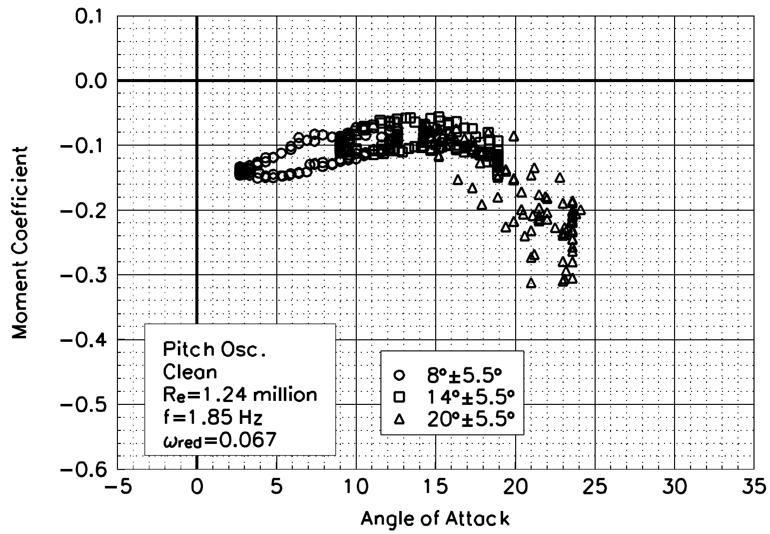

Figure C45. Moment coefficient vs α.

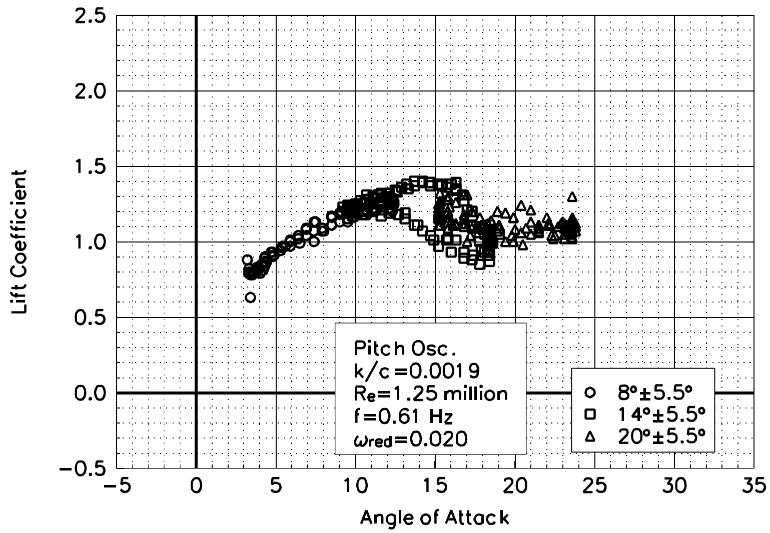

Figure C46. Lift coefficient vs α.

S801
LEGR
Re=1.25 million
$\omega_{reduced}$=0.020

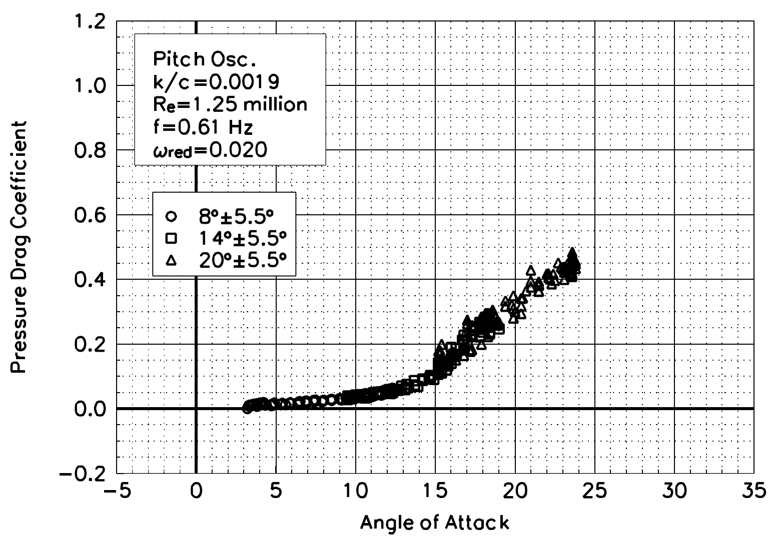

Figure C47. Pressure drag coefficient vs α.

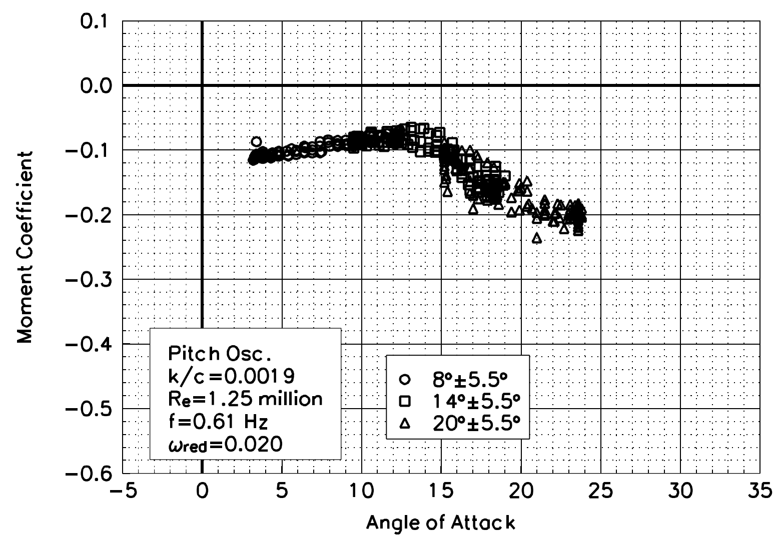

Figure C48. Moment coefficient vs α.

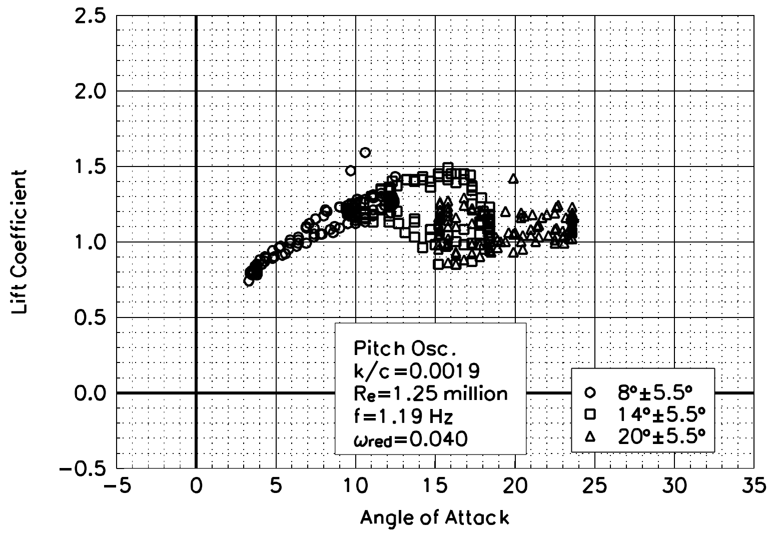

Figure C49. Lift coefficient vs α.

S801
LEGR
Re=1.25 million
$\omega_{reduced}$=0.040

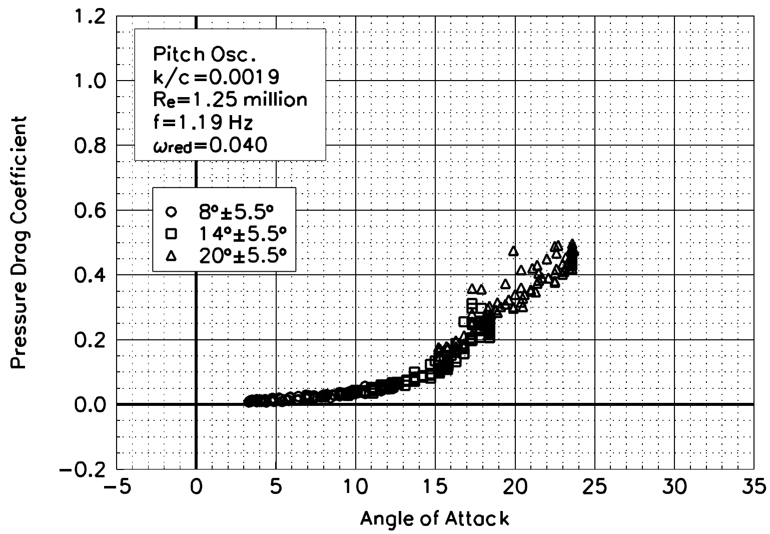

Figure C50. Pressure drag coefficient vs α.

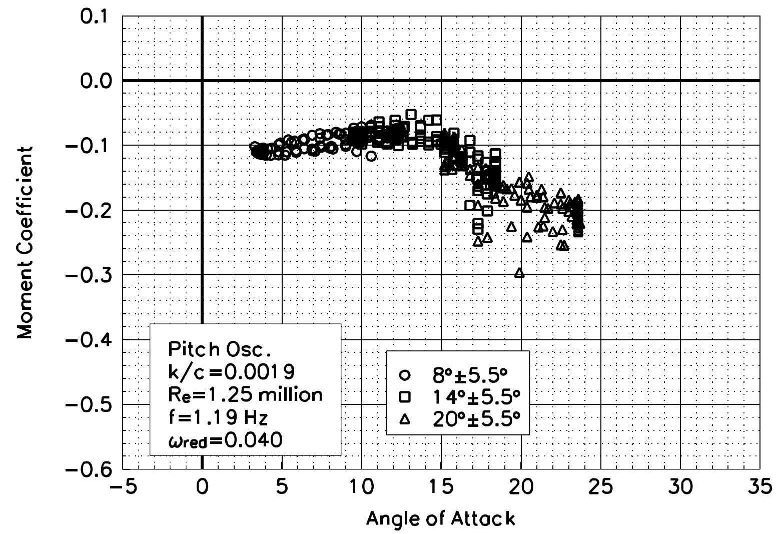

Figure C51. Moment coefficient vs α.

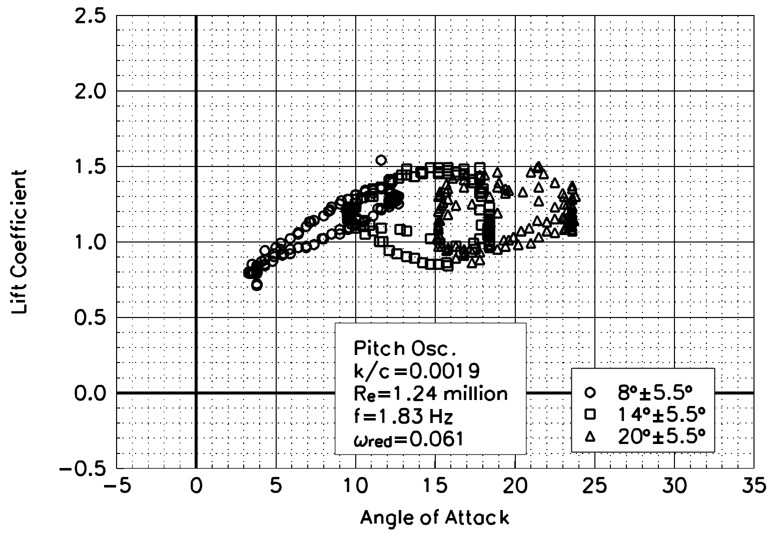

Figure C52. Lift coefficient vs α.

S801
LEGR
Re=1.24 million
$\omega_{reduced}$=0.061

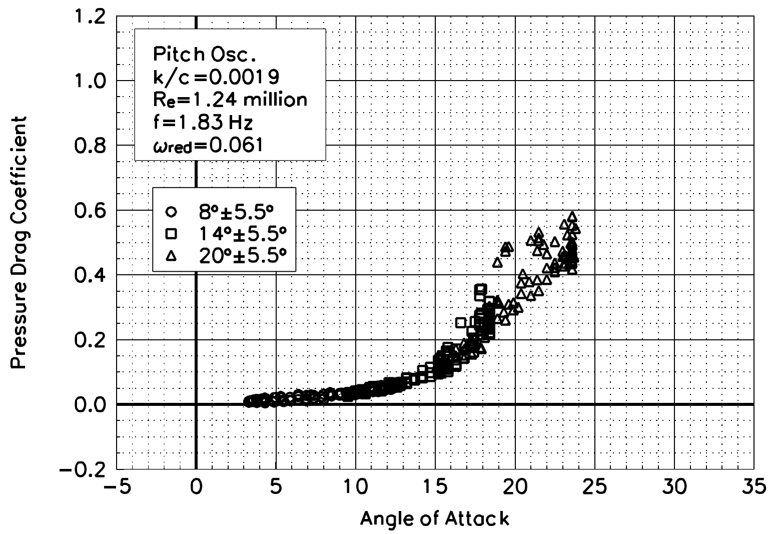

Figure C53. Pressure drag coefficient vs α.

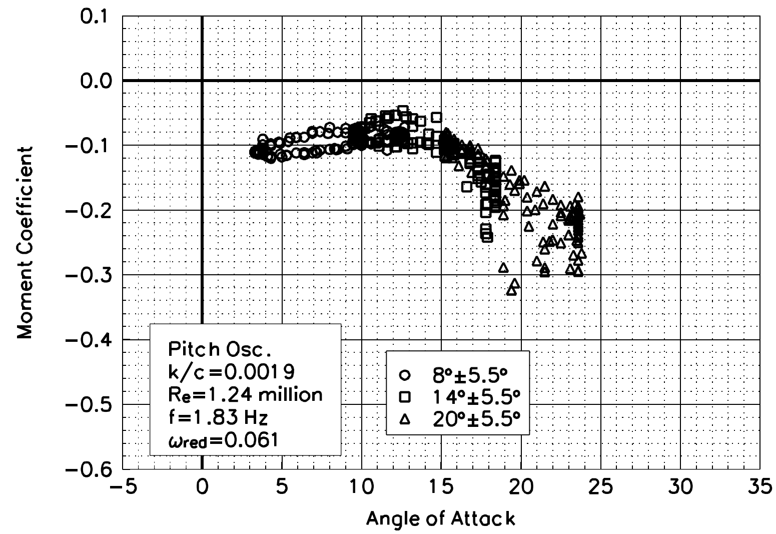

Figure C54. Moment coefficient vs α.

Unsteady Airfoil Characteristics

±5.5° Sine, Re = 1.4 million

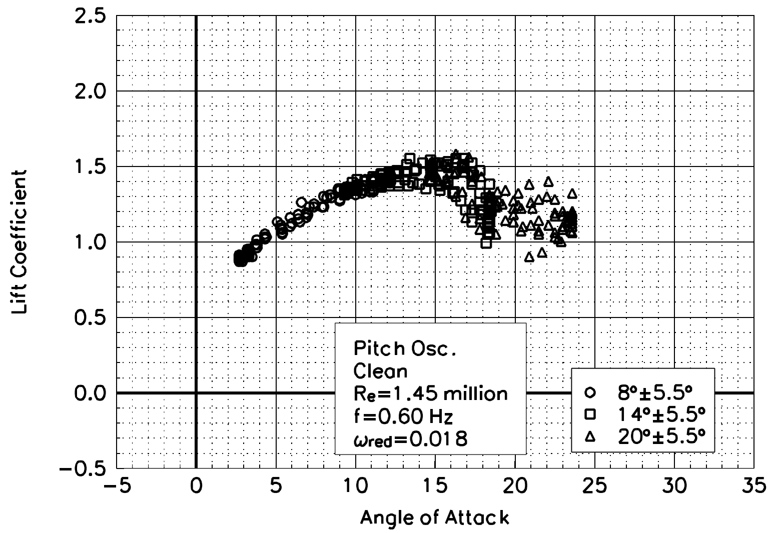

Figure C55. Lift coefficient vs α.

S801
Clean
Re=1.45 million
$\omega_{reduced}$=0.018

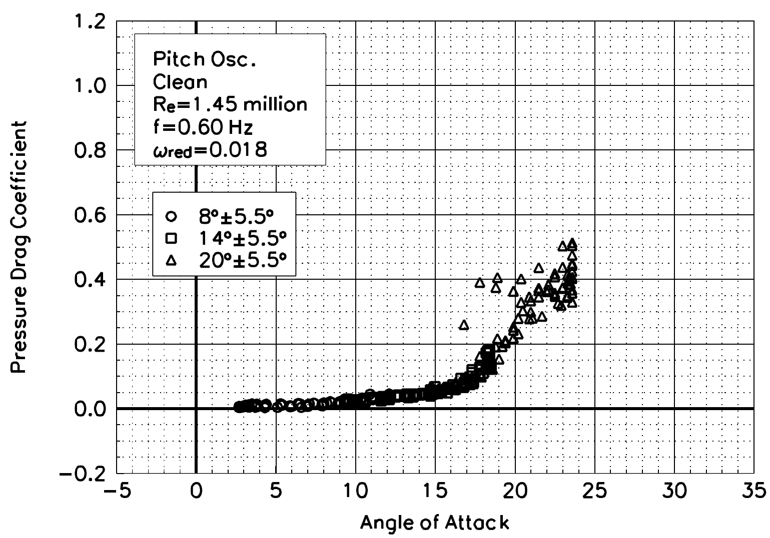

Figure C56. Pressure drag coefficient vs α.

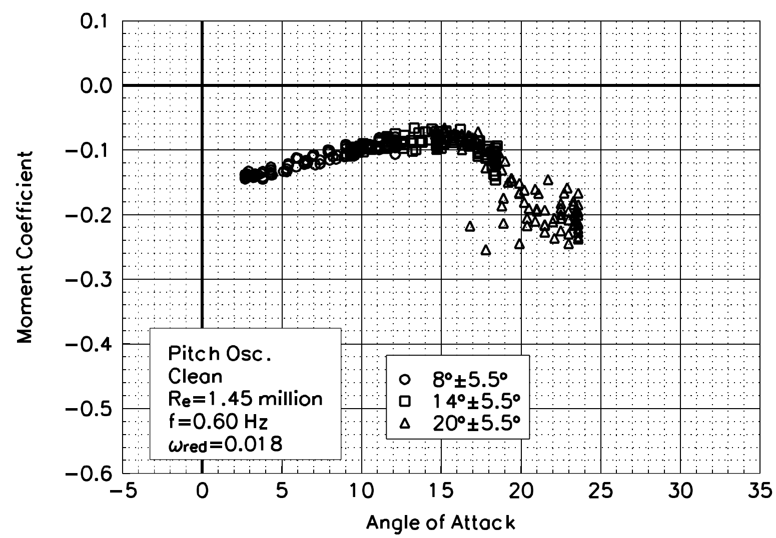

Figure C57. Moment coefficient vs α.

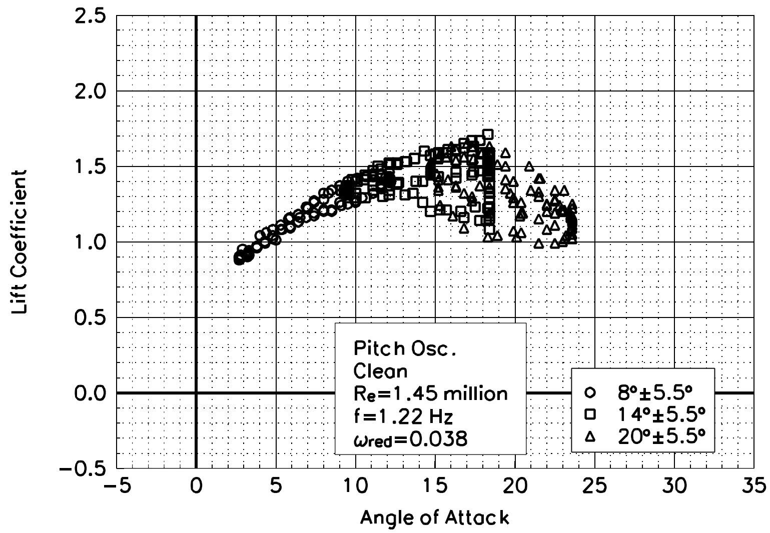

Figure C58. Lift coefficient vs α.

S801
Clean
Re=1.45 million
$\omega_{reduced}$=0.038

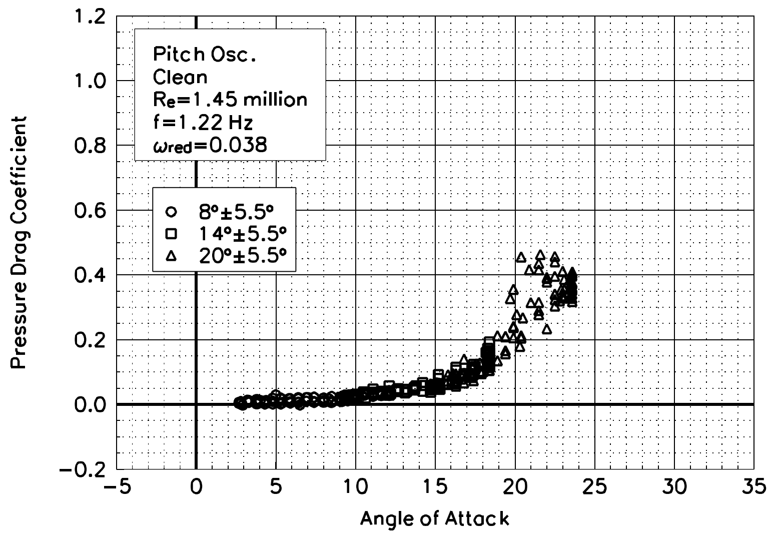

Figure C59. Pressure drag coefficient vs α.

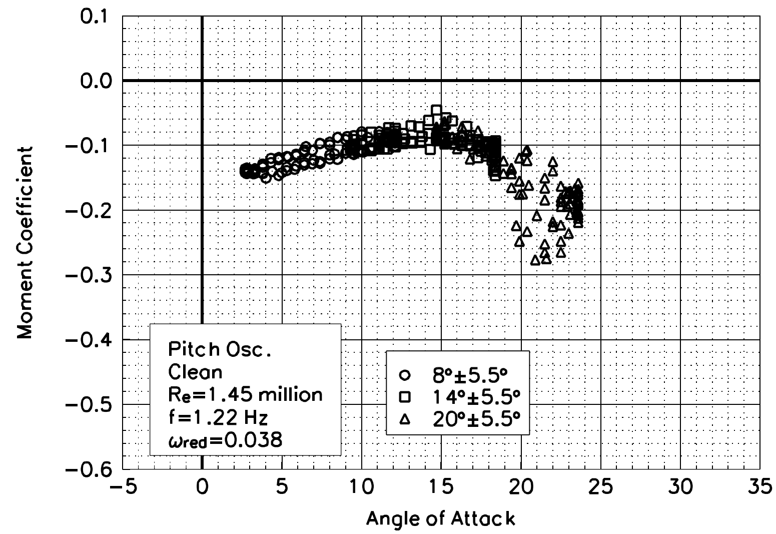

Figure C60. Moment coefficient vs α.

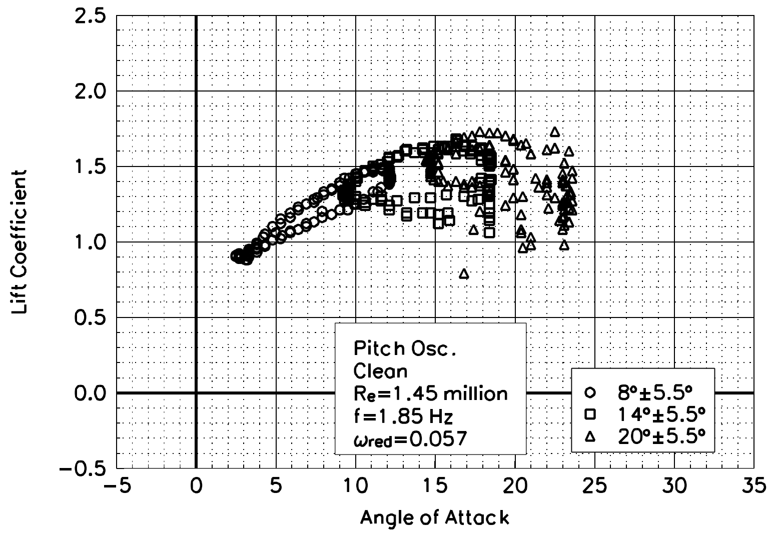

Figure C61. Lift coefficient vs α.

S801
Clean
Re=1.45 million
$\omega_{reduced}$=0.057

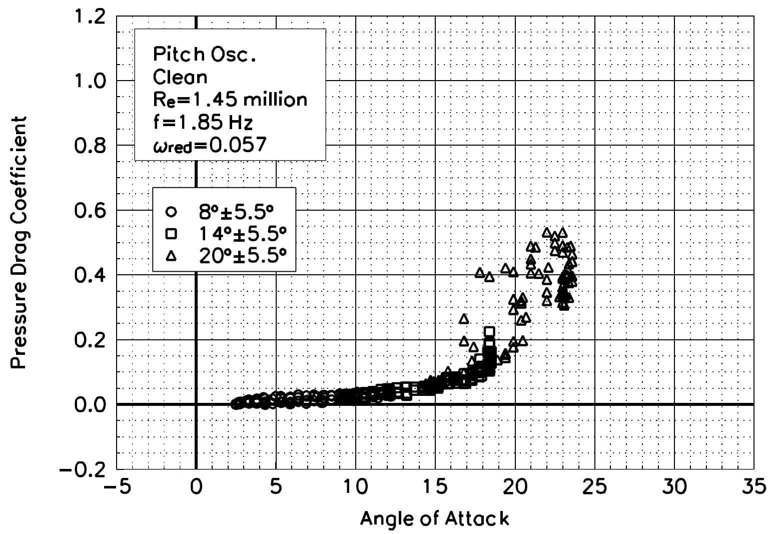

Figure C62. Pressure drag coefficient vs α.

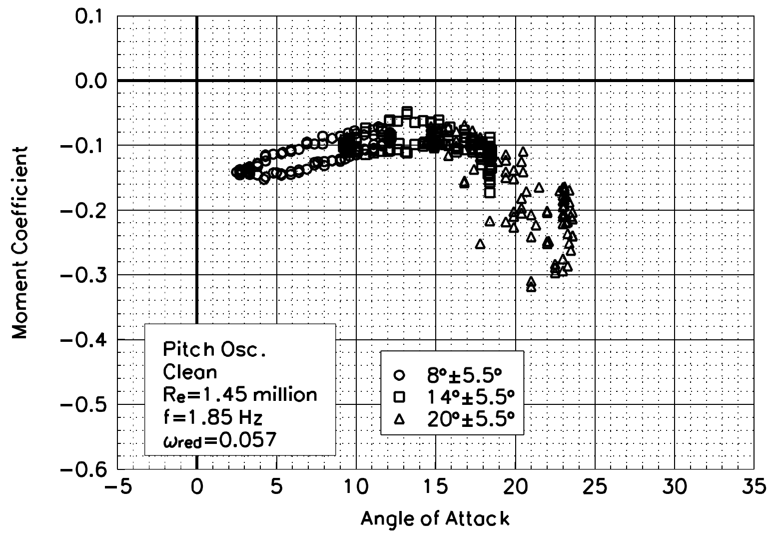

Figure C63. Moment coefficient vs α.

S801
LEGR
Re=1.37 million
$\omega_{reduced}$=0.018

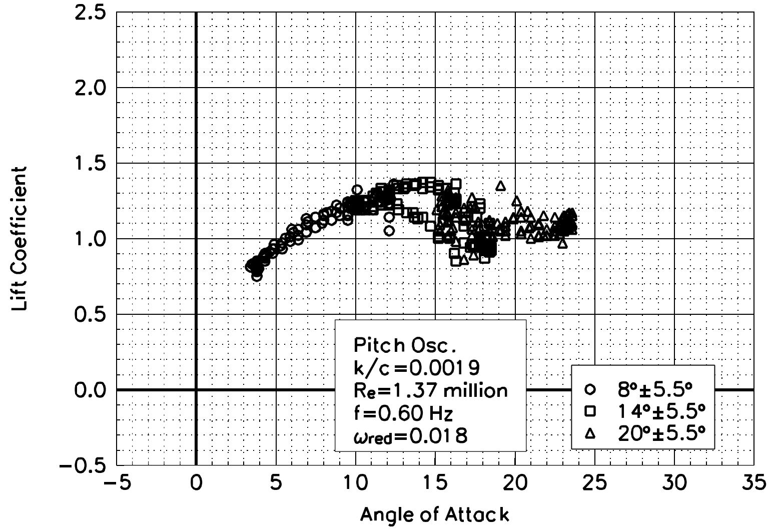

Figure C64. Lift coefficient vs α.

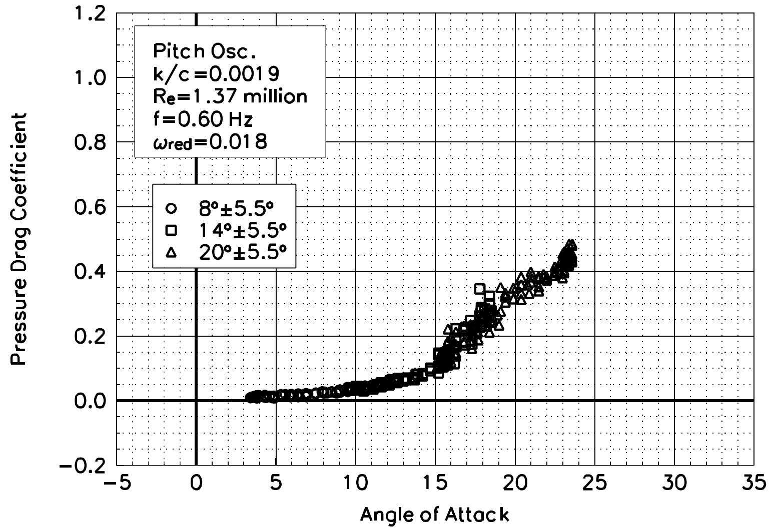

Figure C65. Pressure drag coefficient vs α.

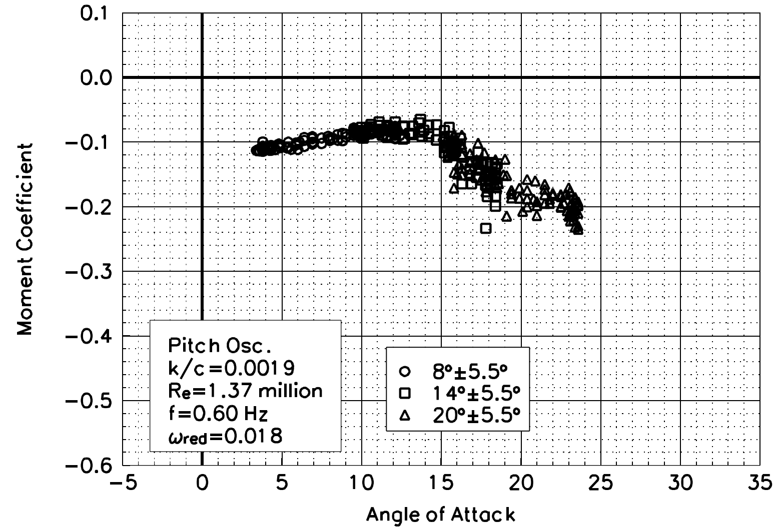

Figure C66. Moment coefficient vs α.

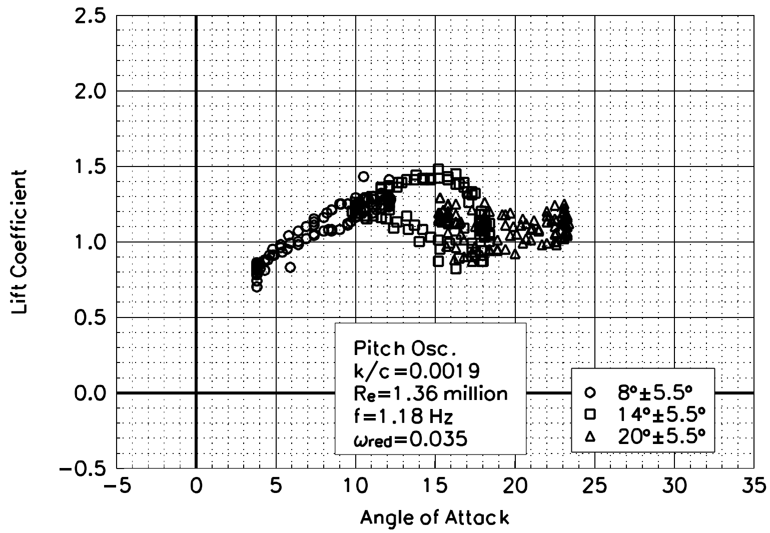

Figure C67. Lift coefficient vs α.

S801
LEGR
Re=1.36 million
$\omega_{reduced}$=0.035

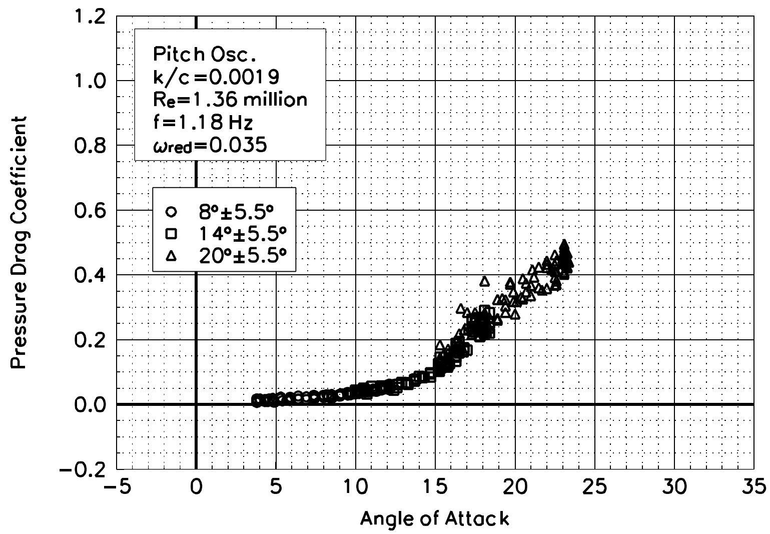

Figure C68. Pressure drag coefficient vs α.

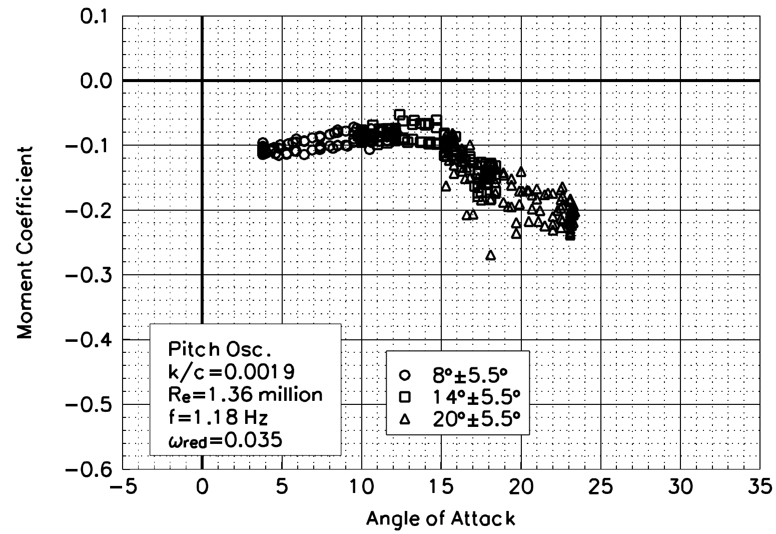

Figure C69. Moment coefficient vs α.

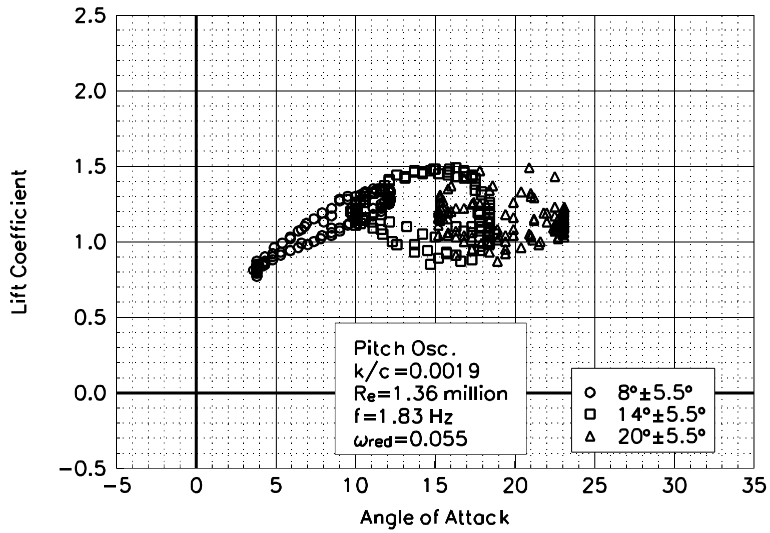

Figure C70. Lift coefficient vs α.

S801
LEGR
Re=1.36 million
$\omega_{reduced}$=0.055

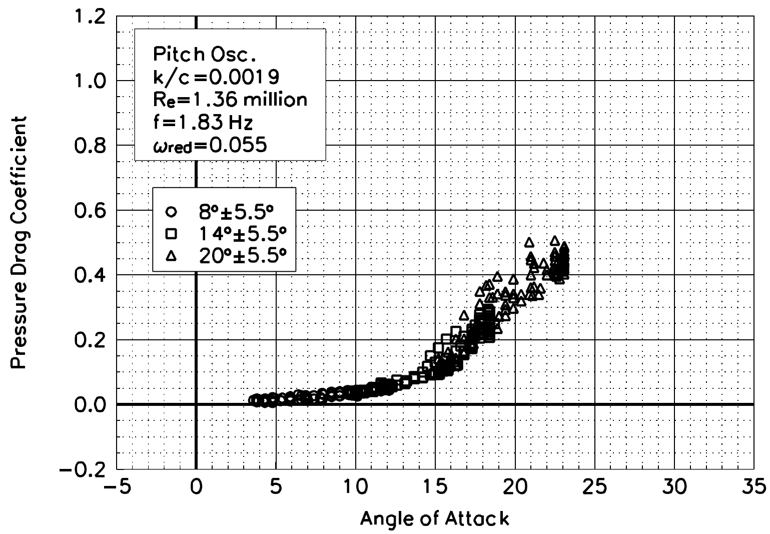

Figure C71. Pressure drag coefficient vs α.

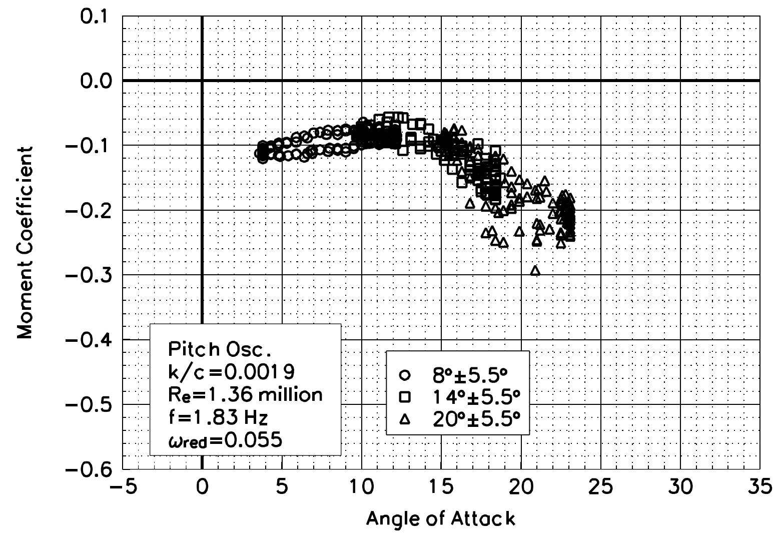

Figure C72. Moment coefficient vs α.

Unsteady Airfoil Characteristics

±10° Sine, Re = 0.75 million

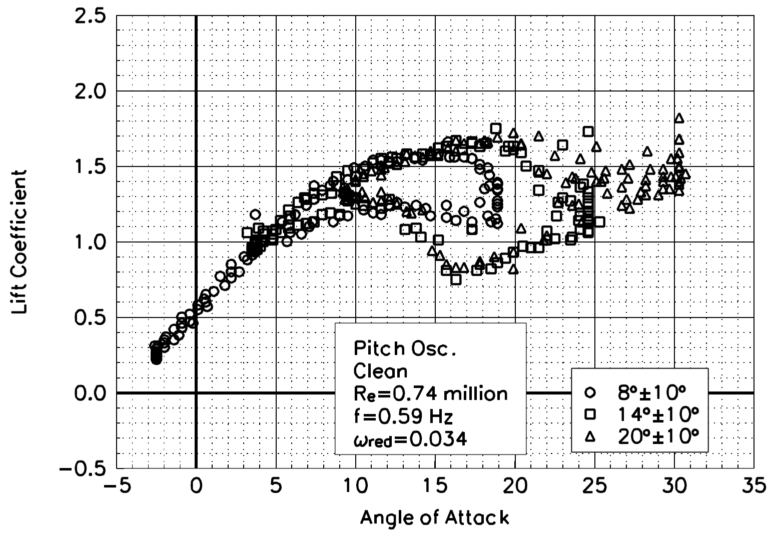

Figure C73. Lift coefficient vs α.

S801
Clean
Re=0.74 million
$\omega_{reduced}$=0.034

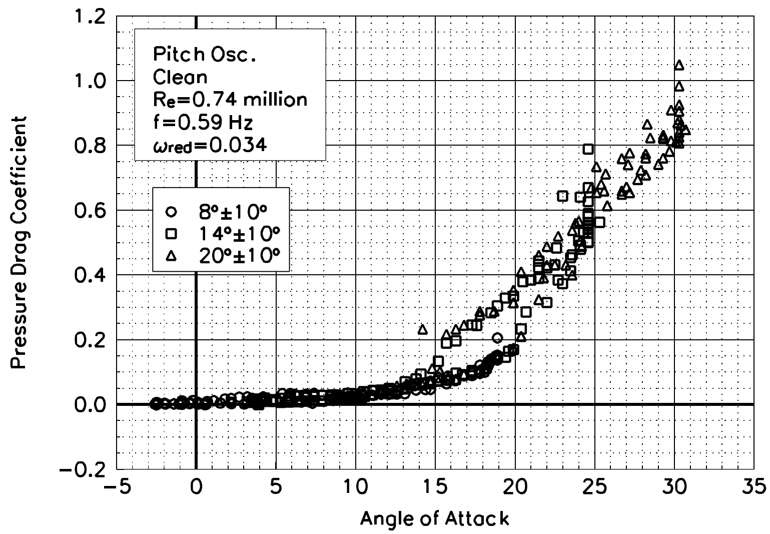

Figure C74. Pressure drag coefficient vs α.

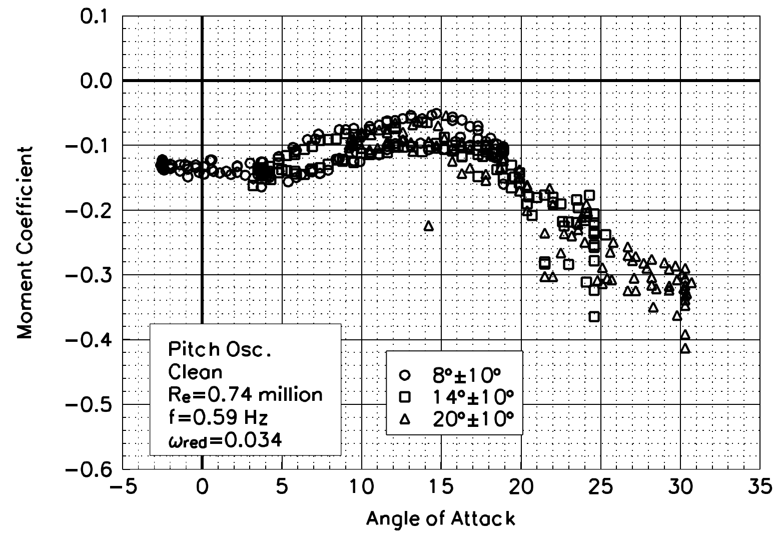

Figure C75. Moment coefficient vs α.

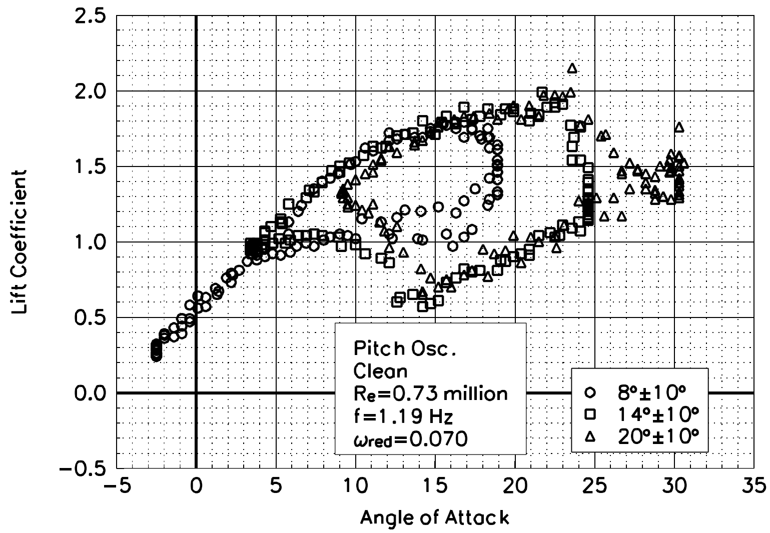

Figure C76. Lift coefficient vs α.

S801
Clean
Re=0.73 million
$\omega_{reduced}$=0.070

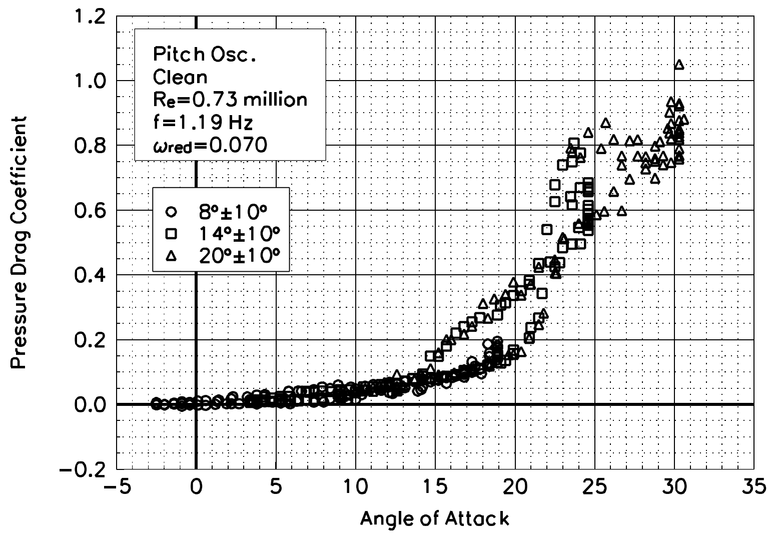

Figure C77. Pressure drag coefficient vs α.

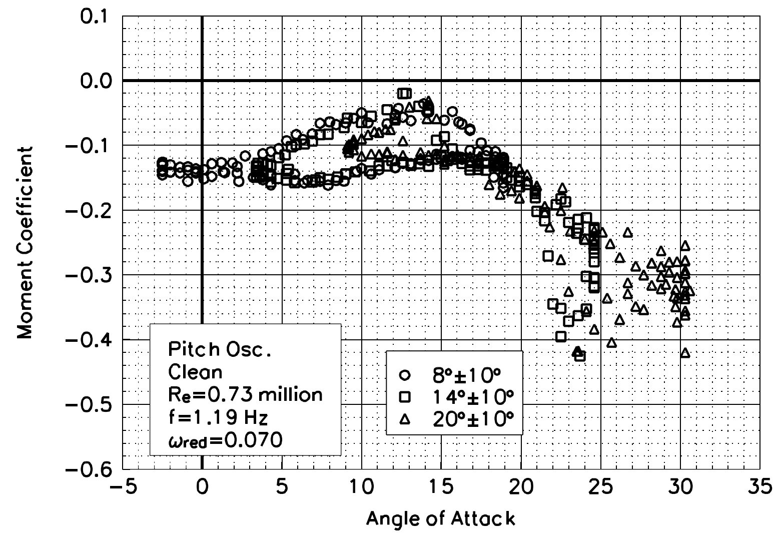

Figure C78. Moment coefficient vs α.

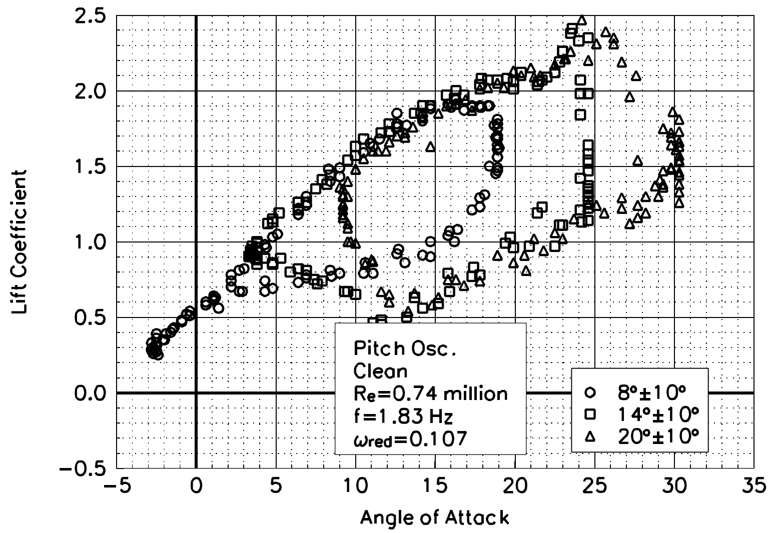

Figure C79. Lift coefficient vs α.

S801
Clean
Re=0.74 million
$\omega_{reduced}$=0.107

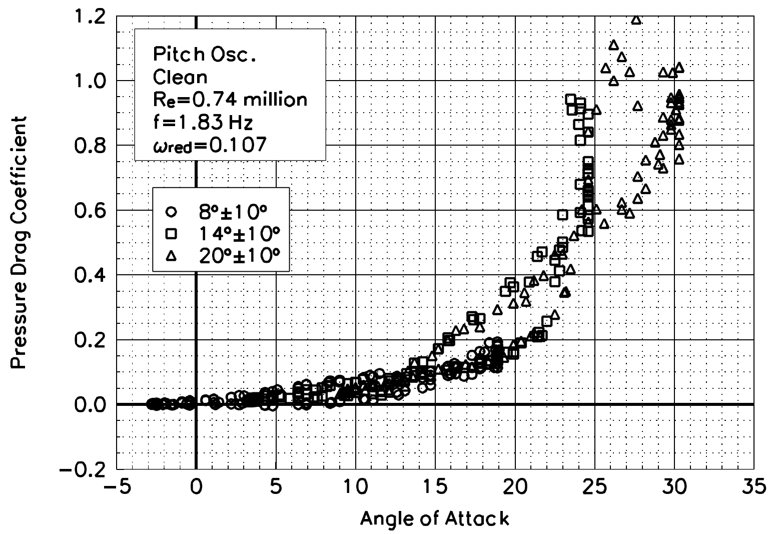

Figure C80. Pressure drag coefficient vs α.

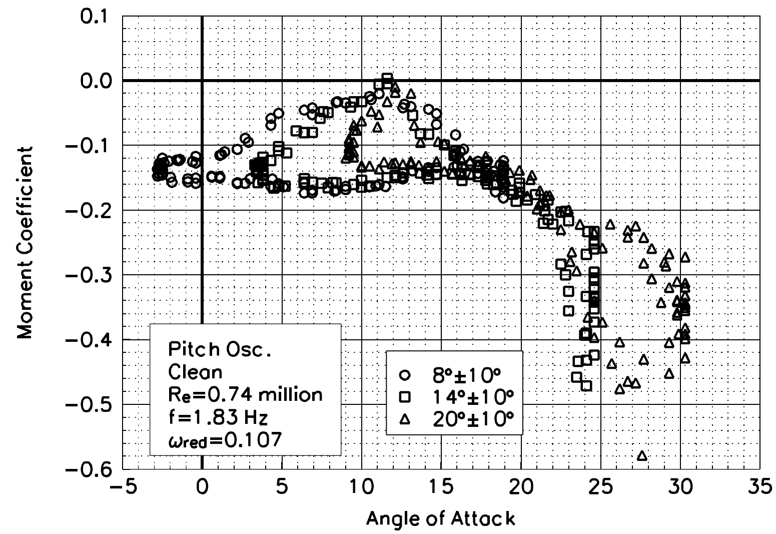

Figure C81. Moment coefficient vs α.

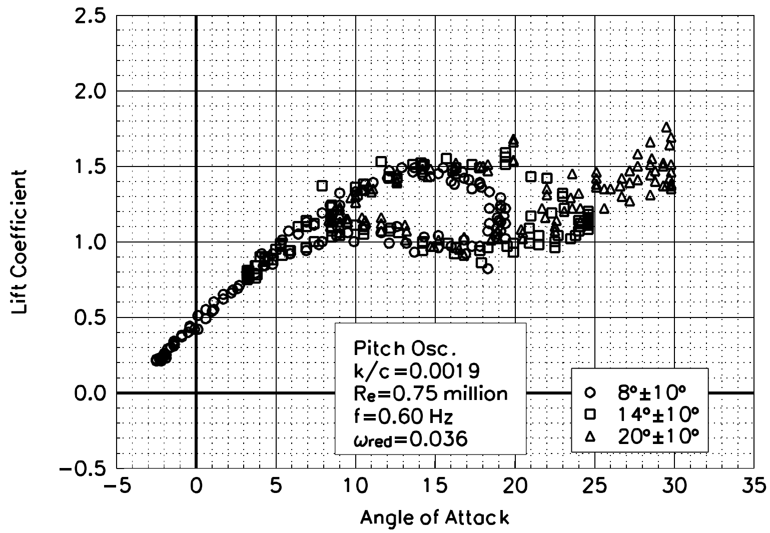

Figure C82. Lift coefficient vs α.

S801
LEGR
Re=0.75 million
$\omega_{reduced}$=0.036

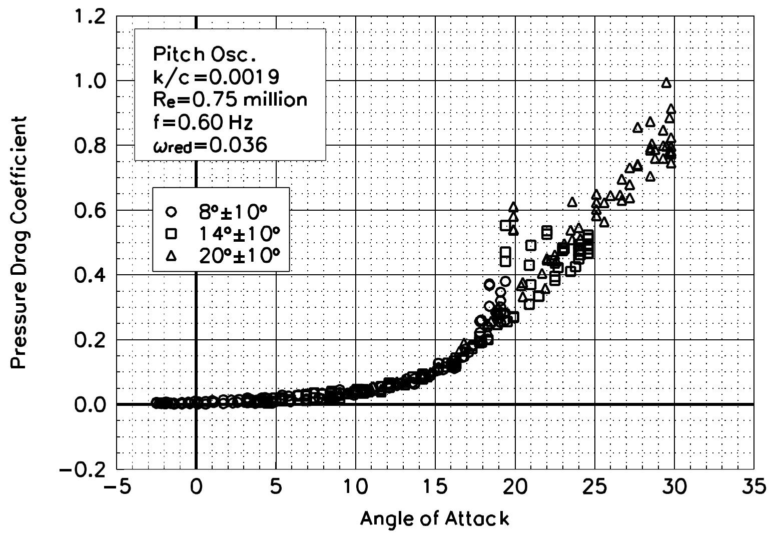

Figure C83. Pressure drag coefficient vs α.

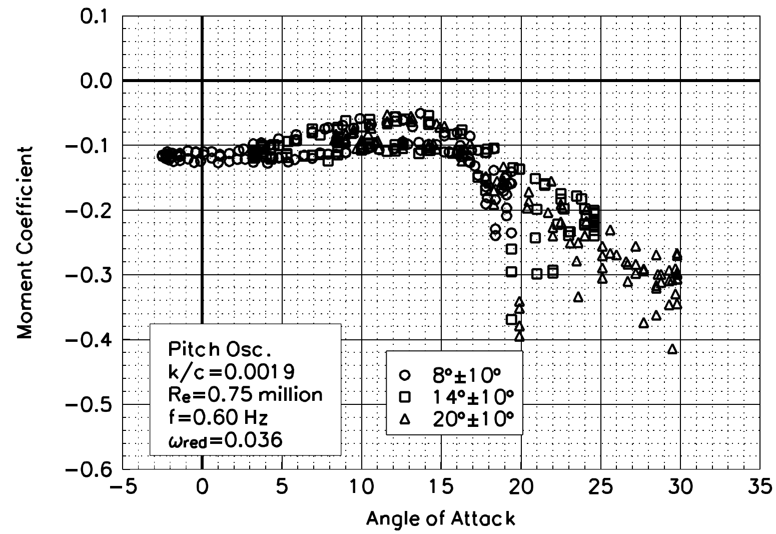

Figure C84. Moment coefficient vs α.

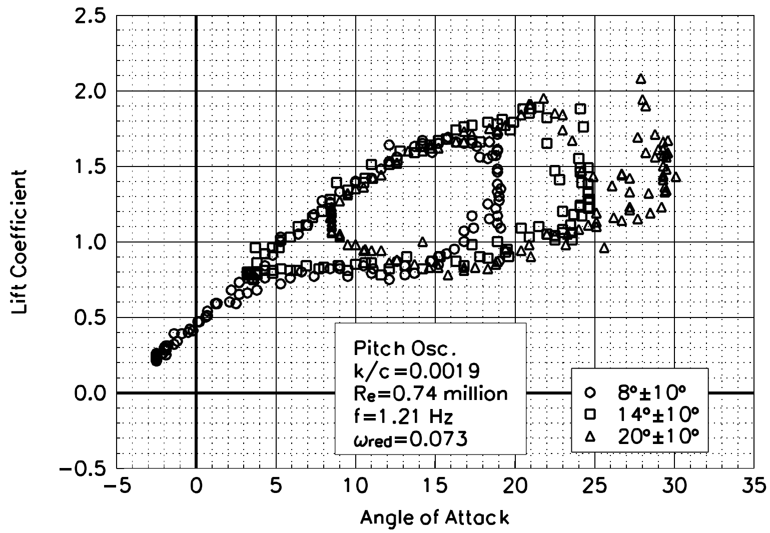

Figure C85. Lift coefficient vs α.

S801
LEGR
Re=0.74 million
$\omega_{reduced}$=0.073

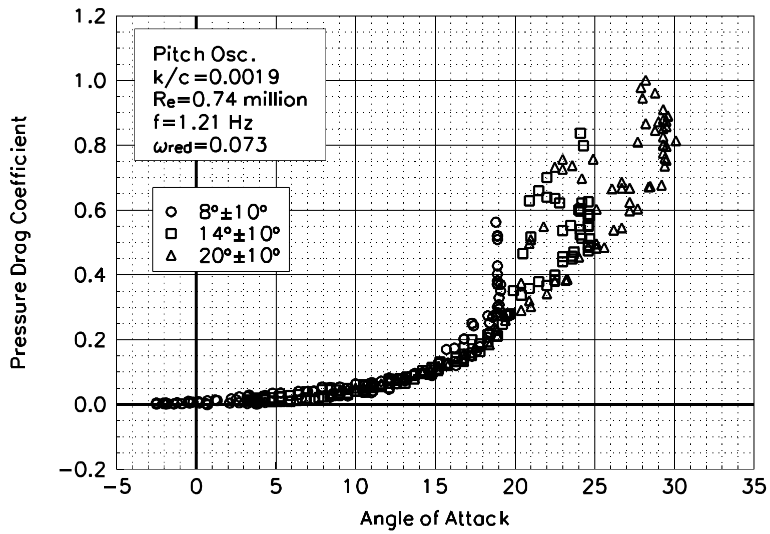

Figure C86. Pressure drag coefficient vs α.

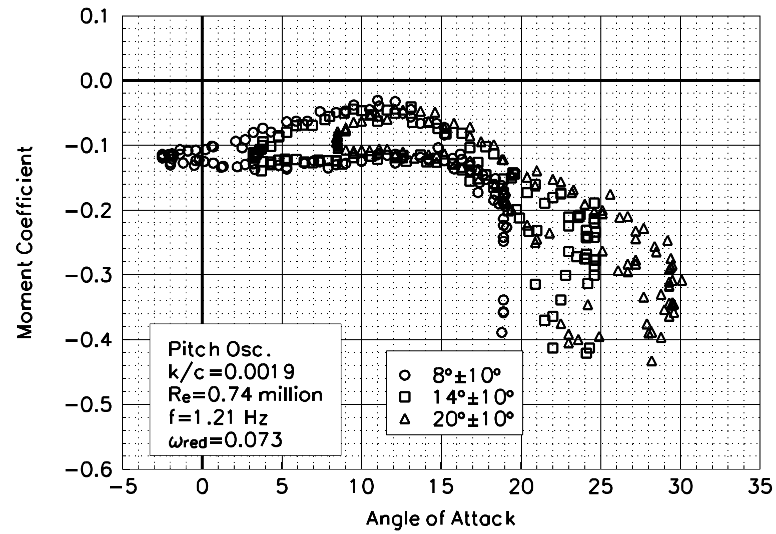

Figure C87. Moment coefficient vs α.

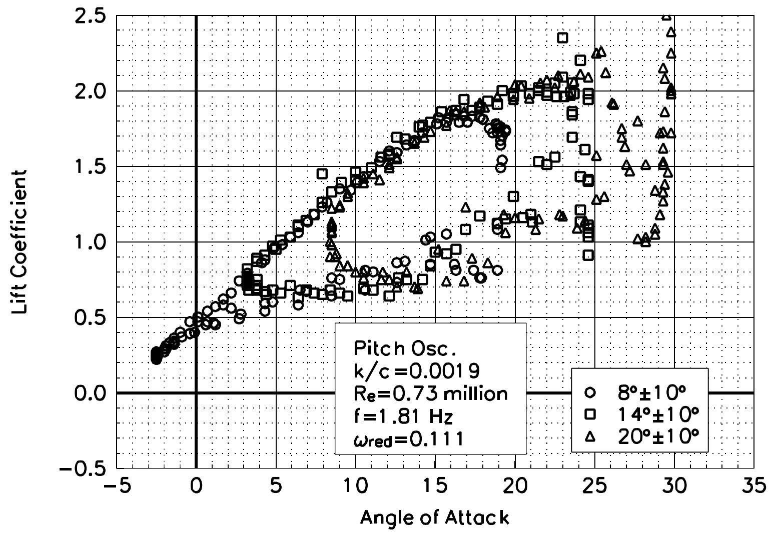

Figure C88. Lift coefficient vs α.

S801
LEGR
Re=0.73 million
$\omega_{reduced}$=0.111

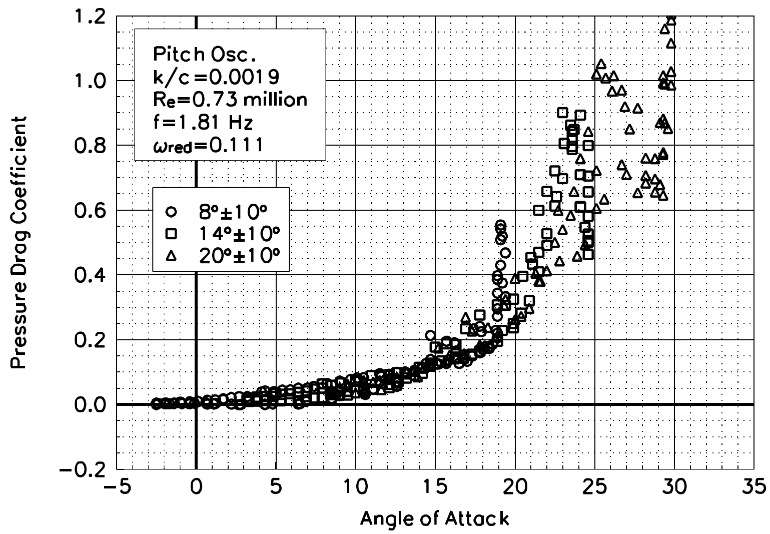

Figure C89. Pressure drag coefficient vs α.

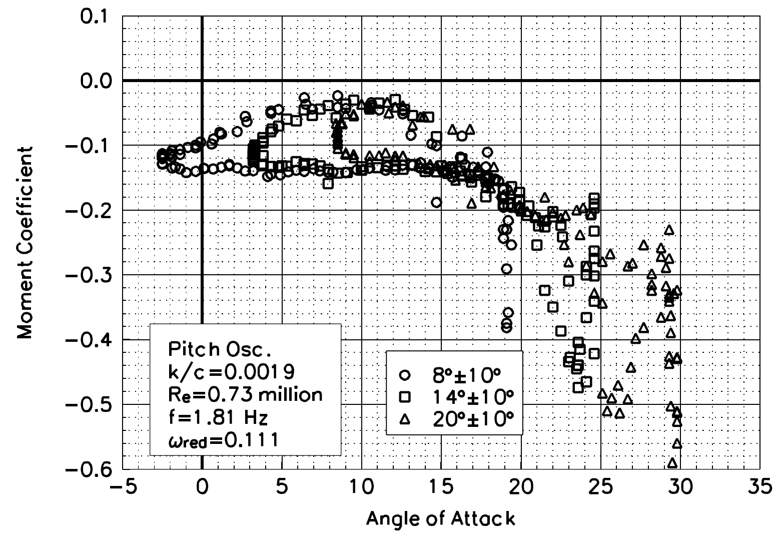

Figure C90. Moment coefficient vs α.

Unsteady Airfoil Characteristics

±10° Sine, Re = 1 million

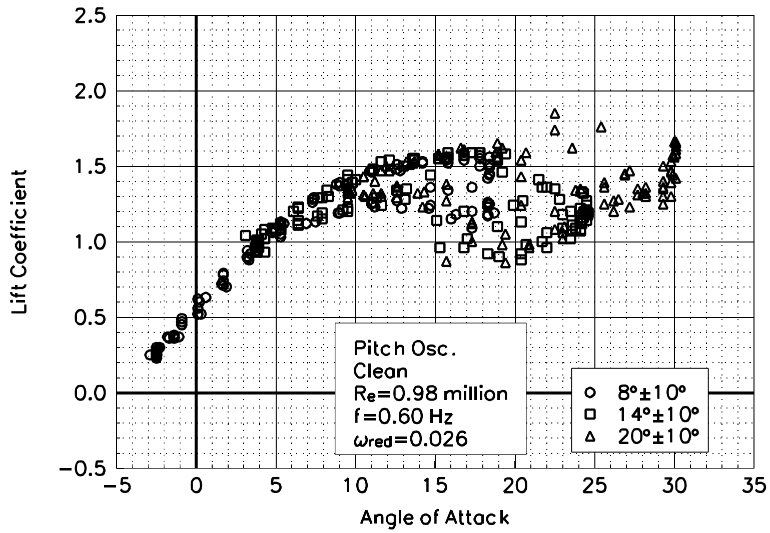

Figure C91. Lift coefficient vs α.

S801
Clean
Re=0.98 million
$\omega_{reduced}$=0.026

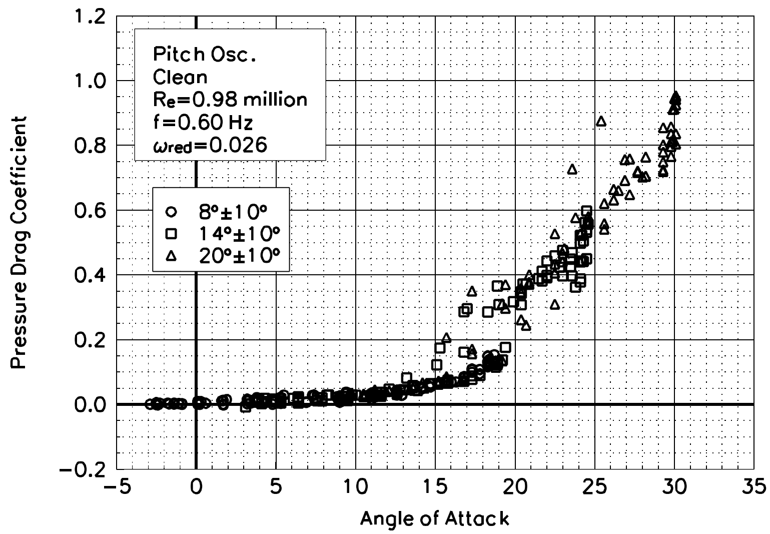

Figure C92. Pressure drag coefficient vs α.

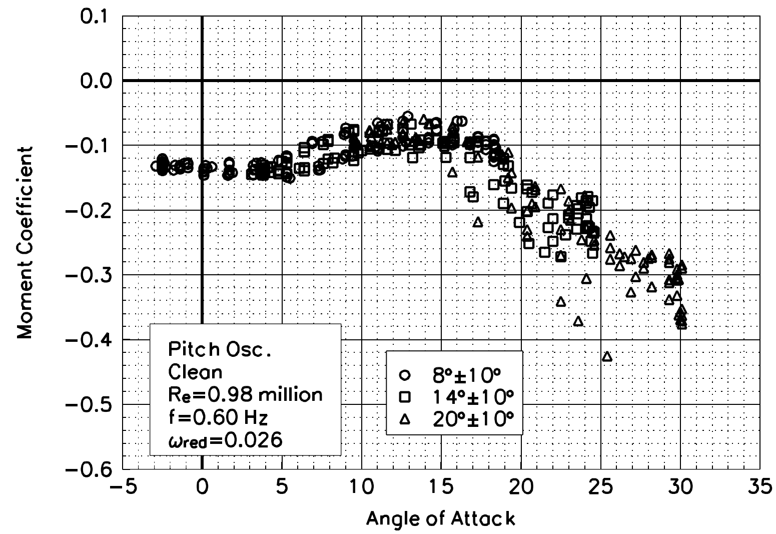

Figure C93. Moment coefficient vs α.

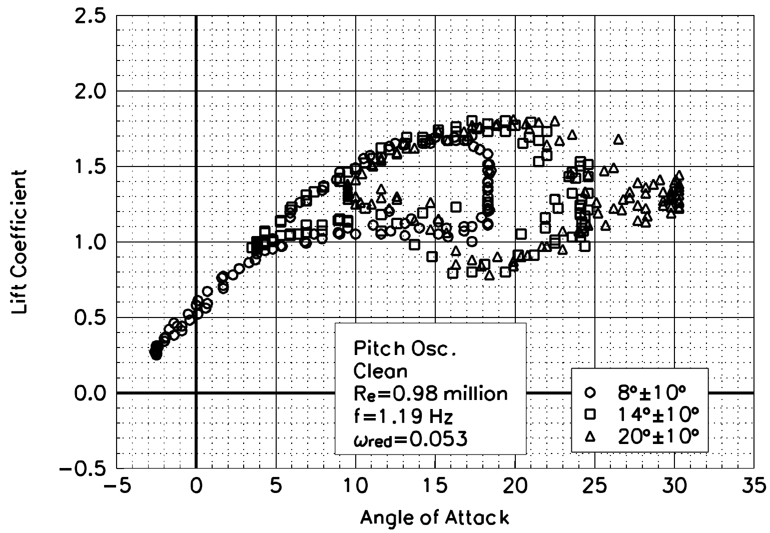

Figure C94. Lift coefficient vs α.

S801
Clean
Re=0.98 million
$\omega_{reduced}$=0.053

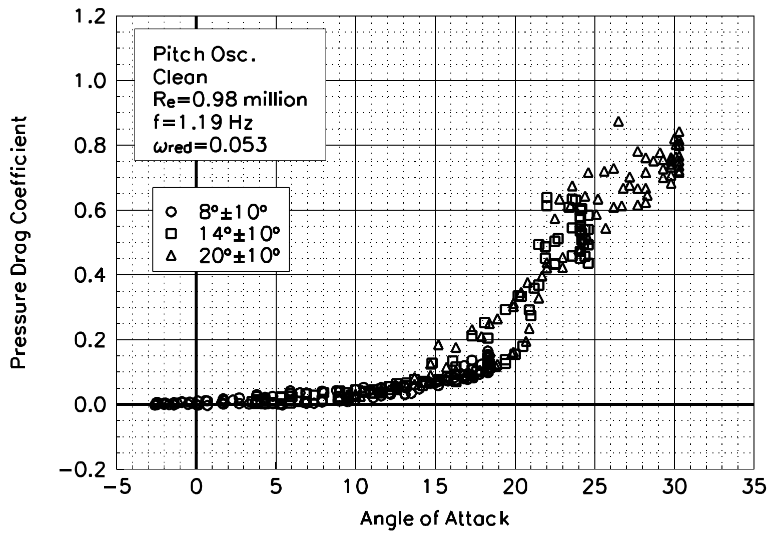

Figure C95. Pressure drag coefficient vs α.

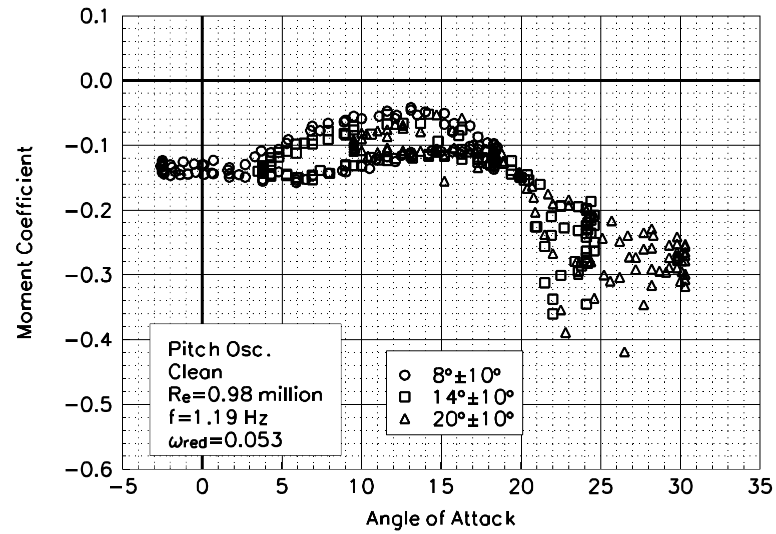

Figure C96. Moment coefficient vs α.

S801
Clean
Re=0.96 million
$\omega_{reduced}$=0.082

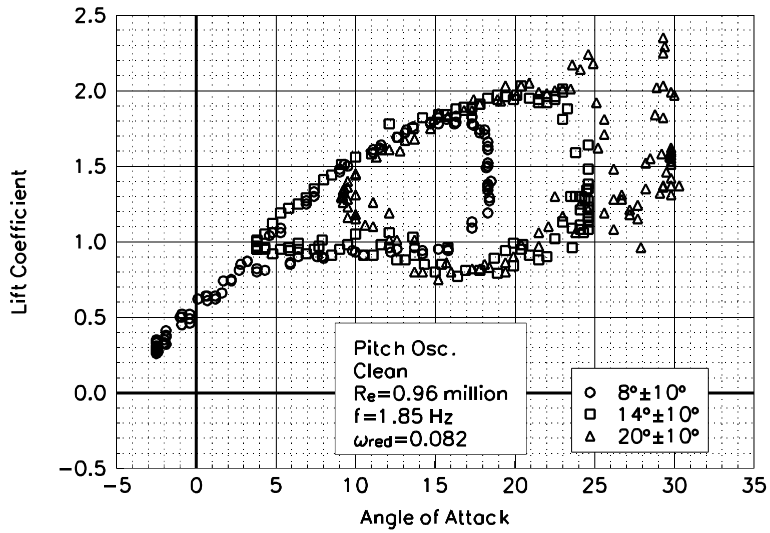

Figure C97. Lift coefficient vs α.

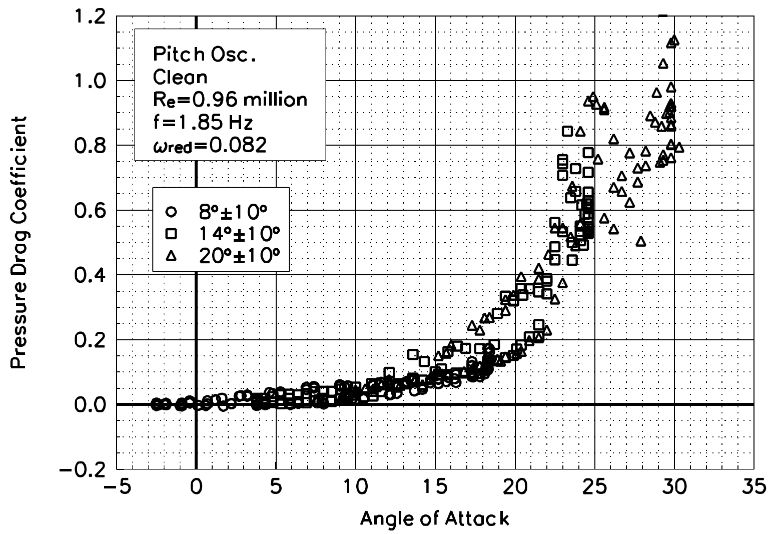

Figure C98. Pressure drag coefficient vs α.

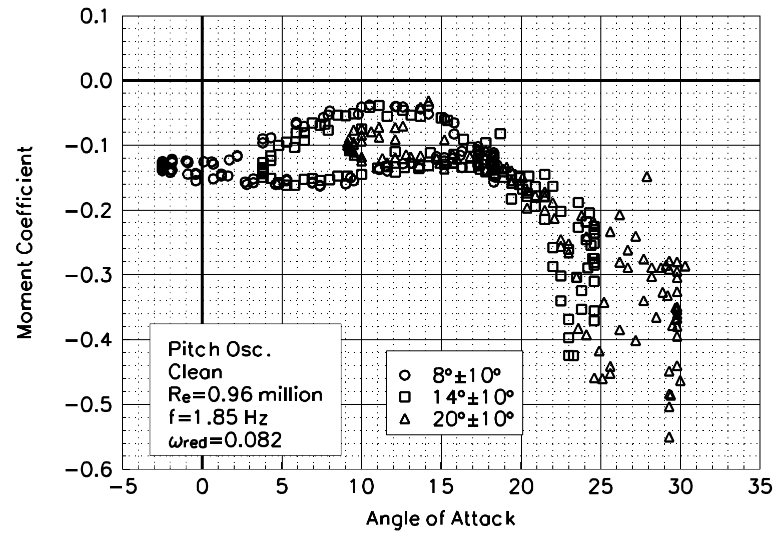

Figure C99. Moment coefficient vs α.

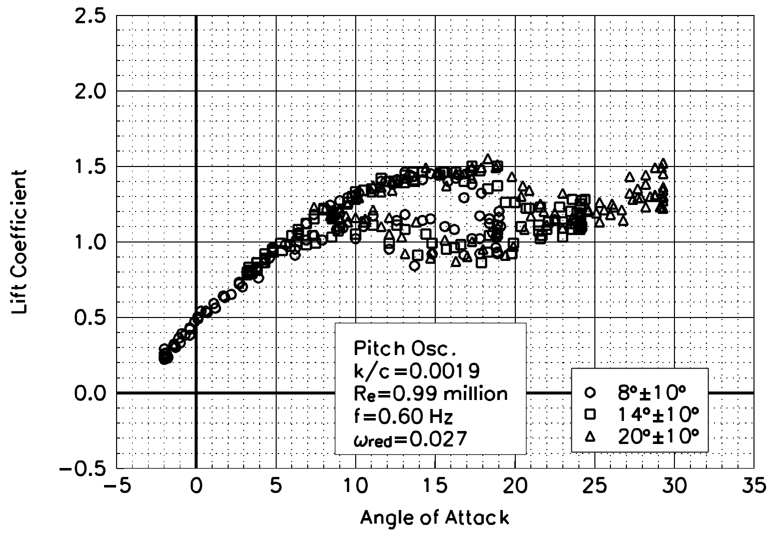

Figure C100. Lift coefficient vs α.

S801
LEGR
Re=0.99 million
$\omega_{reduced}$=0.027

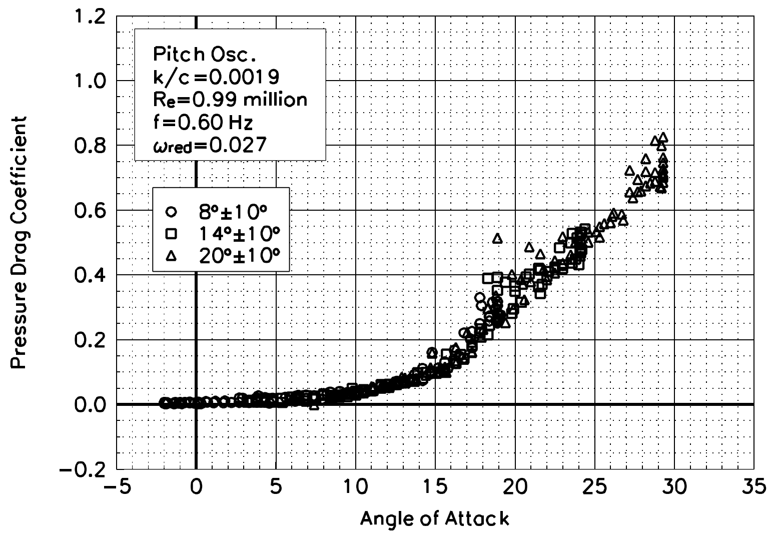

Figure C101. Pressure drag coefficient vs α.

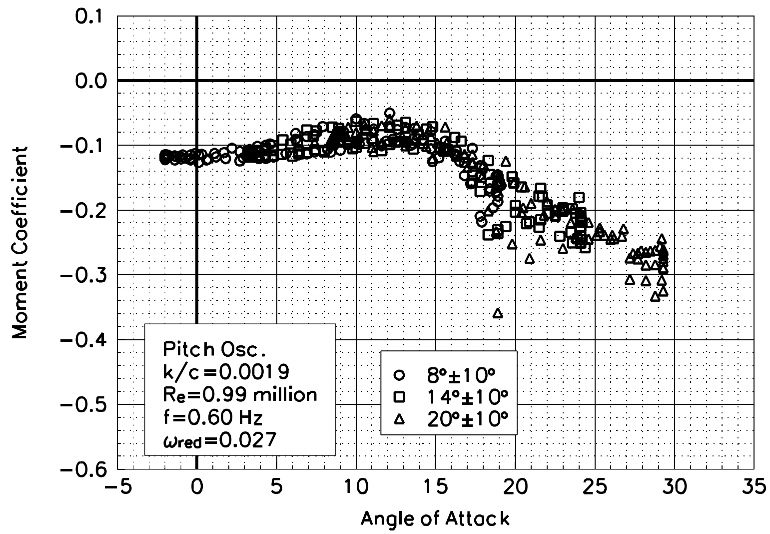

Figure C102. Moment coefficient vs α.

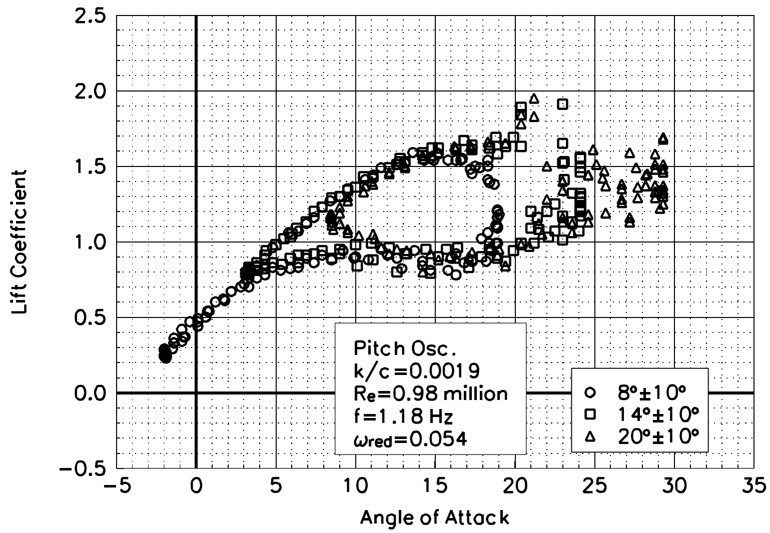

Figure C103. Lift coefficient vs α.

S801
LEGR
Re=0.98 million
$\omega_{reduced}$=0.054

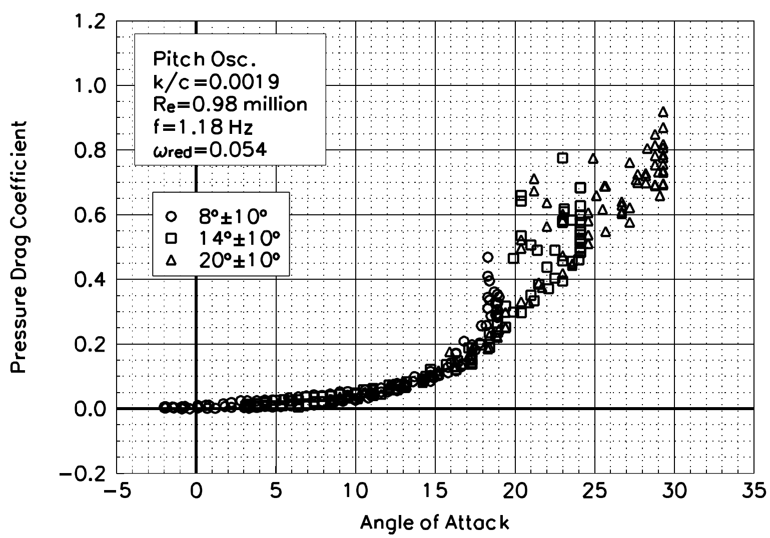

Figure C104. Pressure drag coefficient vs α.

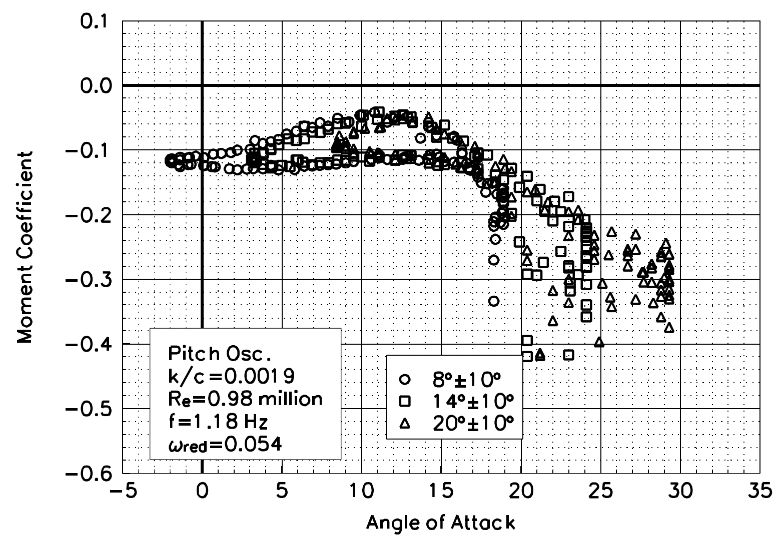

Figure C105. Moment coefficient vs α.

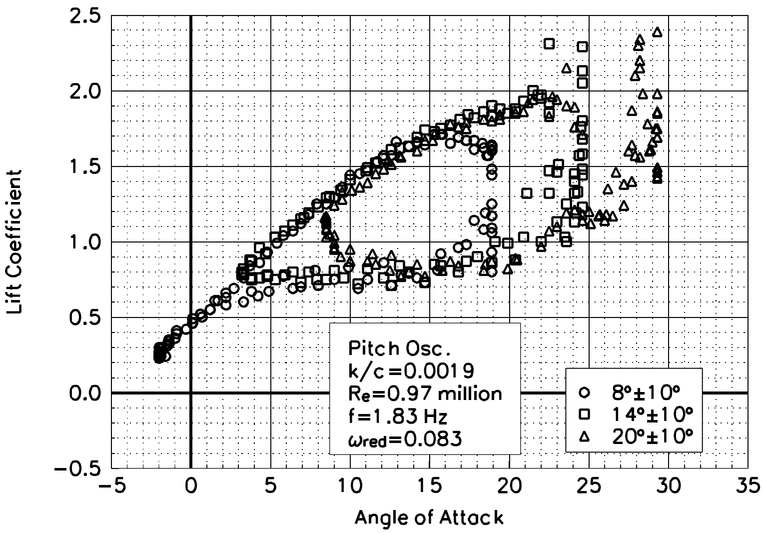

Figure C106. Lift coefficient vs α.

S801
LEGR
Re=0.97 million
$\omega_{reduced}$=0.083

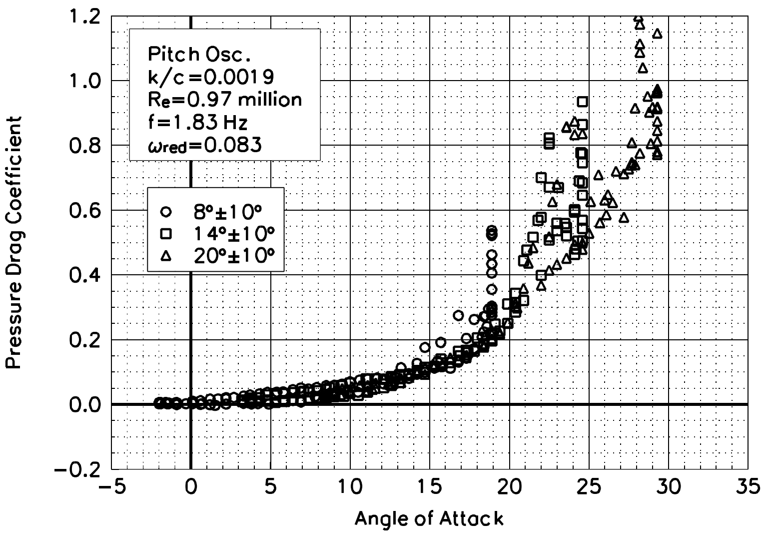

Figure C107. Pressure drag coefficient vs α.

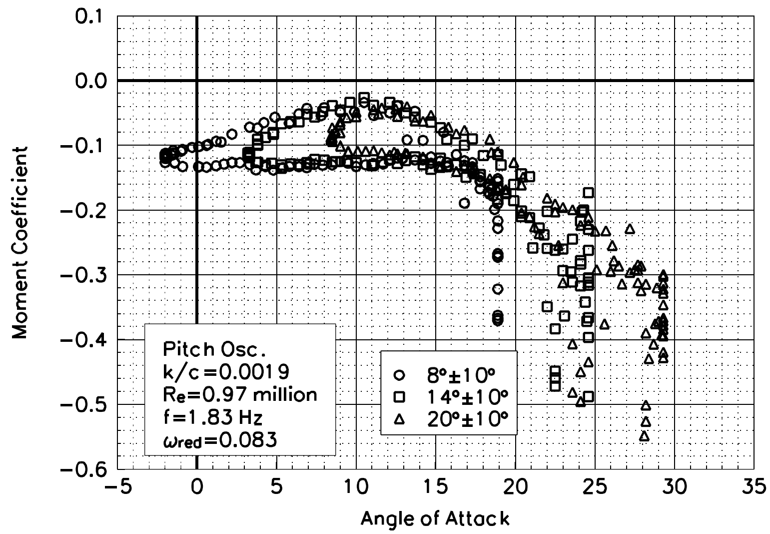

Figure C108. Moment coefficient vs α.

Unsteady Airfoil Characteristics

±10° Sine, Re = 1.25 million

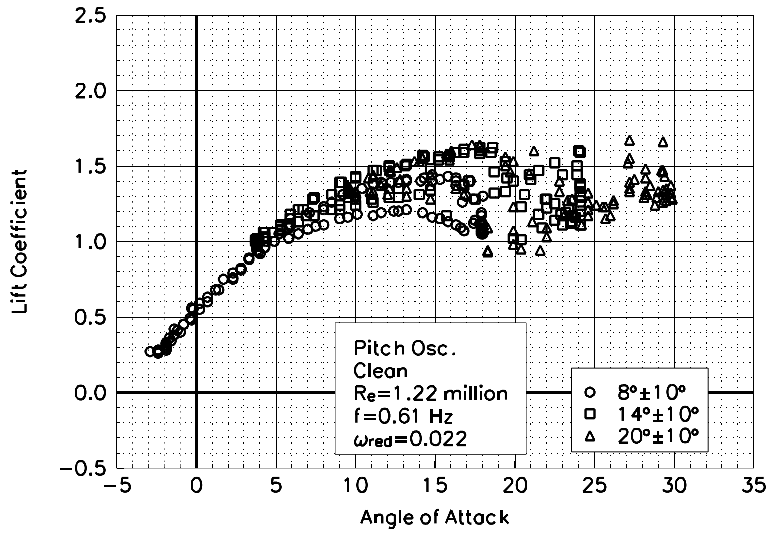

Figure C109. Lift coefficient vs α.

S801
Clean
Re=1.22 million
$\omega_{reduced}$=0.022

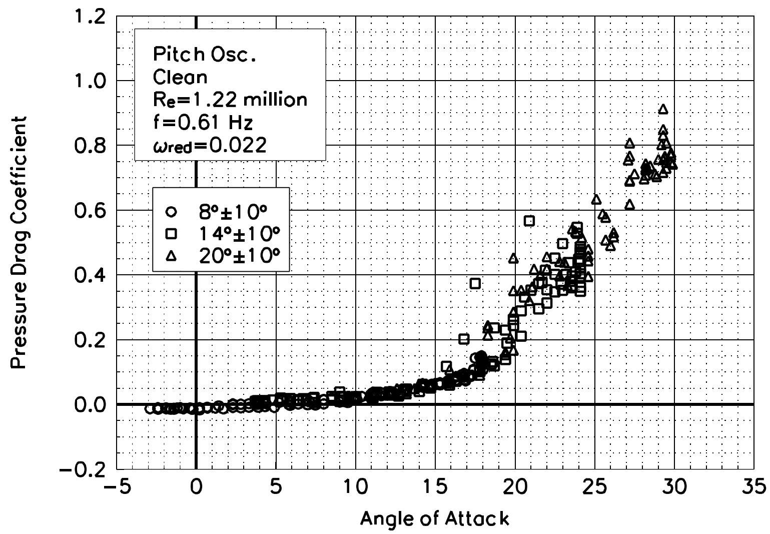

Figure C110. Pressure drag coefficient vs α.

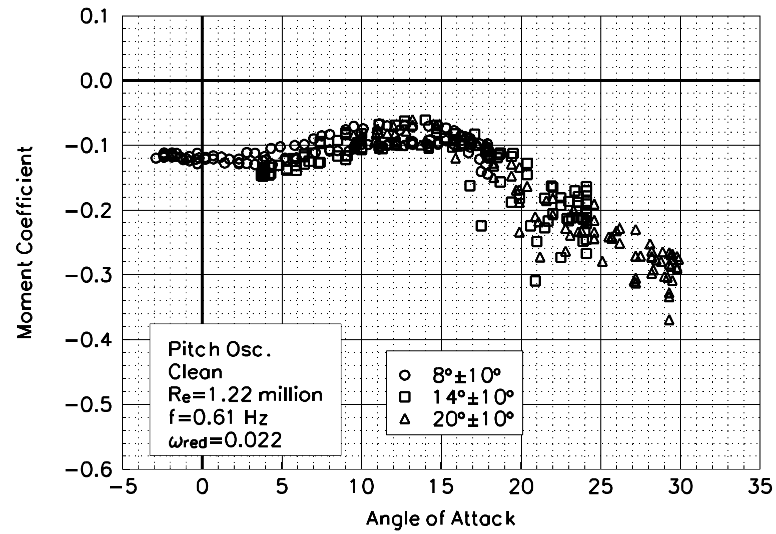

Figure C111. Moment coefficient vs α.

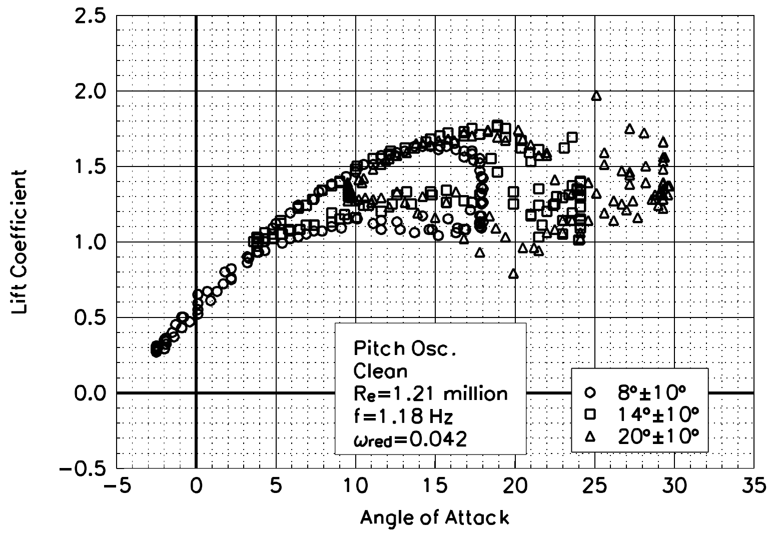

Figure C112. Lift coefficient vs α.

S801
Clean
Re=1.21 million
$\omega_{reduced}$=0.042

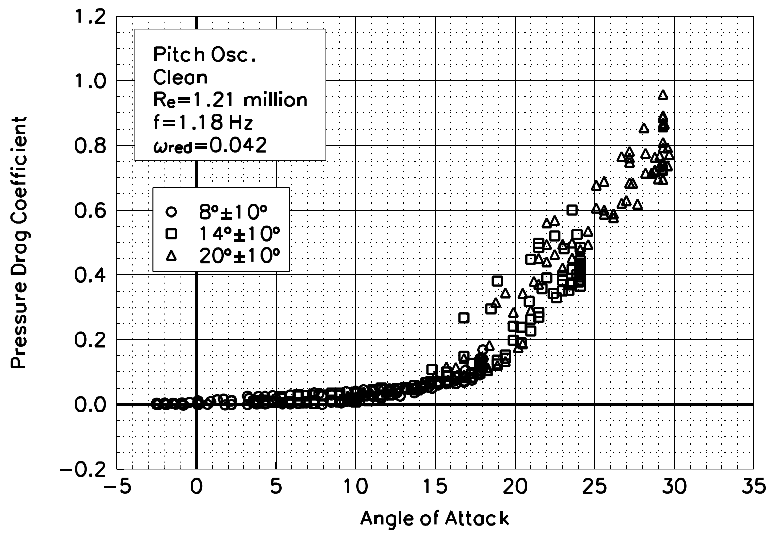

Figure C113. Pressure drag coefficient vs α.

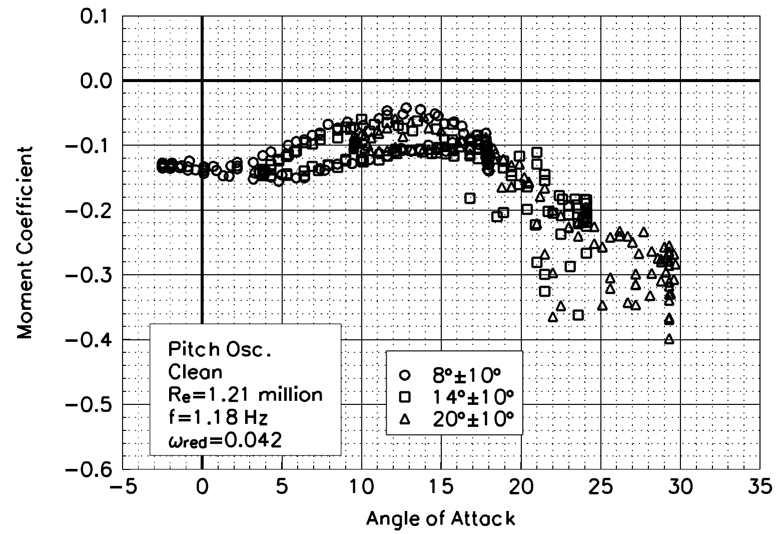

Figure C114. Moment coefficient vs α.

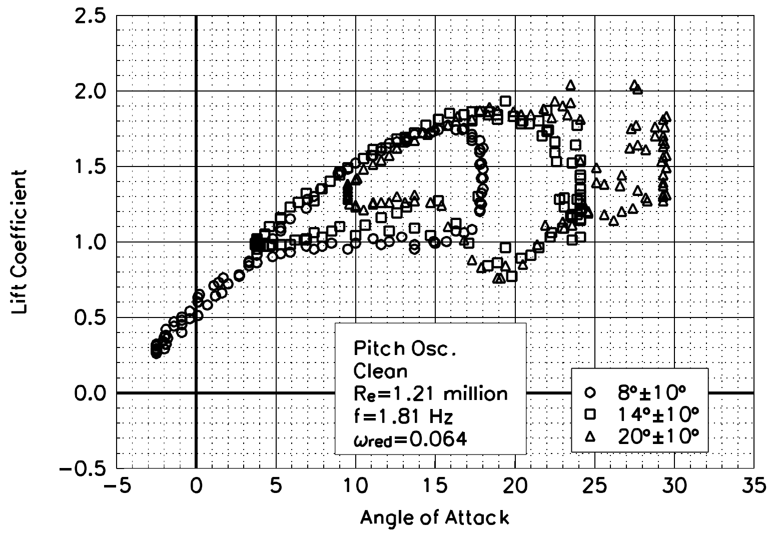

Figure C115. Lift coefficient vs α.

S801
Clean
Re=1.21 million
$\omega_{reduced}$=0.064

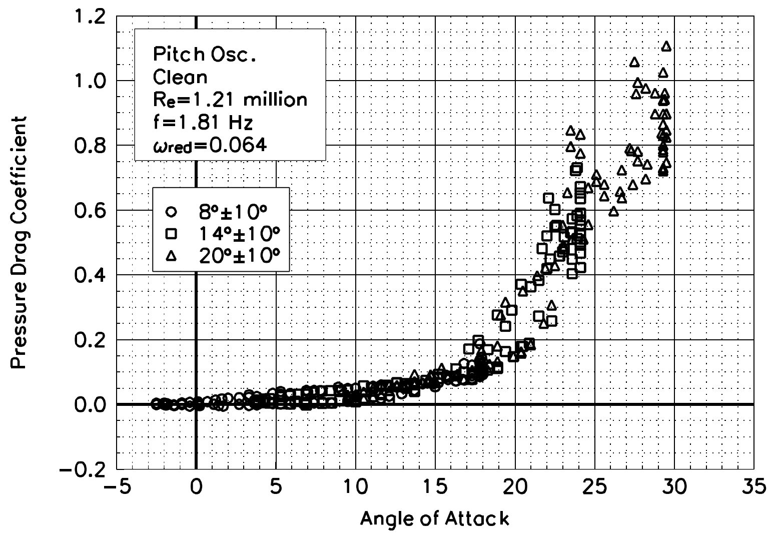

Figure C116. Pressure drag coefficient vs α.

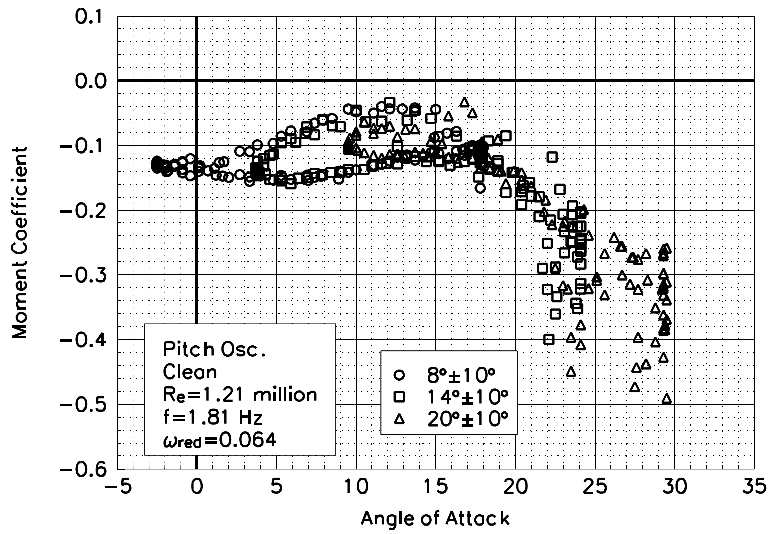

Figure C117. Moment coefficient vs α.

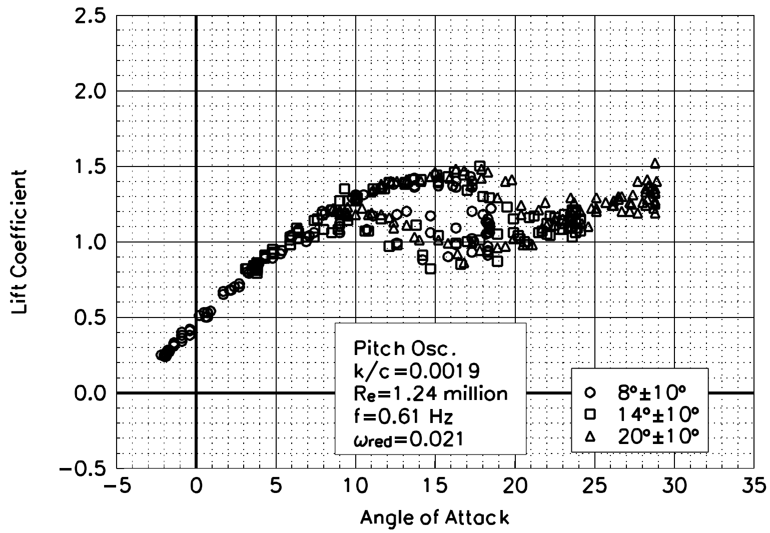

Figure C118. Lift coefficient vs α.

S801
LEGR
Re=1.24 million
$\omega_{reduced}$=0.021

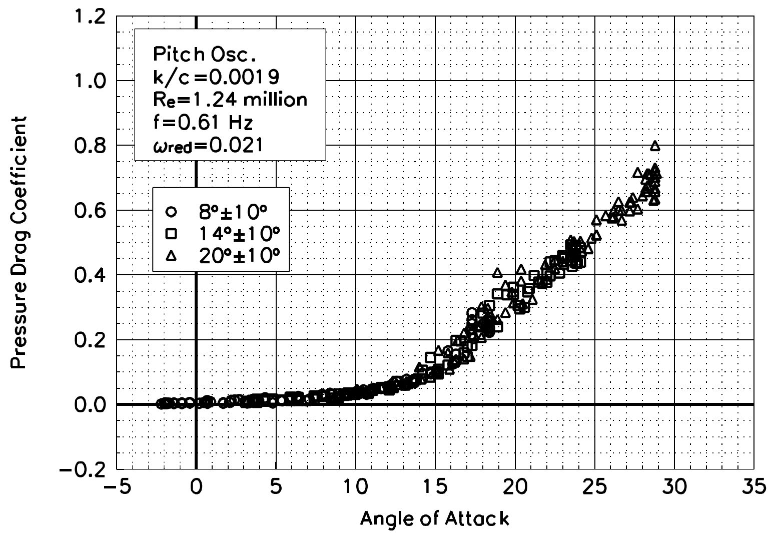

Figure C119. Pressure drag coefficient vs α.

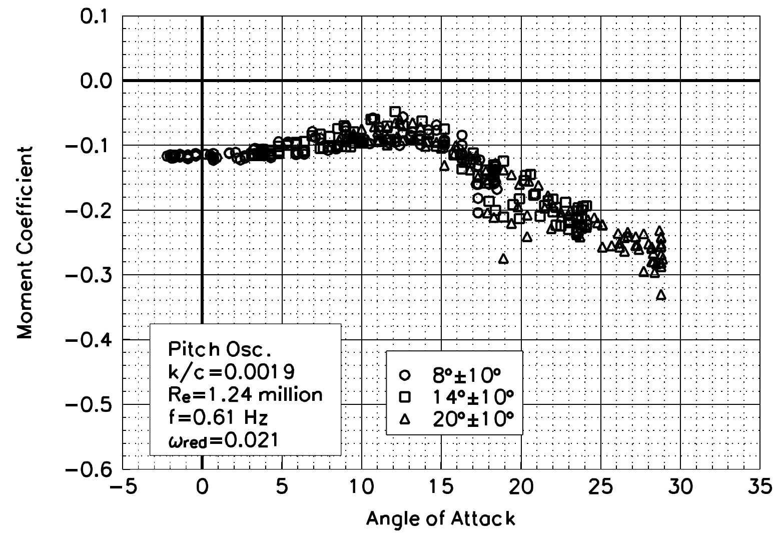

Figure C120. Moment coefficient vs α.

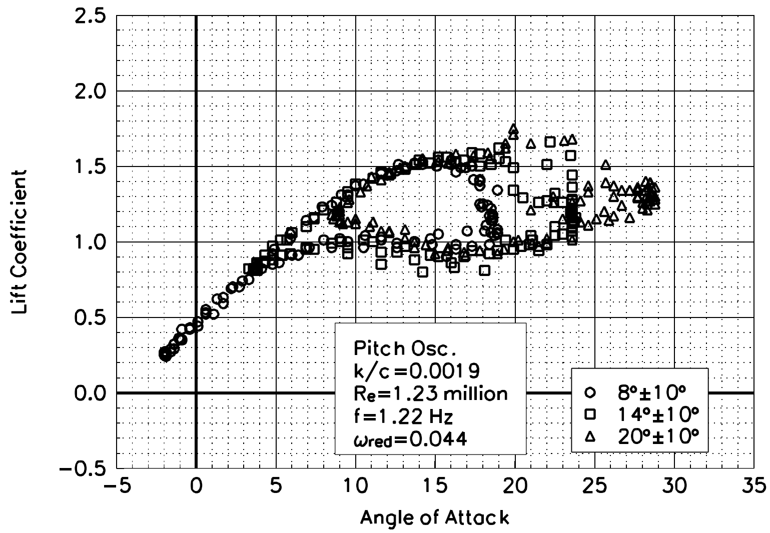

Figure C121. Lift coefficient vs α.

S801
LEGR
Re=1.23 million
$\omega_{reduced}$=0.044

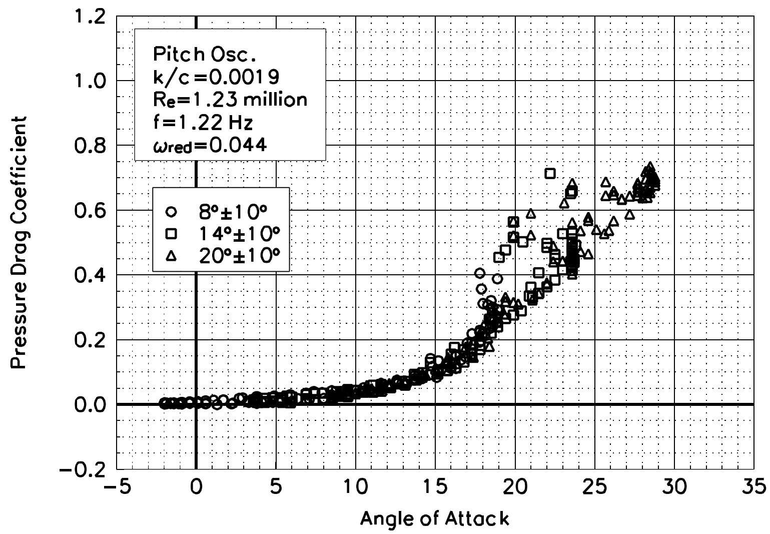

Figure C122. Pressure drag coefficient vs α.

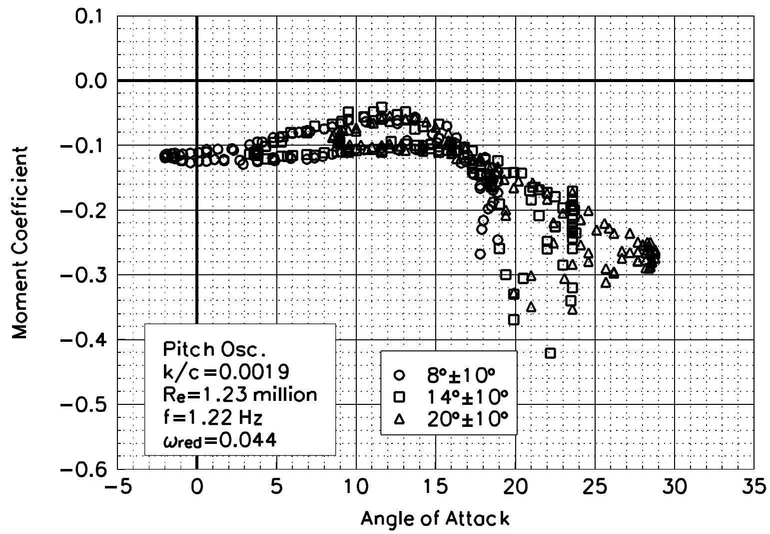

Figure C123. Moment coefficient vs α.

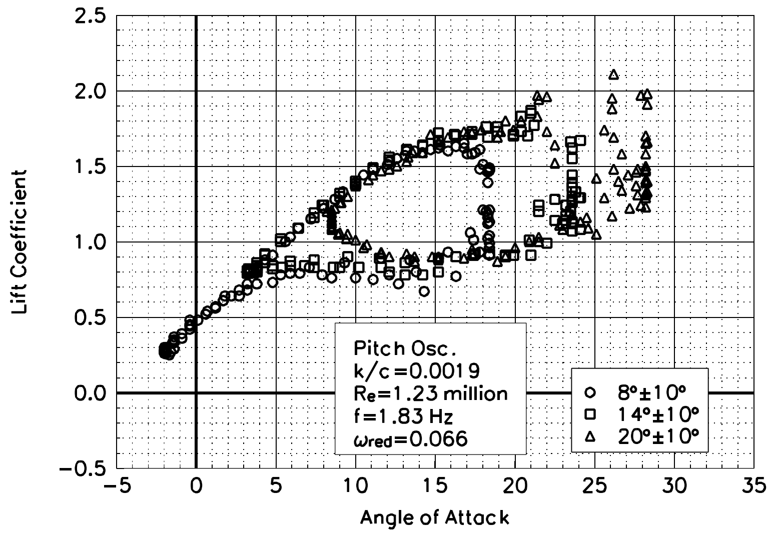

Figure C124. Lift coefficient vs α.

S801
LEGR
Re=1.23 million
$\omega_{reduced}$=0.066

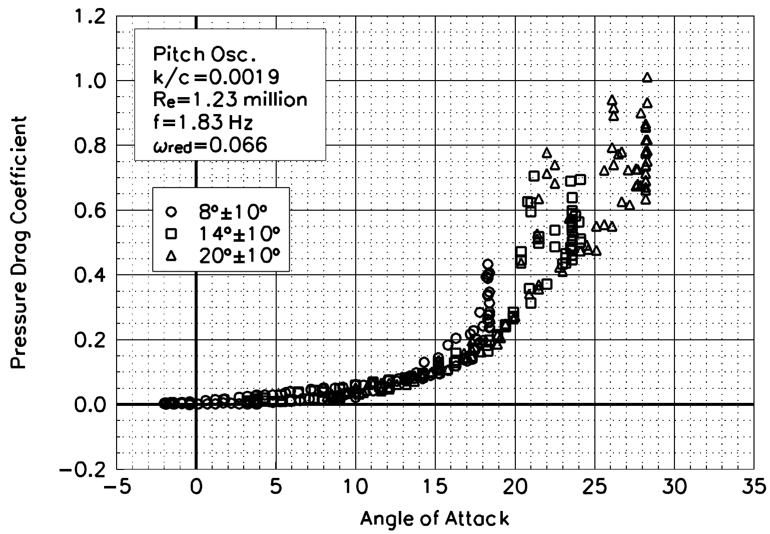

Figure C125. Pressure drag coefficient vs α.

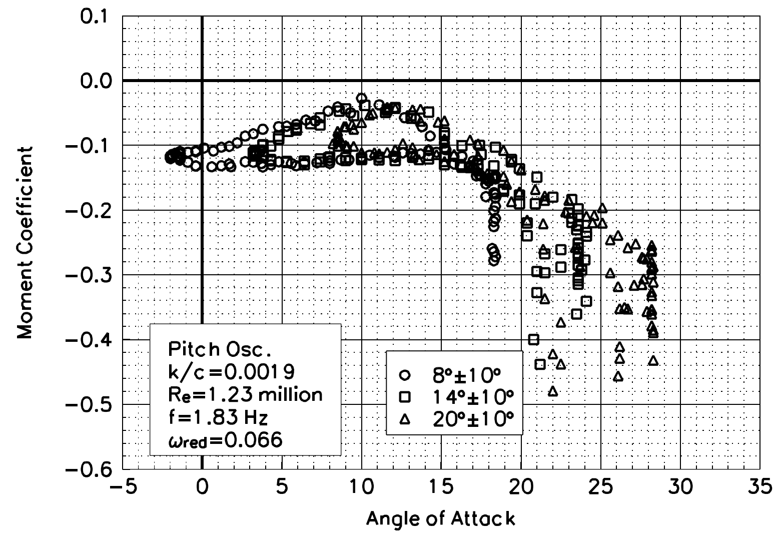

Figure C126. Moment coefficient vs α.

Unsteady Airfoil Characteristics

±10° Sine, Re = 1.4 million

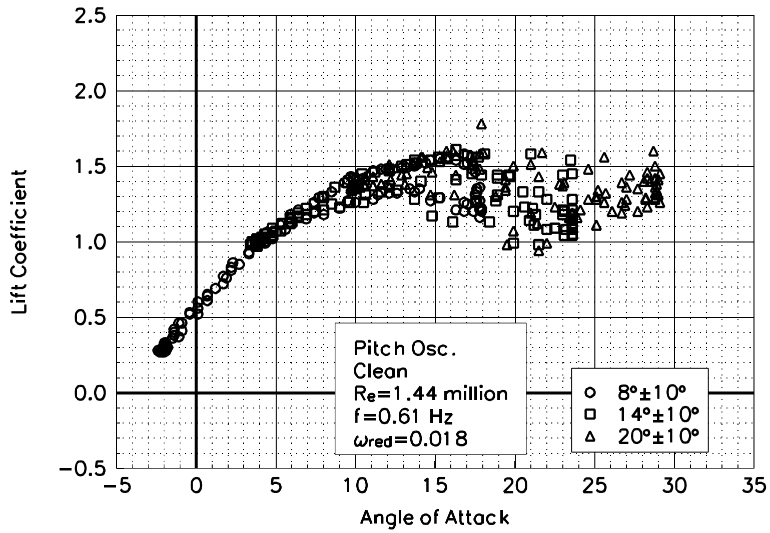

Figure C127. Lift coefficient vs α.

S801
Clean
Re=1.44 million
$\omega_{reduced}$=0.018

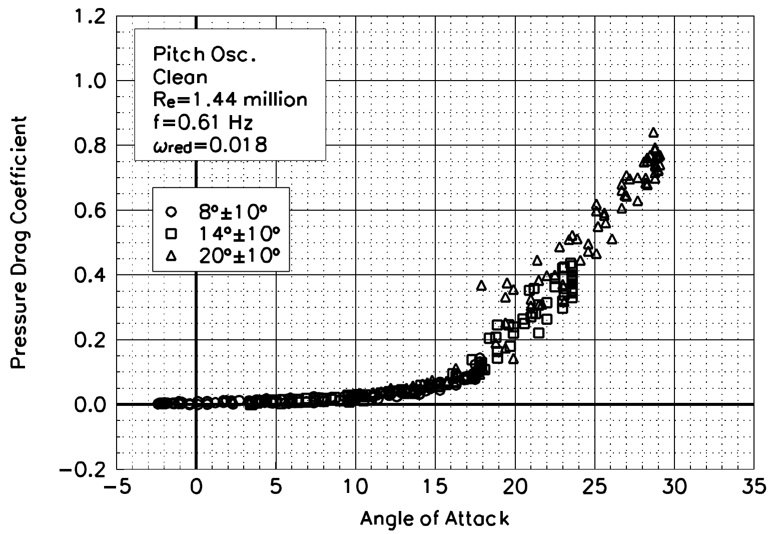

Figure C128. Pressure drag coefficient vs α.

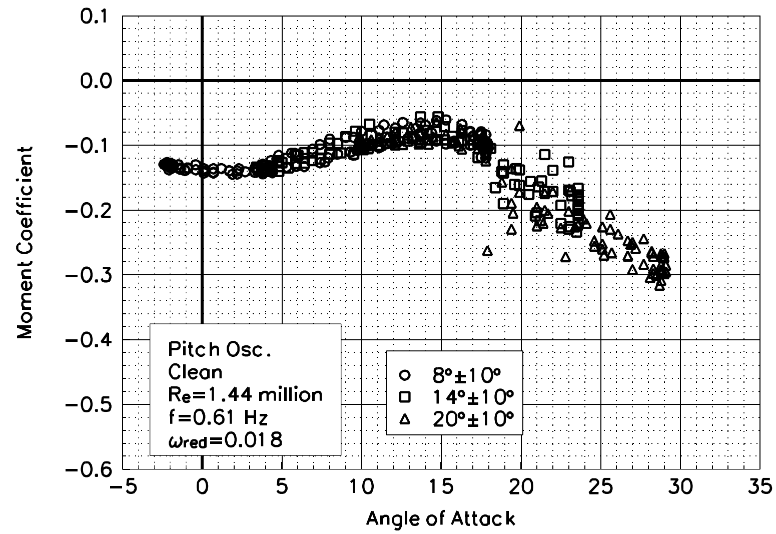

Figure C129. Moment coefficient vs α.

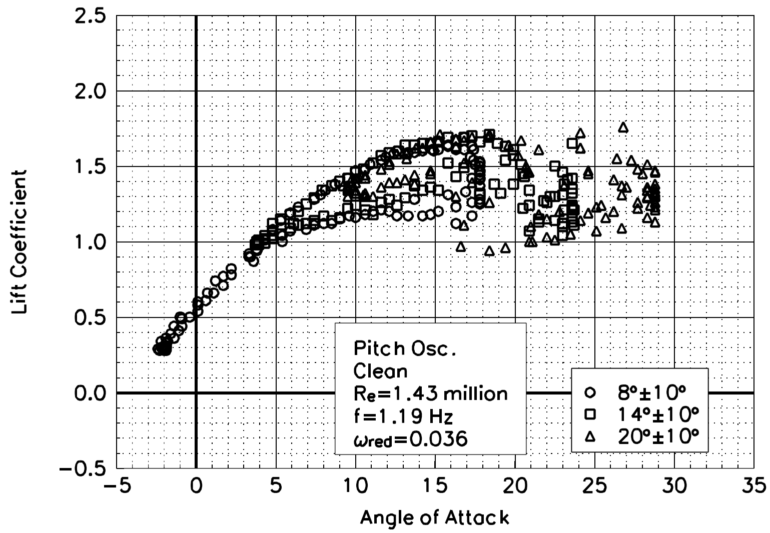

Figure C130. Lift coefficient vs α.

S801
Clean
Re=1.43 million
$\omega_{reduced}$=0.036

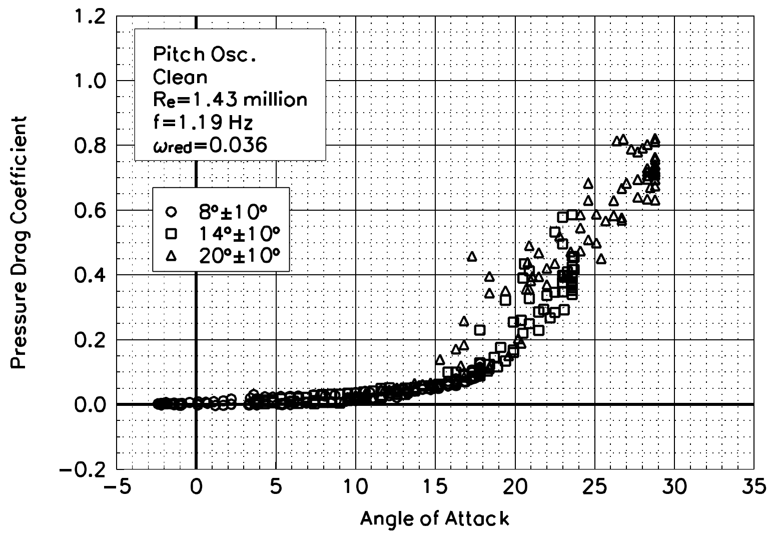

Figure C131. Pressure drag coefficient vs α.

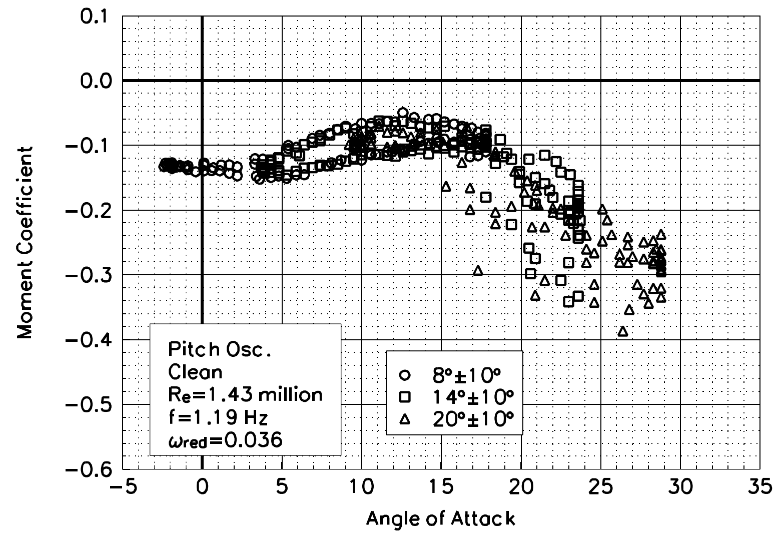

Figure C132. Moment coefficient vs α.

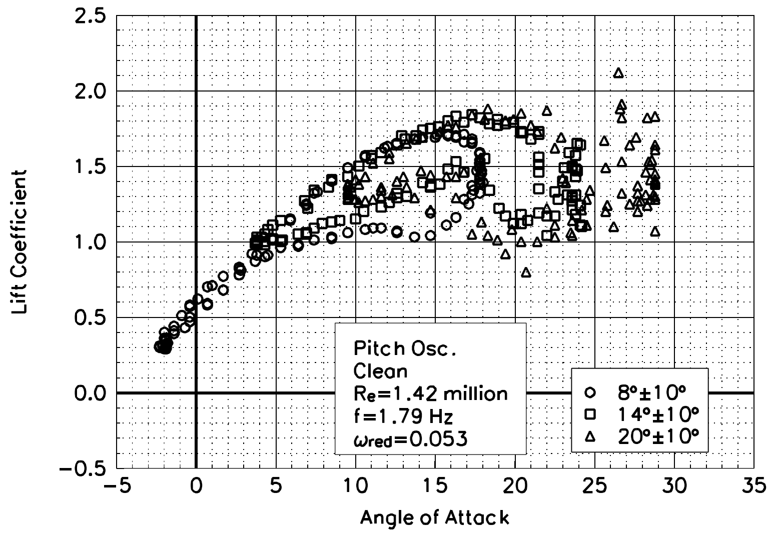

Figure C133. Lift coefficient vs α.

S801
Clean
Re=1.42 million
$\omega_{reduced}$=0.053

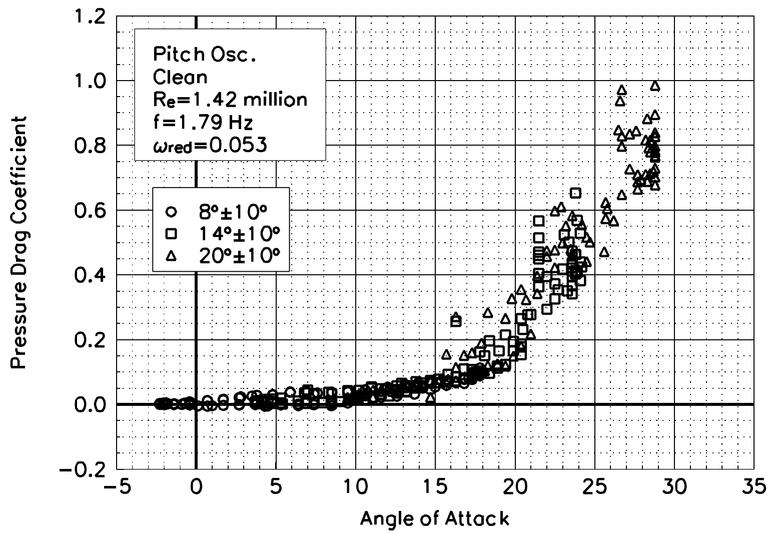

Figure C134. Pressure drag coefficient vs α.

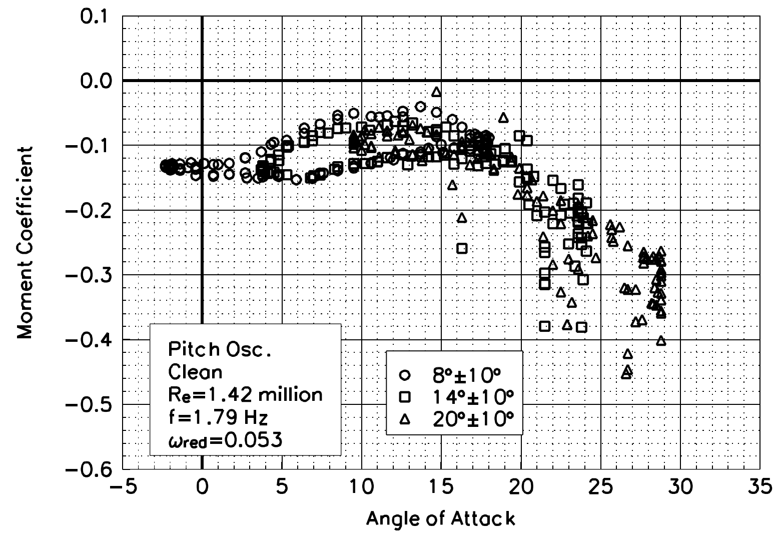

Figure C135. Moment coefficient vs α.

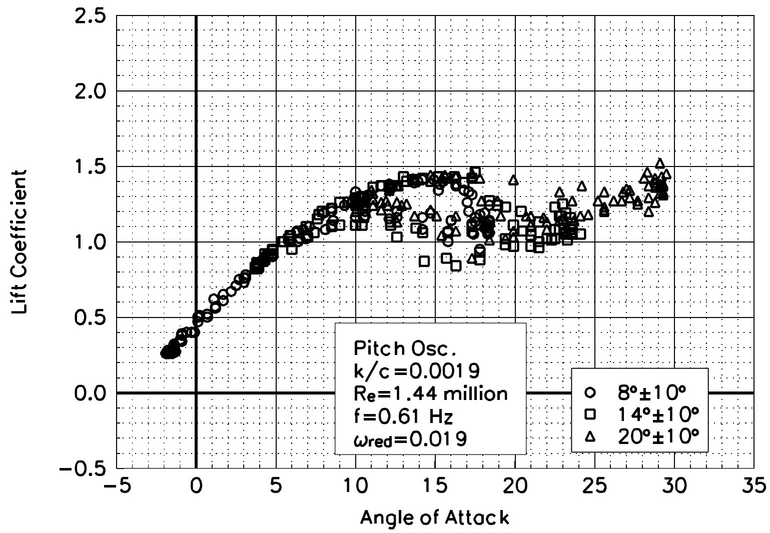

Figure C136. Lift coefficient vs α.

S801
LEGR
Re=1.44 million
$\omega_{reduced}$=0.019

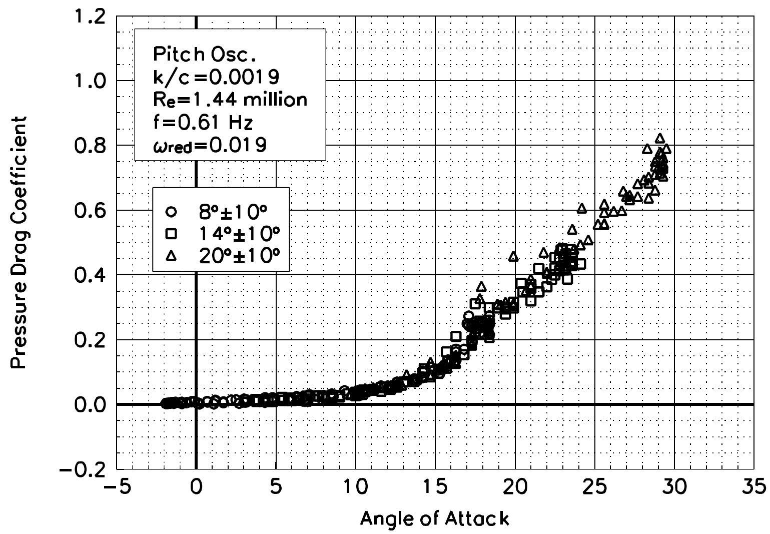

Figure C137. Pressure drag coefficient vs α.

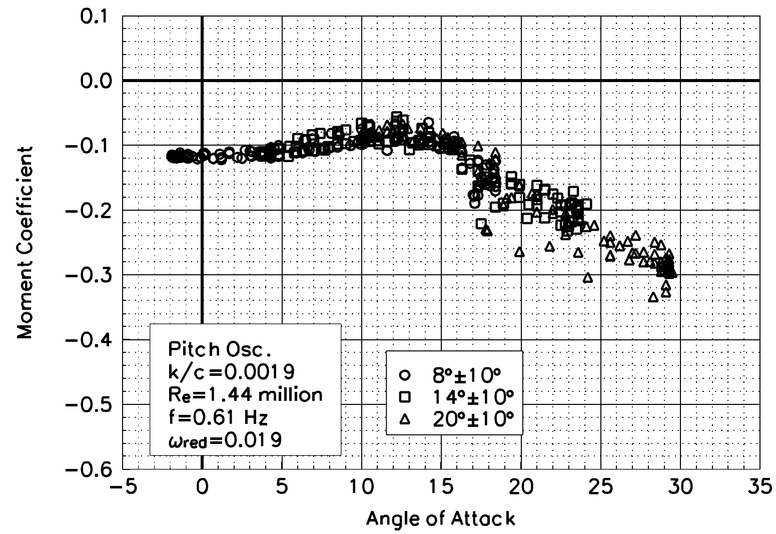

Figure C138. Moment coefficient vs α.

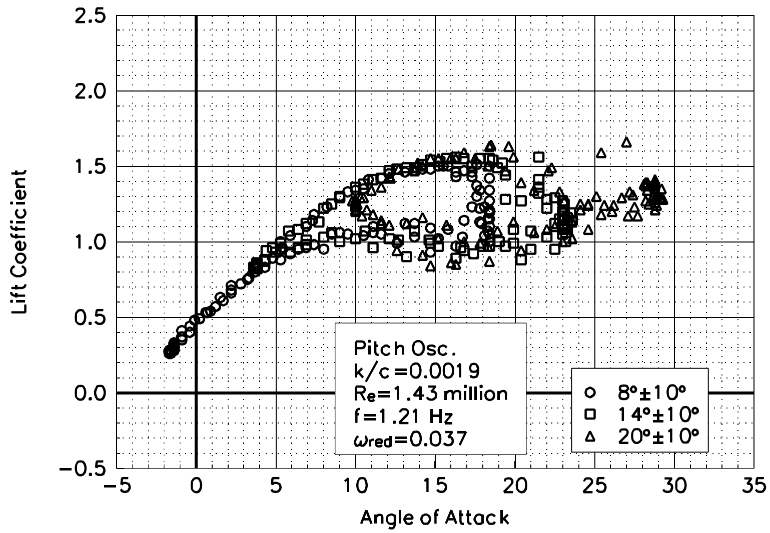

Figure C139. Lift coefficient vs α.

S801
LEGR
Re=1.43 million
$\omega_{reduced}$=0.037

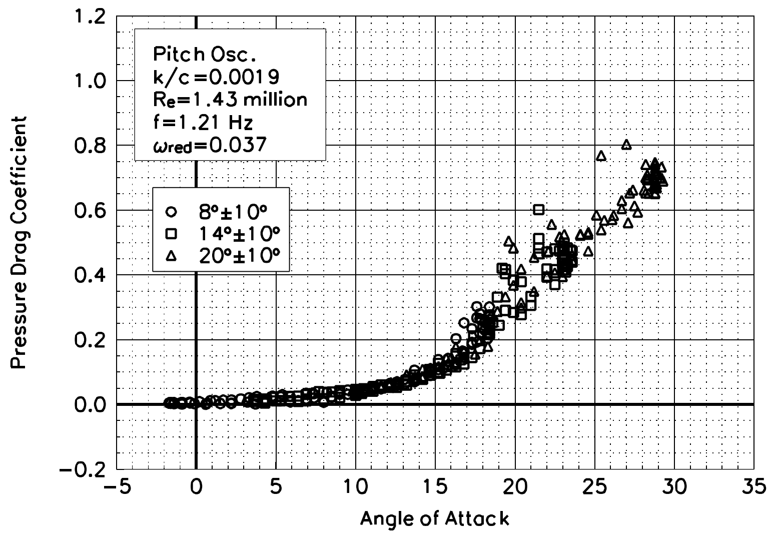

Figure C140. Pressure drag coefficient vs α.

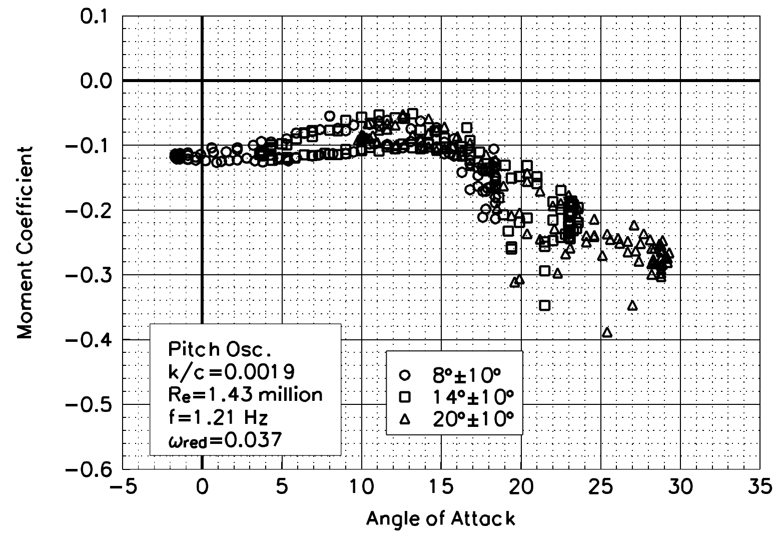

Figure C141. Moment coefficient vs α.

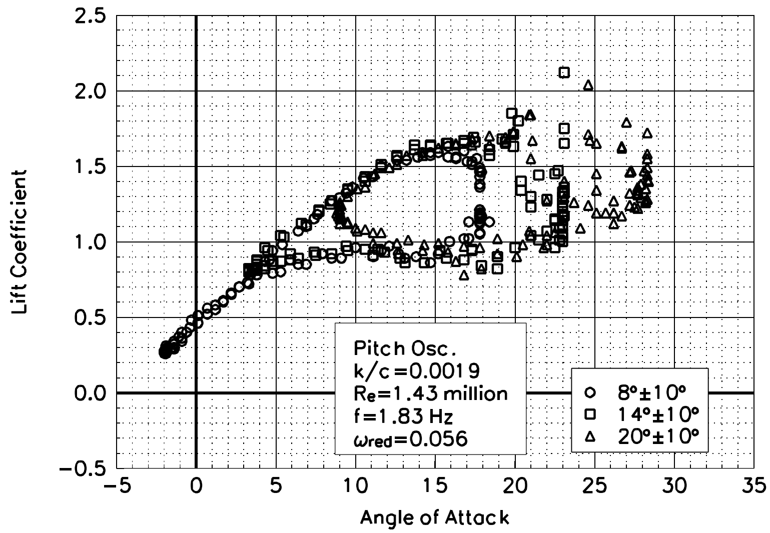

Figure C142. Lift coefficient vs α.

S801
LEGR
Re=1.43 million
$\omega_{reduced}$=0.056

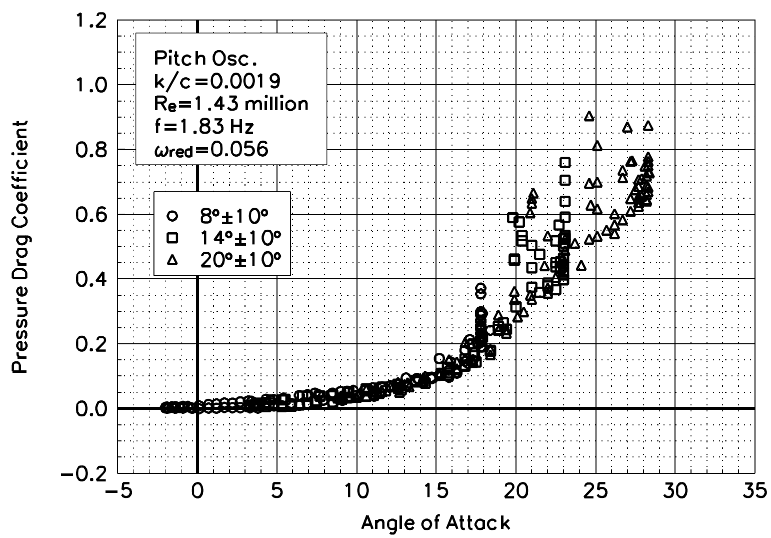

Figure C144. Pressure drag coefficient vs α.

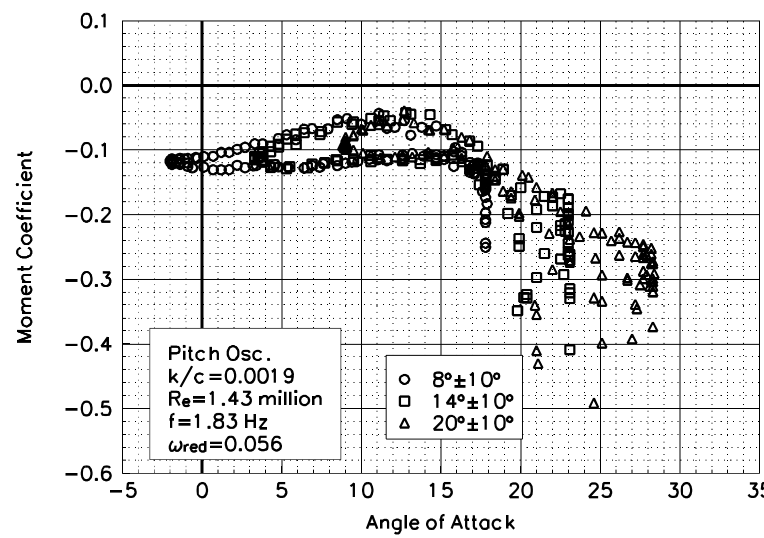

Figure C143. Moment coefficient vs α.